TESIS DE LA UNIVERSIDAD DE ZARAGOZA

2014

42

Patricia Larrea Márquez

The magmatic evolution of Graciosa and Corvo oceanic islands, Azores Archipielago

Departamento
Ciencias de la Tierra

Director/es
Widom, Elisabeth
França, Zilda
Lago San José, Marceliano

ISSN 2254-7606

Prensas de la Universidad Universidad Zaragoza

Universidad Zaragoza
1542

Tesis Doctoral

THE MAGMATIC EVOLUTION OF GRACIOSA AND CORVO OCEANIC ISLANDS, AZORES ARCHIPIELAGO

Autor

Patricia Larrea Márquez

Director/es

Widom, Elisabeth
França, Zilda
Lago San José, Marceliano

UNIVERSIDAD DE ZARAGOZA

Ciencias de la Tierra

2014

THE MAGMATIC EVOLUTION OF GRACIOSA AND CORVO OCEANIC ISLANDS, AZORES ARCHIPELAGO

PATRICIA LARREA MÁRQUEZ

TESIS DOCTORAL 2014
UNIVERSIDAD DE ZARAGOZA

THE MAGMATIC EVOLUTION OF GRACIOSA AND CORVO OCEANIC ISLANDS, AZORES ARCHIPELAGO

PATRICIA LARREA MÁRQUEZ

PhD THESIS 2014

UNIVERSIDAD DE ZARAGOZA
DEPARTAMENTO DE CIENCIAS DE LA TIERRA
GRUPO DE INVESTIGACIÓN GEOTRANSFER

Supervisors

Dr. Marceliano Lago San José (Universidad de Zaragoza, Spain)

Dr. Zilda França (Universidade dos Açores, Portugal)

Dr. Elisabeth Widom (Miami University, USA)

Nalgumas ilhas, onde o vulcanismo se extinguiu há muito e onde as formas, profundamente gastas pela erosão, perderam a sua estrutura primitiva, só o observador entendido se aperceberá de cómo elas se formaram, emergindo das águas pela acumulação sucessiva de materiais eruptivos.

António de Brum Ferreira (1968)

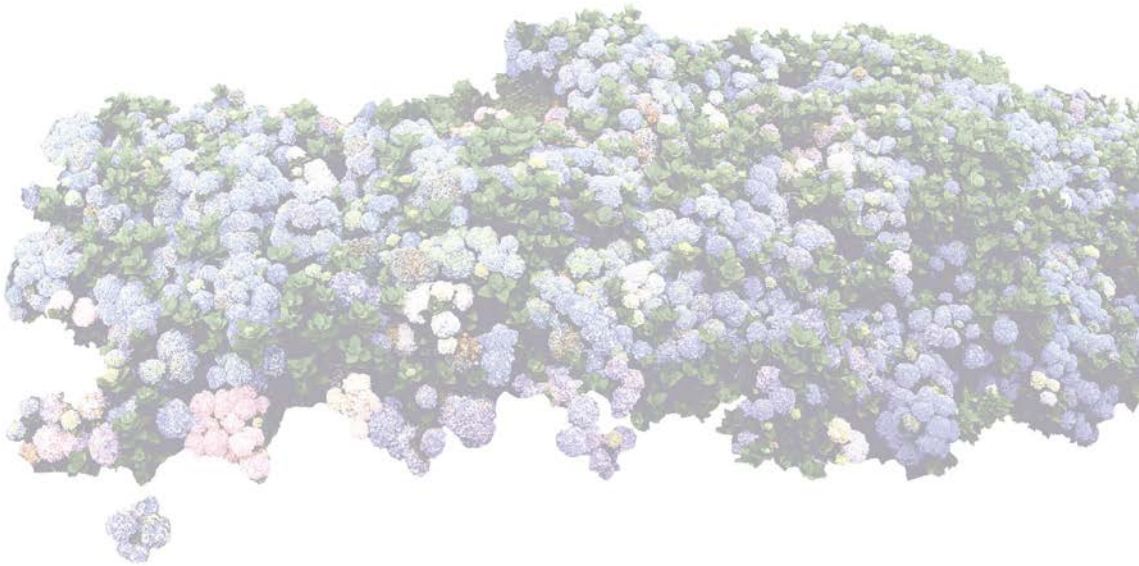

TABLE OF CONTENTS

PART II: STUDY OF GRACIOSA ISLAND

AGRADECIMIENTOS

Una vez llegado a este punto me gustaría tener en cuenta a todas las personas que de un modo u otro han colaborado en la realización de este trabajo de investigación de cuatro años de duración. Son muchos los que han estado ahí, y me han apoyado tanto en los buenos momentos como en los más agridulces, así que espero no dejarme a nadie en estas líneas de agradecimiento.

En primer lugar, quiero agradecer toda la ayuda recibida por parte de mis directores de Tesis, los Dres. Marceliano Lago, Zilda França y Elisabeth Widom. Ellos me dieron la oportunidad de empezar a descubrir el apasionante mundo de la petrología y la geoquímica en un paraje inigualable: el Archipiélago de las Azores.

Marce, como siempre, ha estado dispuesto a ayudar en todo momento, incansable en el campo y totalmente disponible durante el día a día. Me ha enseñado que un buen investigador tiene que cumplir tres requisitos: (1) paso corto, (2) vista larga y (3) mala leche. Y creo que más o menos cumplo los tres requisitos, aunque él diga que del tercero me sobra un poco.

Zilda, se ha convertido en estos años en un gran apoyo para mí; su buen hacer y su cercanía (a pesar de la distancia) ha supuesto un pilar muy importante en el desarrollo de esta tesis. Es una gran conocedora de estas preciosas islas del Atlántico, de tal forma que ha sido la mejor guía de campo, y mi contacto directo con la vulcanología y el complejo mundo de las publicaciones en portugués.

Elisabeth también ha estado disponible en todo momento; nunca pensé que sería tan fácil comunicarse con alguien a pesar de las seis horas de diferencia horaria. Sus aportaciones en la geoquímica de esta tesis son inestimables, además, he aprendido mucho sobre qué y cómo se debe publicar, gracias a sus interminables correcciones

en los primeros *papers*. Le estoy especialmente agradecida por abrirme las puertas de su laboratorio y de su casa, sin apenas conocerme, y facilitar mi primera inmersión al otro lado del Atlántico. Además, no puedo estar más contenta por la oportunidad que me brinda para seguir en este apasionante mundo de la investigación.

También tengo que agradecer infinitamente la ayuda del Dr. Carlos Galé y la Dra. Teresa Ubide, que a pesar de que no figuren como directores de esta tesis, me han dado la oportunidad de trabajar junto a ellos día tras día ¡ni que decir tiene toda su labor formativa e infinita paciencia! Todo lo bueno que pueda decir de ellos se queda corto, ya que no son tan sólo los mejores compañeros de trabajo que he podido soñar, sino que también se han convertido en dos de mis grandes amigos.

Quiero agradecer también el apoyo recibido por el resto de los integrantes del auto-denominado grupo *petroZ*: Kike, Pablo, Tomás y Laura. Asimismo, a los componentes del *coffee break* (Javi, Marta, Juan), de las cenas navideñas del ala este y de las cenas en *petit comité* (con Bea, JM y Luismi) ¡Sois todos geniales!

Durante el trabajo de campo, quiero destacar la ayuda incondicional de Ohi Masatoshi, del Dr. Óscar Pueyo y el Dr. Victor Hugo Forjaz. Quiero, también, darles las gracias por cederme las fantásticas fotos que me han permitido ilustrar esta memoria, y así poder acercar al lector un poquito más la belleza de estas islas. Quisiera también destacar la hospitalidad y cercanía de los miembros de la *Câmara Municipal da Ilha do Corvo*, y de los dueños de la *Casa de Hóspedes Comodoro y del Residencial Ilha da Graciosa,* ya que facilitaron en todo momento nuestra estancia en estas pequeñas islas del Atlántico.

Echando la vista atrás, me gustaría agradecer a mi profe Ana San Ildefonso su gran pasión por la geología y todo lo que me enseñó en mis inicios ¡gracias por ser una gran docente! Asimismo, agradecer a los profesores y demás componentes del Departamento de Ciencias de la Tierra de la Universidad de Zaragoza las facilidades y atención prestadas. También me gustaría recordar con cariño a todos los compañeros que han pasado por la cantera (de jóvenes investigadores), por acogerme tan rápidamente en los inicios y facilitarme el trabajo en todo lo posible. También quisiera destacar el trabajo del Servicio General de Apoyo a la Investigación-SAI de la Universidad de Zaragoza, y en especial el buen hacer de Manolo Tricas, Fernando y Javier del Servicio de Preparación de Rocas y Materiales duros.

Gracias a los responsables y técnicos del servicio de microsonda electrónica del *Centro Nacional de Microscopía Electrónica* de la Universidad Complutense de Madrid, y del laboratorio *IBERCRON* de la Universidad del País Vasco UPV/EHU, por las facilidades y ayudas prestadas durante estos años. Asimismo, agradezco al Dr. José Luis Fernández Turiel y a la Dra. Marta Rejas su ayuda e implicación, y el invitarme a realizar la preparación de muestras para análisis geoquímico por ICP-MS en el labGEOTOP del Institut de Ciències de la Terra Jaume Almera - CSIC. Además, agradecer a los miembros del Departamento de Geoquímica, Petrología y Prospección Geológica de la Universidad de Barcelona el hacerme un huequito en *su despatx de doctorands* siempre que he pasado unos días por allí.

Gracias también al Dr. Jan R. Wijbrans (*VU Universiteit Amsterdam)* por supervisar el proyecto de datación de mi tesis y acogerme en el laboratorio de argón. En especial, quiero agradecer a Roel Van Elsas, técnico responsable del laboratorio de separación mineral, su atención durante el proceso de preparación de muestras, ya que su buen humor y su dedicada atención hizo muy cálida mí llegada al laboratorio. Además, durante la etapa analítica conté con la valiosa ayuda y asistencia técnica de Christel Bontje, Bertram Uunk y de la Dr. Klaudia Kuiper (VU Universiteit Amsterdam).

Quisiera agradecer muy especialmente la ayuda prestada por Dave Kuentz, técnico responsable del I*sotope Geochemistry & Mass Spectrometry Laboratory* de la Miami University (OH, USA). Liz y Dave, junto con su grupo de investigación (con especial mención a Fara y a George) y el resto de integrantes del *Depatment of Geology and Environmental Sciences* hicieron que mi estancia de cuatro meses en el laboratorio fuera estupenda y súper productiva. ¡Nos vemos pronto!

Además, la colaboración con otros grupos de investigación y la asistencia a congresos internacionales a lo largo de estos años, me ha llevado a conocer a personas excepcionales y grandes expertos en el vulcanismo de las Azores como el Dr. Victor Hugo Forjaz (Observatório Vulcanológico e Geotémico dos Açores), la Dra. Luisa P. Ribeiro (*emepc*, *Governo de Portugal*) y el Dr. Vittorio Zanon (Universidade dos Açores), quien además se ofreció a revisar, muy amablemente, esta memoria en sus últimas etapas de creación.

Sin financiación pública, esta tesis no habría sido posible. Por ello, me gustaría agradecer al Gobierno de Aragón la concesión de mi beca y contrato pre-doctorales (B023/10). Asimismo, al *Ministerio de Ciencia e Innovación* la financiación del proyecto de investigación CGL2011-27477, y a la *Fundação Luso-Americana para o Desenvolvimento*

por el proyecto de investigación “Identificação dos perigos vulcânicos do archipélago dos Açores através da caracterização geoquímica das lavas emitidas pelos respectivos vulcões”. Quiero destacar también las ayudas recibidas para las estancias concedidas por el *Programa CAI Europa de Investigación* (CAI - CONAID CB29/11 y CB12/12) y la Universidad de Zaragoza, así como el apoyo económico del Gobierno de Aragón al grupo de investigación consolidado *Geotransfer*.

Durante la realización de esta Tesis he recibido el apoyo, la ayuda y los ánimos de muchos compañeros de promoción y del máster (Universidad de Zaragoza), de compañeros del curso Erasmus 2008/2009 en *Cardiff University* y de becarios del Departamento de Ciencias de la Tierra. Deseo recordar, en especial, a Esther, Rocío, Galo, Pablo, Claire, Alba y Tere que, en diferentes períodos, han sido personas muy importantes en mi vida.

Gracias a las estancias de investigación en Ámsterdam y USA, tuve la oportunidad de conocer a personas muy especiales que se han convertido en grandes amigos. Gracias a Marina y a todo su entorno de físicos locos por hacerme sentir como en casa (espero que *Azores* esté contigo por muchos años), y a Marta y a Sechu por acogerme como invitada en su casa y pasar unos días fantásticos de turismo por el país de los tulipanes. Al otro lado del Atlántico, tuve la suerte de compartir mi tiempo con Nancy (y todo el *Zoology team*), Manu, Sandra, Ferrán y las chicas de Oviedo ¡muchas gracias por ser tan auténticos!

Quiero dedicar también un agradecimiento muy especial a mis amigas Eli, Agar, Elena e Isa. Por estar siempre dispuestas a pasar un buen rato, escuchar mis aventurillas y apoyarme en todo momento, aunque me encuentre a cientos o miles de kilómetros.

En especial, quiero agradecer a mis padres y a mi hermana toda la confianza y todo el cariño que me dan día a día. Sin su apoyo e incondicional ayuda jamás hubiera podido llegar hasta aquí. También quiero tener un recuerdo especial y un agradecimiento al resto de las Márquez (¡incluyendo a los chicos!), a mi tía Leo (siempre orgullosa de mis logros) y a Teo - Jesús junto con el resto de la familia Ferrer, que recientemente se han unido de forma oficial a mi gran familia.

Por último, quería dedicar esta Tesis Doctoral a Ismael, mi otra mitad, por recibirme siempre con una sonrisa, y por haber hecho de este 2013 un año mágico.

Zaragoza, 5 de Diciembre de 2013

RESUMEN

El archipiélago de las Azores se encuentra localizado en el Océano Atlántico, entre las latitudes 37º y 40º N y las longitudes 25º y 31º O. Está constituido por nueve islas y varios montículos submarinos construidos sobre la plataforma de las Azores. Dos de estas islas han sido objeto de estudio en la presente Tesis Doctoral: Graciosa, al este de la dorsal centro-atlántica, y Corvo, al oeste de la misma.

Dado que los estudios previos sobre estas islas son escasos y se han limitado a la descripción geológica y petrológica de las diferentes unidades volcánicas, la presente investigación aborda un completo estudio de la petrología, la mineralogía y la geoquímica de las distintas unidades volcánicas, así como de los procesos magmáticos ocurridos.

En la Isla de Graciosa se han estudiado diferentes coladas de lava y xenolitos de gabros (alcalinos y subalcalinos), de sienitas y de dunitas, pertenecientes a los complejos volcánicos de Serra das Fontes, Serra Branca y Vitória - Vulcão Central. Se ha demostrado que las coladas de lava de los tres complejos volcánicos, junto con los gabros de composición alcalina (cumulados) y las sienitas (*frozen liquids*), están relacionados mediante un proceso de cristalización fraccionada polibárica, que comenzó en una cámara magmática situada a unos 15 km de profundidad. Además, la alternancia temporal de rocas de composición básica y ácida se explica a través de la existencia de varias recargas magmáticas del sistema. Por el contrario, los gabros de composición

subalcalina, que son descritos por primera vez en el archipiélago de las Azores, se interpretan como cumulados relacionados con un proceso de fraccionación de fundidos altamente refractarios en niveles más someros (~ 3 km).

En la Isla Corvo, se han muestreado también todas las unidades volcanoestratigráficas (Pre-, Sin- y Post-caldera), que incluyen coladas de lava, diques y xenolitos de gabro. Tanto algunas de las coladas, como algunos de los diques, presentan antecristales no cogenéticos que fueron incorporados al fundido previamente a la erupción. Se ha puesto de manifiesto, por primera vez en Azores, que la composición geoquímica de roca total está altamente influenciada por la acumulación de estos antecristales, lo que produce un enmascaramiento de los procesos magmáticos de diferenciación que han dado lugar a la formación de estas rocas. Por ello, para identificar los procesos que han dado lugar a la formación de la isla tan solo se han considerado rocas sin antecristales. De este modo, las coladas de lava y los diques sin antecristales, junto con los xenolitos de gabro (cumulados) están relacionados mediante un proceso de cristalización polibárica, que comenzó en una cámara magmática situada a unos 15 km de profundidad y en la que tuvieron lugar procesos de recarga constantes con fundidos más profundos y de gran carga cristalina. Por lo tanto, se propone que la Isla de Corvo ha sido formada a partir de un complejo sistema magmático en el que los diferentes fundidos y su carga de antecristales provienen de diferentes profundidades y han estado en constante interacción a los largo de toda la evolución de la isla.

La Isla de Graciosa ha sido estudiada desde un punto de vista isotópico, para adecuar el conocimiento de la isla con las demás islas del Rift de Terceira. La edades $^{40}Ar/^{39}Ar$ han permitido establecer la evolución temporal de la isla a lo largo del Pleistoceno y el Holoceno, desde los 1056 ± 28.0 ka hasta los 3.9 ± 1.4 ka, en contraste con las edades previas obtenidas por K-Ar y ^{14}C (620 ka a 2 ka). Las composiciones isotópicas de Sr-Nd-Pb han permitido la caracterización de la fuente del manto de los fundidos, señalando una mezcla entre un componente empobrecido de tipo MORB y un componente enriquecido de tipo HIMU. Estos datos son similares a la composición de manto recientemente redefinida como FOZO, la cual parece estar presente en la signatura isotópica de la mayor parte de islas oceánicas.

ABSTRACT

The Azores archipelago is located in the Atlantic Ocean, between 37º - 40º N latitude and 25º - 31º W longitude, and comprises nine ocean islands and several seamounts built on the Azores submarine plateau. Two remote and poorly studied islands from this archipelago have been investigated in the present PhD Thesis: Graciosa and Corvo, which are located to the east and west of the Mid-Atlantic Ridge, respectively.

Overall, previously published studies mainly focused on the geological and petrographic description of the different volcanic units found in both islands. In addition, the small size of these islands with straightforward volcanostratigraphical sequences, make both of them ideal for an in-depth study of the magmatic processes controlling their evolution. Accordingly, a comprehensive study of the petrology, mineralogy and geochemistry of the different magmatic products found across the volcanic units, has allowed for the geochemical characterization of the units and the investigation of the magmatic processes.

In the case of Graciosa Island, lava flows, gabbroic xenoliths (alkaline and subalkaline), syenites and dunites found across the Serra das Fontes, Serra Branca and Vitória - Vulcão Central volcanic complexes have been considered. Lava flows from the three volcanic complexes, together with alkaline gabbros (cumulates) and syenites (frozen liquids), are related by polybaric fractional crystallization starting at ~ 15 km depth. The alternation of basic and evolved products is related to replenishments of the magma chamber with a more primitive melt. Subalkaline gabbro xenoliths, found for the first

time in the Azores Islands, are related to fractionation of highly refractory melts at shallower levels (~ 3 km).

In Corvo Island, representative samples of the complete volcanostratigraphic sequence (Pre-, Syn- and Post-caldera stages) including lava flows, dikes and cumulate gabbroic xenoliths have been studied. Some lava flows and dikes contain non-cogenetic antecrysts, which have been reincorporated into the host lava before eruption. It has been noted for the first time in the Azores, that the accumulation of antecrysts strongly affects the composition of the rocks, and obscures the identification of magmatic processes responsible for the differentiation of the volcanic products. Accordingly, only antecryst-free samples are considered to identify magmatic processes involved in the formation of the island. Corvo antecryst-free lava flows, dikes and cumulate xenoliths can be related by polybaric fractional crystallization starting at ~ 15 km, and several primitive melt magma chamber replenishments. These results suggest that the formation of Corvo Island is related to a complex magmatic plumbing system in which magmas and their crystal cargo, derived from variable depths, have interacted and been tapped throughout the evolution of the island.

In addition, Graciosa Island has been further studied to make data on this island comparable to those obtained in the other two islands of the Terceira Rift (São Miguel and Terceira). $^{40}Ar/^{39}Ar$ age determinations on Graciosa samples have constrained the Pleistocene and Holocene temporal evolution of the island. These new ages, spanning the whole eruptive record of the island, range from 1056 ± 28.0 ka to 3.9 ± 1.4 ka, whereas prior published K-Ar and ^{14}C ages range from 620 - 2 ka. The oldest age provides a new minimum age for the volcanism on the island, contributing to the overall knowledge on the temporal evolution of the Azores archipelago. Moreover, the Sr-Nd-Pb isotopic composition of Graciosa samples has enabled the characterization of its magma source in the context of the Azores archipelago. These data point to mixing between depleted MORB and enriched HIMU mantle components. They also resemble the composition of the redefined FOZO mantle component, which has been recently proposed as the commonest mantle end-member in ocean island basalts.

PART I: INTRODUCTION

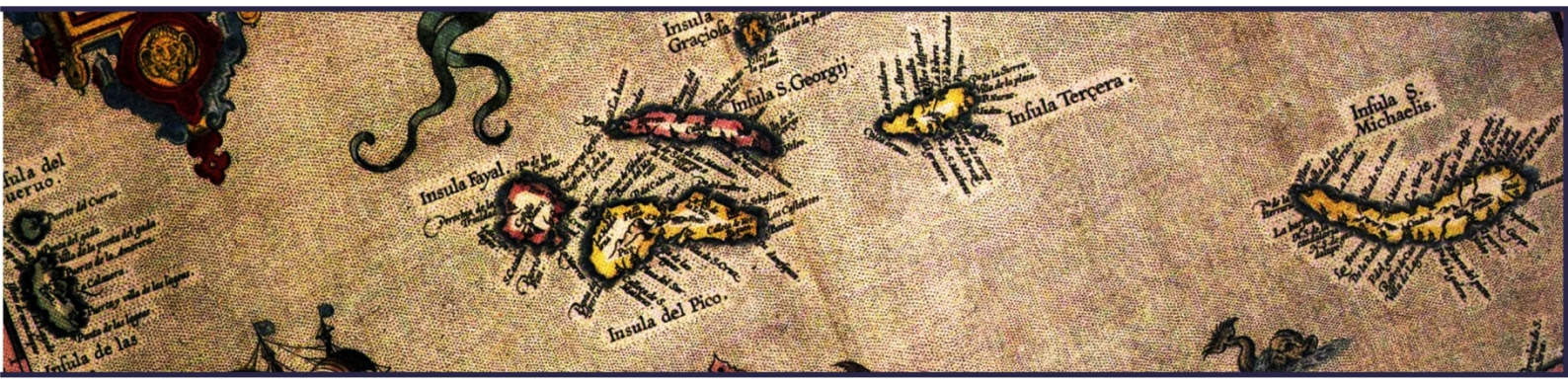

CHAPTER 1: INTRODUCTION

1.1 Interest

The study of oceanic intraplate islands provides information on Earth's mantle composition, processes of magma generation and evolution during magma ascent and eruption. The Azores archipelago is considered an extraordinary natural observatory to study mantle processes and ocean island magmatic systems.

The origin of the Azores plateau, and the formation and evolution of the archipelago have been a matter of intense debate during the past three decades. This archipelago is located near the triple junction where the North American, Eurasian and African plates meet, and represents a classic example of the surface expression of a mantle plume that has interacted with a mid-ocean ridge. Geochemical constraints from igneous rocks collected on the islands and along the nearby Mid-Atlantic Ridge (MAR), together with a variety of geophysical studies have provided data to propose several theories and models explaining the origin and evolution of the Azores plateau at local and regional scales.

The present study is focused on the smallest islands of the archipelago, Graciosa and Corvo, which are located to the east and west of the MAR, respectively. The magmatic processes controlling the evolution of these islands have not been investigated in depth up to now. Overall, published studies have mainly focused on geological mapping and petrographic characterization of the different units (e.g., Zbyszewski, 1970; Forjaz and

Pereira, 1976; Maund, 1985; Gaspar, 1996; Almeida, 2001; Días, 2001; Azevedo et al., 2003). In both islands, it is striking the limited number of geochemical analyses available before the start of this PhD (e.g., Almeida, 2001; França et al., 2003, 2006*a*), most of them widespread in papers dealing with other Azorean Islands (e.g.., White et al., 1976; White et al., 1979, Feraud et al., 1980; Lemarchand, 1987; Lemarchand et al., 1987; França, 1993; Widom and Shirey, 1996; França et al., 2003; Beier et al., 2008, 2010). More recently, Genske (2012) has studied the nature of the western Azores mantle source (Corvo and Flores) using Sr-Nd-Pb-Hf-Os isotope systematics within a broader assessment of the mantle source across the plateau.

This Thesis comprises the first in-depth investigation of Graciosa and Corvo magmatic processes based on the petrology, mineral chemistry and major and trace element composition of the rocks. Furthermore, Sr-Nd-Pb isotopic compositions have been estimated on Graciosa Island in order to complete the isotopic information on the westernmost island of the Terceira Rift. Additionally, dating of the most remarkable volcanic events occurred during the growth of Graciosa Island has constrained its temporal evolution. The dating project has completed recent $^{40}Ar/^{39}Ar$ geochronological studies carried out during the past few years on the other two islands located within the Terceira Rift (Terceira and São Miguel Islands; see section 2.2).

1.2 Aim of the study and Exposition

The present PhD project is focused on the investigation of the petrology, mineralogy, and geochemistry of Graciosa and Corvo magmatic products. This study, together with an evaluation of previous data, aims to investigate the magmatic evolution of Graciosa and Corvo Islands, with particular emphasis on Graciosa as the westernmost island of the Terceira Rift.

The main objectives to be achieved are:

- To characterize the different volcanological units and their formation through a detailed study of mineral and whole rock compositions. For this purpose, it is

required to investigate equilibrium conditions between minerals and host rocks to determine crystal populations, and their influence on whole rock compositions.

- To investigate the petrogenesis of Graciosa and Corvo island xenoliths: their formation and role in magmatic processes, through a detailed study of their mineral modes, mineral compositions and major and trace element concentrations.

- To determine the magmatic evolution of Graciosa and Corvo Islands on the basis of the magmatic processes involved in the formation of their volcanological units, and the different magmatic products studied considering their position within the volcanostratigraphical sequence.

Furthermore, in order to make data on Graciosa Island comparable to those carried out in the other two islands of the Terceira Rift (São Miguel and Terceira), two more objectives are to be achieved:

- To constrain the temporal evolution of Graciosa Island through $^{40}Ar/^{39}Ar$ ages of the most remarkable volcanic events occurred during the formation of the island and the evaluation of previous K/Ar and ^{14}C geochronological data.

- To characterize the mantle source of Graciosa Island magmas in the context of the archipelago and to obtain and compare new Sr-Nd-Pb isotope data with previous isotopic data of the Azores archipelago.

For these purposes, this PhD dissertation has been structured in three parts; after the present introductory part, the following parts are dedicated to the study of Graciosa and Corvo Islands, respectively. These parts are divided in chapters that comprise several sections such as geographic, geomorphologic and geotectonic context, previous studies, volcanostratigraphy, samples and methods, results, discussion and conclusions. There is also a last chapter which includes the final considerations of this PhD project as a whole.

CHAPTER 2: AZORES REGIONAL SETTING

2.1 Geographic and geotectonic setting

The Azores archipelago is located in the Atlantic Ocean between 37º - 40º N latitude and 25º - 31º W longitude. The Archipelago comprises nine ocean islands and several seamounts built on the Azores submarine plateau (Fig. 2.1).

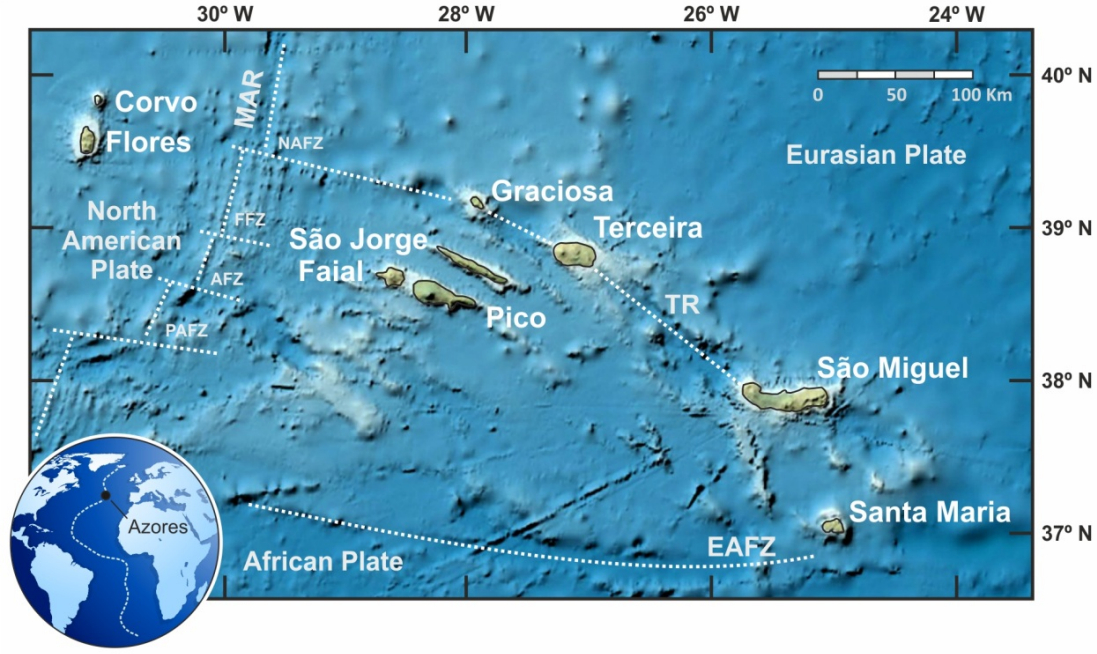

Fig. 2.1 - Location of the Azores Archipelago and general geotectonic setting of the Azores Plateau, modified after the GEBCO world map 2013 (www.gebco.net). EAFZ: East Azores Fracture Zone; TR: Terceira Rift; MAR: Mid.Atlantic Ridge; NAFZ: North Azores Fracture Zone; FFZ: Faial Fracture Zone; AFZ: Açor Fracture Zone; PAFZ: Princess Alice Fracture Zone.

The Archipelago has a WNW to ESE orientation and is 600 km wide. It is geographically divided into three groups: (i) the Eastern Group, formed by Santa Maria and São Miguel Islands, (ii) the Central Group, which includes Terceira, Graciosa, Faial, Pico and São Jorge Islands, and (iii) the Western Group, composed of two Islands Flores and Corvo.

The Azores submarine plateau covers an area of about 400,000 km^2 and has a triangular shape outlined by 2,000 m isobaths (e.g., Needham and Francheteau, 1974; Laughton and Whitmarsh, 1974; Lourenço et al., 1998) that extend to both sides of the Mid-Atlantic Ridge (MAR). This complex tectonic region includes a triple junction between the North American, Eurasian and African (Nubian) plates (Fig. 2.1).

The MAR is a well-defined submarine structure, which crosses the Azores plateau in a approximately north-south direction. It defines the limit between the American Plate to the west, and the Eurasian and African plates to the east. Along the Azores plateau, the MAR is divided into segments (~ 50 - 60 km length; Luis et al., 1994) by several transform faults as the North Azores Fracture Zone (39º 25' N), Faial Fracture Zone (38º 55' N), Açor Fracture Zone (38º 23' N), Princess Alice Fracture Zone (38º 00' N) and Pico Fracture Zone (37º 30' N). The dextral strike-slip movement of the transform faults produces the displacement of the MAR segments and the rotation of the main axis from 7º N to the north of the plateau, to 22º N in the southern area of the plateau (Fig. 2.1; Luis et al., 1994).

The East Azores Fracture Zone is a nearly E-W striking tectonic structure which defines the southern boundary of the Azores plateau at approximately 37º N (Fig. 2.1). It limits a bathymetry drop from the edge of the Azores plateau (~ 2,000 m) to approximately 3500 m depth. The EAZF represents the western segment of the Azores - Gibraltar Fracture Zone (Gloria Fault), which defines the boundary between the Eurasian and African plates to the east of the Azores archipelago (e.g., Laughton et al., 1972).

Classically, the northern boundary of the Azores plateau has been attributed to the Terceira Rift (Machado, 1959), which is a 550 km long, ESE trending ultraslow spreading axis (2 - 4 mm/year) connected to the MAR by the North Azores Fracture Zone (e.g.,

Searle 1980; Vogt and Jung, 2004; Fig. 2.1). It comprises the volcanic Islands of Graciosa, Terceira and São Miguel, the João de Castro seamount, and the non-volcanic basins located among them (e.g., Vogt and Jung, 2004; Georgen and Sankar, 2010).

Except from the East Azores Fracture Zone and the eastern part of São Miguel, which are E-W striking tectonic structures, all other tectonic structures located to the East of the MAR run parallel to the Terceira Rift (e.g., the Islands of Faial, Pico and São Jorge are elongated and align parallel just south of the Terceira Rift; Fig. 2.1). In contrast, the Islands of Flores and Corvo, the only two located to the west of the MAR, lie on a NNE-SSW trending ridge that is subparallel to the MAR. Moreover, the structural influence of the MAR transform faults is reflected by the near linear E-W northern and southern coastlines of Flores (Fig. 2.1) together with a westward displacement of Corvo from Flores of about 1 cm/year (Baptista et al., 1999).

Different geodynamic models have been proposed to explain the boundaries between the North American, Eurasian and African plates. Overall, the boundary between the American and the Eurasian - African plates is believed to be defined by the MAR. In contrast, there is disagreement about the structures defining the Eurasian and African plate boundary in the segment between the MAR and the Gloria Fault.

A classical model suggests that this boundary is defined by the Terceira Rift, forming a Ridge-Ridge-Ridge type triple junction (e.g., Krause and Watkins, 1970; Udías and Arroyo, 1972; Buforn et al., 1988). Other authors (McKenzie, 1972; Laughton and Whitmarsh, 1974; Searle, 1980; Ribeiro, 1982) suggest that the Eurasian and African plate boundary corresponds to a leaky-transform fault passing through São Jorge submarine channel and continuing south of São Miguel Island as far as the Azores - Gibraltar Fracture Zone. Forjaz (1983) proposes the existence of an Azorean microplate limited by the East Azores Fracture Zone in the south, by the MAR in the west and by the North Azores Fracture Zone and the Terceira Axis in the north; he proposes that the strain generated by the MAR and the Terceira Axis produces a compressive regimen oblique to the Gloria Fault. In contrast, geophysical studies (e.g., Luis et al., 1994; Miranda and Luis, 1995) covering the MAR and oceanic crust created ~ 10 Ma ago,

suggest that the volcanism and the tectonic regime of the archipelago are controlled by the movement of the plates and the Azores plateau; i.e., a progressive migration from the East Azores Fracture Zone to the Princess Alice Fracture Zone before the last 10 Ma, from the Princess Alice Fracture Zone to the Açor Fracture Zone in the last 10 Ma, and currently from the Açor Fracture Zone to the Faial Fracture Zone. Moreover, they suggest that the recent migration of the triple junction might have triggered the formation of the youngest Islands of Faial and Pico. More recently, Marques et al. (2013) have determined GPS velocities implying that oblique WSW-ENE extension between the African and Eurasian plates is accommodated across a series of horsts and grabens. These include the Faial - Pico volcanic ridge, which moves mostly with the African plate; Terceira Island, which moves mostly with the Eurasian plate; and São Jorge Island, whose motion is intermediate between that of the African and Eurasian plates. As a conclusion they argue against a rigid or semi-rigid Azores microplate, and instead suggest that the African - Eurasian plate boundary at the longitude of the Azores is diffuse and represented by a ca. 140 km wide zone of deformation.

2.2 The Azorean ages

Studies of the magnetic anomalies in the Atlantic Ocean and kinematic reconstruction models discussed in the previous section have shed light on the temporal evolution of the Azores plateau (Fig. 2.2; e.g., Searle, 1980; Luis et al., 1994; Cannat et al., 1999; Gente et al., 2003). Moreover, $^{40}Ar/^{39}Ar$ ages have been recently obtained from submarine samples dredged from the plateau (Beier, 2006) providing important temporal constraints.

Searle (1980) suggested an age of ~ 53 Ma for the easternmost part of the Azores plateau, based on the age of the oldest magnetic anomaly in the area (Fig. 2.2). In contrast, the $^{40}Ar/^{39}Ar$ age of ~ 39 Ma obtained by Beier (2006) in a sample from the Monaco Bank south of São Miguel Island (Fig. 2.2), indicates that the first intraplate magmas of the Azorean plateau were formed ca. 14 Ma after the formation of the lithosphere. Further to the west, the age of the lithosphere close to the MAR has been estimated to be 10 Ma based on magnetic lineations (Cannat et al., 1999; Fig. 2.2).

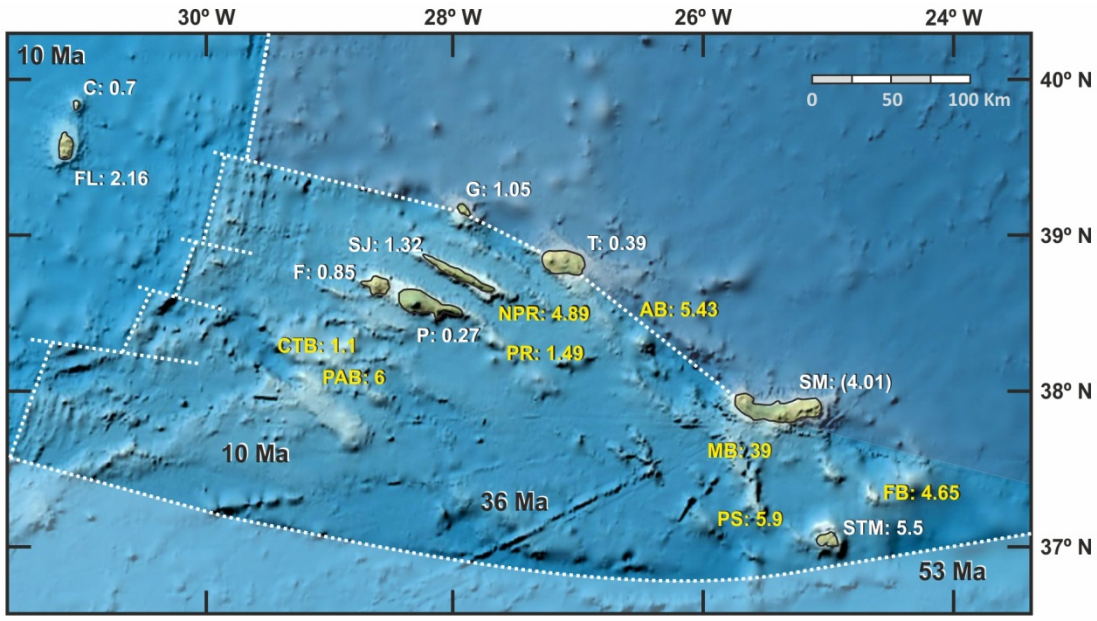

Fig. 2.2 - Bathymetry of the Azores Plateau, modified after the GEBCO world map 2013 (www.gebco.net) with the general geotectonic setting (as in Fig. 2.1; note the different color for each tectonic plate) and the most remarkable ages of the Azores archipelago reported in millions of years (Ma). The preferred ages of each island are reported in white (see section 2.2; STM: Santa Maria - Feraud et al., 1981; SM: São Miguel - Abdel-Monem et al., 1975; T: Terceira - Calvert et al., 2006; G: Graciosa - Larrea et al., 2014; SJ: São Jorge - Hildenbrand et al., 2008; F: Faial - Hildenbrand et al., 2012; P: Pico - Demand et al., 1982; FL: Flores - Azevedo and Ferreira, 2006; C: Corvo - Azevedo et al., 2003. Lithospheric ages (in black) are from Searle (1980), Luis et al. (1994) and Cannat et al. (1999). Submarine samples dredged from the plateau in yellow were obtained by Beier (2006); PS - Ponta Sul Ridge; FB - Formigas Bank; MB - Monaco Bank; AB - Alcatraz Bank; PR - Pico Ridge; CTB - Condor de Terra Bank; PAB - Princess Alice Bank; FR - Faial Ridge.

Moreover, Luis et al. (1994) presented an aeromagnetic survey covering both sides of the MAR up to the anomaly 5 (~ 10 Ma). It is located to the west of São Jorge Island and beneath Faial Island (to the east of the MAR), and to the west of Corvo and Flores Islands (to the west of the MAR).

In contrast, $^{40}Ar/^{39}Ar$ ages calculated in submarine elevations of the Azores plateau reveal that most part of the plateau was formed from 6 to 4.9 Ma (Beier, 2006; Fig. 2.2), which is coincident to the age range proposed for the formation of Santa Maria Island and the Formigas Bank (see below). However, during the last 1.5 Ma, abundant volcanism formed most of the islands and numerous seamounts predominantly situated along the Terceira Rift and the Faial - Pico lineament.

Santa Maria is the easternmost and oldest island of the Azores archipelago (Fig. 2.2). Some authors propose a range of volcanic activity from 5.5 to 3 Ma (Feraud et al., 1980, 1981; Salgueiro, 1991), whereas Abdel-Monem et al. (1975) suggests older ages (8 - 4 Ma). This large variation has been a cause of debate (see discussion in Feraud et al., (1981) and Serralheiro (1993)) as these age calculations are considered erroneous due to the presence of excess argon (see also the problems reported by Carracedo (2011) in the ages obtained by Abdel-Monem et al. (1972) in the Canary Islands). Moreover, ostracods from Santa Maria Island have been categorized as Messinian in age (Meireles et al., 2012; stage from the Late Miocene ranging from 7.246 to 5.322 Ma).

The subaerial formation of São Miguel Island was initiated at ~ 4 Ma according to the K/Ar ages obtained by Abdel-Monem et al. (1975), although this age might be overestimated due to excess argon commonly found in young basalts (see above). This unit has been recently dated by $^{40}Ar/^{39}Ar$ given a younger age of 0.88 Ma (Johnson et al., 1998), in accordance with the reverse polarity paleomagnetic field directions of late Matayuma age. However, the sampled analyzed by Johnson et al. (1998) is a dike intruding the oldest unit of the Nordeste Complex (V.H. Forjaz, pers. com.). Therefore, due to the uncertain ages estimated for this oldest unit, the age of the subaerial formation of São Miguel remains unknown, although it has to be older than 0.88 Ma (Fig. 2.2).

Terceira (3.52 Ma) and Graciosa (2.5 Ma) Islands were considered the oldest islands of the Central Group, based on K/Ar ages in Terceira (Ferreira and Azevedo, 1995) and Rb/Sr apparent ages for Graciosa (White et al., 1976). However, more accurate and recent $^{40}Ar/^{39}Ar$ studies report younger ages for these islands (Fig. 2.2): < 0.39 Ma for Terceira (Calvert et al., 2006) and < 1.05 Ma for Graciosa (Larrea et al., 2014; see chapter 5). São Jorge Island has been recently dated by $^{40}Ar/^{39}Ar$ showing that the first subaerial volcanic phase started at ~ 1.3 Ma (Hildenbrand et al., 2008; Ribeiro, 2011; Fig. 2.2). Pico and Faial Islands lack $^{40}Ar/^{39}Ar$ accurate age data. The oldest K/Ar ages are 0.73 Ma and 0.27 Ma respectively, showing the youth of the Faial - Pico lineament in comparison to the other islands of the Central Group (Fig. 2.2).

The islands located to the west of the MAR have also been dated (Fig. 2.2). The maximum K/Ar age obtained for Flores Island is 2.16 Ma (Azevedo and Ferreira, 2006), while the oldest age obtained in Corvo Island is 0.7 Ma (Azevedo et al., 2003). Comparing these ages with those of the plateau where they are rooted, it is clear that these islands formed after the plateau.

Overall, the geographic distribution of the eruptive centers reveals that the oldest ages are those located most distant to the MAR (Santa Maria Island and Monaco Bank seamount; Fig. 2.2). Nevertheless, the temporal evolution of the archipelago does not appear to be compatible with a conventional hotspot model, in which volcanism is controlled by plate migration with time over a fixed plume, as proposed for other oceanic islands (e.g., Hawaii; Wilson, 1963; Morgan, 1972; DePaolo and Manga, 2003), but rather may be partially controlled by complex extensional tectonics related to the Azores triple junction (e.g., Searle, 1980; Luis et al., 1998; Lourenço, 2007). In order to better constrain the temporal evolution of the Azores archipelago and the potential magmatic and tectonic controls, it is critical to obtain additional and improved age constraints on the islands. Accordingly, a detailed $^{40}Ar/^{39}Ar$ dating project has been carried out in Graciosa Island to better constrain the age of the different volcanological units and reconstruct its volcanic evolution (Larrea et al., 2014; see chapter 5).

The volcanism in the Azores archipelago is still active, with 26 historical eruptions reported; 12 of those were subaerial and located in the Islands of São Miguel, Terceira, São Jorge, Pico and Faial (França et al., 2003). The most recent submarine eruptions were the *Capelinhos* in 1957 - 1958 to the west of Faial Island, and *Serreta* in 1998 - 2000, which occurred 8.5 km to the NW of Terceira Island (Forjaz et al., 2001; Gaspar et al., 2003). Present-day activity is recognized in the Islands of São Miguel, Terceira, Graciosa, Faial, Pico and Flores (Baxter et al., 1999; Cruz et al., 1999; Ferreira and Oskarsson, 1999; Nunes et al., 2001; Cruz and França, 2004) as hot water springs, low-temperature fumarolic degassing fields and soil degassing emissions (e.g., Viveiros et al., 2009).

2.3 The mantle plume beneath the Azores archipelago

The Azores archipelago has been considered as an example of a hotspot interacting with a mid-ocean ridge. A variety of geochemical studies and geophysical observations point out the importance of a mantle plume on the formation of the Azores plateau and the nearby MAR: long-wavelength observations along the MAR, including ridge-axis elevation (Anderson et al., 1973; Vogt, 1976; Le Douaran and Francheteau, 1981; Gente, 1987; Thibaud et al., 1998), geoid topography (Bowin et al., 1984; Cazenave et al., 1992) and geochemical anomalies (Schilling, 1975; White and Schilling, 1978; Bougault and Treuil, 1980; Yu et al., 1997; Dosso et al., 1999).

This mantle plume arrived to the vicinity of the MAR ~ 40 Ma ago (see section 2.2), and is characterized by a slow upwelling rate of ~ 3 - 4 cm/y (Sleep, 1990; Bourdon et al., 2005). It has a buoyancy flux of 1.2 mg/s (Sleep, 1990), which produces small amounts of melts if compared to the unusually strong and long-lived Hawaiian plume, with an estimated plume buoyancy flux of 6.5 - 8.7 mg/s (White and McKenzie, 1989; Davies, 1999).

The present location of the Azores hot spot is not exactly known. However, it is clearly located to the east of the MAR, and probably centered underneath Terceira Island, as suggested by He and Ne isotope ratios (Madureira et al., 2005) and U-series systematics (Bourdon et al., 2005).

Geochemical data on submarine lavas (Schilling, 1975; White et al., 1976; Beier, 2006) reveals that the Azores plateau is alkaline in composition. Accordingly, the composition of the subaereal volcanisms is mainly alkaline, despite few punctual tendencies for transitional basalts; e.g., Furnas Volcanic Complex in São Miguel Island (Rodrigues et al., 1995) and certain lava flows in Pico (França et al., 1995) and Terceira Islands (Madureira, 2006).

A significant isotopic variability characterizes the archipelago, and it is interpreted as a result of small-scale heterogeneities in the mantle source (e.g., França et al., 2006*b*;

Beier et al., 2007, 2008, 2010; Madureira et al., 2011). Most islands from the archipelago show a common isotopic array (linear trend in Sr-Pb, Nd-Pb and Pb-Pb isotopic systems) which suggests the involvement of at least two mixing end-members including a depleted MORB component (related to the nearby MAR) and an enriched mantle component (see chapter 6; Larrea et al., under review). In contrast, São Miguel Island presents a distinct isotopic composition characterized by extremely high $^{207}Pb/^{204}Pb$, $^{208}Pb/^{204}Pb$ and $^{87}Sr/^{86}Sr$ ratios and low $^{143}Nd/^{144}Nd$ ratios extensively discussed elsewhere (e.g., White et al., 1979; Turner et al., 1997; Widom et al., 1997; Beier et al., 2007; Elliott et al., 2007; França et al., 2010).

The isotopic composition of the MAR in the vicinity of the Azores plateau is enriched compared with the N-MORB isotopic composition found in other segments of the MAR (e.g., Schilling, 1975; White and Schilling, 1978; Bourdon et al., 1996; Yu et al., 1997; Dosso et al., 1999). This enrichment might be linked to the isotopic composition of the Azores mantle plume which is affecting the MAR isotopic composition. Recently, a finite-frequency seismic tomography study in the Azores region (Yang et al., 2006) proposed a model of plume-ridge interaction in which the plume conduit is deflected to the southwest (Fig. 2.3), and contributes mantle material and excess melt to the MAR. On the other hand, Foulger (2010) pointed out the impossibility of carrying out surface-wave tomography to resolve bodies smaller than ~ 100 km across and thus, detecting narrow structures such as plumes, so that he considers ambiguous the interpretation of Yang et al. (2006).

Adam et al. (2013) carried out a highly resolved tomography model to characterize mantle convection in the upper mantle beneath the Azores region. These authors found two distinct upwellings in the shallow mantle that converge into a single anomaly at a deeper level (Fig. 2.3). One of the mantle upwellings is proposed to be centered among Faial, Pico, São Jorge, and Graciosa Islands, and the other one is located between Terceira and São Miguel Islands. These authors suggest that the two reservoirs may account for the mantle heterogeneity recognized for the Azores plume, explaining the difference in isotopic signatures observed through the islands and, in particular, the

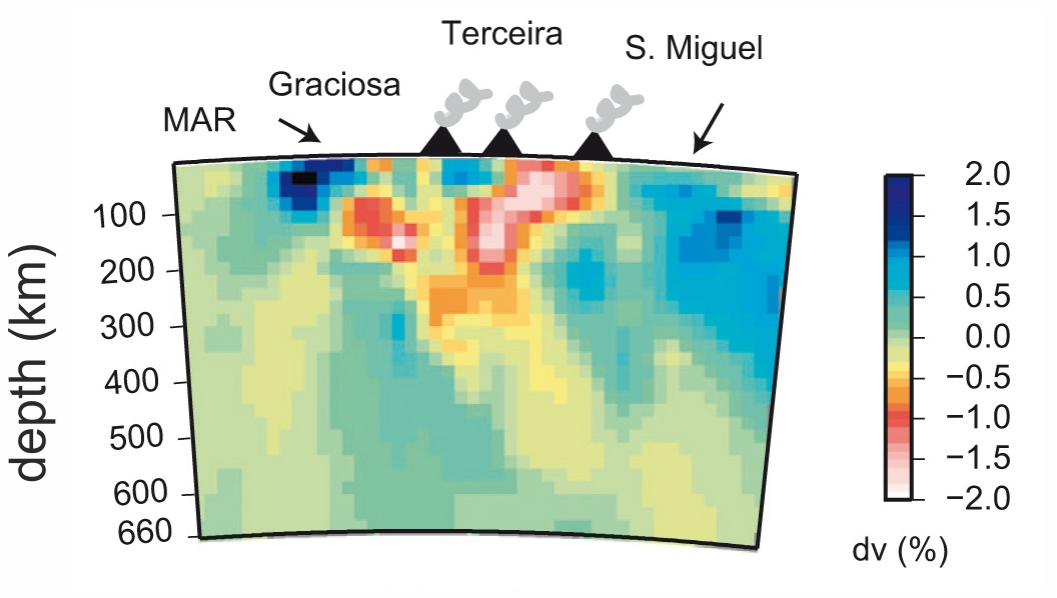

Fig. 2.3 - Depth cross section along the Terceira Rift showing the tomography model of Yang. et al. (2006) (in Adam et al., 2013).

unique isotopic ratios in São Miguel Island lavas. However, it must be taken into account that the isotopic signature of Terceira lavas is much closer to the isotopic compositions of Graciosa and São Jorge lavas than to the distinct isotopic signature found in São Miguel lavas, so this hypothesis is not completely in agreement with geochemical data.

Other authors remark that in the Azores archipelago there are neither flood basalt implying precursory uplift, nor time-progressive volcanism, nor evidence for high source temperature (e.g., Foulger, 2010). These data disagree with the theory of a mantle plume located beneath the Azores. They suggest that the magmatism was enhanced by astenospheric upwelling beneath the ridge branches, and also by the long-term tectonic instability and migration of major fault zones at the Azores (e.g., Searle, 1980; Madeira and Ribeiro, 1990; Gente et al., 2003; Luis and Miranda, 2008). In agreement to these works, a recent study by Neves et al. (2013) hypothesizes that linear volcanic ridges are the result of magma emplacement into pre-existing damaged lithosphere, without the need of enhanced magmatic pulses related to mantle plume activity. They suggest that the construction of the islands is dominated by episodic fissural eruptions whose size and frequency depend on melt availability (anomalous amount of melt production over a relatively long period) and tectonic stress.

CHAPTER 3: Materials and Methods

3.1 Field work and sampling strategy

This PhD Thesis comprises the magmatic evolution of Graciosa and Corvo Islands. After a careful review of the material sampled previously by members of the research group and the studies published previously on both islands (e.g., Gaspar, 1996; Almeida, 2001; Dias, 2001), two field campaigns were planned in 2011 - 2012.

The main aim of the field work was the revision of the volcanostratigraphy (see chapters 4 and 7), and a thorough sampling of the different units. All diverse magmatic products found in both islands were sampled, with special emphasis on those not sampled previously. Moreover, field observations on the petrology, composition and emplacement characteristics of the outcrops were used to sample the least altered material in each case.

A summary of samples are presented in Tables 3.1 and 3.2. These tables include the sampled unit, the campaign in which the sample was collected, and the location, UTM coordinates, classification, texture of the samples, as well as the methods applied in each case. All of the samples were studied macro- and microscopically, and the most representative samples were selected for geochemical determinations.

Table 3.1 - Summary of samples studied from Graciosa Island and methods applied (see chapter 4).

Unit	Subunit	Sample	Campaign	Location	UTM Coordinates	Classification	Texture	Thin Section	EMP	WR	Isotopes	Ar ages
Vulcão Central lavas	VCU-g	GRZF5	1	South of Canada Longa	26S 0413670 4319206	Basalt	porphyritic	x	x	x		
	VCU-g	GRZF19	2	Quarry. Canada da Chicha	26S 0414049 4320557	Basalt	porphyritic	x		x	x	x
	VCU-f	GRZF16	1	North of Beco	26S 0415266 4319817	Benmoreite	microporphyritic	x	x	x	x	x
	VCU-d	GRZF1	1	Baía do Folga	26S 0413669 4319206	Hawaiite	porphyritic	x	x	x	x	x
	VCU-b	GRZF6	1	Enxudreiro	26S 0414756 4318450	Trachyte	microporphyritic	x	x	x		
	VCU-b	GRZF7	1	Enxudreiro	26S 0414756 4318451	Basalt	porphyritic	x	x	x		
	VCU-b	GRZF14	1	Carapacho	26S 0416894 4318520	Basalt	porphyritic	x	x	x	x	x
	VCU-b	GRZF15	1	Portela	26S 0417178 4320652	Basalt	porphyritic	x		x		
	VCU-b	GRZF18	2	Baía do Folga	26S 0413376 4319314	Hawaiite	porphyritic	x	x	x		
	VCU-b	GRZF36	2	Praia town	26S 0415628 4322545	Mugearite	microporphyritic	x	x	x		
	VCU-b	GRZF37	2	Enxudreiro	26S 0414960 4318607	Trachyte	microporphyritic	x				
	VCU-b	GRZF38	2	Enxudreiro	26S 0414960 4318607	Basalt	porphyritic	x				
Vitória lavas	VU-c	GRZF2	1	Pico Timão	26S 0413698 4321723	Basalt	microporphyritic	x	x	x		
	VU-c	GRZF3	1	Quarry. Praia town	26S 0415701 4323383	Basalt	microporphyritic	x	x	x	x	x
	VU-c	GRZF21	2	Feteira	26S 0413059 4322312	Basalt	microporphyritic	x		x		
	VU-a	GRZF11	1	Pico do Barcelo	26S 0409099 4325197	Basalt	microporphyritic	x		x		
	VU-a	GRZF12	1	Serra Branca Windmills	26S 0410857 4321152	Basalt	porphyritic	x	x	x		
	VU-a	GRZF4	1	Quitadouro	26S 0414611 4323676	Basalt	porphyritic	x		x		
	VU-a	GRZF9	1	Airport	26S 0410809 4327836	Basalt	microporphyritic	x		x		
	VU-a	GRZF10	1	Da Barca lighthouse	26S 0409239 4327560	Basalt	microporphyritic	x	x	x		
	VU-a	GRZF17	1	Ponta Pesqueira	26S 0413479 4327011	Basalt	porphyritic	x	x	x		
	VU-a	GRZF22	2	Quitadouro	26S 0415369 4324445	Basalt	porphyritic	x	x	x	x	x
	VU-a	GRZF23	2	Quitadouro	26S 0415369 4324445	Basalt	porphyritic	x		x		
	VU-a	GRZF24A/ 24B	2	Quitadouro	26S 0415369 4324445	Basalt	porphyritic	x		x		
	VU-a	GRZF25	2	Quitadouro	26S 0415369 4324445	Basalt	microporphyritic	x	x	x		
	VU-a	GRZF26	2	Quitadouro	26S 0415369 4324445	Basalt	porphyritic	x	x	x		
	VU-a	GRZF27	2	Quitadouro	26S 0415374 4324445	Basalt	porphyritic	x	x	x	x	x
	VU-a	GRZF30	2	Baía da Vitória cliff	26S 0408606 4326149	Basalt	porphyritic	x	x	x		
	VU-a	GRZF31	2	Baía da Vitória cliff	26S 0408606 4326149	Basalt	microporphyritic	x	x	x		
	VU-a	GRZF32A	2	Baía da Vitória cliff	26S 0408606 4326149	Basalt	porphyritic	x		x		
	VU-a	GRZF32B	2	Baía da Vitória cliff	26S 0408606 4326149	Basalt	porphyritic	x		x		

Table 3.1 - Summary of samples studied from Graciosa Island and methods applied (see chapter 4).

Unit	Subunit	Sample	Campaign	Location	UTM Coordinates	Classification	Texture	Thin Section	EMP	WR	Isotopes	Ar ages
	VU-a	GRZF33	2	Baía da Vitória cliff	26S 0408606 4326149	Basalt	porphyritic	x		x		
	VU-a	GRZF34	2	Baía da Vitória cliff	26S 0408606 4326149	Basalt	microporphyritic	x		x		
	VU-a	GRZF35	2	Baía da Vitória road	26S 0408684 4326193	Basalt	porphyritic	x	x	x		
Serra Branca	SB-b	GRZF13	2	Serra Branca top	26S 0410307 4320366	Trachyte	trachytic	x	x	x		
	SB-a	GRZF20	2	Pedras Brancas	26S 0413930 4321502	Trachyte	trachytic	x	x	x	x	x
Serra das Fontes lavas	SF	GRZF8	1	West of Sontes	26S 0411886 4324666	Basalt/ Hawaiite	microporphyritic	x	x	x	x	x
	SF	GRZF28	2	South of Fontes	26S 0413107 4323848	Mugearite	microporphyritic	x		x		
	SF	GRZF29	2	South of Fontes	26S 0412823 4324220	Hawaiite/ Mugearite	microporphyritic	x		x		
Xenoliths	VU - Cxb	GRZF1x1	1	Baía do Folga	26S 0413669 4319206	Gabbro	Heteroadcumulate	x	x	x	x	x
	VU - Cxb	GRZF1x2	1	Baía do Folga	26S 0413669 4319206	Gabbro	Heteroadcumulate	x	x	x		
	VU - Cxb	GRZF1x5	1	Baía do Folga	26S 0413669 4319206	Gabbro	Orthocumulate	x	x	x		
	VU - Cxb	GRZF1x6	1	Baía do Folga	26S 0413669 4319206	Gabbro	Orthocumulate/ Heteroadcumulate	x	x	x	x	
	VU - Cxb	GRZF1x8	1	Baía do Folga	26S 0413669 4319206	Gabbro	Orthocumulate	x	x	x		
	VU - Cxb	GRZF1x9	1	Baía do Folga	26S 0413669 4319206	Gabbro	Heteroadcumulate	x				
	VU - Cxb	GRZF1x10	1	Baía do Folga	26S 0413669 4319206	Gabbro	Orthocumulate	x	x	x		
	VU - Cxb	GRZF1x13	1	Baía do Folga	26S 0413669 4319206	Gabbro	Orthocumulate	x	x	x		
	VU - Cxb	GRZF1x14B	1	Baía do Folga	26S 0413669 4319206	Gabbro	Orthocumulate	x	x			
	VU - Cxb	GRZF1x15	2	Baía do Folga	26S 0413669 4319206	Gabbro	Orthocumulate	x				
	VU - Cxb	GRZF1x16	2	Baía do Folga	26S 0413669 4319206	Gabbro	Heteroadcumulate	x				
	VU - Cxb	GRZF1x17	2	Baía do Folga	26S 0413669 4319206	Gabbro	Orthocumulate	x				
	VU - Cxb	GRZF1x18	2	Baía do Folga	26S 0413669 4319206	Gabbro	Orthocumulate	x				
	VU - Cxb	GRZF1x19	2	Baía do Folga	26S 0413669 4319206	Gabbro	Orthocumulate	x	x	x		
	VU - Cxb	GRZF1x20	2	Baía do Folga	26S 0413669 4319206	Gabbro	Orthocumulate	x				
	VU - Cxb	GRZF1x21	2	Baía do Folga	26S 0413669 4319206	Gabbro	Heteroadcumulate	x				
	VU - Cxb	GRZF1x22	2	Baía do Folga	26S 0413669 4319206	Gabbro	Orthocumulate	x	x	x		
	VU - Cxb	GRZF1x24	2	Baía do Folga	26S 0413669 4319206	Gabbro	Orthocumulate	x	x	x		
	VU - Cxb	GRZF1x25	2	Baía do Folga	26S 0413669 4319206	Gabbro	Orthocumulate	x				
	VU - Cdvi	GRENX-1	2	Enxudreiro	26S 0414683 4318546	Syenite	Inequigranular	x	x	x		
	VU - Cdvi	GRENX-2	2	Enxudreiro	26S 0414683 4318547	Syenite	Inequigranular	x	x	x		
	VU - Vb	GRZF17A	1	Ponta Pesqueira	26S 0413479 4327011	Gabbro	Inequigranular	x	x	x		
	VU - Vb	GRZF17B	2	Ponta Pesqueira	26S 0413479 4327011	Gabbro	Inequigranular	x	x	x	x	

Table 3.1 - Summary of samples studied from Graciosa Island and methods applied (see chapter 4).

Unit	Subunit	Sample	Campaign	Location	UTM Coordinates	Classification	Texture	Thin Section	EMP	WR	Isotopes	Ar ages
Xenoliths	VU - Vb	GRZF17C	2	Ponta Pesqueira	26S 0413479 4327011	Gabbro	Inequigranular	x	x	x	x	
	VU - Vb	GRZF17D	2	Ponta Pesqueira	26S 0413479 4327011	Gabbro	Inequigranular	x	x	x		
	VU - Vb	GRZF17E	2	Ponta Pesqueira	26S 0413479 4327011	Gabbro	Orthocumulate	x	x	x		
	VU - Vb	GRZF17F	2	Ponta Pesqueira	26S 0413479 4327011	Gabbro	Inequigranular					
	VU - Vb	GRZF17G	2	Ponta Pesqueira	26S 0413479 4327011	Gabbro	Orthocumulate	x	x			
	VU - Vb	GRZF17H	2	Ponta Pesqueira	26S 0413479 4327011	Gabbro	Inequigranular					
	VU - Vb	GRZF17I	2	Ponta Pesqueira	26S 0413479 4327011	Gabbro	Inequigranular					
	VU - Vb	GRZF17J	2	Ponta Pesqueira	26S 0413479 4327011	Gabbro	Inequigranular					
	VU - Vb	GRZF17K	2	Ponta Pesqueira	26S 0413479 4327011	Gabbro	Inequigranular					
	VU - Vb	GRZF17L	2	Ponta Pesqueira	26S 0413479 4327011	Gabbro	Inequigranular					
	VU - Vb	GRZF17M	2	Ponta Pesqueira	26S 0413479 4327011	Gabbro	Inequigranular					
	VU - Vb	GRZF17N	2	Ponta Pesqueira	26S 0413479 4327011	Gabbro	Inequigranular					
	VU - Vb	GRZF17Ñ	2	Ponta Pesqueira	26S 0413479 4327011	Gabbro	Inequigranular					
	VU - Vb	GRZF17O	2	Ponta Pesqueira	26S 0413479 4327011	Gabbro	Inequigranular					
	VU - Vb	GRZF17P	2	Ponta Pesqueira	26S 0413479 4327011	Gabbro	Inequigranular					
	VU - Vb	GRQUx1	2	Quitadouro	26S 0415078 4324328	Dunite	Equigranular	x	x	x	x	
	VU - Vb	GRZF24C	2	Quitadouro	26S 0415078 4324328	Dunite	Equigranular	x	x			
	VU - Vb	GRQUx2	2	Quitadouro	26S 0415078 4324328	Gabbro	Inequigranular					
	VU - Vb	GRQUx3	2	Quitadouro	26S 0415078 4324328	Gabbro	Inequigranular	x	x	x		
	VU - Vb	GRQUx4	2	Quitadouro	26S 0415078 4324328	Gabbro	Inequigranular	x	x	x	x	
	VU - Vb	GRQUx5	2	Quitadouro	26S 0415078 4324328	Gabbro	Inequigranular	x	x	x		
	VU - Vb	GRQUx6	2	Quitadouro	26S 0415078 4324328	Gabbro	Inequigranular					
	VU - Vb	GRQUx7	2	Quitadouro	26S 0415078 4324328	Gabbro	Inequigranular	x	x	x		
	VU - Vb	GRQUx8	2	Quitadouro	26S 0415078 4324328	Gabbro	Inequigranular					
	VU - Vb	GRQUx9	2	Quitadouro	26S 0415078 4324328	Gabbro	Inequigranular					
	VU - Vb	GRQUx10	2	Quitadouro	26S 0415078 4324328	Gabbro	Inequigranular					
	VU - Vb	GRQUx11	2	Quitadouro	26S 0415078 4324328	Gabbro	Inequigranular					
	VU - Vb	GRQUx12	2	Quitadouro	26S 0415078 4324328	Gabbro	Inequigranular					
	VU - Vb	GRQUx13	2	Quitadouro	26S 0415078 4324328	Gabbro	Inequigranular					
	VU - Vb	GRQUx14	2	Quitadouro	26S 0415078 4324328	Gabbro	Inequigranular					
	VU - Vb	GRQUx15	2	Quitadouro	26S 0415078 4324328	Gabbro	Inequigranular					

3.1.1 Graciosa Island

Lava flows and xenoliths were sampled from Graciosa Island. The first sampling campaign was carried out in September 2007 (campaign-1; Table 3.1) by members of the research group. In this campaign some lava flows (from GRZF1 to GRZF17; Fig. 3.1A-B), most xenoliths from *Baía da Folga* and one xenolith from *Ponta da Pesqueira* were sampled. Once the main petrographic characterization of the volcanic units of the island was done, a second sampling campaign was carried out in January 2011 in the context of this PhD project (campaign-2; Table 3.1). In the second campaign the whole volcanostratigraphical sequence was sampled (lava flows; Fig. 3.1C), representing the full range of recognized compositions (see chapters 5 and 6). Xenoliths hosted in these lavas were also collected (see chapters 6) in four different sites: *Baía da Folga, Enxudreiro*, *Ponta da Pesqueira* (Fig. 3.1D) and *Quitadouro*.

Fig. 3.1 - Photographs taken during the 2007 (a - b) and 2011 (c - d) field work campaigns in Graciosa Island.

Table 3.2 - Summary of samples studied from Corvo Island and methods applied (see chapter 7).

Unit	Sample	Campaign	Location	UTM Coordinates	Classification	Texture	Thin Section	EMP	WR
Post-caldera lavas	COR 1	1	Pão de Açucar	25 S 0661387 4393621	Hawaite	Microporphyritic	x		x
	COR 51	2	Pão de Açucar	25 S 0661674 4393585	Hawaite	Microporphyritic	x		x
	COR 61	3	Pão de Açucar	25S 0661387 4393621	Hawaite	Microporphyritic	x		x
	COR 60	3	Quarry. Ribeira do Feno	25 S 0663063 4396119	Tephrite	Porphyritic	x		
	COR 31 -31/R	1	Quarry. Ribeira do Feno	25 S 0663073 4396307	Tephrite	Porphyritic	x	x	x
	COR 21	1	Quarry. Ribeira do Feno	25 S 0663032 4396246	Basalt	Porphyritic	x		x
	COR 20	1	Quarry. Ribeira do Feno	25 S 0663023 4396202	Basalt	Porphyritic	x	x	x
	COR 54	2	Cova Vermelha	25 S 0661596 4394413	Hawaite	Microporphyritic	x	x	x
	COR 2	1	Cova Vermelha	25 S 0661494 4394825	Hawaite	Microporphyritic			
	COR 5	1	Cova Vermelha	25 S 0661778 4394167	Hawaite	Microporphyritic	x		x
	COR 22	1	Montinho do Queijo (Caldeirão)	25 S 0662321 4397645	Hawaite	Microporphyritic			x
Syn-caldera lavas	COR 43	1	Portal Viewpoint	25 S 0662215 4393430	Trachyte	Glassy			
	COR 29	1	Fojo. East coast	25 S 0664136 4396487	Trachyte	Glassy			
	COR 27	1	Alqueve	25 S 0663669 4395710	Trachyte	Glassy			
	COR 59	3	Ribeira do Poço de Agua	25 S 0663736 4395873	Trachyte	Glassy	x		x
	COR 26	1	Vigia de Baleias	25 S 0663737 4395894	Trachyte	Glassy	x	x	x
	COR 28	1	Fojo. East Coast	25 S 0664179 4396298	Benmoreite	Glassy	x	x	x
Pre-caldera lavas	COR 33	1	Ponta Negra	25 S 0661737 4392793	Basalt	Microporphyritic	x		
	COR 41	1	NE Morro da Fonte	25 S 0662536 4394645	Basalt	Microporphyritic			
	COR 42	1	NE Morro da Fonte	25 S 0662536 4394645	Basalt	Microporphyritic			
	COR 48	1	Caldera Arc. Estreitinho	25 S 0661580 4396023	Basalt	Porphyritic			
	COR 44	1	Vila Nova do Corvo	25 S 0661981 4393432	Basalt	Microporphyritic			
	COR 49	1	Paus Altos	25 S 0662477 4395146	Basalt	Porphyritic			
	COR 36	1	Praia da Areia	25 S 0661114 4393162	Basalt	Microporphyritic			
	COR 32	1	Ribeira do Cerrado das Vacas	25 S 0662522 4394729	Basalt	Microporphyritic			
	COR 8	1	Ribeira de Pingas	25 S 0661425 4395382	Basalt	Porphyritic			
	COR 6	1	Ribeira da Fonte Doce	25 S 0661515 4395236	Basalt	Microporphyritic			
	COR 17	1	Caldera Arc	25 S 0662071 4398347	Basalt	Porphyritic	x		x
	COR 16	1	Caldera Arc	25 S 0662572 4398047	Basalt	Porphyritic	x		x
	COR 13	1	Caldera Arc	25 S 0662857 4397805	Hawaite	Microporphyritic	x		x
	COR 12	1	Caldera Arc	25 S 0662855 4397776	Basalt	Porphyritic	x		x

Table 3.2 - Summary of samples studied from Corvo Island and methods applied (see chapter 7).

Unit	Sample	Campaign	Location	UTM Coordinates	Classification	Texture	Thin Section	EMP	WR
Pre-caldera lavas	COR 7	1	Next to Ribeira de Pingas	25 S 0661501 4394817	Basalt	Porphyritic	x	x	x
	COR 9 -9/R	1	Fonte Doce	25 S 0661484 4394534	Picrite	Porphyritic	x		x
	COR 4	1	Calçada	25 S 0662816 4394074	Hawaite	Microporphyritic	x	x	x
	COR 3	1	Viewpoint. Miradouro Portal	25 S 0662155 4393390	Hawaite	Microporphyritic	x		x
	COR 50	2	Porto da Casa	25 S 0662020 4393020	Hawaite/ Tephrite	Microporphyritic	x		x
	COR 11	1	Porto da Casa	25 S 0661991 4392975	Hawaite	Microporphyritic	x		x
	COR 58	3	Porto da Casa	25 S 0662212 4393245	Basalt	Porphyritic	x		x
	COR 23	1	Pingas. West coast	25 S 0661315 4394415	Mugearite	Microporphyritic	x	x	x
Pre-caldera dikes	COR 52	2	Caldera Arc	25 S 0662772 4397712	Basalt	Porphyritic	x		x
	COR 14	1	Caldera Arc. Estreitinho	25 S 0662693 4397630	Basalt	Porphyritic	x		x
	COR 15	1	Caldera Arc. Estreitinho	25 S 0662781 4397655	Picrite	Porphyritic	x	x	x
	COR 53	2	Morro da Fonte	25 S 0661597 4393856	Basalt	Porphyritic	x		
	COR 57	2	Vila Nova do Corvo East coast cliff	25 S 0662335 4393266	Basalt	Porphyritic	x		x
	COR 56	2	Vila Nova do Corvo East coast cliff	25 S 0662335 4393266	Basalt	Porphyritic	x		x
	COR 55	2	Vila Nova do Corvo East coast cliff	25 S 0662335 4393266	Basalt	Porphyritic	x		x
	COR 35	1	Vila Nova do Corvo East coast cliff	25 S 0662403 4393293	Basalt	Microporphyritic	x		x
	COR 25	1	Pingas. West coast	25 S 0661316 4394402	Basalt	Porphyritic	x	x	x
	COR 24	1	Pingas. West coast	25 S 0661316 4394402	Mugearite	Microporphyritic	x	x	x
Xenoliths	COR ENC-1	1	Fajã da Vila Nova	25 S 0661114 4393162	Gabbro	Heteroadcumulate	x	x	x
	COR ENC-2	1	Fajã da Vila Nova	25 S 0661114 4393162	Gabbro	Heteroadcumulate	x		
	COR ENC-3	1	Fajã da Vila Nova	25 S 0661114 4393162	Gabbro	Heteroadcumulate	x	x	x
	COR ENC-4	1	Fajã da Vila Nova	25 S 0661114 4393162	Gabbro	Heteroadcumulate	x	x	x
	COR ENC-5	1	Fajã da Vila Nova	25 S 0661114 4393162	Gabbro	Heteroadcumulate	x		

3.1.2 Corvo Island

All of the diverse igneous materials in Corvo including lava flows, dikes and xenoliths were sampled for petrological and geochemical studies (see chapter 8). In this island, two field campaigns were carried out before this PhD project by the research group.

Fig. 3.2 - Photographs taken during the 2001 (a - b), 2005 (c - d) and 2012 (e - f) field work campaigns in Corvo Island.

In 2001, lavas and xenoliths were collected from the whole volcanostratigraphical sequence of the island (including some lavas and dikes sampled by boat), in order to investigate the evolution of the magmatic plumbing system (campaign-1; Table 3.2; Fig. 3.2A-B). In June 2005 all the dikes were sampled (campaign-2; Table 3.2; Fig. 3.2C-D). This field campaign was done in collaboration with Dr. Óscar Pueyo (Universidad de Zaragoza) to model the relationship between flow directions and Anisotropy of Magnetic Susceptibility (AMS). A third campaign was carried out in the context of this PhD project, in March 2012, with the key aim of characterizing previous samples according to the volcanostratigraphy proposed by França et al. (2002) (campaign-3; Table 3.2; Fig. 3.2E-F).

Moreover, some previously studied lava flows were re-sampled for dating purposes (out of the scope of this PhD Thesis).

3.2 Laboratory work

The samples were first studied macroscopically to select areas of interest for microscopic examination. Thin sections of the samples (30 µm thickness) were prepared by the Servicio General de Apoyo a la Investigación of the Universidad de Zaragoza (Spain). They were studied under the petrographic microscope of the Servicio General de Apoyo a la Investigación of the Universidad de Zaragoza (Spain) to describe the petrography of the samples (mineral assemblage, mineral modes and texture). The petrographic study led to the selection of representative thin sections for mineral analyses and whole rock chemical analyses.

The mineral chemistry study involved mineral classification and a careful evaluation of the different crystal populations. This was particularly relevant in Corvo Island, where three main populations were defined: phenocrysts, crystals co-genetic with their magmatic host; antecrysts, co-magmatic crystals which are recycled one or several times before inclusion in the host magma; and microcrysts, which represent small co-genetic crystals which nucleate and grow rapidly on decompression and eruption. Mineral major element compositions were determined on polished thin sections by electronic microprobe (EMP) at the Centro Nacional de Microscopía Electrónica of the Universidad Complutense de Madrid (Spain) (Fig. 3.3).

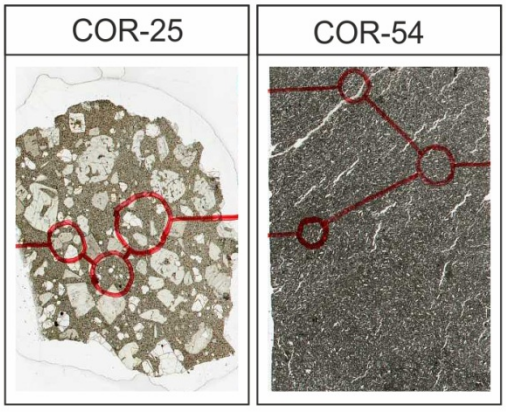

Fig. 3.3 - Scanned thin sections (2.5 cm width) of porphyritic (left) and microporphyritic (right) textures of Corvo Island rocks. Whole rock compositions are strongly influenced by the volume fraction and type of macrocrysts (see chapter 8). Circles indicate areas analyzed by EMP.

Lava flow, dike and xenolith samples were carefully selected for whole rock chemistry considering the nature of the rocks

(composition - primitive or evolved, and texture - porphyritic, microporphyritic, trachytic or glassy for the lavas and dikes, and cumulate, equigranular or inequigranular textures for xenoliths). The selected samples were crushed in a manganese steel jaw-crusher and milled in an agate vibrating cup mill at the Servicio General de Apoyo a la Investigación of the Universidad de Zaragoza (Spain).

These samples were analyzed by different techniques and in different laboratories according to the field work campaign in which they were collected (see details in chapters 6 and 8). Major and trace element concentrations of lava flow and xenoliths samples from Graciosa Island were determined in two different laboratories (see chapter 6 for analytical details and procedures). Samples of the first fieldwork campaign-1 (Table 3.1) were analyzed at the IBERCRON laboratory of the Universidad del País Vasco (Spain) by ICP-MS. In contrast, samples collected during fieldwork campaign-2 (Table 3.2) were analyzed by ICP-MS at the labGEOTOP laboratory of the Institut de Ciències de la Terra Jaume Almera (Spain). Samples from Corvo were determined in three different laboratories. The major and trace element concentrations of lava flow samples collected in fieldwork campaign-1 (Table 3.2) were determined the same year at the ACTLAB laboratory (Canada), using an ICP-OES for major elements and ICP-MS for trace elements. Whole rock analyses for dikes (campaign-1) and xenoliths (campaign-2) were carried out in 2006 (Table 3.2). Major element contents were analyzed by X-Ray Fluorescence Spectrometry at the Servicio de Espectrometría y Difracción de rayos X of the Universidad de Oviedo, and trace elements were analyzed at the Centro de Instrumentación Científica of the Universidad de Granada by ICP-MS (see chapter 8 for analytical details and procedures).

Sample preparation and analysis for Sr, Nd and Pb isotope ratios were performed at the Isotope Geochemistry & Mass Spectrometry Laboratory of the Miami University (Ohio, USA) during a research stay (August - December 2012) under the supervision of Prof. Dr. Elisabeth Widom (Fig. 3.4; see details in chapter 6). Samples were crushed in an alumina jaw-crusher and powdered in a high-purity alumina mixer mill. The isotopic compositions of Sr, Nd and Pb were measured by thermal ionization mass spectrometry (TIMS).

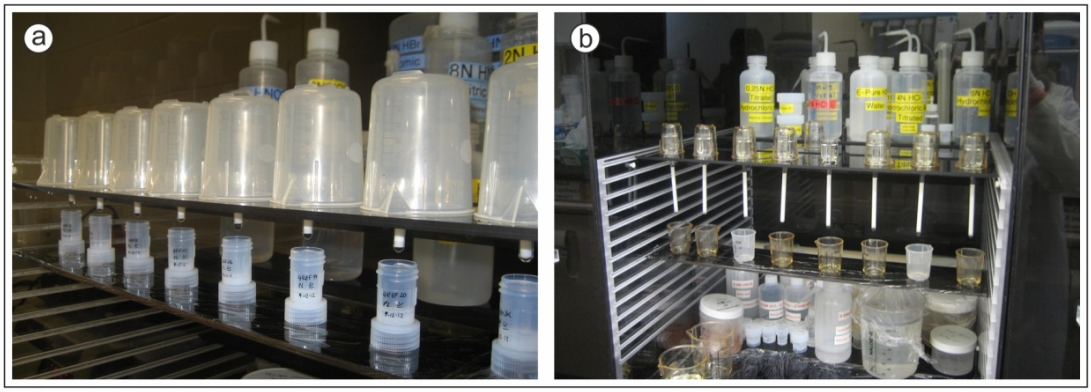

Fig. 3.4 - Sampling preparation for isotopic analysis. Process of extraction and purification of (a) Sr and (b) Nd carried out at the Geochemistry & Mass Spectrometry Laboratory of the Miami University.

$^{40}Ar/^{39}Ar$ geochronology was carried out on feldspars and groundmass separates at the Argon Geochronology laboratory of the VU University Amsterdam (The Netherlands). Two research stays were done under the supervision of Prof. Dr. Jan R. Wijbrans. The separates were prepared at the Mineral Separation Laboratory of the VU University Amsterdam during the first research stay (May 2011); each sample was crushed, sieved and separated (groundmass or feldspar crystals) using heavy liquids and Frantz® magnetic separator if necessary. The separated fractions were purified by HNO_3-leaching and hand-picking under a binocular microscope (Fig. 3.5). The final separates together with laboratory standard packages were sent for irradiation to the Cd-lined RODEO facility of the High Flux Reactor (HFR) at Petten (The Netherlands).

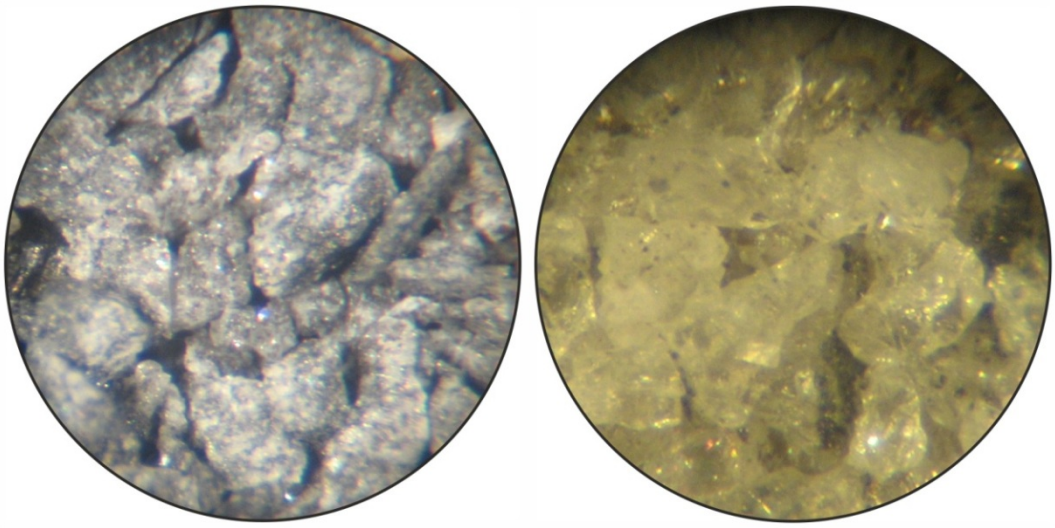

Fig. 3.5 - Photomicrographs of a 400 - 500 µm homogeneous groundmass (left) and plagioclase (right) grain separates after being selected by hand-picking prior to irradiation for Ar dating.

Experiments on Ar isotope ratios were carried out during the second research stay (February - March 2012) to obtain crystallization ages. The separates were first pre-heated and then analyzed with a CO_2 laser heating system by incremental heating (groundmass) or total fusion (feldspars). The purified gas fractions were analyzed with an Automated Gas Extraction System (AGES) noble gas quadrupole mass spectrometer (see details in chapter 5).

3.3 Data treatment

Mineral and whole-rock geochemical data were mainly treated with ad-hoc built spreadsheets. Structural formulae were calculated for each EMP spot analysis on minerals for classification and modeling purposes. The different crystal populations (xenocrysts, antecrysts, phenocrysts, and microcrysts) were determined after a careful evaluation of mineral-melt equilibrium (olivine, clinopyroxene and amphibole; see chapters 6 and 8). Recalculations and normalizations were applied to whole rock compositions as appropriate. Trace element fractional crystallization models were calculated from whole-rock compositions and mineral modes. A large geochemical dataset was constructed with new and previously published isotopic data from the Azores archipelago for the discussion section in chapter 6.

The major element fractional crystallization models were carried out using the MELTS algorithm (Ghiorso and Sack, 1995; Asimow and Ghiorso, 1998; http://melts.ofm-research.org). MELTS is a software package designed to facilitate thermodynamic modeling of phase equilibria in magmatic systems and quantify natural processes and test petrological and mineralogical hypotheses (see chapters 6 and 8).

The contribution and effect of antecrysts to the whole rock composition of porphyritic rocks has been quantified for the first time in the Azores archipelago (Larrea et al., 2013; see chapter 8) using the MINSQ software (Herrmann and Berry, 2002). It is a least squares regression model that calculates the proportions of constituent phases in a rock according to the composition of the phases and the whole rock (see chapter 8).

The ArArCALC2.5 dedicated data reduction software (Koppers, 2002; http://earthref.org/tools/ararcalc/) was used for the calculation of $^{40}Ar/^{39}Ar$ ages. Previously published K/Ar and ^{14}C ages were compiled and discussed together with new Ar ages to constrain the temporal evolution of Graciosa Island.

3.4 Presentation of results

Petrological, mineralogical and geochemical data have been interpreted and discussed to characterize individual volcanological units and investigate the magmatic evolution of Graciosa and Corvo Islands. Moreover, the ages obtained in Graciosa have allowed to better constrain the temporal evolution of this island.

This Thesis contains material published, accepted or currently under review for publication in peer-reviewed journals:

- Chapter 5: Larrea, P., Wijbrans, J.R., Galé, C., Ubide, T., Lago, M., França, Z. and Widom, E. (2014). $^{40}Ar/^{39}Ar$ constraints on the temporal evolution of Graciosa Island, Azores (Portugal). *Bulletin of Volcanology*, doi: 10.1007/s00445-014-0796-8.

- Chapter 6: Larrea, P., Galé, C., Ubide, T., Widom, E., Lago, M. and França, Z. (under review). Magmatic evolution of Graciosa island (Azores, Portugal). *Journal of Petrology*.

- Chapter 8*: Larrea, P., França, Z., Lago, M., Widom, E., Galé, C. and Ubide, T. (2013). Magmatic processes and the role of antecrysts in the genesis of Corvo island (Azores archipelago, Portugal). *Journal of Petrology* 54, 769-793.

* The geochemical dataset of this chapter is available in the global geochemical database GEOROC (http://georoc.mpch-mainz.gwdg.de/georoc/)

In addition, some of the results have been also presented in numerous national and international meetings:

- Larrea, P., Widom, E., Galé, C., Ubide, T., Lago, M. and França, Z. (2013). New Sr-Nd-Pb isotopic data on Graciosa island lavas (Azores). *Mineralogical Magazine* 77 (5), 1547. Goldschmidt Conference (poster).

- Larrea, P., Galé, C., Ubide, T., Widom, E., Lago, M., França, Z. and Tierz, P. (2012). Magmatic Evolution of the Western Azores Islands (Corvo and Flores). Abstract DI51A-2353, AGU 2012 Fall Meeting (poster).

- Larrea, P., Lago, M., França, Z., Widom, E., Galé, C., Ubide, T., Arranz, E. and Tierz, P. (2012). The influence of antecrysts on the whole-rock composition of lava flows and dykes from Corvo Island (Azores). *Geophysical Research Abstracts* 14, EGU2012-115. EGU General Assembly (poster).

- Larrea, P., Lago, M., França, Z., Widom, E., Galé, C., Ubide, T., Tierz, P. and Sanz, T. (2012). Equilibrios mineral-fundido en las lavas de la Isla Graciosa (Azores, Portugal): inferencias sobre la etapa proto-isla. *Geogaceta* 53, 77-80.

- Larrea, P., França, Z., Lago, M., Widom, E., Galé, C., Ubide, T., Arranz, E., Forjaz, V.H., Ribeiro, L. and Pueyo, O. (2011). Origin of lavas and xenoliths of Graciosa volcanic island (Açores, Portugal). Abstract #1921. IUGG General Assembly (poster).

- Larrea, P., Lago, M., França, Z., Widom, E., Galé, C., Ubide, T., Forjaz, V.H., Pueyo, O., Arranz, E. and Tierz, P. (2011). Magma chamber recharge in Corvo volcanic Island (Açores, Portugal). *Geophysical Research Abstracts* 13, EGU2012-6867. EGU General Assembly (poster).

- Larrea, P., Lago, M., França, Z., Widom, E., Galé, C., Ubide, T. and Arranz, E. (2010). Cumulate origin of the alkaline xenoliths from Graciosa Island (Açores, Portugal): geochemical modelling. *Geogaceta* 49, 75-78.

- Larrea, P., Lago, M., França, Z., Widom, E., Galé, C., Ubide, T. and Pueyo, O. (2010). Mineralogy of gabbroic xenoliths in the Graciosa Island Vulcão Central Unit (Azores, Portugal). *Macla* 13, 133-134. Spanish Mineralogical Society Meeting (oral).

- Larrea, P., Lago, M., França, Z., Widom, E., Galé, C., Ubide, T. and Arranz, E. (2010). Geochemistry of gabbroic xenoliths in the Graciosa Island Vulcão Central Unit (Azores, Portugal). *Macla* 13, 131-132. Spanish Mineralogical Society Meeting (oral).

PART II: STUDY OF GRACIOSA ISLAND

CHAPTER 4: GRACIOSA ISLAND: A REVIEW

4.1 Geographic, geomorphologic and geotectonic setting

Graciosa Island (the graceful or enchanting island in Portuguese) is the northernmost island of the Central Group, located between 39º and 39º06' N latitude and 27º56' and 28º05' W longitude. It is situated on the Terceira Rift and distanced ca. 150 km from the Mid-Atlantic Ridge, 57 km from Terceira Island and 36.5 km from São Jorge (Fig. 4.1).

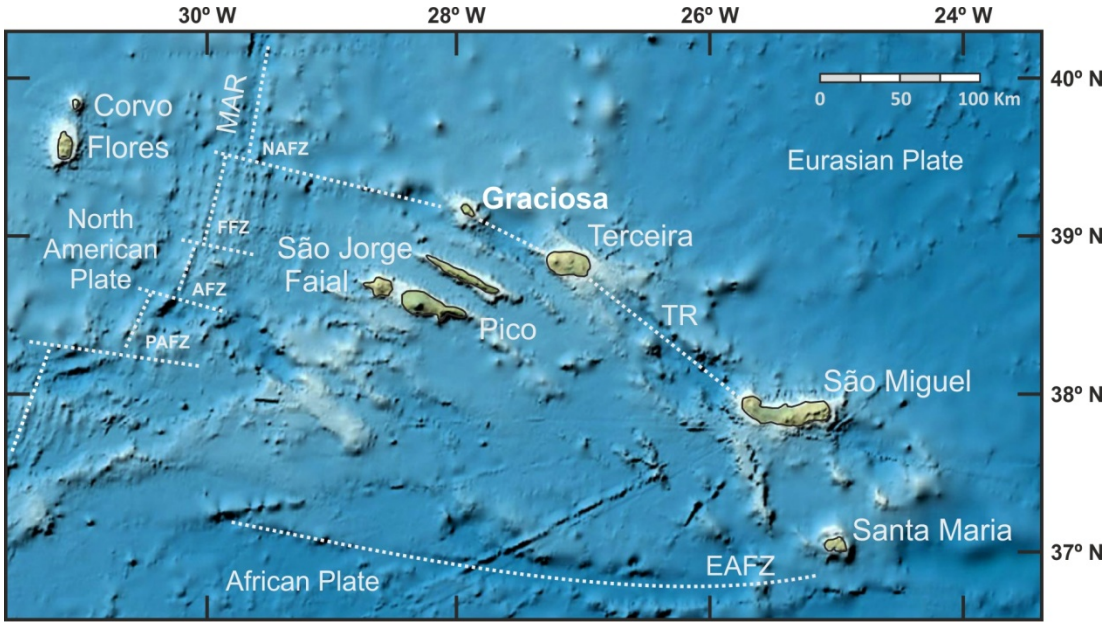

Fig. 4.1 - Location of Graciosa Island within the Azores archipelago and general geotectonic setting of the studied area modified after the GEBCO world map 2013 (www.gebco.net). EAFZ: East Azores Fracture Zone; TR: Terceira Rift; MAR: Mid.Atlantic Ridge; NAFZ: North Azores Fracture Zone; FFZ: Faial Fracture Zone; AFZ: Açor Fracture Zone; PAFZ: Princess Alice Fracture Zone.

Classified by UNESCO as a Biosphere Reserve since 2007, the island of Graciosa is the second smallest island of the Azores archipelago (after Corvo) with a total area surface of 60.7 km² and 38.9 km of coastline. Graciosa has a WNW-ESE elongated shape with a maximum length of 12.6 km and a width of 7 km. Presently, the island has approximately 4,400 inhabitants, mainly distributed throughout the municipality of *Santa Cruz da Graciosa* (*Guadalupe*, *Luz*, *Praia* and *Santa Cruz*).

Overall, Graciosa is the flattest island of the Azores archipelago and is divided into four geomorphological zones (Fig. 4.2): (1) the *Caldeira*, located on the southeastern part of the island, comprising a well preserved stratovolcano and its caldera with the highest altitude of 405 m within the east rim; (2) the *Serra das Fontes* massif, located along the northeastern coast; (3) The *Serra Dormida* and *Serra Branca* highlands, occupying a third of the central island with the highest altitude of 398 m at *Pico Timão*; (4) the NW platform, characterized by a topographical relief that is gently sloping to the south (approximately 50 meters) with several isolated cones.

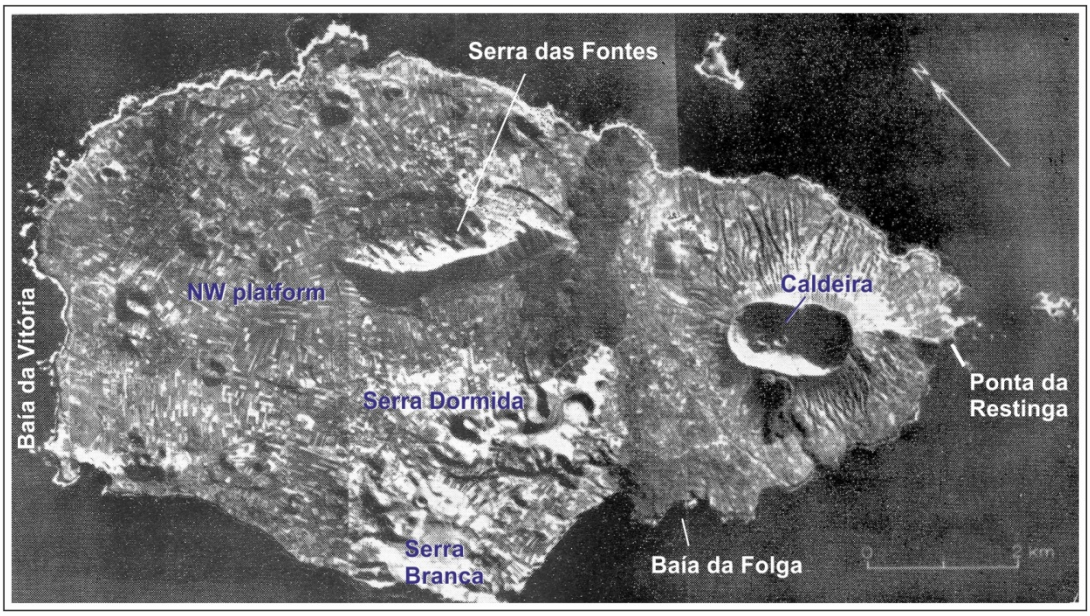

Fig. 4.2 - Aerial photo of Graciosa Island from Ferreira (1968), with the most remarkable geomorphological features labeled.

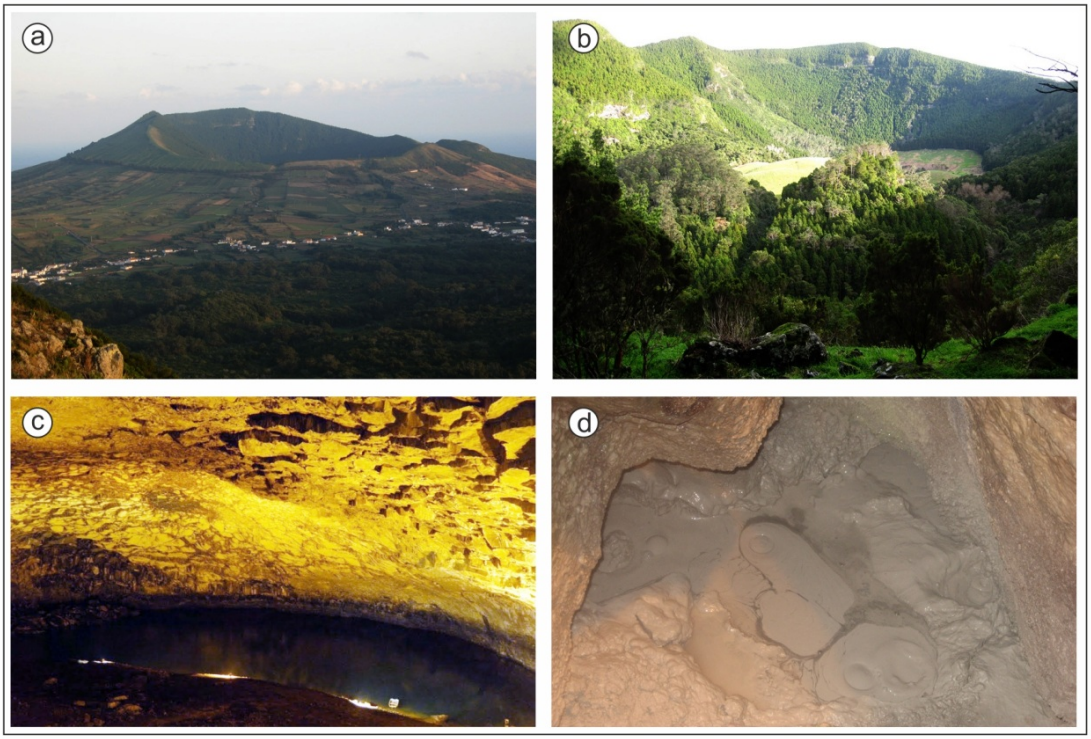

Fig. 4.3 - Photographs of the southern area of Graciosa Island: (a) panoramic view of the *Caldeira*, (b) interior of the *Caldeira* - note the abundant vegetation covering the walls (cryptomeria, acacia, pine trees and incense), (c) *Furna do Enxofre* cave and (d) boiling mud pool found in the *Furna do Enxofre*.

The *Caldeira* is a remarkable feature of the island landscape (Fig. 4.3A). It is an elliptical caldera formed as a result of the draining of the stratovolcano during a particularly large and violent eruption (Gaspar, 1996). This caldera has a NW-SE length of 1,625 m, 875 m width and a depth of 350 m (Zbyszewski et al., 1972) and is fully covered by vegetation (Fig. 4.3B). At its center lays the *Furna do Enxofre*, an enormous cave with a diameter of 130 m and vault reaching a height of 80 m (Fig. 4.3C). Inside the cave, there is a 10 m deep and 120 m wide subterranean lake with warm sulphurous water. Since 1939, the *Furna do Enxofre* can be accessed through a spiral staircase tower that allows the observation of boiling mud pools (Fig. 4.3D) and a degassing field. This fumarolic field releases mainly H_2O, CO_2 and other minor gases (H_2S, H_2, CH_4 and N_2) with concentration levels monitored by the CVARG (Centro de Vulcanologia e Avaliação de Riscos Geológicos da Universidade dos Açores) and the local visitor center.

Fig. 4.4 - (a) Panoramic view of the northeastern coast at *Santa Cruz da Graciosa* town, note the isolated cones of the NW platform and the *Serra das Fontes* massif in the background, (b) Serra Branca northwestern coast and (c) *Ponta da Restinga* cliffs at the southeastern coast.

The coast is generally characterized by short steep cliffs (< 10 m high; Fig. 4.4A) and numerous bays (e.g., *Baia da Folga* and *Baia da Vitória*; Fig. 4.2). However, the northwestern coast along the *Serra Branca* massif (Fig. 4.4B) and the southwestern coast (*Ponta da Restinga*; Fig. 4.4C) show cliffs that could exceed 200 m height.

The main structures on Graciosa Island were studied by Gaspar (1996), who defined a main NW-SE trending fault system that controls the WNW-ESE elongated shape of the island and is linked to the Terceira Rift tectonics (e.g., Hildenbrand et al., 2008).

4.2 History and previous studies

The Azores archipelago was first mapped during the 14th century, after a non-official exploration during the late 13th century that mentioned an archipelago composed of seven islands in the Atlantic Ocean. In these maps however, Graciosa seems to be missing. The first exploration of Graciosa Island was carried out during the first quarter

of the 15th Century by Portuguese navigators. The exact date of its discovery is uncertain, but it was after the discovery of Terceira Island. The Portuguese Vasco Gil Sodré settled in the island soon after its discovery. The first settlers occupied the area around *Carapacho* (southeastern coast), but they rapidly moved inwards in search of more favorable grounds. New settlements were built, such as *Santa Cruz* which became the main town and administrative center on the island in 1486, and *Praia* which was upgraded to town in 1546. During this time, the island received a new influx of settlers from The Netherlands and continental Portugal (*Beiras* and *Minho*) who contributed to the economic development of the island.

The first reference to the geology of Graciosa Island was made by Hartung (1860), who gave a general geological and geomorphological account of the Azores as a whole. The first specific geomorphological work on Graciosa was carried out by Moniz (1884). A few years later the first petrographic study of the archipelago was published (Esenwein, 1930), and it considered lavas from Graciosa. Berthois (1953) described the lithological variety of the Azores rocks, including sediments and volcanic rocks from Graciosa Island. Ferreira (1968) carried out an important study about the physical and human geography of Graciosa.

The first regional geological survey on the island was undertaken by Zbyszewski (1970), who published a geological map of Graciosa on scale 1:25,000 (Zbyszewski et al., 1972), mainly based on petrographic observations. Forjaz and Pereira (1976) completed this study with stratigraphic data and established the preliminary 1:25,000 volcanic map.

The Vulcão Central was studied by Agostinho (1937), Morais (1953), Krejci-Graf (1961) and Saucier (1965), who investigated the formation of the caldera, the lava lake and the *Furna do Exnofre*. However, the first study of the evolution of the Vulcão Central as a whole was carried out by Maund (1985), who accomplished a detailed petrographic and geochemical characterization of its volcanic products.

These previous studies were compiled and enhanced by Gaspar (1996) who, based on the spatio-temporal development of the main eruptive centers on the island and their

associated volcaniclastic deposits, published the most recent volcanostratigraphic map of Graciosa (Gaspar and Queiroz, 1995). Recent studies by the same research group comprised the study of the tectonic structures of the island (Hipólito, 2009) and the geochemistry of the volcanic products (Almeida, 2001).

Moreover, petrographic, geochemical and isotopic datasets from Graciosa have been published in papers that deal with other Azorean Islands (White et al., 1976; White et al., 1979; Feraud et al., 1980; Lemarchand et al., 1987; França, 1993; Widom and Shirey, 1996; França et al., 2003; Beier et al., 2008). Some of these previous studies included K-Ar datings (Feraud et al., 1980), ^{14}C datings (Maund, 1985; Gaspar, 1996) and a Rb-Sr apparent age calculated by White et al. (1976).

4.3 Volcanostratigraphy and previous dating results

Gaspar (1996) established the volcanostratigraphy of Graciosa based on the spatio-temporal development of the main eruptive centers and their associated volcaniclastic deposits. Three major volcanic complexes were defined, in order of decreasing age: the Serra das Fontes complex, the Serra Branca complex and the Vitória - Vulcão Central complex. Gaspar (1996) subunits have been grouped and renamed in order to simplify the volcanostratigraphy according to the main volcanic events in Graciosa; the equivalence between the subunits of Gaspar (1996) and those used in this Thesis can be found in Fig. 4.5.

The Serra das Fontes volcanic complex (hereafter referred to as Serra das Fontes) is the oldest subaerial part of the island. It comprises a shield volcano with its main eruptive center located in the current *Serra Branca* massif (Fig. 4.6; Gaspar 1996). Today, it is only exposed in the SW flank of the *Serra das Fontes* massif (Fig. 4.7) and in inaccessible cliffs on the NE and SW coasts (Fig. 4.6). It was mainly built by Hawaiian eruptions alternating with short explosive periods (Gaspar, 1996) producing basic volcanic rocks (basalts to

Volcanic Units	Gaspar (1996)	Present Study	Volcanic products
Serra das Fontes	Fb	SF	Basic lava flows and undifferentiated volcanoclastic deposits
Serra Branca	Bt	SB-a	Evolved lavas flows
	Bdvi	SB-b	Undifferentiated volcanoclastic deposits
	Bbt	SB-c	Evolved breccias
Vulcão Central	Rpi	VCU-a	Basic lava flows, associated pyroclastic deposits (subaerial and submarine) and hydromagmatic deposits
	Rb		
	Rpyb		
	Rdpi		
	Rhm		
	Cb	VCU-b	Basic lava flows
	Cpyb	VCU-c	Pyroclastic deposits associated to VCU-b subunit
	Cdvi		
	Cxb	VCU-d	Basaltic lava flows bearing gabbroic xenoliths
	Csh	VCU-e	Caldera hydromagmatic sequence
	Cd	VCU-f	Evolved lava flows and domes
	Lb	VCU-g	Basic lava flows
	Cfm	VCU-h	Intracaldera phreatomagmatic deposits
Vitória	Vb	VU-a	Basic lava flows
	Vpyb	VU-b	Pyroclastic deposits (subaerial and submarine) associated to VU-a subunit
	Vpi		
	Tb	VU-c	Basic lava flows
	Tpyb	VU-d	Subaerial pyroclastic deposits associated to VU-c subunit

Fig. 4.5 - Description of the volcanostratigraphic sequence of Graciosa Island. Equivalence between Gaspar (1996) subunits and those used in the present study.

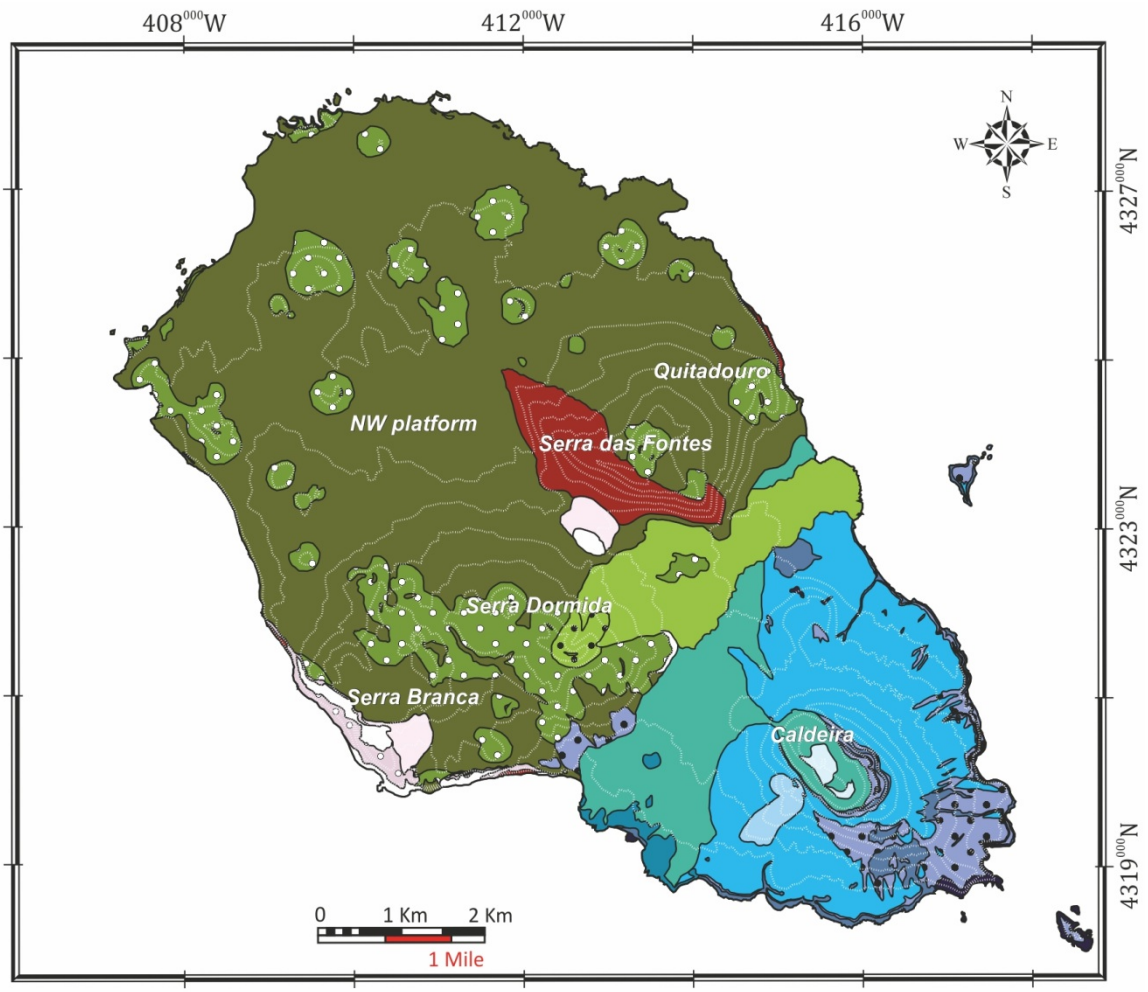

Fig. 4.6 - Geological map of Graciosa Island modified from Gaspar and Queiroz (1995). Contour interval: 50 m. Volcanostratigraphic units are described in Fig. 4.5.

hawaiites; Gaspar, 1996; Almeida, 2001; Larrea et al., under review). Feraud et al. (1980) obtained a K-Ar age of 620 ± 120 ka, whereas preliminary Rb-Sr data (White et al. 1976) suggest older ages of ca. 2.5 Ma (Table 4.1).

The Serra Branca volcanic complex (hereafter referred to as Serra Branca) was formed by the evolution of the Serra das Fontes magmatic system, which eventually produced a central composite volcano (Gaspar, 1996). Most of the products of Serra Branca have been eroded and covered by younger volcanic rocks (Vitória - Vulcão Central volcanic complex rocks), so at the present time this complex is only exposed in the W coast (*Serra Branca* massif; Fig. 4.7), in the central plateau, and in isolated outcrops on the coast to the north of *Quitadouro* volcano (Fig. 4.6). It is mainly composed of evolved products (Gaspar, 1996; Almeida, 2001; Larrea et al., under review), including minor lava flows

(SB-a subunit in Figs. 4.5 - 4.6) and highly explosive volcaniclastic deposits (pyroclastic flows as pumice fall deposits, ignimbrites, surges and *lahars*; SB-b and SB-c subunits in Figs. 4.5 - 4.6). Two samples from Serra Branca were analyzed by K-Ar (Feraud et al., 1980), giving an age range from 350 ± 40 to 260 ± 20 ka (Table 4.1).

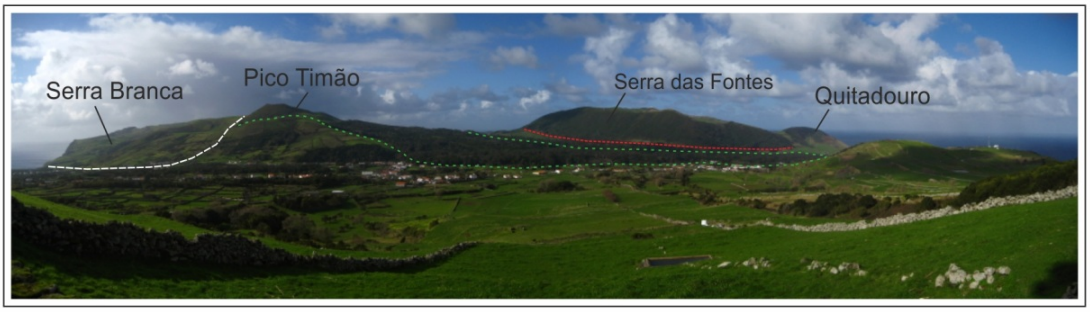

Fig. 4.7 - Graciosa Island panoramic view taken from the Vulcão Central northern flank, showing *Serra das Fontes* and *Serra Branca* massifs, *Quitadouro* volcano and *Pico Timão* and related youngest lava flow.

The Vitória - Vulcão Central volcanic complex is the most recent and comprises two units: Vitória and Vulcão Central. The Vitória Unit was formed after a period of volcanic inactivity in Graciosa, allowing for the erosion of the former central composite volcano (Gaspar, 1996). Vitória Unit volcanism was characterized by weakly explosive volcanism (isolated scoria and spatter cones; VU-b, d subunits in Figs. 4.5 - 4.6) and the emission of their associated lava flows (VU-a, c subunits in Figs. 4.5 - 4.6), which formed the present Vitória Unit NW platform (Gaspar, 1996; Fig. 4.8).

Fig. 4.8 - Panoramic view of the Vitória Unit NW platform. Note the isolated monogenetic cones distributed throughout the Vitória Unit platform.

In contrast, the formation of the Vulcão Central Unit started to the south of the oldest volcanic structures. Pre-caldera volcanism was initially strombolian, forming monogenetic volcanoes that alternated with minor surtseyan eruptions (Maund, 1985; Gaspar, 1996; VCU-a subunit in Figs. 4.5 - 4.6 and Fig. 4.9). Afterwards, volcanism became associated with a main eruptive center, forming a stratovolcano (the Vulcão Central). This period was characterized by alternating lava flows (VCU-b, d, subunits in Figs. 4.5 - 4.6 and Fig. 4.9) and associated pyroclastic deposits (VCU-c subunit in Figs. 4.5 - 4.6) that occasionally became more explosive (plinian to sub-plinian pumitic deposits and *lahars*).

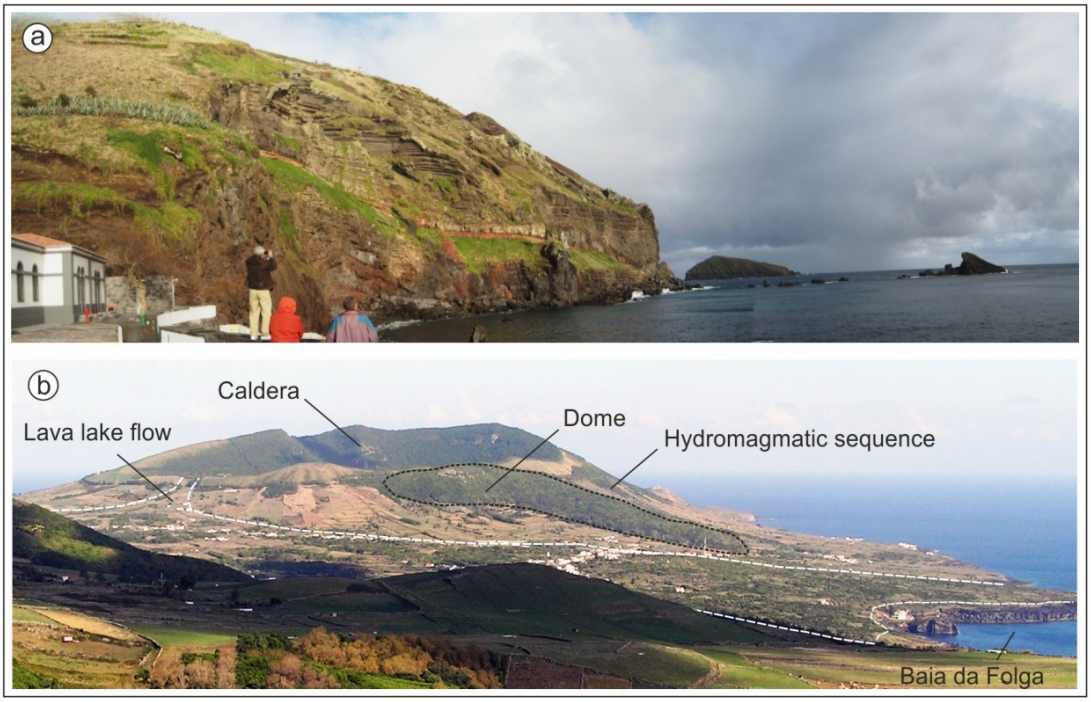

Fig. 4.9 - Photographs of Graciosa Vulcão Central Unit: (a) pre-caldera VCU-a subunit, (b) Vulcão Central panoramic view, showing the pre-caldera *Baia da Folga* lava flow bearing xenoliths (VCU-d subunit), the caldera and its associated hydromagmatic sequence (VCU-e subunit), and the post-caldera volcanic dome (VCU-f subunit) and lava lake flow (VCU-g subunit).

Afterwards, the caldera forming event was characterized by highly explosive hydromagmatic eruptions (syn-caldera stage), which produced the present caldera and the most extensively exposed pyroclastic sequence (products of stratovolcano draining during a particularly large and violent eruption; Maund, 1985; Fig. 4.9). This hydromagmatic sequence consist of airfall, base surge and *lahar* deposits (VCU-e subunit

Table 4.1 - Compilation of the available geochronological data of Graciosa Island prior to this PhD Thesis. It includes K/Ar ages from Feraud et al. (1980), ^{14}C ages from Maund (1985) and Gaspar (1996) and an Rb-Sr apparent age calculated by White et al. (1976). Ages are plotted in Fig. 4.10 according to their location as described in each work.

Author	Method	Age	Sample	Location
Feraud et al. (1980)	K/Ar	620 ± 120 Ka	Basaltic lava	*Caminho da Igreja*; 400 m NNE from *Guadalupa*
		350 ± 40 ka	Trachytic lava	250 m W from *Canada Longa*
		260 ± 40 ka	Trachytic lava	30 m NW from *Serra Branca* top
White et al. (1976)	Rb/Sr	2.5 Ma	Rb-Sr apparent age	-
Gaspar (1996)	^{14}C	12200 ± 90 y	Wood fragment	*Fonte de Areia*
Maund (1985)	^{14}C	12740 ± 70 y	Wood fragment	*Beira Mar*; 15 m below cliff top in soil
		29660 ± 580 y	Wood fragment	*Caldeira*, midway between *Baía Engrade* and *Baía Homizados*
		31350 ± 280 y	Wood fragment	*Baía Homizados*, 40 m below cliff top in basalt scoria
		31407 ± 300 y	Peat / wood	*Baía Engrade*, 50 m below cliff top in soil horizon

in Figs. 4.5 - 4.6; Maund, 1985). The post-caldera stage was mainly effusive, forming a lava dome (VCU-f subunit in Figs. 4.5 - 4.6 and Fig. 4.9) on the caldera southern flank and a lava lake (VCU-g subunit in Figs. 4.5 - 4.6 and Fig. 4.9) in the caldera. This lava lake overspilled the rim at two points before partially draining out (Maund, 1985), allowing the subsequent formation of two small intracaldera pyroclastic cones (VCU-h subunit in Figs. 4.5 - 4.6). Compositionally, the Vulcão Central Unit comprises a wide range of compositions (basaltic to trachytic), whereas the Vitória Unit is mostly basaltic (Gaspar, 1996; Almeida, 2001; Larrea et al., under review).

The Vitoria Unit has not been dated before. In contrast, several ^{14}C ages were determined in peat and wood fragments found within pyroclastic deposits (Maund, 1985; Gaspar, 1996; Table 4.1) from the Vulcão Central Unit. These ages range from 31 ± 0.3 to 12.2 ± 0.09 ka, but only some of them (mentioned below) were used to constrain the temporal evolution of the island.

Maund (1985) based on his knowledge of the geology of the island, indicates that most of the Vulcão Central Unit was formed from 50 to 10 ka (excluding the earliest and inaccessible deposits, which are probably older than 50,000 years).

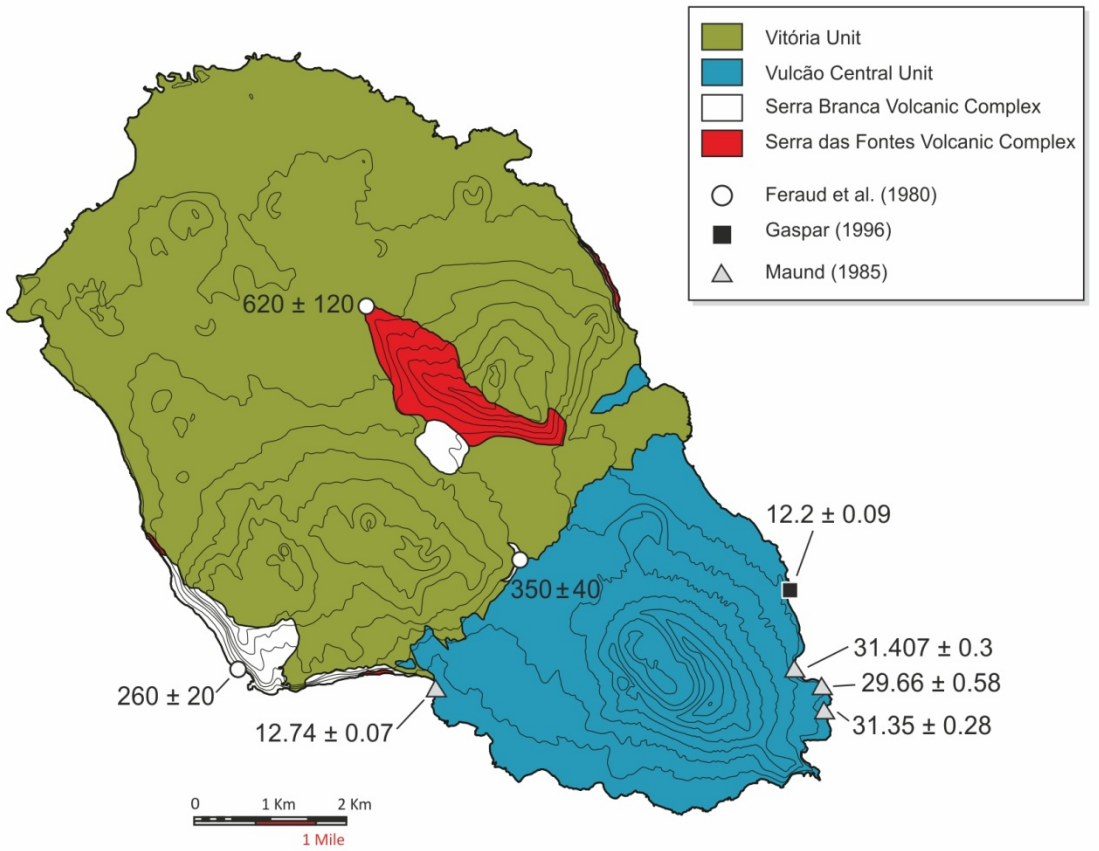

Fig. 4.10 - Geological map of Graciosa Island simplified from Gaspar (1996), showing geochronological data from Feraud et al. (1980), Gaspar (1996) and Maund (1985) (ages given in thousands of years); see Table 4.1. Contour interval: 50 m.

Gaspar (1996) mentioned a pumice deposit found within the Vitória Unit volcanic sequence, which seems to be related to the Vulcão Central plinian activity (12.2 ± 0.09 ka; Gaspar, 1996). Following this assumption, Gaspar (1996) suggested that most volcanic products of the Vitória Unit are older than the caldera-formation event.

In addition, the *Pico Timão* - Vitória subunit (VU-c, d in Figs. 4.5 - 4.6) has been proposed as the most recent eruption on Graciosa Island (Walker unpublished data, in Maund (1985); Fig. 4.7). These authors correlate a thin pumice horizon lying below a *Pico Timão* lava flow (VU-c) with a pumice bed that originated from a plinian eruption on Faial Island at approximately 2 ka.

CHAPTER 5: $^{40}Ar/^{39}Ar$ CONSTRAINTS ON THE TEMPORAL EVOLUTION OF GRACIOSA ISLAND

5.1 Introduction

Most of the available ages in Azorean Islands were determined using K-Ar (lava samples) and ^{14}C (peat, charcoal and carbonized wood fragments) dating techniques. Only a few recent studies of São Miguel (Johnson et al., 1998), Terceira (Beier, 2006; Calvert et al., 2006; Gertisser et al., 2010) and São Jorge (Ribeiro, 2011) have used the more recent $^{40}Ar/^{39}Ar$ dating method. In order to better constrain the temporal evolution of the Azores archipelago and the potential magmatic and tectonic controls, it is critical to obtain high quality age data.

Previous studies on the petrology and geochemistry of the volcanism on Graciosa Island included K-Ar and ^{14}C datings (Feraud et al., 1980; Maund, 1985; Gaspar, 1996) and provided ages from 620 to 2 ky for the volcanic activity on the island (see chapter 4). In contrast, Rb-Sr data yielded ages up to 2.5 Ma for the formation of the island (White et al., 1976). In order to better constrain the age of the individual volcanological units and reconstruct the volcanic evolution of the island, a new $^{40}Ar/^{39}Ar$ dating campaign has been carried out. For this purpose lava samples from all of the recognized volcanological units and a genetically related gabbro cumulate (Larrea et al., under reviewer*;* chapter 6) have been analyzed. The new $^{40}Ar/^{39}Ar$ ages, together with an evaluation of the previously published ages, enable a new geochronological characterization of the development of the volcanism on Graciosa Island.

5.2 Samples and dating methodology

5.2.1 Location and description of samples

A total of 10 samples were selected for dating using the $^{40}Ar/^{39}Ar$ method (UTM coordinates in chapter 3, Table 3.1). These samples are categorized according to the volcanostratigraphy described in chapter 4. The sample set comprises 9 lava flows from the three different volcanic complexes and 1 gabbro xenolith (Fig. 5.1).

One lava flow was analyzed from the Serra das Fontes shield volcano. The oldest part of the volcanic complex is exposed in inaccessible cliffs. Therefore, the oldest accessible Serra das Fontes lava flow was collected on the SW flank of the Serra das Fontes massif (GRZF8 from SF unit; Fig. 5.1) in order to better define the age of this volcanic complex. A sample from the same outcrop was previously dated by the K-Ar method (Feraud et al., 1980; Fig. 4.10).

One sample from the Serra Branca volcanic complex (GRZF20 from SB-a subunit; Fig. 5.1) was analyzed. The evolution of the Serra das Fontes - Serra Branca magmatic system produced a central composite volcano (Gaspar, 1996; see chapter 4). Therefore, GRZF20 sample was collected in the central plateau outcrop as it represents the oldest accessible part of this volcanic complex and allows to better define the maximum age of the Serra Branca volcanic complex. The oldest age (350 ± 40) obtained by Feraud et al. (1980) within Serra Branca was sampled from the same outcrop (Fig. 4.10).

The other seven samples were collected from the youngest volcanic complex because lava flows from the Vitória and Vulcão Central units have not been dated before. The Vitória Unit was formed by coalescence of volcanic products from different scoria and spatter cones. As a result, it is difficult to ascertain the precise area in which the formation of the NW platform started. Nevertheless, the NE coast was selected because the volcanic succession is well exposed and accessible. Lava flows from the bottom and

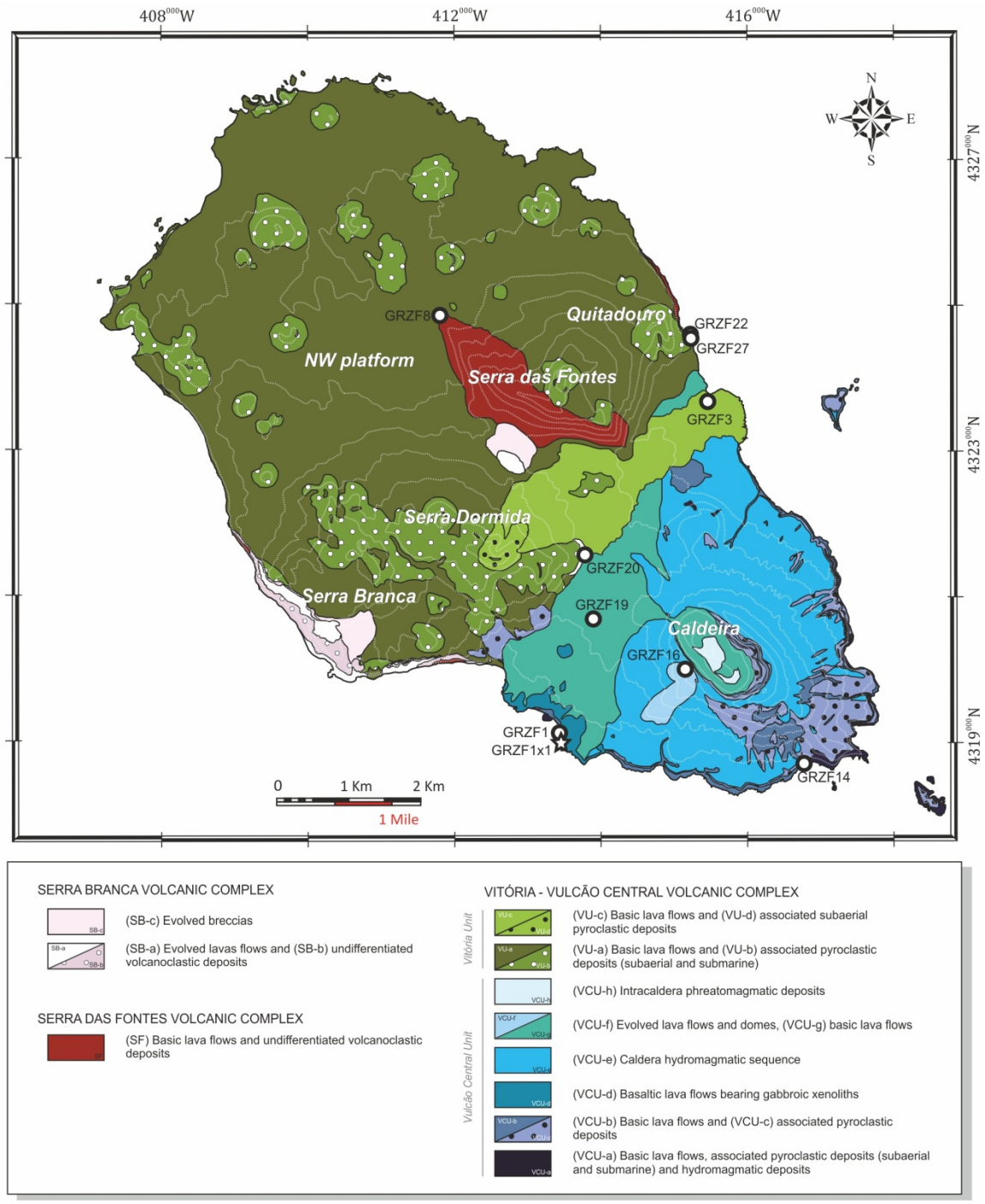

Fig. 5.1 - Geological map of Graciosa Island (modified from Gaspar and Queiroz (1995)) indicating the sample locations from this study (lava flows: white and black circles; xenolith: white and black star). Contour interval: 50 m

top of a cliff sequence were selected for analysis (GRZF22 and GRZF27 samples respectively, from VU-a subunit; Fig. 5.1) in order to define the range of ages for the formation of the Vitória platform in the NE coast. In contrast, the volcanostratigraphy of the Vulcão Central Unit is well defined (Maund, 1985; Gaspar, 1996) and a systematic

sampling of the volcanic sequence from bottom to top of the unit is easier. The oldest subunit (VCU-a; Fig. 5.1), related to the initial monogenetic volcanoes, is only exposed in the southernmost extreme of the island and was not accessible during the fieldwork campaign owing to severe sea conditions. However, lava flow samples from the other Vulcão Central stratovolcano subunits were collected (Fig. 5.1). Pre-caldera samples from the VCU-b (GRZF14) and VCU-d (GRZF1) subunits were sampled in the coastline (Fig. 5.1) in order to obtain ages for these lower stratovolcano subunit. The syn-caldera hydromagmatic sequence was not sampled because these pyroclastic products are not appropriate for Ar dating purposes. However, two post-caldera samples were analyzed, delimiting the age of the caldera forming event. The post-caldera samples belong to the VCU-f lava dome subunit (GRZF16) and the VCU-g lava lake subunit (GRZF19). In addition, the most recent lava flow from the *Pico Timão* eruption center (GRZF3 from VU-c; Fig. 5.1) was sampled, as it may represent the most recent eruption within Graciosa Island (Walker unpublished data, in Maund (1985); see chapter 4).

One gabbro xenolith hosted in a Vulcão Central lava flow (VCU-d; Fig.5.1) has also been analyzed (GRZF1x1). It has been interpreted as a magma chamber cumulate, formed during fractional crystallization of Graciosa basaltic magmas within the crust (Larrea et al., under review; chapter 6). This age is important to better constrain the magmatic evolution of the island.

Thorough petrographic studies were performed on all samples selected for $^{40}Ar/^{39}Ar$ dating (see chapter 6). Most lava samples have porphyritic (Fig. 5.2A) and microporphyritic (Fig. 5.2B) textures. They are characterized by the presence of mm- to cm-sized crystals of olivine, clinopyroxene, feldspars and less abundant amphibole and Fe-Ti oxides, embedded in a holocrystalline to hypocrystalline groundmass. The groundmass is composed of microcrysts of olivine, feldspars, clinopyroxene and Fe-Ti oxides. The microcrystalline groundmass was selected for $^{40}Ar/^{39}Ar$ analysis in all of these samples. In contrast, sample GRZF20 from Serra Branca is more evolved and exhibits a trachytic texture (Fig. 5.2C). It consists of isolated < 1 cm alkali feldspar

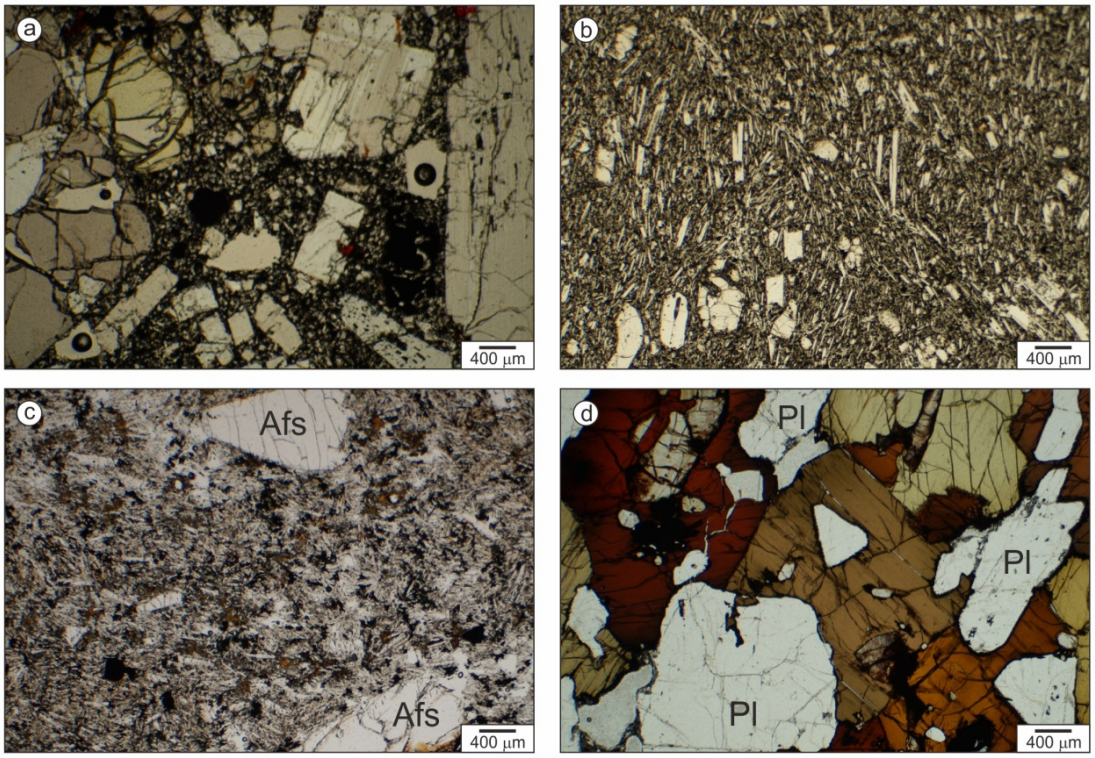

Fig. 5.2 - Plane-polarized transmitted light photomicrographs of the samples dated in this study. (a) porphyritic lava flow; sample GRZF14 is a groundmass separate; (b) microporphyritic lava flow; sample GRZF3 is a groundmass separate; (c) trachytic lava flow; sample GRZF20 is a alkali feldspar (Afs) separate; (d) heteroadcumulate gabbro; sample GRZF1x1 is a plagioclase (Pl) separate.

crystals embedded in a groundmass composed predominantly of sub-parallel, minute (< 0.5 mm), acicular to tabular alkali feldspar microcrysts, with scarce clinopyroxene and opaque microcrysts. In this case, the larger alkali feldspar crystals were separated for $^{40}Ar/^{39}Ar$ analysis. The gabbro sample (GRZF1x1) displays a coarse-grained heteroadcumulate texture (Fig. 5.2D) composed of amphibole (35 %), plagioclase (35 %), clinopyroxene (22 %), olivine (5 %) and Fe-Ti oxides (3 %). Cumulus phases are plagioclase, olivine and clinopyroxene, and amphibole forms poikilitic crystals larger than 2 cm. Plagioclase was separated from this gabbro xenolith. The groundmass and feldspars separates were analyzed for K_2O prior to $^{40}Ar/^{39}Ar$ dating to ensure that they have sufficient K_2O contents (Larrea et al., under review; see chapter 6). Groundmass samples have whole rock K_2O contents varying from 0.54 to 2.59 wt. %. The alkali feldspar crystals separated from sample GRZF20 are classified as anorthoclase (An_{4-0} Ab_{71-66} Or_{25-34}) with 4.27 - 6.17 wt. % K_2O contents. The plagioclase separate crystals from sample GRZF1x1 have lower K_2O contents (0.15 - 0.57 wt. %) and their composition ranges from labradorite to andesine (An_{60-31} Ab_{39-67} Or_{1-0}).

5.2.2 $^{40}Ar/^{39}Ar$ methodology

The groundmass and feldspar separates were prepared at the Mineral Separation Laboratory of the Vrije Universiteit (VU), Amsterdam (The Netherlands). Each sample was crushed and sieved to select the 250 - 500 µm fraction, which was washed with demineralised water and dried at 50 ºC. Heavy liquid separations were done using the LOC-50 (Liquid Overflow Centrifuge model-50; IJlst, 1973). After each step of heavy liquid separation, samples were cleaned with acetone. Magnetic separations were carried out with the Frantz® separator. The samples were sieved a second time to select the 400 - 500 µm fraction and leached with 20 ml HNO_3 (3 %, 10 minutes) to remove alteration, and cleaned with water and methanol. Finally, samples were handpicked under a binocular microscope to obtain homogeneous separates. A summary of the mineral separation methods applied to each sample is presented in Table 5.1.

Table 5.1 - Separated fractions for $^{40}Ar/^{39}Ar$ analyses and mineral separation methods applied.

Sample	Separated phase	Heavy liquids (g/cm^3)	Franz magnet (mA)	Sieve (µm)	Leaching HNO_3	Hand-picking (g)	Final weight (mg)
GRZF1	Groundmass	2.8 - 2.9	-	400 - 500	Yes	0.979	~ 500
GRZF3	Groundmass	2.8 - 2.9	-	400 - 500	Yes	1.102	~ 500
GRZF8	Groundmass	2.9 - 3.0	-	400 - 500	Yes	1.063	~ 500
GRZF14	Groundmass	2.8 - 2.9	-	400 - 500	Yes	0.601	~ 500
GRZF16	Groundmass	2.7 - 2.8	-	400 - 500	Yes	1.071	~ 500
GRZF19	Groundmass	2.9 - 3.0	-	400 - 500	Yes	0.602	~ 500
GRZF20	Alkali feldspar	2.64 - 2.7	> 3000	400 - 500	Yes	0.542	542
GRZF22	Groundmass	2.9 - 3.0	-	400 - 500	Yes	0.513	~ 500
GRZF27	Groundmass	2.9 - 3.0		400 - 500	Yes	0.598	~ 500
GRZF1X1	Plagioclase	2.64 - 2.7	> 3000	400 - 500	Yes	0.618	618

Each sample, together with a laboratory standard package (Drachenfels sanidine - DRA; 25.42 Ma, calibrated following Kuiper et al. (2008)), was wrapped in Al foil and loaded into a quartz tube. Sample weights were 600 - 1000 mg for groundmass, ~ 600 mg for feldspars and 20 mg for the DRA standard. They were irradiated for 1 hour in the Cd-lined RODEO facility of the High Flux Reactor (HFR) at Petten, The Netherlands. Samples were then stored for about 8 months after irradiation, allowing ^{37}Ar to decay.

Dating experiments were carried out at the Geochronology Laboratory of the VU University Amsterdam. Approximately 500 mg of the irradiated groundmass was spread out evenly in a 13 mm diameter hole of a 60 mm diameter copper disc with 5 positions, whereas the total amount of each irradiated feldspars separate was divided and spread out in several 6 mm diameter holes (21 positions per copper disc). The standards were loaded in 3 mm diameter holes of a 185 hole copper disc (1 sanidine grain per hole and 7 replicates per standard).

In all cases, sample-bearing discs were loaded into a custom made sample house, and heated overnight at 150 ºC with a 500 W heat lamp to remove as much undesirable atmospheric argon as possible. For feldspars separates a second pre-heating step (20 W) was performed to facilitate release of a larger proportion of undesirable air argon. After the pre-heating steps, samples were placed in an ultra-high vacuum extraction line. To extract argon from the prepared fractions, a CO_2 laser heating system was used for all the experiments. The sample house was moved during laser-heating following an x–y raster pattern to guarantee heating of all sample grains. For each groundmass sample an incremental heating technique was used with twelve to fifteen steps with laser intensities increasing from 15 W to 240 W. In contrast, feldspars separates were expected to have lower ^{40}Ar contents and therefore, they were analyzed by total fusion to ensure high signals, using a laser intensity of 150 W. Standards were also analyzed by total fusion, with laser intensities of 120W.

The purified gas fractions were analyzed for isotopic composition with an Automated Gas Extraction System (AGES) noble gas quadrupole mass spectrometer (Schneider et al., 2009). Procedural blanks were measured every one or two steps, and at the beginning and the end of each sample experiment. The ArArCALC2.5 dedicated data reduction software (Koppers, 2002; http://earthref.org/tools/ararcalc/) was used for the calculation of plateau ages, isochrons and total fusion ages following the regression of the $^{40}Ar/^{39}Ar$ mass spectrometry data. The irradiation parameter *J* for each sample was determined by the respective standards. Values used for the decay constants and the abundance of ^{40}K are those recommended by the International Union of Geological Sciences (IUGS) Subcommission on Geochronology (Steiger and Jäger, 1977).

5.3 Results

The analytical results are summarized in Table 5.2. Full data tables are available as electronic supplementary material, where the results are reported as given by the ArArCALC2.5 software. Age spectra, K/Ca spectra and inverse isochron plots are presented in Figs. 5.3 - 5.7, with uncertainties quoted at 1σ.

The calculation of plateau ages met commonly accepted criteria (McDougall and Harrison, 1999): (1) a well-defined plateau with at least three contiguous temperature steps, which together comprised more than 50 % of the ^{39}Ar release and (2) a $^{40}Ar/^{36}Ar$ isochron intercept not significantly different from the present-day air ratio of 295.5. The lowest temperature steps are often excluded because they mostly contained abundant atmospheric argon, and the highest temperature steps if they revealed extraneous (excess or inherited) argon (e.g., Wijbrans et al., 2007; Weinstein et al., 2013). If the $^{40}Ar/^{36}Ar$ intercept for the trapped argon deviated from the present-day atmospheric ratio, the inverse isochron age was preferred over the plateau age (e.g., McDougall and Harrison, 1999). If not, the preferred age was chosen according to the values of the mean squares of deviates (MSWD), which measure the extent to which the scatter of data can be explained by analytical uncertainty (e.g., McDougall and Harrison, 1999; Ubide, 2013; Ubide et al., under review;). For the analyzed samples, preferred crystallization ages (plateau or inverse isochron ages) are marked in bold in Table 5.2 and in red in Figs. 5.3 - 5.7. Most preferred ages showed MSWD values below the cut-off value of 2.5 (O'Connor et al., 2007; Table 5.2), with the exception of samples GRZF14 and GRZF19, which nevertheless presented acceptable inverse isochron ages. The K/Ca diagrams (Figs. 5.3 - 5.7) provide information about the chemical composition of the mineral phases contributing to the spectrum (e.g., Wijbrans et al., 2007; Ubide, 2013; Ubide et al., under review). The K/Ca variation between steps never exceeded one order of magnitude, documenting the purity of the separates.

Sample GRZF8 (groundmass) yielded an age spectrum with abundant atmospheric argon in the first step and inherited argon at higher temperature steps (Fig. 5.3). The K/Ca

Table 5.2 - Summary of $^{40}Ar/^{39}Ar$ data; preferred ages are marked in bold. Full data tables are available in the electronic supplement. Gr: groundmass; Pl: plagioclase; Afs: alkali feldspar; Gab: gabbro; Lv: lava.

Sample	Unit	Separated phase	Rock Type	Plateau age (ky)	±1σ	MSWD	39Ar, n step	$^{40}Ar/^{36}Ar$ intercept	Inverse isochron age	± 1σ	MSWD	K/Ca	± 1σ
GRZF8	SF	Gr	Lv	1075.3	±23.3 ±2.17%	1.75	55.36 6	302.2±5.8	**1056.9**	**±28.0** **±2.65%**	**1.63**	0.0433	±0.0027
GRZF20	SB-a	Afs	Lv	450.5	±2.7 ±0.60%	0.75	100 10	311.2±11.8	**433.5**	**±12.9** **±2.97%**	**0.6**	29.9	±3.1
GRZF22	VU-a	Gr	Lv	331.7	±27.0 ±8.14%	2.53	78.42 9	308.6±4.0	**96.3**	**±32.3** **±33.52%**	**1.13**	0.247	±0.030
GRZF27	VU-a	Gr	Lv	305.2	±80.2 ±26.27%	4.81	70.39 6	308.1±4.4	**45.7**	**±22.2** **±48.64%**	**1.99**	0.132	±0.007
GRZF3	VU-c	Gr	Lv	94.8	±17.1 ±18.03%	4.56	86.58 10	308.6±3.8	**3.9**	**±1.4** **±35.27%**	**2.07**	0.299	±0.028
GRZF14	VCU-b	Gr	Lv	89.2	±13.8 ±15.46%	3.7	70.79 6	305.4±9.1	**56.3**	**±21.1** **±37.43%**	**3.62**	0.752	±0.077
GRZF1	VCU-d	Gr	Lv	145.5	±20.1 ±13.84%	5.1	83.14 8	310.4±5.2	**58.8**	**±19.2** **±32.61%**	**2.41**	0.133	±0.026
GRZF1x1	VCU-d	Pl	Gab	**865.6**	**±61.1** **±7.06%**	**0.81**	100 7	296.1±11.8	833.8	±312.7 ±37.51%	1.01	0.0486	±0.0009
GRZF16	VCU-f	Gr	Lv	47.3	±7.1 ±15.08%	0.94	76.79 8	295.4±14.7	**47.6**	**±16.6** **±34.84%**	**1.1**	0.601	±0.040
GRZF19	VCU-g	Gr	Lv	166.4	±36.4 ±21.86%	7.33	93.23 11	306..9±2.8	**11.1**	**±3.7** **±33.16%**	**2.91**	0.149	±0.026

spectrum in these high temperature steps indicates that most of the gas was released by other Ca-rich phases (contamination of the groundmass separate). Hence, to calculate the plateau age, only steps with homogeneous K/Ca contents were considered. The calculated plateau age was 1075.3 ± 23.3 ka. No excess argon was found in these steps as the $^{40}Ar/^{36}Ar$ intercept was indistinguishable from atmosphere, and the plateau and inverse isochron ages are concordant. Nevertheless, the inverse isochron age of 1056.9 ± 28.0 ka is preferred owing to its lower MSWD value (Table 5.2).

Sample GRZF20 was dated using 10 total fusion experiments of several alkali feldspar crystals. The result of each experiment is represented as a step in Fig. 5.3. The relatively flat age and K/Ca spectra document homogeneity of the alkali feldspar grains, apart

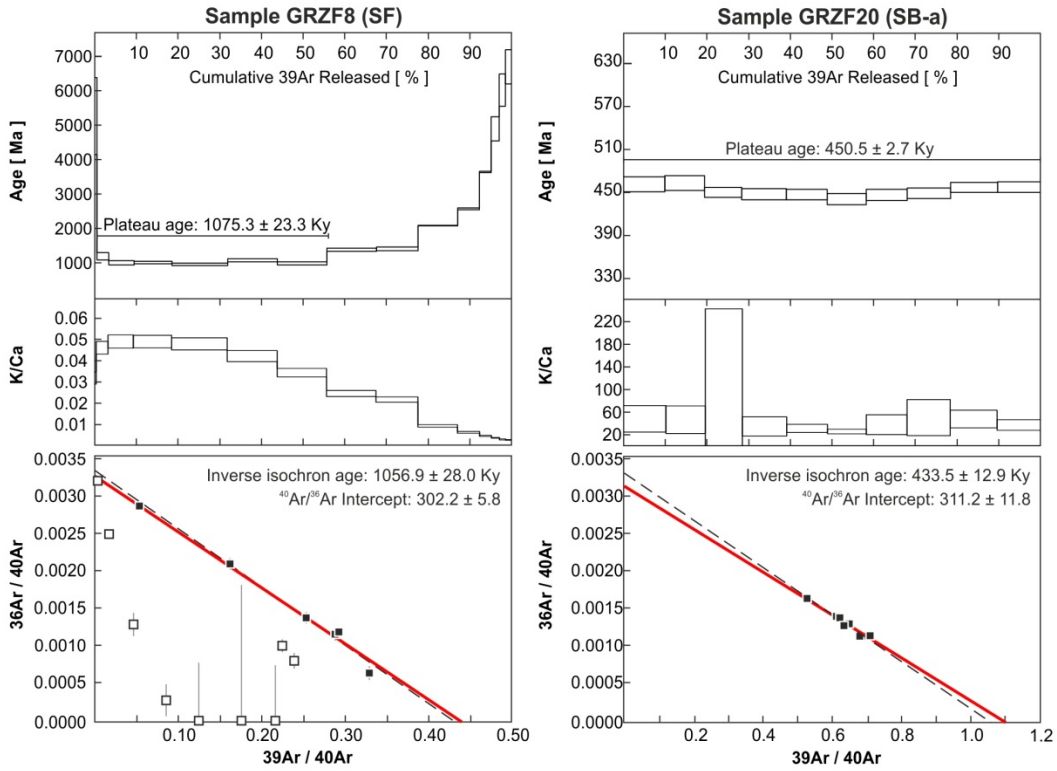

Fig. 5.3 - Age spectra, K/Ca spectra and inverse isochron plots for $^{40}Ar/^{39}Ar$ incremental heating results of GRZF8 groundmass separate sample, and for single fusion of GRZF20 alkali feldspar separate sample. In the age and K/Ca spectra, the horizontal line shows the selected steps to calculate the plateau age and the thickness of each step reflects the associated uncertainty. In the inverse isochron diagrams, the dashed line represents the ideal atmospheric radiogenic mixing line, whereas the solid line represents the inverse isochron calculated with the plateau selected steps (black squares); error bars smaller than symbol size when not shown. The preferred crystallization age is marked with a thicker red line.

from one datum with a large associated error. In total fusion experiments, 100 % of ^{39}Ar released is considered for calculating the plateau and the inverse isochron ages (Fig. 5.3). The inverse isochron plot confirmed the presence of excess argon, as the $^{40}Ar/^{36}Ar$ intercept was higher than atmosphere. Therefore, the inverse isochron age of 433.5 ± 12.9 ka is considered a more accurate estimate of the crystallization age.

Sample GRZF22 (groundmass) yielded quite flat age and K/Ca spectra (except for one K/Ca-rich step, which probably indicates contamination of the sample but nevertheless yields an acceptable age). Almost 85 % of the ^{39}Ar released was considered for the plateau age, leaving out the first steps with abundant atmospheric argon and the last steps that likely contained extraneous argon (Fig. 5.4). The inverse isochron treatment of the data revealed excess argon in the samples. Even though the sample had little

radiogenic argon, an inverse isochron age of 96.3 ± 32.3 ka was obtained for this lava sample.

Sample GRZF27 (groundmass) produced relatively flat age and K/Ca spectra (Fig. 5.4). The high temperature steps yield irregular ages and a decrease in K/Ca that might be related to contamination of the groundmass separate with low K/Ca phases supplying inherited argon. Only consecutive steps that had similar K/Ca results were considered for the age calculation. The inverse isochron treatment of the data showed the low radiogenic argon content of the sample and the existence of excess argon. Hence, the inverse isochron age of 45.7 ± 22.0 ka is considered the most accurate age for this groundmass separate.

Sample GRZF14 (groundmass) produced an age spectrum with abundant atmospheric argon in the first step and inherited argon in the last steps (Fig. 5.5). The steps selected for the plateau age are relatively homogeneous K/Ca values, whereas the sharp decrease of the K/Ca values in the last steps denotes the presence of contaminant phases. Excess argon was detected by the inverse isochron treatment of the data, so the 56.3 ± 21.1 ky value is considered the most likely age for this sample.

Sample GRZF1 (groundmass) yielded an age spectrum with abundant atmospheric argon in the first two steps and extraneous argon in the last steps (Fig. 5.5). Even though the selected steps for the plateau age are fairly flat, the associated K/Ca values are heterogeneous, probably due to a change in the groundmass composition. Moreover, the inverse isochron treatment of the data confirmed excess argon in the samples. Consequently, the well-defined isochron age of 58.8 ± 19.2 ka is preferred.

Sample GRZF1x1 was dated using 7 total fusion experiments of several plagioclase crystals. The result of each experiment is represented as a step in Fig. 5.6. The $^{40}Ar/^{39}Ar$ experiment yielded a slightly disturbed age spectrum, but most values are within the range of analytical error (Fig. 5.6). The K/Ca values are homogeneous, indicating the purity of the separate.

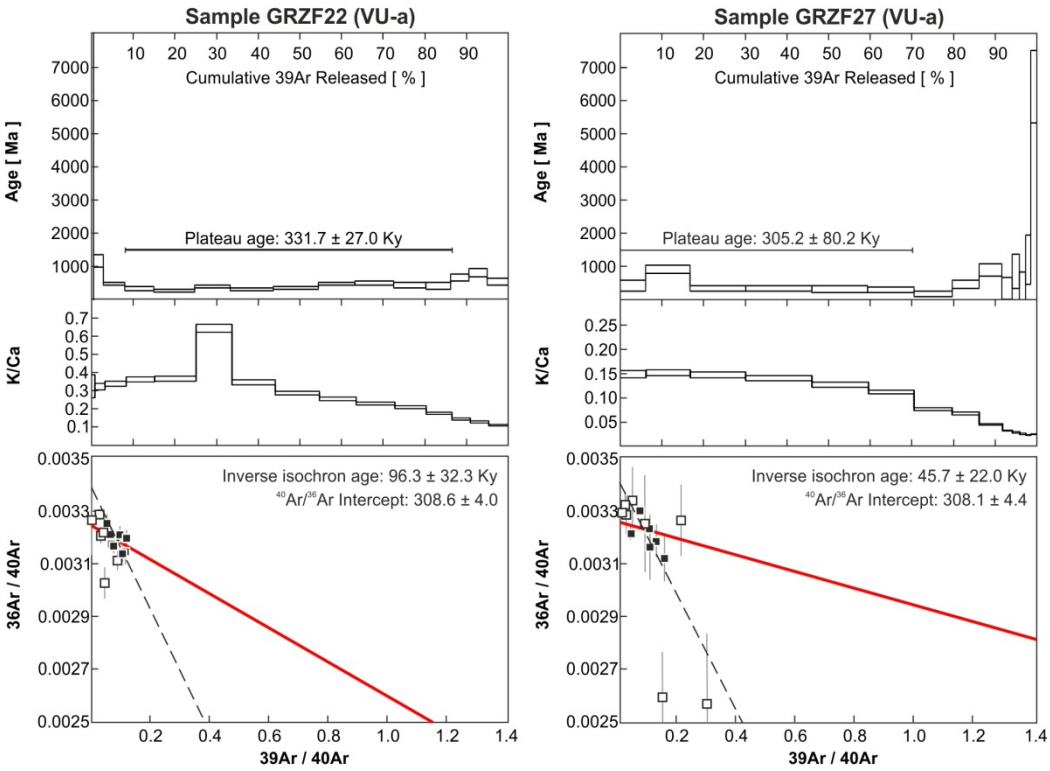

Fig. 5.4 - $^{40}Ar/^{39}Ar$ incremental heating results for samples GRZF22 and GRZF27. Explanation is as in Fig. 5.3.

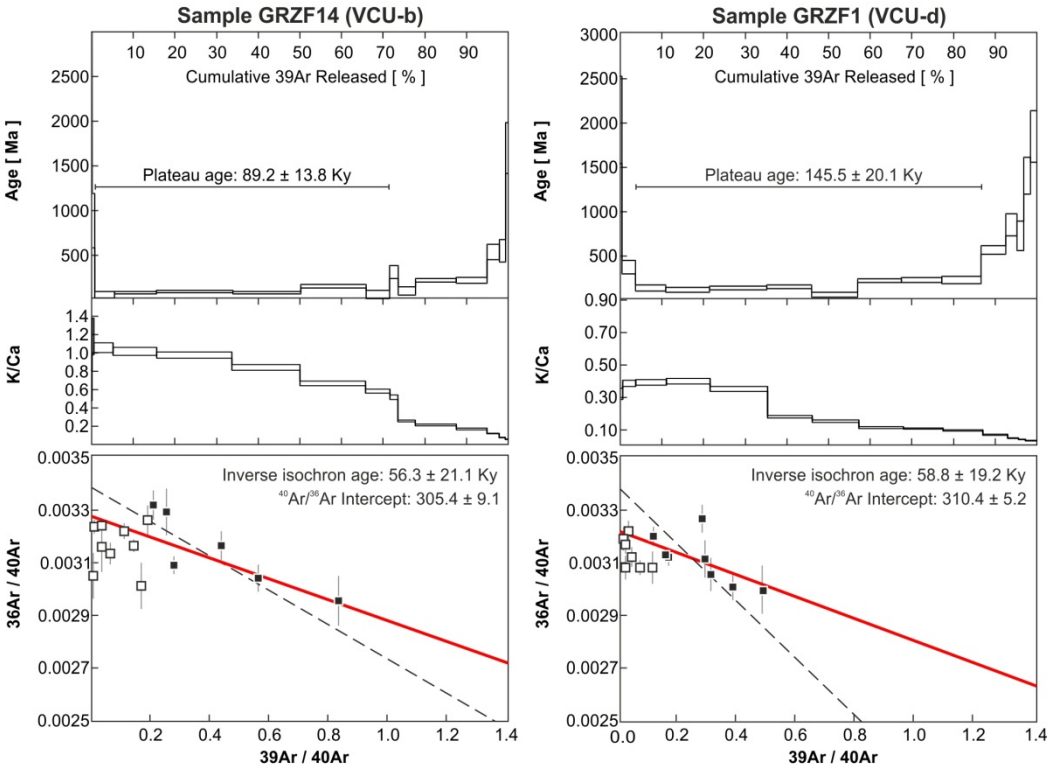

Fig. 5.5 - $^{40}Ar/^{39}Ar$ incremental heating results for samples GRZF14 and GRZF1. Explanation is as in Fig. 5.3.

All of the ^{39}Ar released was considered for calculating the plateau and the inverse isochron ages, which were very similar. No excess argon was found as the $^{40}Ar/^{36}Ar$ intercept was concordant with atmosphere values. Hence, the plateau age of 865.6 ± 61.1 ka is preferred due to its lower MSWD value (Table 5.2).

Sample GRZF16 (groundmass) produced an age spectrum with abundant atmospheric argon in the first step and probably excess argon in the last steps as indicated by the homogeneous K/Ca spectrum (Fig. 5.6). The isochron treatment of the data indicated the presence of excess argon, as the $^{40}Ar/^{36}Ar$ intercept was higher than the atmosphere value. Accordingly, the well-defined inverse isochron age of 47.6 ± 16.6 ka is considered the most accurate estimate of the age of the sample.

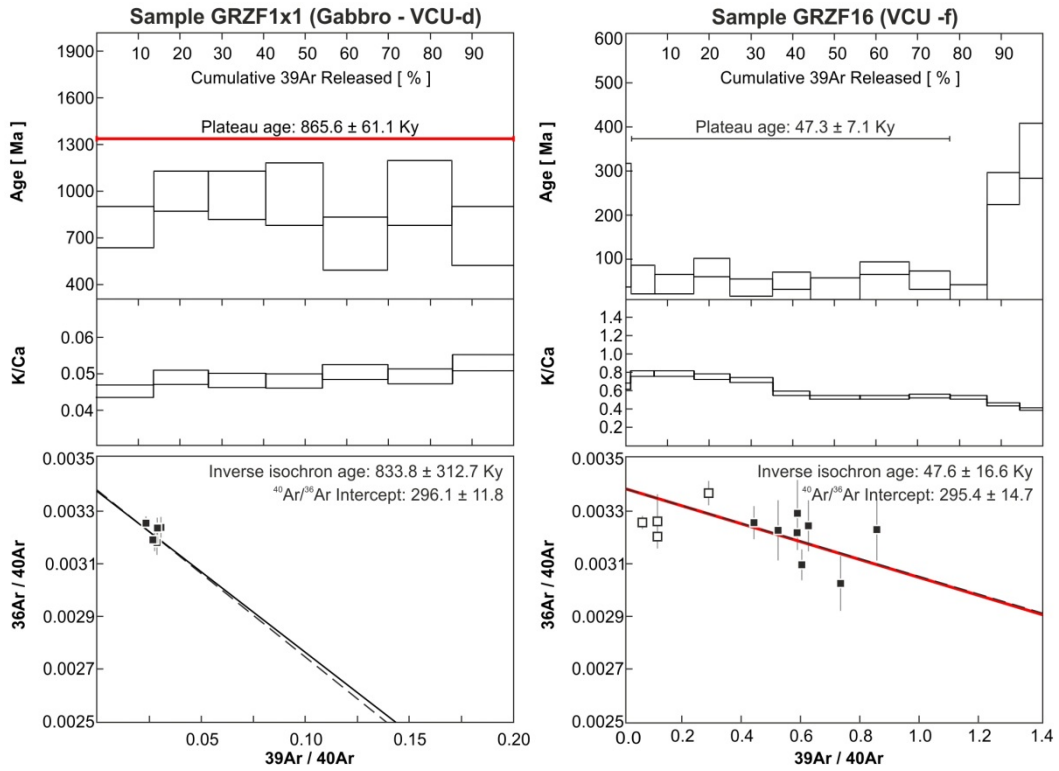

Fig. 5.6 - $^{40}Ar/^{39}Ar$ single fusion results for sample GRZF1x1 and incremental heating results for sample GRZF16. Explanation is as in Fig. 5.3.

Groundmass samples GRZF19 and GRZF3 belong to the youngest lava flows on the island. They have low amounts of radiogenic argon, probably due to their low K_2O content, and therefore are near the limit of the technique (Wijbrans et al., 2011). In both samples, the age spectrum was somewhat disturbed but ca. 90 % of the ^{39}Ar released

was considered for calculating the plateau and the inverse isochron ages (Fig. 5.7). Steps with the lowest K/Ca were probably related to certain contamination of the groundmass separate that may have supplied extraneous argon, so they were omitted for the age calculations. Excess argon was found as the $^{40}Ar/^{36}Ar$ intercepts were higher than atmosphere values and consequently, the inverse isochron age was preferred in both cases. Therefore, GRZF19 and GRZF3 are inferred to be 11.1 ± 3.7 ka and 3.9 ± 1.4 ka old, respectively.

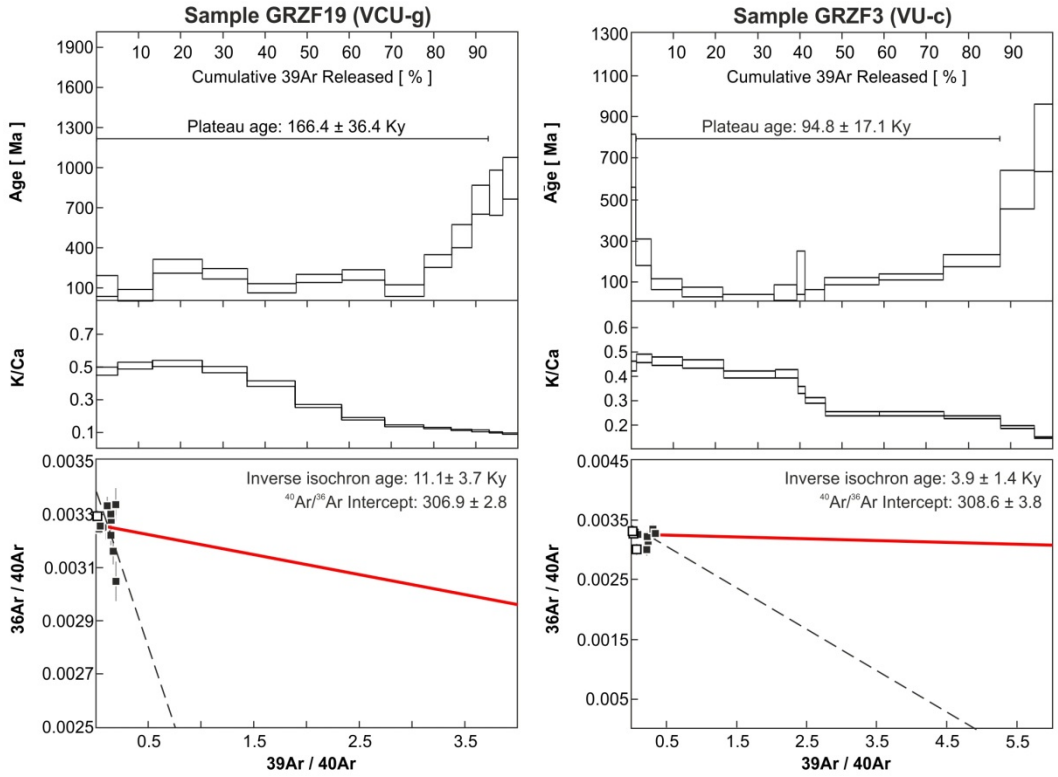

Fig. 5.7 - $^{40}Ar/^{39}Ar$ incremental heating results for samples GRZF19 and GRZF3. Explanation is as in Fig. 5.3.

5.4 Discussion

5.4.1 $^{40}Ar/^{39}Ar$ constraints on the temporal evolution of Graciosa Island

The obtained $^{40}Ar/^{39}Ar$ crystallization ages are plotted in Graciosa Island geological map (Fig. 5.8), and in the chronostratigraphic chart (Fig. 5.9) together with previous K-Ar ages dated by Feraud et al. (1980).

Serra das Fontes volcanic complex

The stratigraphically oldest accessible lava flow yielded a $^{40}Ar/^{39}Ar$ age of 1056.9 ± 28.0 ka (GRZF8 – SF unit). Another sample from the same outcrop was previously analyzed by K-Ar (Feraud et al., 1980), giving a younger age of 620 ± 120 ka (Fig. 5.9). Given the large error reported by these authors, the new result is considered more accurate. In accordance, the oldest accessible subaerial part of the island has an age of 1056.9 ± 28.0 ka and this is therefore a minimum age for the formation of the Serra das Fontes volcanic complex.

Serra Branca volcanic complex

Two previous K-Ar ages for Serra Branca were obtained by Feraud et al. (1980) (Fig. 5.9). These authors collected samples from two different sites, yielding ages of 260 ± 20 ka (Serra Branca massif) and 350 ± 40 ka (central plateau outcrop). In order to better constrain the oldest age of the unit, the oldest sample was analyzed from the central plateau outcrop (GRZF20 – SB-a subunit). The $^{40}Ar/^{39}Ar$ age of 433.5 ± 12.9 ka is slightly older than the age reported by Feraud et al. (1980).

The Serra Branca volcanic complex represents an evolved stage of the Serra das Fontes magmatic system, forming the Serra das Fontes - Serra Branca composite volcano

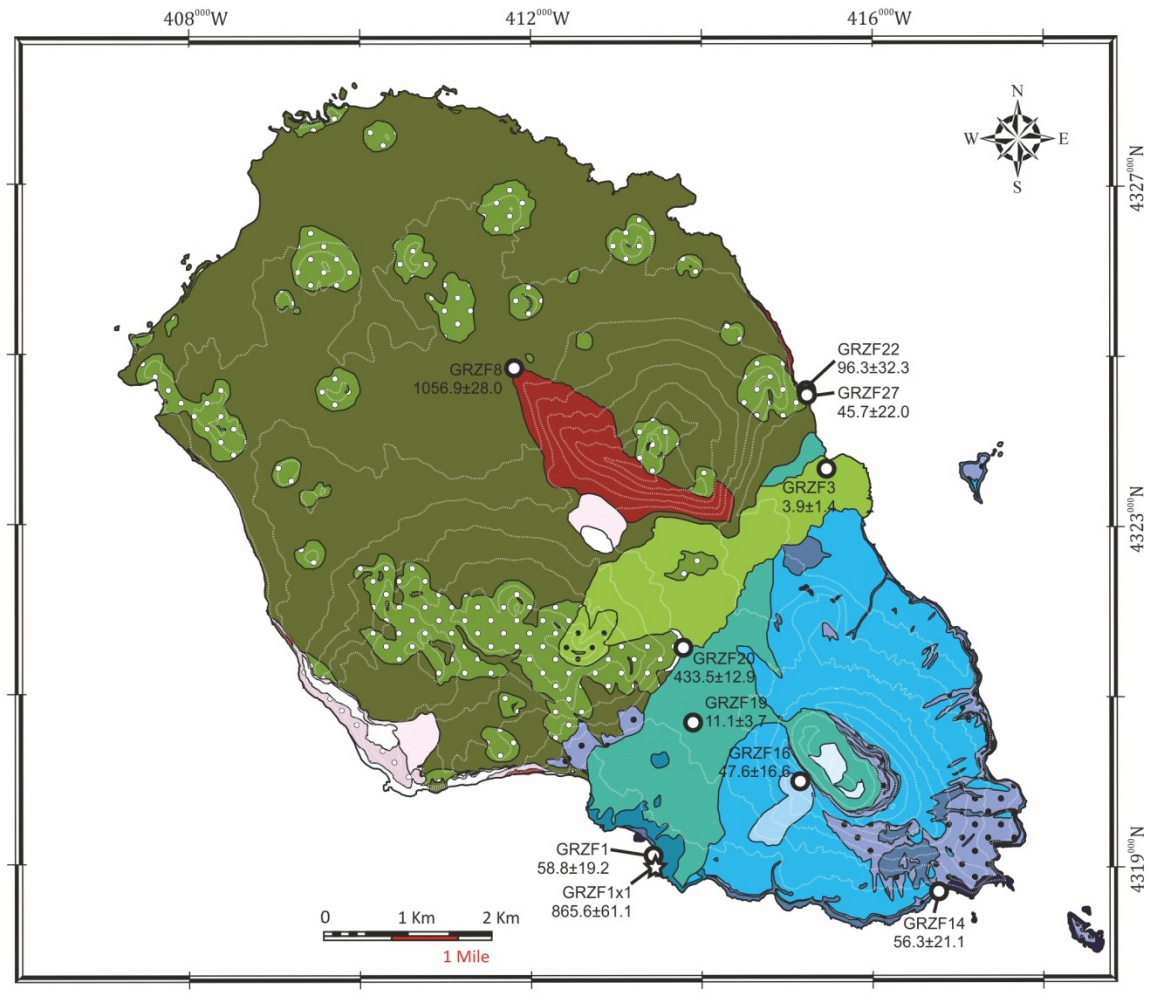

Fig. 5.8 - Geological map of Graciosa Island modified from Gaspar and Queiroz (1995), indicating the calculated $^{40}Ar/^{39}Ar$ ages (given in thousands of years) for the studied samples (lava flows: white and black circles; xenolith: white and black star). Contour interval: 50 m. Legend as in Fig. 5.1.

(Gaspar, 1996; Larrea et al., under review). In accordance, magmatic activity related to the Serra Branca evolved products started ca. 600 ky after the first subaerial basaltic volcanism within the island (Fig. 5.9).

Vitória Unit

The Vitória Unit has been dated for the first time. Lava flows from the bottom (GRZF22 – VU-a subunit) and top (GRZF27 – VU-a subunit) of a well exposed volcanic succession in the NE coast produced $^{40}Ar/^{39}Ar$ ages of 96.3 ± 32.3 ka and 45.7 ± 22.0 ka, respectively (Fig. 5.9). These results indicate that the formation of Vitória may have started after a

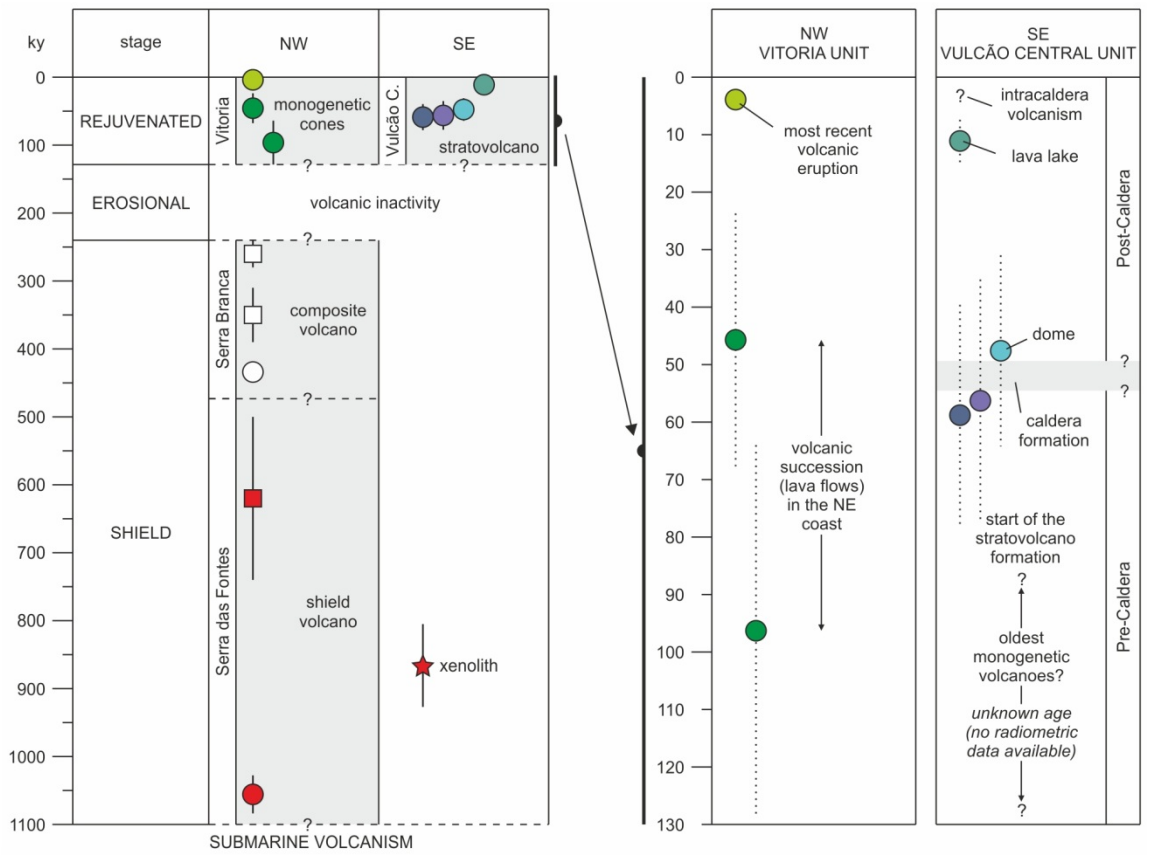

Fig. 5.9 - Chronostratigraphic chart for Graciosa Island volcanism. Circles (lava flows) and star (xenolith) represent the $^{40}Ar/^{39}Ar$ ages from this study. Vertical lines represent 1σ uncertainties associated with our calculated radiometric ages when larger than the symbol size. Squares represent K/Ar data from Feraud et al. (1980).

long period of volcanic inactivity on the island (ca. 160 ky based on the youngest age - 270 ± 20 ka - proposed by Feraud et al. (1980) for the Serra Branca volcanic complex; Fig. 5.9), during which the older volcanic edifices were eroded as suggested by Gaspar (1996).

The *Pico Timão* volcanic eruption belongs to the Vitória Unit. This eruption formed the most recent lava flow (GRZF3 – VU-c subunit) within the island (Fig. 5.9). Previous authors proposed that this subunit was younger than 2 ka because it is located over a thin pumice horizon related to a plinian eruption on Faial Island that occurred at ca. 2 ka (Walker unpublished data, in Maund (1985)). The $^{40}Ar/^{39}Ar$ dating experiment yielded an age of 3.9 ± 1.4 ka for the eruption of the lava flow. Therefore, the lava flow seems to be slightly older than previously inferred. The pumice horizon therefore may not be related to the plinian eruption in Faial Island, but rather came from elsewhere.

Vulcão Central Unit

The Vulcão Central volcanostratigraphy was established based on field observations (Maund, 1985; Gaspar, 1996). The oldest part of the unit (VCU-a subunit) comprises monogenetic volcanoes formed to the south of the Serra das Fontes – Serra Branca oldest volcanic complexes. This subunit was not accessible during the sampling campaign, so its age remains unknown, but lava flows from the rest of the Vulcão Central subunits were dated by $^{40}Ar/^{39}Ar$. Pre-caldera samples GRZF14 and GRZF1 were taken at the bottom of VCU-b and VCU-d subunits. They have $^{40}Ar/^{39}Ar$ ages of 56.3 ± 21.1 ka and 58.8 ± 19.2 ka, respectively (Fig. 5.9), similar to the oldest age of ca. 50 ka proposed by Maund (1985). Therefore, the formation of the Vulcão Central stratovolcano may have started prior to 50 ka.

Post-caldera sample GRZF16 (VCU-f subunit) belongs to an evolved dome located on the southwestern flank of the Vulcão Central stratovolcano. Field evidence suggests that this subunit formed subsequent to the formation of the caldera and its related hydromagmatic sequence (Maund, 1985; Gaspar, 1996). The age of 47.6 ± 16.6 ka obtained for the evolved dome therefore requires an older age for the formation of the caldera (syn-caldera stage; Fig. 5.9). A previous estimate for the age of the caldera-forming event suggested a relatively young age of 12.74 ± 0.070 ka , based on ^{14}C dating of a carbonized wood fragment found within the caldera hydromagmatic sequence (VCU-e subunit) (Maund, 1985; see chapter 4). Given that this age was based on a single analysis of a wood fragment for which the location and description are vague, the new $^{40}Ar/^{39}Ar$ age of 47.6 ± 16.6 ka for the evolved dome sample is considered to represent a more reliable estimate of the minimum age for this subunit.

According to Maund (1985), subsequent effusion of basaltic magmas into the caldera resulted in the formation of a lava lake. Lava filled the caldera up to a height of 240 m and overspilled the rim at two points before partially draining out (Maund, 1985). Sample GRZF19 (VCU-g subunit) was collected from the lava flow overspill, and gave an age of 11.1 ± 3.7 ka for this event (Fig. 5.9). The last eruptions of the Vulcão Central Unit

formed two small pyroclastic cones situated within the caldera; these were not considered in this study due to the lack of associated lava flows (VCU-h subunit).

Finally, a gabbroic xenolith (GRZF1x1) hosted in the GRZF1 lava flow (VCU-d subunit) from the Vulcão Central Unit yielded a $^{40}Ar/^{39}Ar$ age of 865.6 ± 61.1 ka (Fig. 5.9). This age is significantly older than that of the host lava (58.8 ± 19.2 ka) and suggests that the formation of the gabbro was linked to the Serra das Fontes rather than to the Vulcão Central Unit (Fig. 5.9). These results indicate that gabbro xenolith, interpreted to represent a magma chamber cumulate (Larrea et al., under review) was formed by fractional crystallization of the Serra das Fontes basaltic magmas and subsequently carried to the surface by the younger GRZF1 lava flow.

5.4.2 Comparison of Graciosa temporal evolution with other oceanic islands

New $^{40}Ar/^{39}Ar$ ages on Graciosa Island volcanic products have constrained the Pleistocene and Holocene temporal evolution of the subaerial volcanism (1056 ± 28.0 - 3.9 ± 1.4 ka). According to these new ages, Graciosa Island is contemporaneous with São Jorge, and older than Terceira and the southern Islands of Pico and Faial (see chapter 2). Overall, this Central Group is contemporaneous with the Western Group (Corvo and Flores Islands) but younger than the Eastern Group. The age of São Miguel remains unclear, while the easternmost island of Santa Maria is clearly the oldest (see chapter 2). If the age of the Azores archipelago is compared to well-studied Hawaii and Canary Islands, Azores is clearly the youngest archipelago. However, the formation of Graciosa is contemporaneous with the youngest islands of these archipelagos: the western group of islands from the Canary Islands (El Hierro and La Palma; Carracedo, 2011), and the southeastern islands of Hawaii (East Maui, Kaho'olowe and Hawai'i; McDonald et al., 1983).

Four clearly differentiated stages are observed in the evolution of oceanic islands (e.g., Walker, 1990; Carracedo, 2011). These stages are (1) the submarine stage (frequently poorly studied) which comprises up to 80 % of the volume of an island, under the sea level, and the subsequent subaerial stages: (2) the shield stage, (3) the erosional stage

and (4) the rejuvenated stage. These stages can be recognized in the temporal evolution defined for Graciosa Island, although the submarine stage is not exposed. The shield stage comprised the formation of the Serra das Fontes shield volcano (starting at least at 1.05 Ma) and its evolution to the Serra Branca composite volcano. Therefore, this stage lasted ca. 850 ky (Fig. 5.9). The erosional stage was characterized by volcanic inactivity and erosion of the Serra das Fontes - Serra Branca volcanic edifices and lasted ca. 110 ky (Fig. 5.9). Currently, the island is in the rejuvenated stage, represented by the youngest and most extensive volcanic complex on the island (Vitória - Vulcão Central). On the NW part of the island, this stage started prior to ~ 100 ka as monogenetic cones that built the Vitória Unit NW platform. In contrast, in the SE part of the island, this stage started prior to 60 ka. Volcanism was initially associated with monogenetic cones and later became associated with a main eruptive center forming the Vulcão Central stratovolcano. Present-day activity continues as a boiling mud pool in the *Furna do Enxofre* (caldera cave) and hot water springs at the *Termas do Carapacho* and the *Baía dos Homiziados*.

Overall, the evolutionary stages defined in Graciosa Island are slightly different than those of Hawaii and the Canary Islands. Each stage appears to be shorter in time in Graciosa, as together the shield, erosional and rejuvenated stages lasted only slightly more than 1 Myr. For example, Gran Canaria Island shows a temporal evolution similar to Graciosa but it formed over ca. 16 Myr (Schminke, 2004). Similarly, El Hierro and La Palma Islands have similar ages to Graciosa but are still in the shield stage (Carracedo, 2011). The erosional stage in Graciosa was very short (ca. 110 ky) but highly destructive. For instance, Gomera Island has an age of 10 Ma and is within the erosive phase since 4 Ma. In Graciosa Island, the rejuvenated stage has been extremely active, generating most of the current surface of the island as the Vitória NW platform and Vulcão Central SE stratovolcano, although present-day activity is scarce within the island. The rejuvenated stage is also particularly active in the older, eastern and central Canary Islands which have experienced three or more magmatic phases. In contrast, the volume of rejuvenated lavas in Hawaii archipelago is very small (Schminke, 2004).

5.5 Conclusions

This work provides new constraints on the geochronological evolution of Graciosa Island volcanism. New $^{40}Ar/^{39}Ar$ dates for 9 lava flows and 1 gabbro cumulate produced ages ranging from 1056 ± 28.0 to 3.9 ± 1.4 ka.

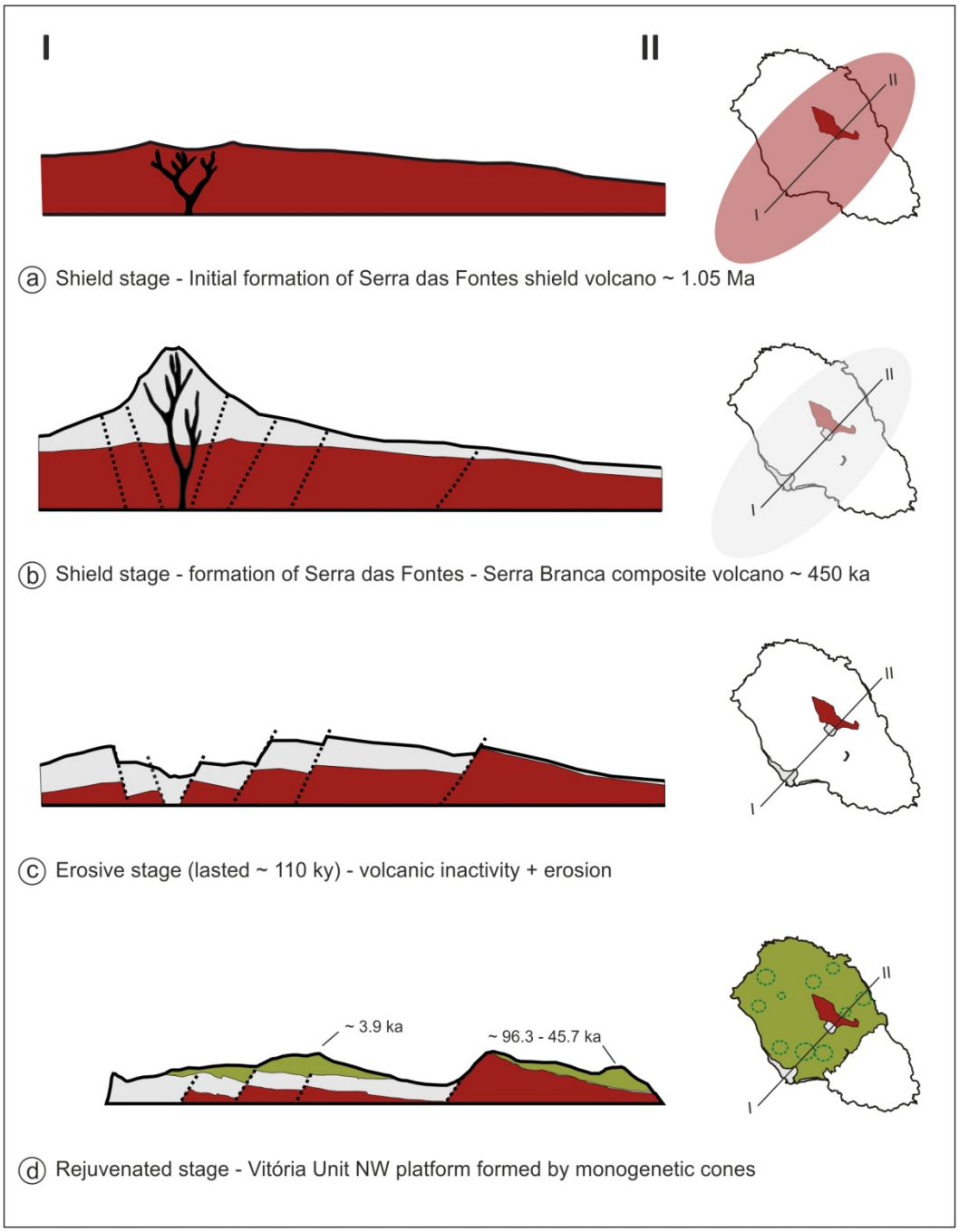

Fig. 5.10 - Time-spatial evolution of the northern part of Graciosa Island modified from Gaspar (1996). Note that each step is represented on a map of the current island morphology, indicating the possible surface extension.

The oldest age is older by ~ 400 ky than the previous K-Ar estimate for the same unit, and provides a new minimum age for the inception of subaerial volcanism on the island. The new $^{40}Ar/^{39}Ar$ data, combined with data from the literature, make it possible to develop a new chronology for the evolution of Graciosa Island, as summarized below.

The shield stage in Graciosa Island started at least 1.05 Ma ago with the formation of the Serra das Fontes shield volcano (Fig. 5.10A). At some point around 450 ka, the evolution of the Serra das Fontes magmatic system allowed the formation of evolved magmas and the initial formation of the Serra das Fontes - Serra Branca composite volcano (Fig. 5.10B).

The shield stage remained active for ca. 850 ky. The erosive stage lasted ca. 110 ky and was characterized by volcanic inactivity and erosion of volcanic edifices (Fig. 5.10C). The rejuvenated stage generated two main volcanic units. On the NW of the island, volcanism re-started in association with monogenetic cones that built the current Vitória Unit NW platform and covered most of the remaining volcanic units (e.g., the NE coast was formed between 96.3 ± 32.3 ka and 45.7 ± 22.0 ka; Fig. 5.10D). The Vulcão central Unit was formed to the south of the oldest Serra das Fontes – Serra Branca predecessor. The initial volcanism of the Vulcão Central Unit was associated with the activity of monogenetic cones of unknown age (Fig. 5.11A). Afterwards, the volcanism became associated with a main eruptive center (Fig. 5.11B), forming the Vulcão Central stratovolcano, its caldera (Fig. 5.11C), a lava dome and a lava lake (Fig. 5.11D) in a period of ~ 60 ky. The most recent volcanic eruption took place at ~ 3.9 ka at *Pico Timão* (Fig. 5.10D). Present-day activity continues in the form of a boiling mud and hot water springs. The temporal stages defined in oceanic islands (submarine, shield, erosional and rejuvenated stages), are developed much faster in Graciosa Island than in other islands from the well-studied Canary and Hawaii archipelagos.

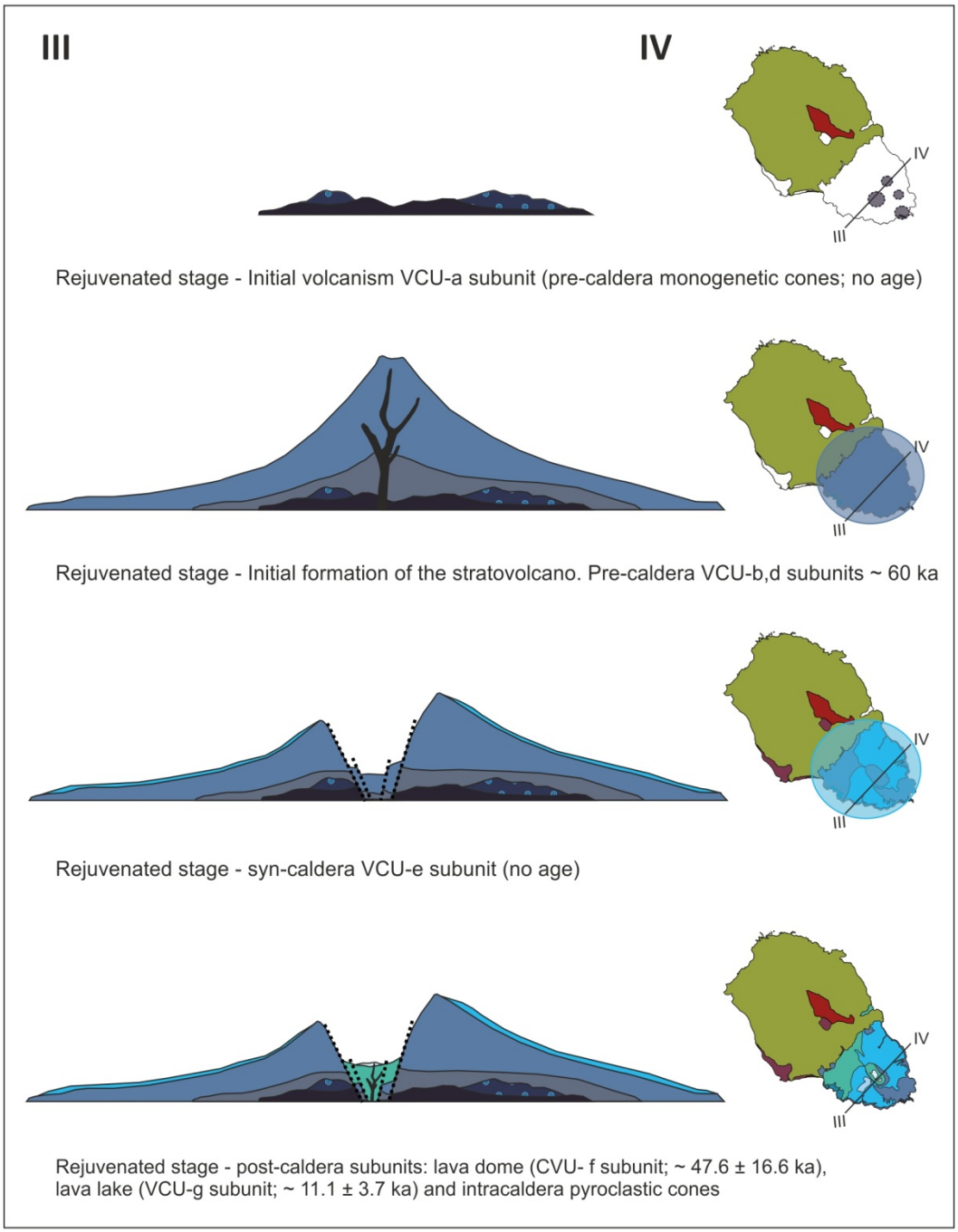

Fig. 5.11 - Time-spatial evolution of the southern part of Graciosa Island modified from Gaspar (1996). Note that each step is represented on a map of the current island morphology, indicating the possible surface extension.

CHAPTER 6: MAGMATIC EVOLUTION OF GRACIOSA ISLAND

6.1 Introduction

Graciosa Island is the westernmost island of the Terceira Rift, located to the east of the Mid-Atlantic Ridge. The aim of this work is to investigate the magmatic processes that control the genesis of Graciosa Island. The different magmatic products across the volcanostratigraphic sequence have been studied, including lava flows, gabbroic xenoliths (alkaline and subalkaline in composition), syenites and dunites. A detailed study of the mineral compositions, whole-rock compositions (major and trace elements) and isotopic data have allowed for the characterization of the individual volcanological units and the investigation of the magmatic evolution of the island.

6.2 Samples and analytical methods

Lava flows and xenoliths from Graciosa Island were sampled for petrological and geochemical studies. In this study, samples are categorized according to the volcanostratigraphy described in chapter 4. Lava flows were sampled from the three different volcanic complexes in several locations; diverse xenoliths hosted in these lavas were also sampled (Fig. 6.1; UTM coordinates in chapter 3, Table 3.1). A total of 39 fresh lava flow and 54 xenolith samples were collected, representing the full range of recognized compositions. Most lava flow samples were collected from the Vitória - Vulcão Central volcanic complex (34 samples) because it accounts for ca. 85 % of the surface of the island. The oldest samples were collected from Serra das Fontes (3 samples). Evolved lavas were sampled from the accessible outcrops of Serra Branca (2

samples), in order to evaluate the complete evolutionary trend of the magmatic system. The xenoliths were found in four sites (Fig. 6.1): *Baía da Folga* (19 samples) and *Enxudreiro* (2 samples) within the Vulcão Central Unit, and *Ponta da Pesqueira* (17 samples) and *Quitadouro* (16 samples) within the Vitória Unit. Their size is highly variable, but only those larger than 3 cm were extracted. The *Baía da Folga* and *Ponta da Pesqueira* xenoliths were collected from lava flows. The *Quitadouro* and *Enxudreiro* xenoliths were found within scoria cone and *lahar* deposits, respectively.

All of the samples were studied macro- and microscopically. The petrographic study led to the selection of 50 representative thin sections for mineral analyses (25 from lava samples and 25 from xenoliths samples). Mineral major element compositions were determined on polished thin sections by electron microprobe (EMP) at the *Centro Nacional de Microscopía Electrónica* at the Universidad Complutense de Madrid (Spain). A JEOL JXA-8900 M electron microprobe equipped with five wavelength dispersive spectrometers was used; the beam diameter was 5 µm and elemental counting times were 10 s on the peak and 5 s on each of two background positions. Analyses were performed using an accelerating voltage of 15 kV and an electron beam current of 20 nA. Corrections for inter-elemental effects were made using a ZAF (atomic number (Z), absorption (A) and fluorescence (F)) procedure.

A total of 37 lava flows and 22 xenolith samples were selected for whole rock chemical analyses. Samples were crushed in a manganese steel jaw-crusher and milled in an agate vibrating cup mill at the Servicios de Apoyo a la Investigación of the Universidad de Zaragoza (Spain). The major and trace element concentrations of lava flow and xenolith samples were determined in two different laboratories according to the campaign in which they were collected (Table 3.1). Samples of the first fieldwork campaign (September 2007) were analyzed at the IBERCRON laboratory of the Universidad del País Vasco (Spain) by ICP-MS. Whole rock analyses for the samples collected in the 2011 fieldwork campaign were carried out by ICP-MS at the labGEOTOP laboratory of the Institut de Ciències de la Terra Jaume Almera (Spain). Details of the analytical procedures and detection limits are available in Appendix - Table I. In order to compare

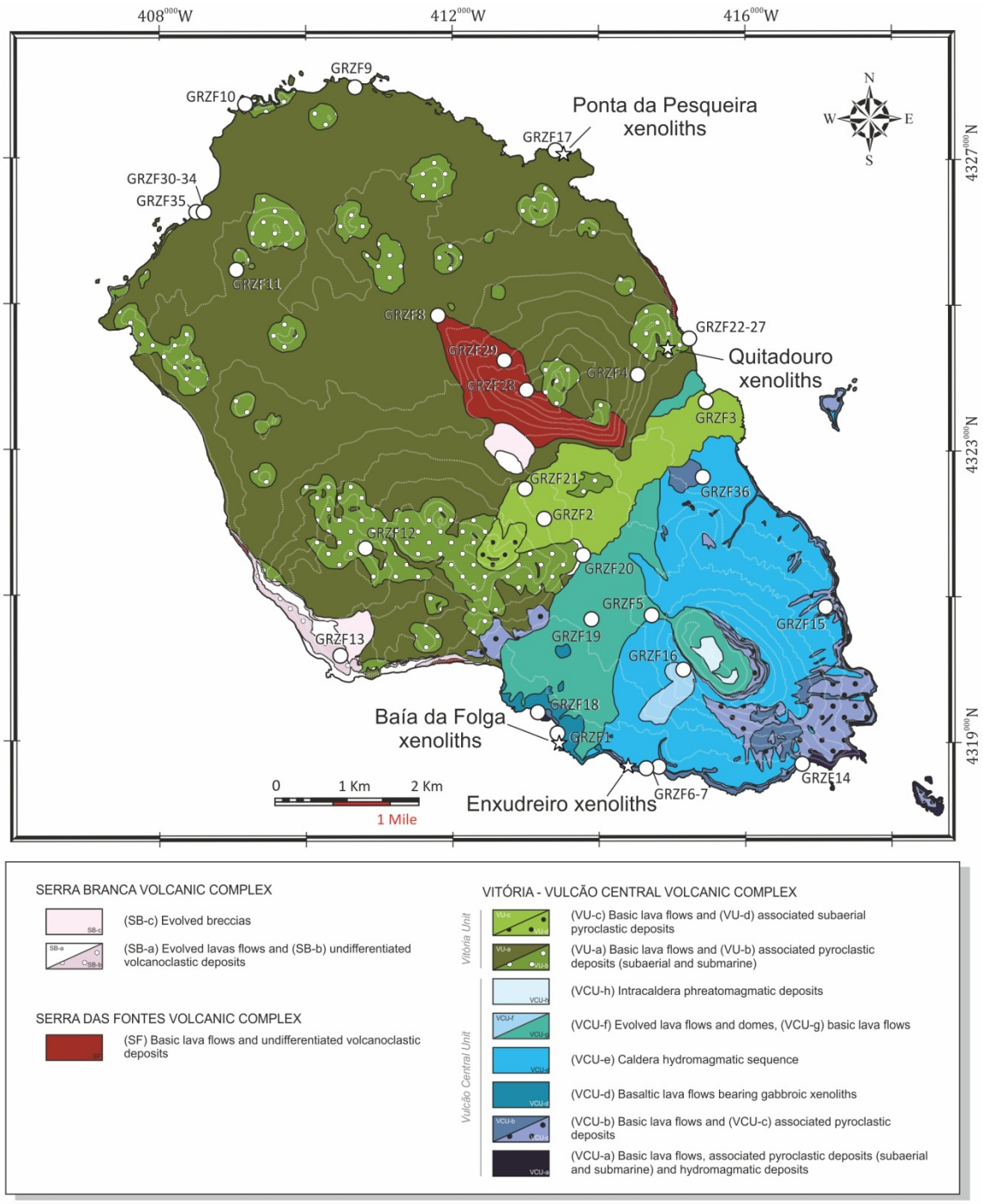

Fig. 6.1 - Simplified geological map of Graciosa Island modified from Gaspar and Queiroz (1995) indicating the sample sites from this study. Contour interval: 50 m.

the results, the highest detection limits were considered for each element. Whole rock analyses can be found in Appendix - Table II.

Nine lavas and 6 xenoliths were selected for Sr, Nd and Pb isotope analyses (Appendix - Table II). Sample preparation and analysis were performed at the Isotope Geochemistry

& Mass Spectrometry Laboratory of the Miami University (Ohio, USA). Samples were crushed in an alumina jaw-crusher and powdered in a high-purity alumina mixer mill. Approximately 200 mg of powdered samples were used to extract and purify Sr, Nd and Pb. Samples were digested overnight in Savillex® Teflon beakers with concentrated HF (4 ml) and HNO_3 (2 ml) on a hotplate at 80 ºC. After drying, 0.5 - 1 ml of HNO_3 was added to beakers, to break up the sample cake; samples were evaporated to dryness on a hotplate at 80 ºC (this step was repeated). After dryness, 1 ml of concentrated HCl was added to the samples to break up insoluble fluorides for at least 1 hour. In order to avoid undissolved materials, the samples were redissolved in 5 ml of ultrapure E-pure™ H_2O, leaving them on the hot plate at 80 ºC overnight. After total dissolution, samples were evaporated to dryness on the hot plate. The Sr, Nd and Pb purified fractions were all extracted from the same digested sample. Pb was first processed using anion exchange columns with BioRad AG1-X8 100 - 200 mesh resin and HBr and HNO_3. The Sr was recovered using a Eichrom Industries Sr-Resin and HCl and HNO_3. The sample residue was passed through AG-50W-X8 cation resin to remove iron, and then LN-Spec columns and HCl was used for Nd purification.

The isotopic compositions of Sr, Nd and Pb were measured by thermal ionization mass spectrometry (TIMS). Sr and Nd isotope ratios were corrected for fractionation using $^{86}Sr/^{88}Sr = 0.1194$ and $^{144}Nd/^{146}Nd = 0.7219$. Measurements of NBS 987 Sr standard and La Jolla Nd standard show a long-term reproducibility of $^{87}Sr/^{86}Sr = 0.71024 \pm 0.00002$ (2 SD) and $^{143}Nd/^{144}Nd = 0.511846 \pm 0.000007$ (2 SD), respectively, which represent the external reproducibilities of Sr and Nd isotopic measurements. Pb isotope ratios were corrected for fractionation by 0.1 % ($^{206}Pb/^{204}Pb$), 0.097 % ($^{207}Pb/^{204}Pb$) and 0.102 % ($^{208}Pb/^{204}Pb$) per amu, based on deviations of measured ratios in NBS 981 Pb standard from values in Todt et al. (1996). Long-term external reproducibility (2 SD) for $^{206}Pb/^{204}Pb$, $^{207}Pb/^{204}Pb$ and $^{208}Pb/^{204}Pb$ is $\pm$ 0.015, 0.020, and 0.062, respectively. Procedural blanks were better than 0.1 ng for Sr, 0.1 ng for Nd and 0.2 ng for Pb.

6.3 Petrology

The composition of sampled lavas ranges from basalt to trachyte following the TAS classification by Le Bas et al. (1986) (Fig. 6.2). Basalts and hawaiites are the most abundant rock compositions in Serra das Fontes (48.09 - 52.47 wt. % SiO_2 and 3.58 - 3.92 wt. % total alkalis ($Na_2O + K_2O$)) and the Vitória - Vulcão Central (46.18 - 55.94 wt. % SiO_2 and 1.97 - 5.81 wt. % total alkalis) volcanic complexes, apart from some more evolved rocks (mugearite - trachyte; 57.12 - 59.81 wt. % SiO_2 and 4.68 - 6.29 wt. % total alkalis) in the Vulcão Central Unit. On the contrary, Serra Branca is entirely trachytic in composition (> 65.44 wt. % SiO_2 and > 6.37 wt. % total alkalis). These rocks are characterized by porphyritic, microporphyritic and trachytic textures (Table 3.1).

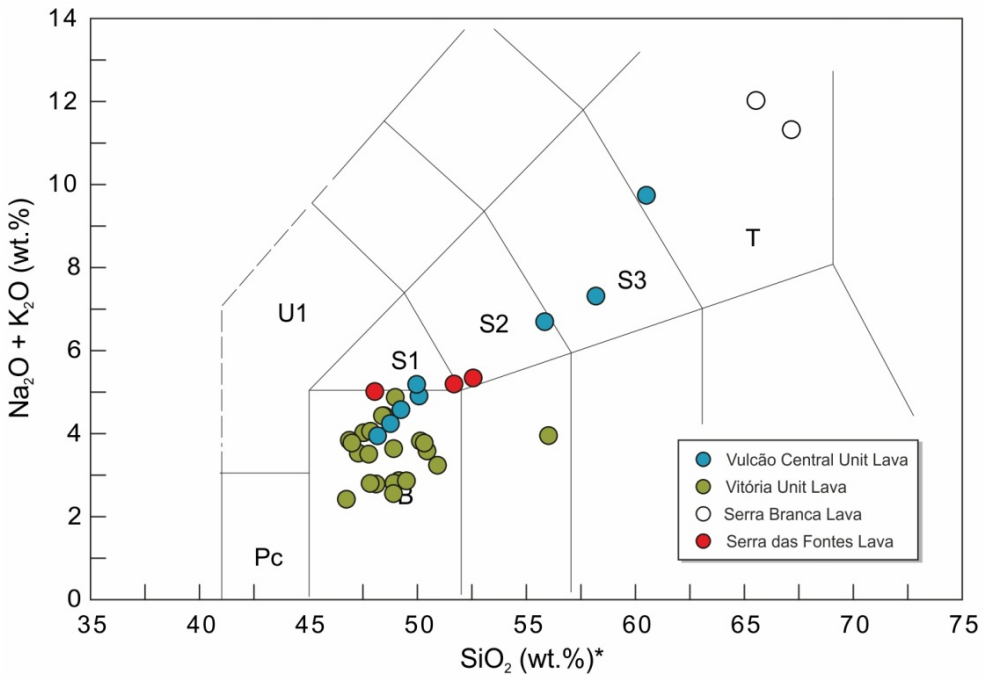

Fig. 6.2 - Total Alkalis vs. Silica (TAS) diagram for Graciosa Island lava flows (after Le Bas et al. (1986)). Pc: picrobasalt; U1: tephrite; B: basalt; S1: hawaiite, S2: mugearite; S3: benmoraite; T: trachyte. * The SiO_2 content of the samples analyzed in the LabGEOTOP laboratory has been estimated as SiO_2 = 100 - Σ (total oxide content + LOI) given the analytical procedure in this laboratory (see Appendix- Table I-II).

The porphyritic rocks (Fig. 6.3A) are characterized by the presence of 15 - 50 % large crystals (2 - 10 mm) embedded in a holocrystalline to hypocrystalline groundmass.

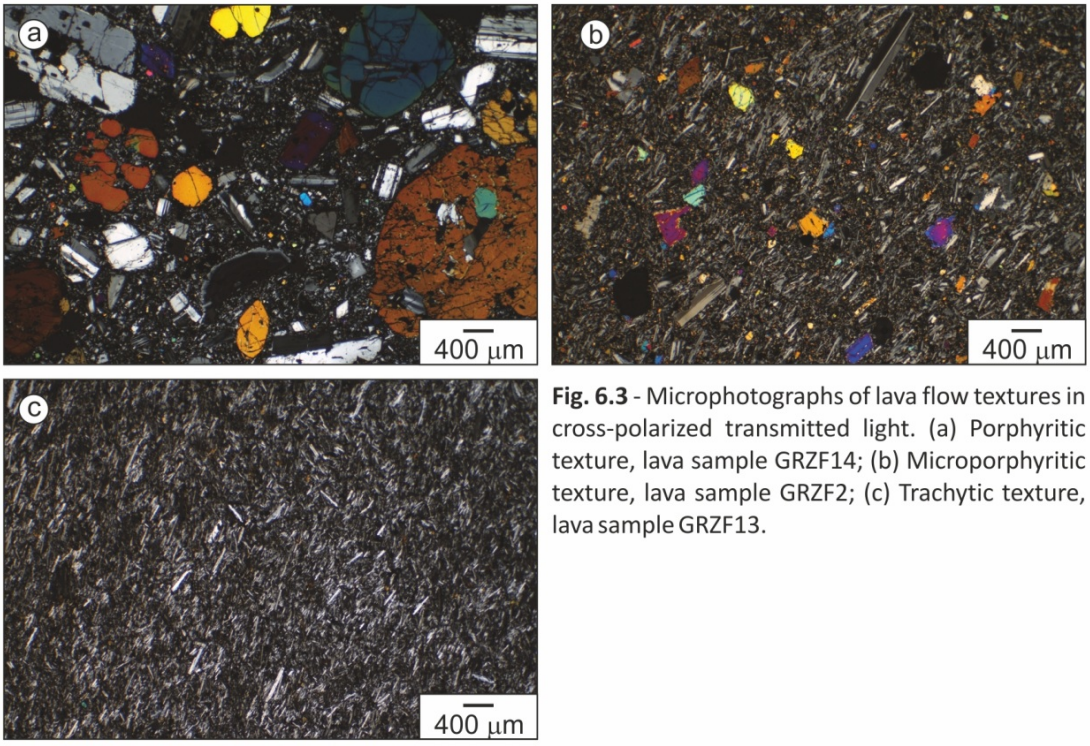

Fig. 6.3 - Microphotographs of lava flow textures in cross-polarized transmitted light. (a) Porphyritic texture, lava sample GRZF14; (b) Microporphyritic texture, lava sample GRZF2; (c) Trachytic texture, lava sample GRZF13.

According to crystal size, the term macrocryst is used for crystals larger than 2 mm, whereas those smaller than 2 mm are referred to as microcrysts. The macrocryst assemblage comprises subhedral to anhedral olivine, clinopyroxene, feldspars and less abundant amphibole and Fe-Ti oxides. The groundmass is composed of microcrysts of olivine, feldspars, clinopyroxene and Fe-Ti oxides.

The microporphyritic rocks (Fig. 6.3B) are holocrystalline to hypocrystalline and are composed of microcrysts of feldspars, olivine, clinopyroxene and Fe-Ti oxides with a bimodal size distribution (Fig. 6.3B); most microcrysts are smaller than 0.5 mm, although crystals of 0.5 - 2 mm are also recognized. Amphibole microcrysts are also present in the evolved rocks (benmoreites and trachytes). In some microporphyritic samples are observed larger (> 1 mm) isolated olivine, clinopyroxene and feldspar crystals that are highly corroded and have rounded rims.

Samples from Serra Branca exhibit a trachytic texture. They consist of isolated < 1cm tabular feldspar crystals embedded in a groundmass predominantly composed of sub-

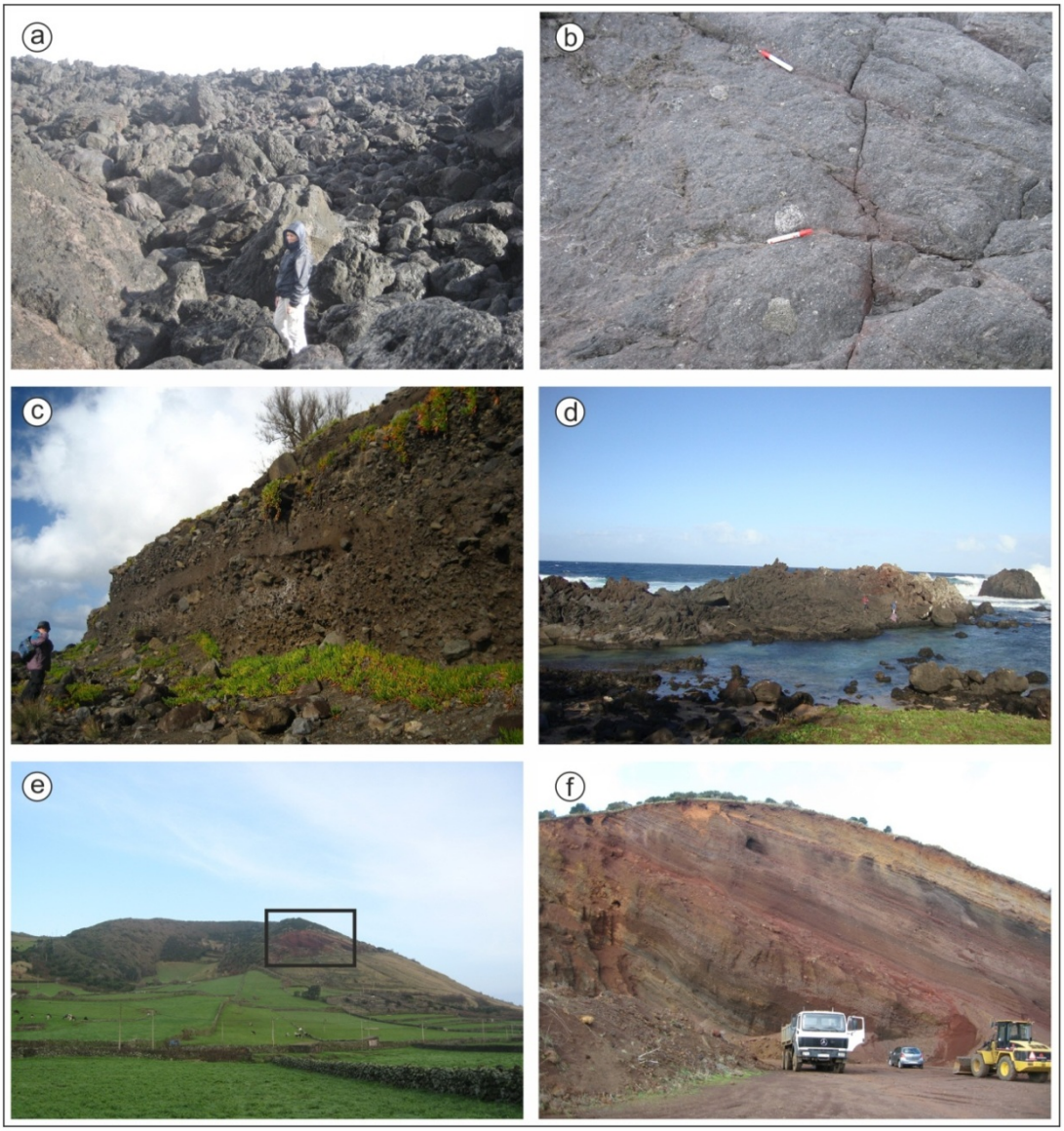

Fig. 6.4 - Xenolith sampling sites in Graciosa Island. (a) *Baía da Folga* sampling area; (b) distribution of the xenoliths at this site; (c) *Enxudreiro* outcrop; (d) *Ponta da Pesqueira* site; (e) *Quitadouro* scoria cone; (f) sampled quarry; note its location in (e).

parallel, minute (< 0.5 mm), acicular to tabular feldspar microcrysts, with scarce clinopyroxene and opaque microcrysts (Fig. 6.3C).

The xenoliths are 3 to 20 cm long and show sub-rounded to angular shapes and a medium- to coarse-grained plutonic textures. They present sharp contacts with the host lavas and occur without any apparent preferred orientation in the different outcrops *(Baía da Folga*, *Enxudreiro*, *Ponta da Pesqueira* and *Quitadouro*; Fig. 6.4). These

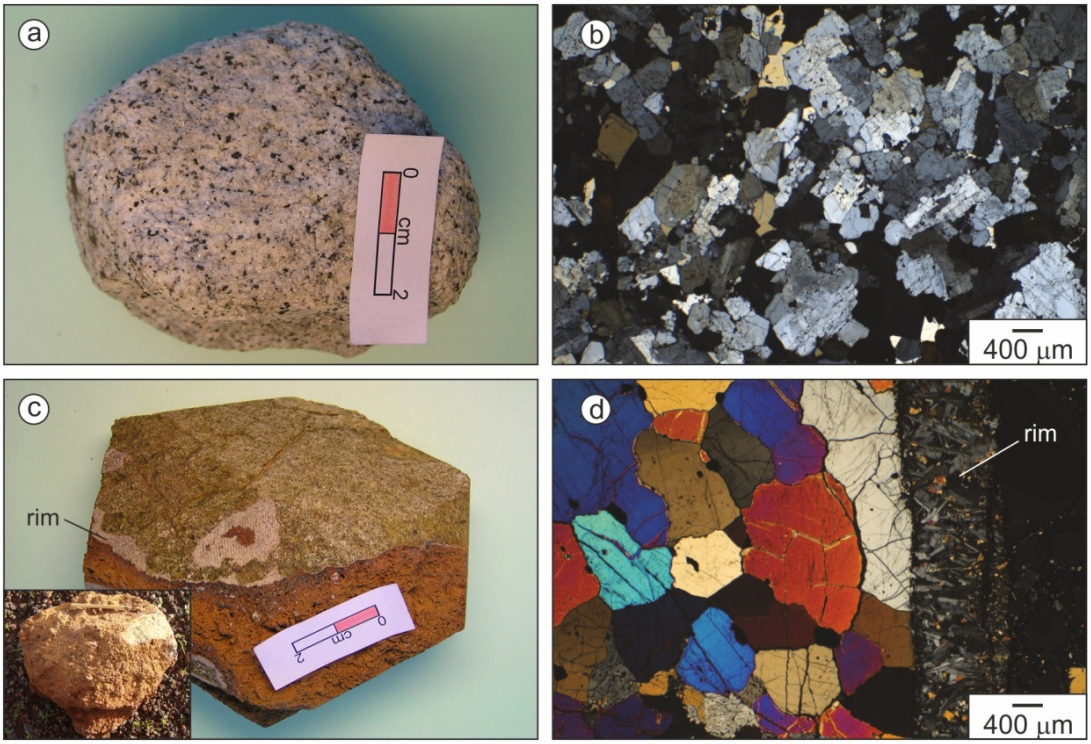

Fig. 6.5 - (a) Syenite (GRENx-1) hand specimen and (b) photomicrograph of the syenite in cross-polarized transmitted light; (c) dunite sample (GRQUx1) after sawing and as hand specimen found in the sampling site, within the inset; (d) photomicrograph of the dunite (GRQUx1) in cross-polarized transmitted light.

xenoliths are classified according to Le Maitre (2002) as syenite, dunite and gabbro (Table 3.1). The latter comprises two types: alkaline and subalkaline gabbros (see mineral chemistry and whole rock chemistry sections).

Two syenites were collected from a *lahar* deposit at *Enxudreiro* outcrop (Figs. 6.4C and 6.5A). They occur as an inequigranular (0.1 - 2 mm), allotriomorphic mosaic composed of major alkaline feldspar (~ 90 %), amphibole (~ 7 %), Fe-Ti oxides (~ 2 %), and pyroxene, quartz, biotite, sphene and zircon as accessory minerals (Fig. 6.5B).

Two dunite samples were found at the *Quitadouro* outcrop (Figs. 6.4E-F and 6.5C). One of them was collected from a pyroclastic layer of the scoria cone and the other one was found within a lava flow. These samples have a phaneritic texture constituted by an equigranular mosaic of ~ 90 % olivine crystals and minor clinopyroxene crystals (~ 5 %). Cr-rich spinel crystals (~ 5 %) are located along grain boundaries or included in olivine

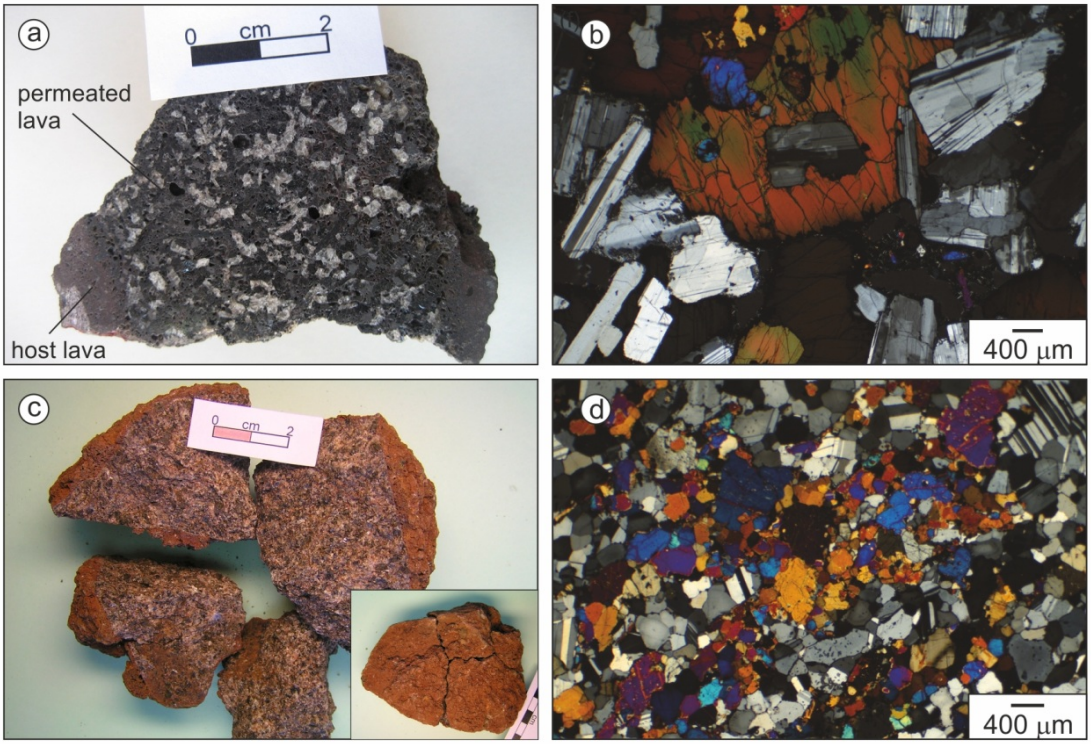

Fig. 6.6 - (a) Alkaline gabbro (GRZF1x13) hand specimen; (b) photomicrograph of the alkali gabbro (GRZF1x1) in cross-polarized transmitted light; (c) subalkaline gabbro (GRQUx4) hand specimen as found in the sampling site; (d) photomicrograph of the subalkaline gabbro (GRQUx4) in cross-polarized transmitted light.

grains. They have fractures but do not present infiltrating glass. The dunite found in the lava flow is smaller (< 2 cm) and shows reddish iron oxide alteration within some olivine crystals and fractures, so this sample is only used for petrographic and mineral chemistry analyses. The dunite found in the pyroclastic layer shows a mm-thick, brownish rim in contact with the host rock. This rim is composed of fine-grained olivine and feldspar crystals in a palisade arrangement (Fig. 6.5D).

Alkaline gabbros were found in *Baía da Folga* and *Ponta da Pesqueira* outcrops (Figs. 6.4A-B and 6.6A). They have been described by Larrea (2010) and Larrea et al. (2010). They display a medium- to coarse-grained orthocumulate texture and are composed of variable proportions of feldspars (10 - 80 %), clinopyroxene (8 - 35 %), amphibole (5 - 70 %), olivine (0 - 20 %), Fe-Ti oxides (3 - 20 %) and apatite (up to 3 % in some samples; Fig. 6.6B). Euhedral to subhedral feldspars, olivine and clinopyroxene are the main cumulus phases. Amphibole is the principal intercumulus phase in all the cases; when it develops large poikilitic crystals (up to 2 cm), the xenolith texture can be described as

heteroadcumulate. Some alkaline xenoliths are permeated by the host lava (5-15 % of the total volume fraction; Fig. 6.6A); in these cases, a discontinuous reaction rim between the xenoliths and the host basalt has been recognized. Where the feldspars, olivine or pyroxene crystals are in contact with the host basalt, a clear contact appears; in contrast, a thick rim is observed between amphibole phases and the host basalt (see section 6.4).

Subalkaline gabbros are only present in the Vitória Unit outcrops (*Ponta da Pesqueira* and *Quitadouro*; Figs. 6.4D-F and 6.6C). They consist of olivine (5 - 20 %), clinopyroxene (10 - 70 %), feldspars (8 - 80 %) and accessory opaque minerals (< 1 %). These xenoliths present inequigranular textures characterized by a clear bimodal distribution of sizes. Anhedral to subhedral crystals (1 - 2 mm in size) are surrounded by a framework of polygonal grains smaller than 0.5 mm (Fig. 6.6D).

6.4 Mineral chemistry

All mineral phases and crystal types present in lava flows and xenoliths were analyzed. Major element compositions were determined by electron microprobe and are accessible in Tables 6.1 - 6.7 of the electronic supplement.

6.4.1 Olivine

Olivine compositions are plotted in Fig. 6.7A. The macrocryts and microcrysts of lava flows show normal zoning, with decreasing forsterite (Fo_{89-60} and Fo_{85-55}, respectively) and NiO (< 0.36 wt. %) contents, and increasing MnO (0.01 - 0.86 wt. %) and CaO (0.13 - 0.51 wt. %) concentrations from core to rim. In the gabbroic xenoliths, olivine crystals are characterized by a normal compositional zoning with Fo_{84-74}, < 0.21 wt. % NiO, 0.11 - 0.38 wt. % MnO and < 0.13 wt. % CaO in the subalkaline gabbros, and Fo_{78-54}, < 0.10 wt. % NiO, 0.05 - 1.37 wt. % MnO and 0.02 - 0.20 wt. % CaO in the alkaline group. The olivine crystals in dunites are weakly zoned Fo_{92-90} and have high NiO (0.40 - 0.19 wt. %), and low MnO (0.08 - 0.20 wt. %) and CaO (< 0.05 wt. %) concentrations.

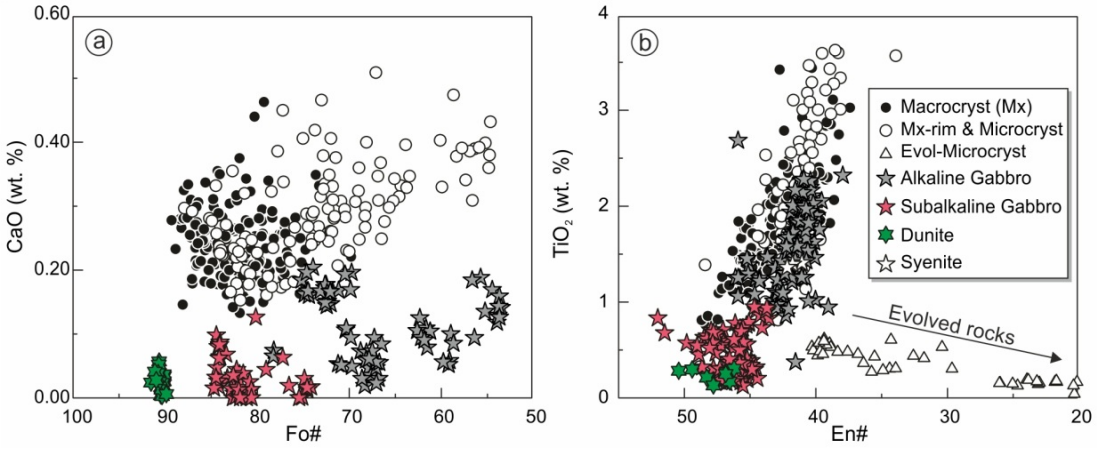

Fig. 6.7 - (a) Olivine CaO (wt. %) vs. Fo# contents from Graciosa lava and xenolith analyzed crystals. (b) Clinopyroxene TiO_2 (wt. %) vs En# diagram ; Evol-Microcryst: microcryst analyzed within trachytes.

6.4.2 Clinopyroxene

Clinopyroxene compositions are shown in Fig. 6.7B. Macrocrysts and microcrysts of clinopyroxene from the lava flows are classified as augite and diopside (Morimoto et al., 1988; Fig. 6.8). Clinopyroxene macrocrysts (Wo_{42-46} En_{49-37} Fs_{10-16}) and microcrysts (Wo_{36-48} En_{49-34} Fs_{15-13}) analyzed in the basaltic to hawaiitic lava flows define a variation trend with 0.33 - 3.63 wt. % TiO_2 and 1.05 - 10.34 wt. % Al_2O_3 contents. In contrast, clinopyroxene in the evolved rocks (Wo_{44-43} En_{40-20} Fs_{16-36}), classified as augite-hedenbergite, forms a clearly distinct trend characterized by high SiO_2 (> 50 wt. %) and the lowest TiO_2 (< 0.63 wt. %) and Al_2O_3 (< 1.43 wt. %) contents, similarly to trachytic rocks from *Sete Cidades* volcano from São Miguel (Beier et al., 2006). Clinopyroxene crystals from the gabbroic and syenite xenoliths are classified as augite and diopside. In the alkaline gabbros, clinopyroxene compositions display an alkaline trend in the Ti vs Ca+Na (per formula unit) diagram by Leterrier et al. (1982) (not shown). Clinopyroxene in subalkaline gabbros is more primitive (Wo_{35-48} En_{52-44} Fs_{13-8}), with 0.13 - 0.95 wt. % TiO_2 and 1.58 - 4.68 wt. % Al_2O_3, than clinopyroxene in alkaline gabbros (Wo_{45-47} En_{46-38} Fs_{9-15}; 0.37 - 2.68 wt. % TiO_2 and 1.34 - 6.95 wt. % Al_2O_3). Clinopyroxene crystals in the syenites are barely zoned Wo_{45} En_{42-41} Fs_{13-14} with intermediate TiO_2 (1.36 - 1.41 wt. %) and Al_2O_3 (4.28 - 4.44 wt. %) contents. The clinopyroxene crystals in dunites are the most primitive (Wo_{46-51} En_{50-46} Fs_3) with low TiO_2 (0.13 - 0.31 wt. %) and Al_2O_3 (1.31 - 2.38 wt. %) contents.

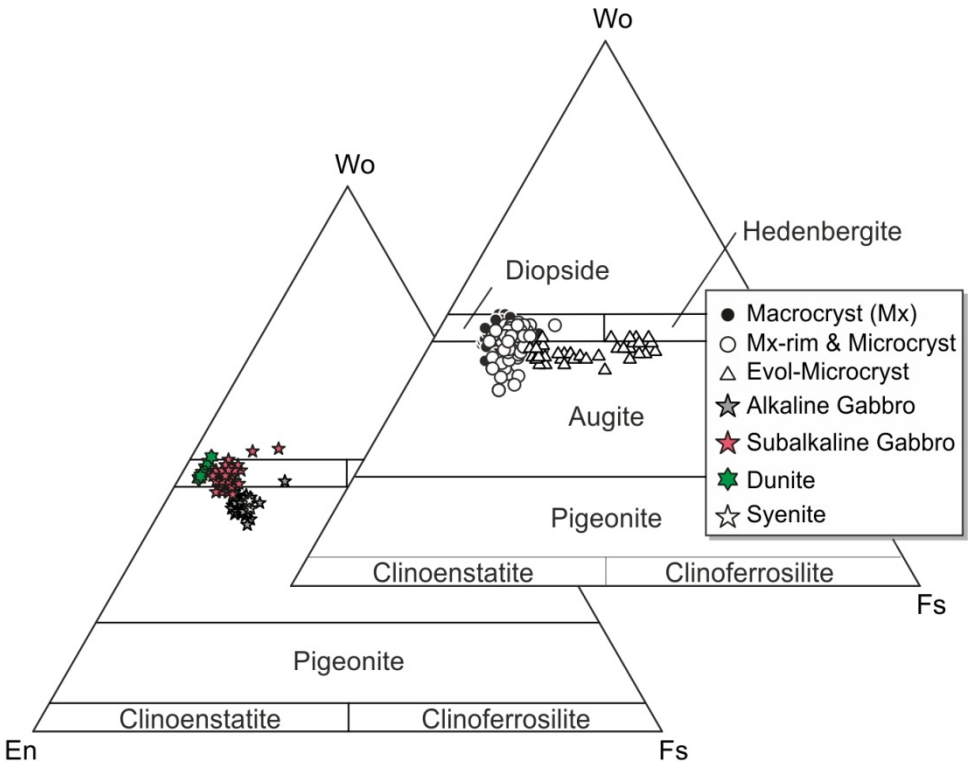

Fig. 6.8 - Clinopyroxene classification diagram wollastonite - enstatite - ferrosilite (Morimoto et al., 1988).

6.4.3 Feldspars

The macrocrysts and microcrysts in lava flow samples range from bytownite to anorthoclase (An_{82-0} Ab_{17-66} Or_{0-34}). The subalkaline xenolith crystals range from anorthite to bytownite (An_{98-76} Ab_{2-24} Or_{0-0}), whereas the alkaline gabbro crystals are bytownite to andesine (An_{76-31} Ab_{23-67} Or_{0-3}). Syenite xenoliths are characterized by the presence of major alkaline feldspar and minor Na-rich plagioclase (An_{16-0} Ab_{81-22} Or_{3-78}). The ternary classification diagram Ab-An-Or for feldspars is shown in Fig. 6.9.

6.4.4 Amphibole

In general, amphibole crystals are scarce in Graciosa lava flows. However, they are a common macrocryst phase in the basaltic lava flow that carries the *Baía da Folga* alkaline gabbros (GRZF1 sample) and they appear as microcrysts in the evolved rocks. Amphibole shows quite varied compositions, classified as kaersutite, magnesiotaramite and riebeckite depending on their Ca and Na contents (Leake et al., 1997; Fig. 6.10).

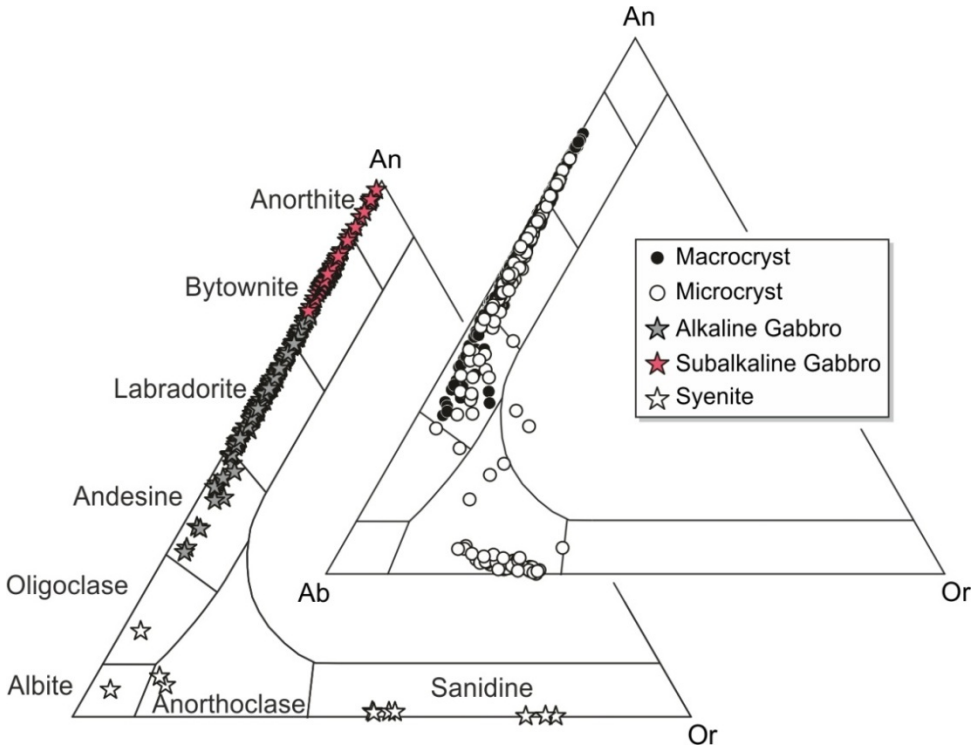

Fig. 6.9 - Ternary classification diagram Ab-An-Or for feldspars, showing the chemical variability of Graciosa lava and xenolith feldspars.

In contrast, kaersutite and/or magnesiohastingsite (depending on the Ti content) are a major mineral phase in the alkaline gabbros. The amphibole crystals observed within the alkaline gabbros and in their host lava present a thick rim (200 to 400 µm) composed of tiny allotriomorphic olivine, pyroxene, plagioclase, ilmenite and Ti-magnetite crystals. Finally, syenite samples have Ti-poor calcic amphiboles classified as ferro-hornblende and ferro-edenite.

6.4.5 Opaque minerals

Opaque minerals in lava flows and in gabbroic and syenite xenoliths occur mainly as small crystals (< 0.5 mm). Some isolated macrocrysts are found as well. They are principally Al-bearing titanomagnetite (25.96 - 4.37 wt. % TiO_2), but ilmenite has been also recognized (45.89 - 53.47 wt. % TiO_2) and Cr-Spinel crystals (scarcer; 1.13 - 1.57 wt. % TiO_2 and chromium numbers from 0.37 to 0.59; Cr# = Cr/(Cr+Al)). Cr-Spinel is the only opaque phase present in the dunite samples (0.29 - 0.41 wt. % TiO_2 and Cr# = 0.43 - 0.54).

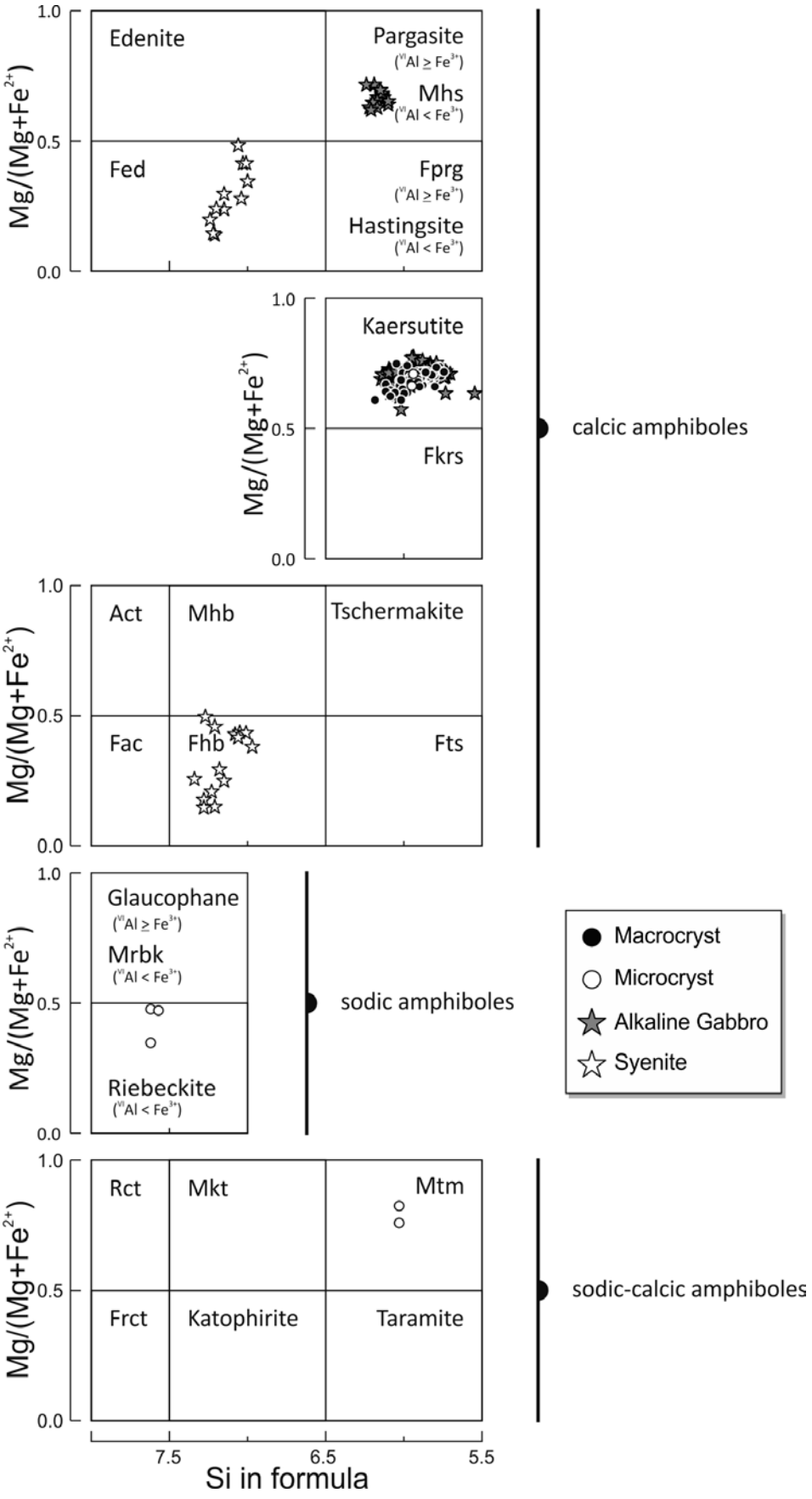

Fig. 6.10 - Amphibole classification diagrams (Leake et al., 1997). Mineral abbreviations are according to Whitney and Evans (2010).

6.4.6 Other minerals

Apatite is present as microcrysts in alkaline gabbros and evolved rocks. It is classified as F-apatite and has variable contents of CaO (53.20 - 57.26 wt. %), P_2O_5 (38.35 - 43.99 wt. %), F (1.75 - 2.59 wt. %) and Cl (< 0.73 wt. %).

Zircon (~ 66 wt. % ZrO_2), biotite (7.08 - 8.39 wt. % K_2O and 0.2 - 0.35 wt. % Na_2O), sphene (27.89 - 28.68 wt. % TiO_2 and 28.27 - 28.41 wt. % CaO) and quartz are accessory mineral phases in the syenite samples.

6.5 Whole rock chemistry

Whole rock major element, trace element and isotopic analyses of the studied samples are available in Appendix - Table II.

6.5.1 Major elements

Lava samples from the Vitória Unit are the most magnesium-rich (10.58 - 6.57 MgO wt. %), followed by samples from Vulcão Central Unit (7.04 - 1.15 MgO wt. %) and Serra das Fontes (4.39 - 3.07 MgO wt. %). Serra Branca samples are the most evolved with MgO contents < 0.38 wt. %. Analyzed lavas have been plotted in Harker type diagrams vs. MgO (Fig. 6.11). A continuous variation trend is observed in these diagrams, although there is a clear change in the slope at MgO contents of 5 wt. % for most oxides. TiO_2, Fe_2O_3, and CaO decrease with decreasing MgO, whereas Na_2O and K_2O increase with decreasing MgO. In contrast, Al_2O_3 slightly increases within the whole range of MgO values.

The geochemical composition of the xenoliths clearly reflects the mineralogic and petrologic observations. The dunite sample has the highest MgO concentration (39.41 wt. %; not shown) as it contains up to 96 % volume fraction of mafic minerals. The

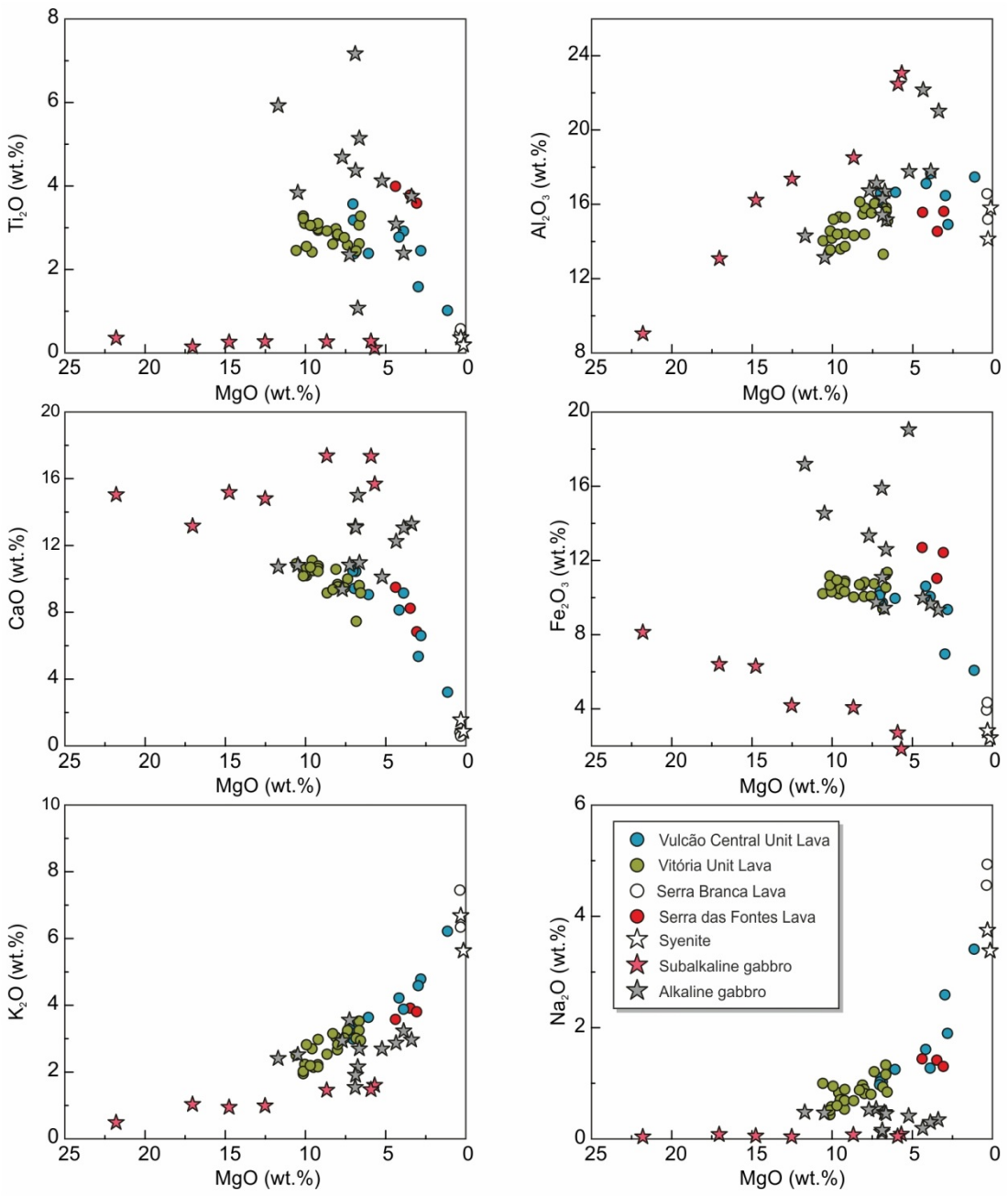

Fig. 6.11 - Major element contents plotted vs. MgO contents for lava flow, gabbroic xenoliths and syenite samples from Graciosa Island.

syenites are the most evolved xenoliths (< 0.32 wt. % MgO) describing the same trend as the evolved rocks from Serra Branca (Fig. 6.11). Among the gabbros, the subalkaline group is more Mg-, Al- and Ca-rich, whereas the alkaline gabbros have higher contents in the rest of major elements. Overall, the alkaline gabbros have higher concentrations of the major elements than the subalkaline gabbros, with the exception of Al_2O_3 and CaO. Gabbroic xenoliths display an Al_2O_3 and Na_2O increase and a Fe_2O_3 decrease with

decreasing MgO, whereas CaO, K_2O and TiO_2 contents are quite constant or do not show a defined trend (Fig. 6.11).

6.5.2 Trace elements

Primitive mantle-normalized multi-element patterns (Fig. 6.12) of the studied lavas from the Serra das Fontes and the Vitória - Vulcão Central volcanic complexes are fairly parallel. They show negative anomalies for Th, K, Pb and Ti (when detected) and a Nb enrichment. Overall, trachytic rocks from Serra Branca are more enriched in incompatible trace elements, especially in Zr-Hf, whereas sharp depletions are recognized for Ba, Sr, P, Eu and Ti.

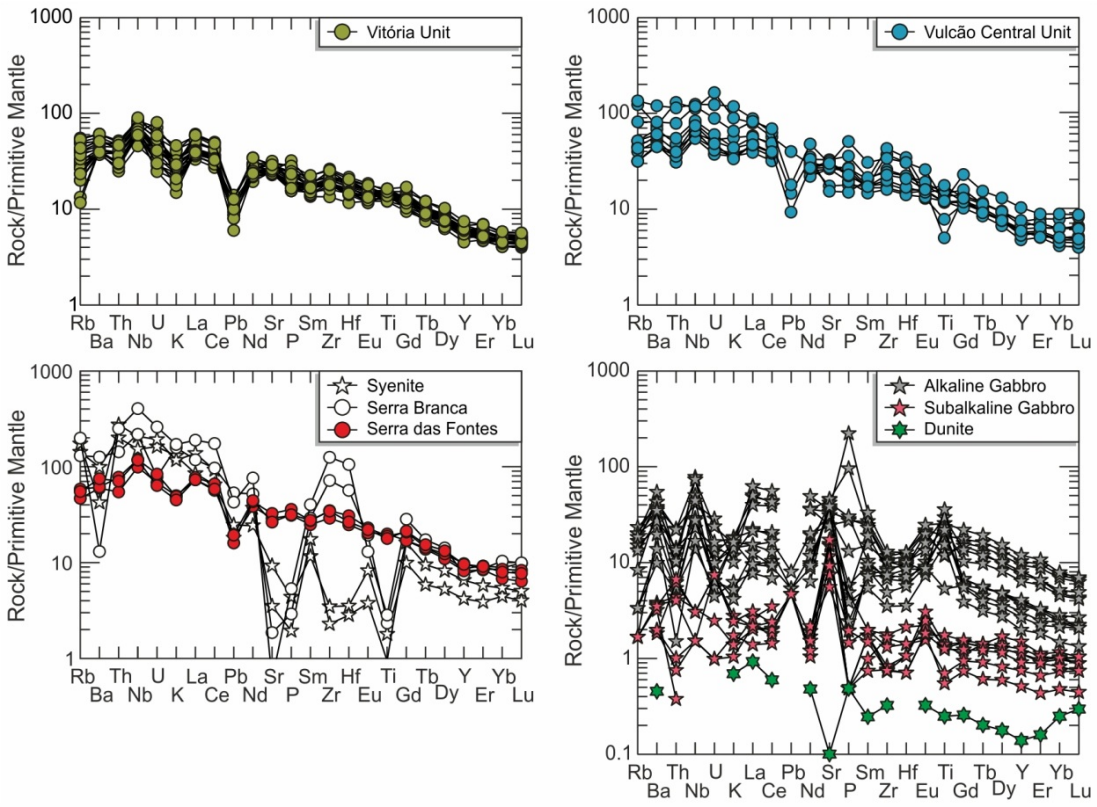

Fig. 6.12 - Primitive mantle-normalized (McDonough and Sun, 1995) multi-element diagrams for Graciosa lava flows and xenoliths.

The multi-element patterns of the gabbroic xenoliths clearly cluster in two groups according to their affinity: alkaline gabbros and subalkaline gabbros (Fig. 6.12). Alkaline gabbros share some features with lava flows including the negative Th, K and Pb

anomalies, and the Nb enrichment. The most pronounced differences are the positive Sr, Eu and Ti anomalies and the varied P contents. Subalkaline gabbros show normalized patterns depleted in all incompatible elements compared to the alkaline gabbros. The subalkaline group shows positive Pb, Sr and Eu anomalies, negative Ti and P anomalies and varied Th contents. The syenites share the characteristics described for the Serra Branca trachytes, however they are less enriched in incompatible elements and show a distinct Zr-Hf depletion. The dunite sample is depleted in incompatible elements relative to primitive mantle. It shows a sharp negative Sr anomaly and a slight enrichment in heavy rare earth elements Er-Lu.

6.5.3 Isotopic data

The Sr, Nd and Pb isotopic data obtained for lava flows, alkaline and subalkaline xenoliths and a dunite from Graciosa Island are plotted in Fig. 6.13 (Appendix - Table II).

Lavas from Serra das Fontes and Vitória - Vulcão Central volcanic complexes display minor variability in $^{87}Sr/^{86}Sr$ (0.70336 - 0.70358) and $^{143}Nd/^{144}Nd$ (0.512922 - 0.512964) ratios, whereas the evolved sample from Serra Branca has higher $^{87}Sr/^{86}Sr$ (0.70390) and lower $^{143}Nd/^{144}Nd$ (0.512883) ratios. Moreover, all lava samples define a positive trend in Pb-Pb isotope systems ($^{206}Pb/^{204}Pb$ from 19.419 to 20.096; $^{207}Pb/^{204}Pb$ from 15.588 to 15.659; $^{208}Pb/^{204}Pb$ from 39.038 to 39.520). Gabbroic xenoliths and the dunite plot within the array described by the lavas. In the alkaline and subalkaline xenoliths the $^{87}Sr/^{86}Sr$ isotopic composition ranges from 0.70338 to 0.70378, $^{143}Nd/^{144}Nd$ from 0.512945 to 0.513011, $^{206}Pb/^{204}Pb$ from 19.513 to 20.032, $^{207}Pb/^{204}Pb$ from 15.595 to 15.622 and $^{208}Pb/^{204}Pb$ from 38.981 to 39.393. One of the alkaline xenoliths shows notable unradiogenic $^{206}Pb/^{204}Pb$ (18.710) and $^{208}Pb/^{204}Pb$ (38.424). The dunite sample has an isotopic signature within the range of the other studied samples, with $^{87}Sr/^{86}Sr$ = 0.7035, $^{143}Nd/^{144}Nd$ = 0.51294, $^{206}Pb/^{204}Pb$ = 19.70, $^{207}Pb/^{204}Pb$ = 15.59 and $^{208}Pb/^{204}Pb$ = 39.14.

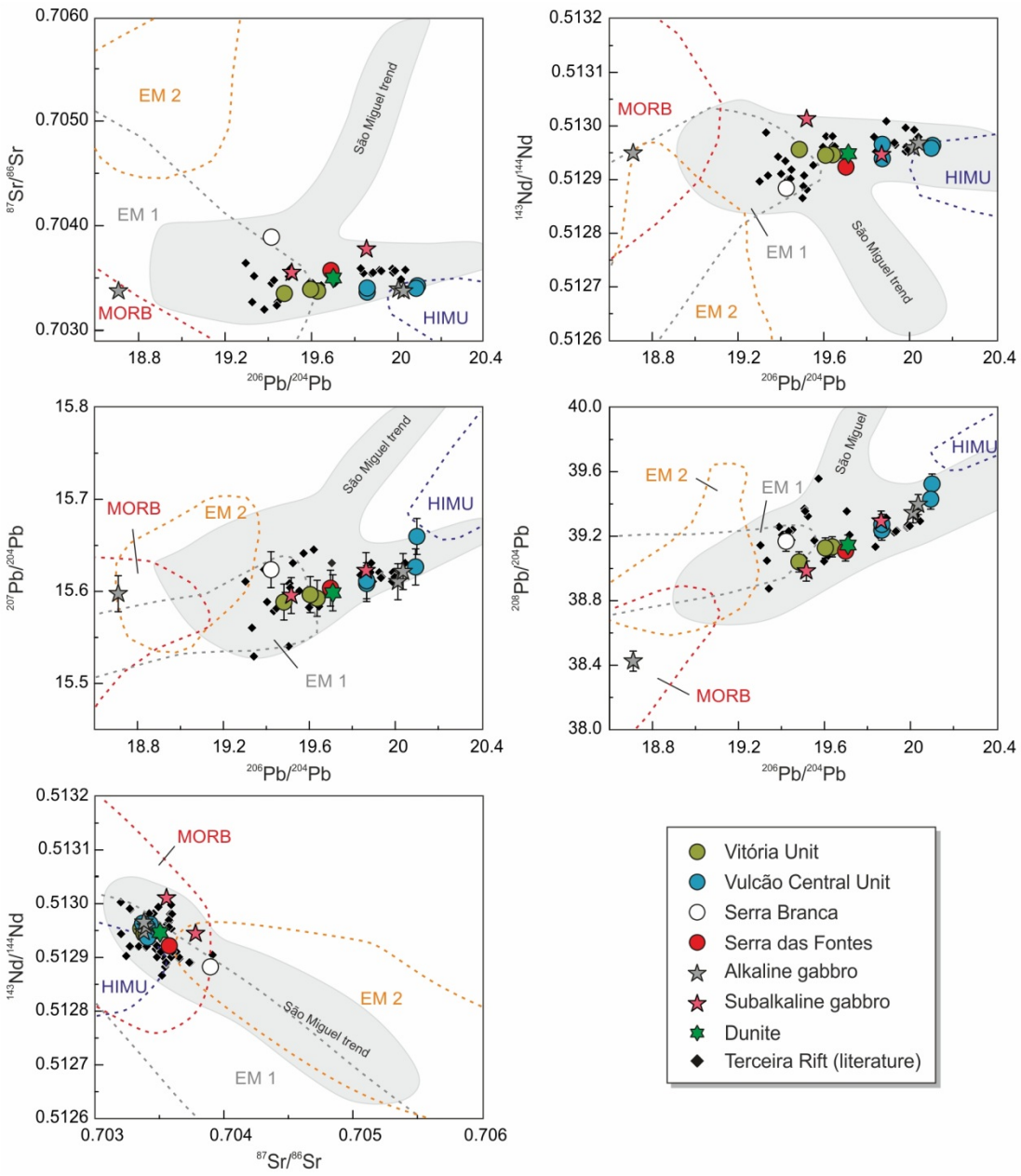

Fig. 6.13 - Isotope systematics of the studied Graciosa lavas and xenoliths (error bars smaller than symbol size when not shown). Mantle component fields based on data compiled in GEOROC (http://georoc.mpch-mainz.gwdg.de/georoc) and PETDB (http://www.earthchem.org/petdb)for Atlantic MORB (MORB), Saint Helena (HIMU), Samoa and Society (EM2) and Tristan da Cunha, Gough and Pitcairn (EM1). Previous published data from Azores are from Davies et al. (1989), Hawkesworth et al. (1979), Turner et al. (1997), Widom et al. (1997), França (2000), Beier et al. (2006), França et al. (2006*b*), Beier et al. (2007), Elliott et al. (2007), Beier et al. (2008, 2010), Millet et al. (2009), Madureira et al. (2011), Ribeiro (2011), Beier et al. (2013) and Genske et al. (2012).

6.6 Discussion

6.6.1 Origin of lava crystal populations

The macrocrysts and microcrysts found in Graciosa lavas are olivine, clinopyroxene, plagioclase, amphibole and Fe-Ti oxides. The macrocrysts show either more primitive or similar compositions to microcrysts. Nevertheless, they define a common evolution trend (e.g., Fig. 6.7 and Fig. 6.9) pointing to a comagmatic origin for these crystals. The macrocrysts could potentially be classified as cogenetic phenocrysts or non-cogenetic antecrysts with the host groundmass (Jerram and Martin (2008) and references therein). The existence of antecrysts in the volcanic products from other Azorean Islands (Corvo and Flores) and their influence on whole rock chemistry have been investigated by Larrea et al. (2012, 2013). Mineral-melt equilibrium diagrams are useful to decipher the origin of comagmatic crystals (Rhodes et al., 1979; Fig. 6.14). Equilibrium curves respond to the iron-magnesium distribution coefficient of the mineral: 0.30 ± 0.03 for olivine (Roeder and Emslie, 1970), 0.26 ±0.05 for clinopyroxene (Akinin et al., 2005) and 0.38 for amphibole (LaTourrette et al., 1995). Most analyzed olivine, clinopyroxene and amphibole macrocryst cores plot within or just below the equilibrium curve, so they are phenocrysts in equilibrium with the rock in which they are included. Microcryst and phenocryst rims fall below the equilibrium curve due to progressive fractionation of the magma. On the other hand, some macrocryst cores plot noticeably above the equilibrium curve, so they are non-cogenetic crystals (antecrysts) in disequilibrium with their host rock. Two types of antecrysts are recognized: (1) large, isolated, highly corroded crystals in disequilibrium with the host rock, which are embedded in a fine-grained groundmass (olivine, clinopyroxene and amphibole antecrysts from samples GRZF8, GRZF16, GRZF6 and GRZF13) and (2) large crystals with cores in disequilibrium overgrown by rims in equilibrium with the host rock and equivalent to the microcrysts (clinopyroxene from sample GRZF14). Some clinopyroxene crystals analyzed in trachytes from Serra Branca and Vulcão Central Unit appear to be in disequilibrium; however, the Fe-Mg distribution coefficients used for the equilibrium diagram may be not applicable to the low Mg# content of these rocks [Mg# = MgO/(FeO+MgO)·100 and FeO = $0.9 \cdot Fe_2O_3^T$].

6.6.2 Magmatic differentiation in Graciosa Island

Differentiation of Graciosa magmas by fractional crystallization: genesis of lavas, alkaline xenoliths and syenites

All of the studied lavas from Graciosa Island fall within a single liquid line of descent, pointing to a comagmatic origin and a single fractionating process involved in their genesis. In addition, the presence of alkaline xenoliths with cumulate textures potentially indicates their origin as magma chamber cumulates (e.g., Shamberger and Hammer, 2006) and therefore, magmatic differentiation controlled by fractional crystallization. Moreover, olivine Fo_{78-54} and CaO contents (0.02 - 0.20 wt. %) in the alkaline gabbros indicate that they were not formed in the mantle (e.g., Stormer, 1973; Jurewicz and Watson, 1988). Fractional crystallization has been evaluated as a potential mechanism for magmatic differentiation using both major and trace elements, aiming to establish (a) the conditions of magma evolution and fractionation (crystallization pressure and temperatures), (b) the extent of fractional crystallization needed to reproduce the studied lava compositions, (c) the composition of the fractionated mineral assemblage controlling the fractional crystallization process and (d) a comparison between these fractionated phases and the studied xenoliths.

A major element model was carried out using the MELTS algorithm (Ghiorso and Sack, 1995; Asimow and Ghiorso, 1998). Sample GRZF12 has a MgO content of 10.58 % and a Ni content of 200 ppm and the olivine and clinopyroxene macrocrysts are in equilibrium with the bulk rock composition (see Fig. 6.14). Therefore, sample GRZF12 represents the naturally occurring major element composition closest to a primary magma (~ 12 wt. % MgO and 200 - 300 ppm Ni contents have been proposed for Azores primitive melts (Beier et al., 2006, 2008; Madureira et al., 2011) and can be used as the starting composition for the model. The MELTS fractional crystallization model was run with cooling steps of 5 ºC under isobaric conditions at different pressures (1000, 700 and 500 MPa) and under polybaric conditions (starting at 500 with dP/dT = 1).

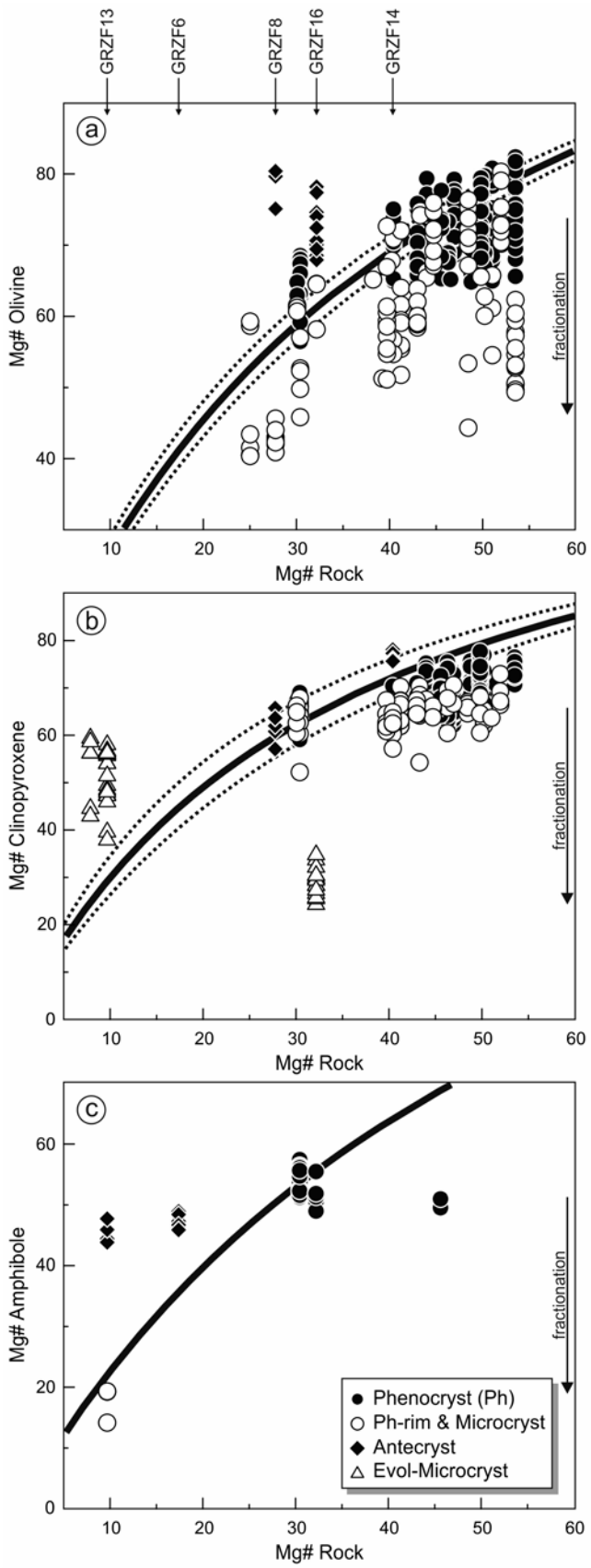

Fig. 6.14 - Mg# in mineral vs. Mg# in whole rock [(Mg# = MgO/(FeO+MgO)·100 and FeO = 0.9·$Fe_2O_3^T$] for olivine (a), clinopyroxene (b) and amphibole (c). The black curves represent the range of equilibrium compositions between mineral and melt. Evol-Microcryst: microcryst analyzed within an evolved rock.

Table 6.1 - Parameters of the MELTS modeling runs; the grey row indicates the best fit MELTS run.

Starting P (MPa)	% H_2O	dT (ºC)	dP (Mpa)	dP/dT	Buffer fO_2 QFM	Liquidus T (ºC)	Final P (MPa	Final T (ºC)	initial logfO_2	Final logfO_2	Fractionated phases
1000	2	5	0	-	0	1315	1000	900	-6.41	-11.61	Cpx, Amp, Pl, Opx, Opq, Ap, Grt
1000	1	5	0	-	0	1345	1000	900	-6.13	-11.61	Cpx, Amp, Pl, Opx, Opq, Ap, Grt, Wht
1000	0.5	5	0	-	0	1375	1000	error at 1105	-5.87	-8.65	Cpx, Amp, Pl, Opx, Opq, Grt, Wht
700	2	5	0	-	0	1285	700	900	-6.9	-11.89	Ol, Cpx, Amp, Pl, Opx, Opq, Ap, Grt
700	1	5	0	-	0	1305	700	900	-6.71	-11.89	Ol, Cpx, Amp, Pl, Opx, Opq, Ap, Grt
700	0.5	5	0	-	0	1330	700	900	-6.48	-11.89	Ol, Cpx, Amp, Pl, Opx, Opq, Ap, Wht
500	2	5	0	-	0	1275	500	990	-7.14	-12.08	Ol, Cpx, Amp, Pl, Opq, Ap, Grt
500	1	5	0	-	0	1285	500	900	-7.04	-12.08	Ol, Cpx, Amp, Pl, Opx, Opq, Ap
500	0.5	5	0	-	0	1305	500	error at 1165	-6.85	-8.32	Ol, Cpx, Pl, Opq
500	2	5	4	0.8	0	1280	48	715	-7.09	-16.39	Ol, Cpx, Amp, Pl, Opx, Opq, Ap, Btt
500	1	5	4	0.8	0	1285	76	760	-6.99	-15.29	Ol, Cpx, Amp, Pl, Opx, Opq, Ap
500	0.5	5	4	0.8	0	1305	12	700	-6.8	-16.81	Ol, Cpx, Amp, Pl, Opq, Ap, sph

Mineral abbreviations are according to Whitney and Evans (2010)

Different initial water contents (0.5, 1 and 2 % H_2O) were considered according to the presence of hydrous amphibole (Eggler, 1972; Ustunisik and Kilinc, 2011). Based on redox condition estimates by Mallmann and O'Neill (2009) for OIBs, oxygen fugacity was fixed relative to the QFM buffer. These authors show that OIBs record a very restrict range of relative oxygen fugacity between QFM and QFM+1. The parameters used in these MELTS runs are summarized in Table 6.1.

The major element compositions of Graciosa lavas are best modeled by a MELTS polybaric fractionation process (500 - 10 MPa) starting at a pressure of 500 MPa (ca. 15 km depth) with 0.5 % of H_2O content, for which conditions the liquidus temperature is 1305 ºC. The residual melt compositions obtained from this polybaric fractional crystallization model thoroughly reproduce the compositions of Graciosa lava flows (Fig. 6.15), with the following fractionated phases: olivine, clinopyroxene, plagioclase, Fe-Ti

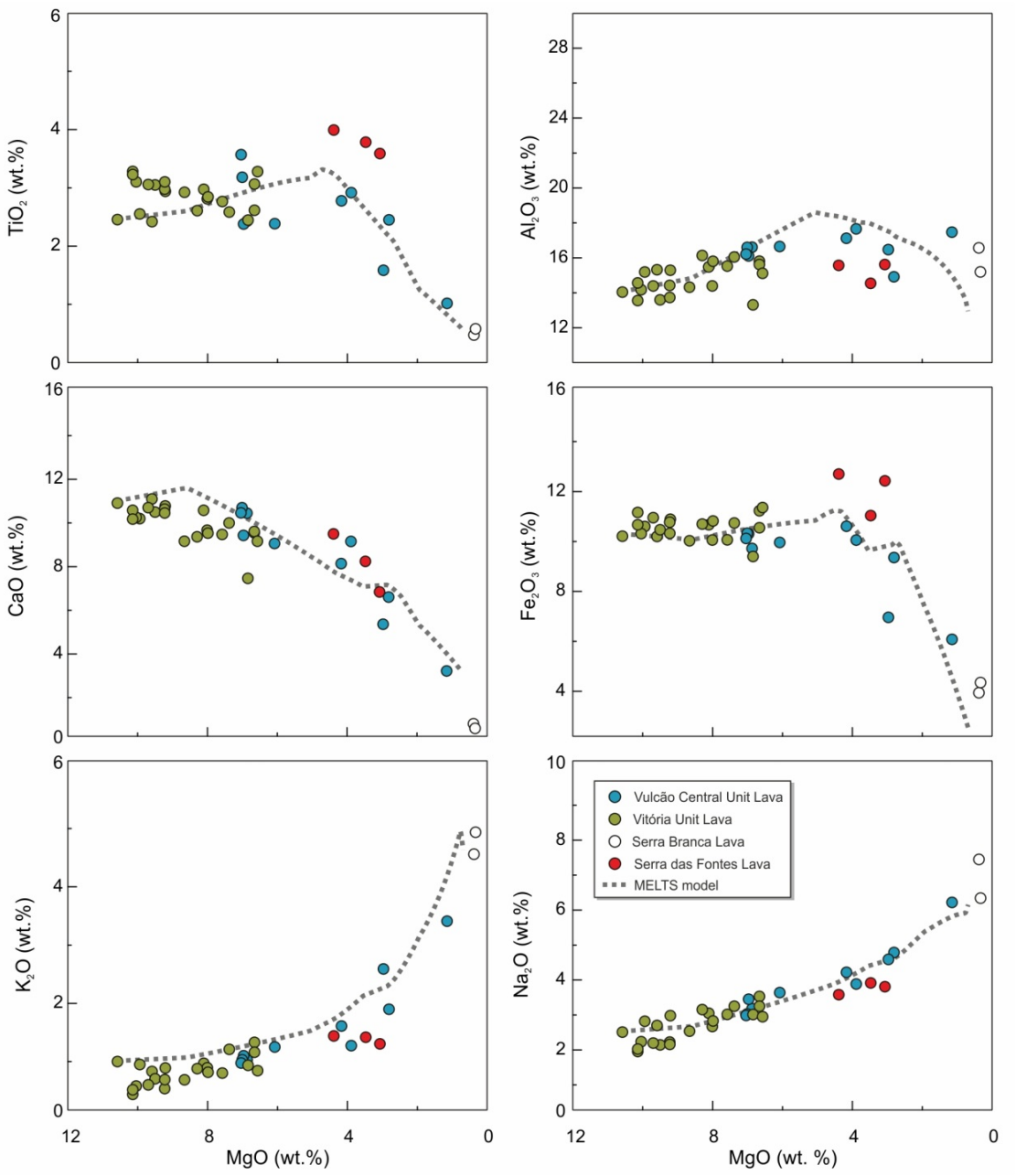

Fig. 6.15 - Major element contents plotted vs. MgO contents for Graciosa lavas. The best-fit MELTS-1 polybaric fractional crystallization model (dotted lines) was obtained at an initial pressure of 500 MPa with decreasing steps of 5 MPa and cooling steps of 5 ºC with a water content of 1 % and considering GRZF12 sample as the initial composition.

oxides, apatite and an additional Ti-rich ferromagnesian phase. The latter, with low Si and high Al and Ti contents, is interpreted as amphibole (kaersutite), because the MELTS thermodynamic database does not include this Ti-rich amphibole (M.S. Ghiorso, pers. com.). The fractionated mineral assemblage and the composition of these minerals in the range of temperature from ~ 1235 to 800 ºC (MELTS-1; Table 6.2) is broadly consistent with that of the alkaline xenoliths and lavas, suggesting that these alkaline

xenoliths are the fractionated solids (cumulates) formed during the fractional crystallization process. In accordance, their bulk composition deviates from the composition of the lava flows, due to the accumulation of olivine, clinopyroxene, plagioclase, kaersutite, opaque minerals and apatite. For instance, the positive Ti anomaly can be related to the accumulation of kaersutite, Ti-rich clinopyroxene and opaque minerals, complementary to the lava flows, some of which are depleted in Ti (negative anomaly). Similarly, the variable P contents can be linked to the presence or absence of apatite (Fig. 6.12). Moreover, the composition of the fractionating mineral phases occurring below 900 ºC in the MELTS-1 model (feldspars, clinopyroxene, amphibole, sphene and Ti-magnetite) resembles the mineral compositions of the syenite sample (Table 6.2). Therefore, it is important to determine whether these syenites are cumulates like the alkaline xenoliths or if they represent frozen liquid compositions (residual magma completely solidified within the magma chamber). Their bulk composition is quite similar to the trachytic samples (Fig. 6.12), except for a glaring Zr-Hf depletion in the syenites. In addition, the Eu/Eu* anomaly ($Eu_N/(Sm_N+Gd_N)/2$) in the syenites is negative (Eu/Eu* < 1) and similar to that of the trachytes (Appendix - Table II), implying that there is minimal accumulation of alkali feldspar. According to these data, the syenites represent a frozen bulk trachyte liquid, similar to the syenite nodules studied by Widom et al. (1993) in Agua de Pau Volcano on São Miguel Island. The low Zr, Hf, Y and Lu, yet similar La concentrations of the Graciosa syenites relative to trachytes indicates that there was likely incomplete digestion of syenite zircons during sample dissolution by acid digestion.

The fractional crystallization process was further appraised using trace element data, considering those trace elements for which partition coefficients are available for all fractionated phases. The trace element model was carried out by applying the fractional crystallization equation of Rayleigh (1896). Due to changes in the proportions of fractionating mineral assemblage during fractional crystallization, at least two different stages were needed to reproduce the whole range of Graciosa sample compositions. The partition coefficients used in both models were taken from previous studies in alkaline rocks with similar compositions and are listed Table 6.8 of the electronic

Table 6.2 - Composition of the obtained fractionated phases in MELTS-1 and MELTS-2 models, and those of the studied xenoliths and lavas for comparison.

Mineral Phase		MELTS-1	Alkaline gabbros	Syenites	Lavas	MELTS-2	Subalkaline gabbros
Olivine	Fo#	86 - 53	78 - 54	-	89 - 55	89 - 71	84 - 74
	SiO_2	40.3 - 35.3	38.3 - 34.7	-	40.8 - 34.0	40.8 - 37.9	40.5 - 37.9
Clinopyroxene	Mg#	75 - 9*	75 - 59	66 - 64	78 - 25	79 - 58	85 - 74
	TiO_2	3.9 - 0.1	2.6 - 0.4	1.4 - 1.3	3.6 - 0.1	0.5 - 1.5	0.1 - 1
Kaersutite	Mg#	75 - 9*	58 - 43	30 - 9	57 - 14	-	-
Feldspars	An	70 - 4	76 - 31	16 - 0	82 - 0	85 - 45	98 - 76
	Al_2O_3	31.6 - 19.5	33.4 - 24.9	22.9 - 18.4	34.2 - 18.1	34.2 - 27.2	36.24 - 30.6

*Mg# values for the ferromagnesian phases (including clinopyroxene and kaersutite) estimated by MELTS

supplement. In the trace element model-1 (Fig. 6.16), the GRZF4 lava sample was used as starting point because it has the least enriched trace element composition and therefore may represent the least fractionated magma. The starting lava used for the trace element model is different from the one used for the major element MELTS model (GRZF12) because the latter is more enriched in trace elements, despite being slightly less evolved in major and minor element composition. Fractionated mineral phases were chosen according to the most primitive alkaline xenolith mineral modes and in accordance to the MELTS-1 model estimates (27 % olivine, 21 % clinopyroxene, 33 % amphibole, 12 % plagioclase and 7 % ilmenite; see discussion above). If the results of the trace element model-1 are compared to the composition of the Graciosa lavas, a good agreement is observed for samples from Serra das Fontes (50-70 % fractional crystallization) and Vitória - Vulcão Central volcanic complex (10-70 % fractional crystallization). However, no agreement is observed between the model and the most evolved samples (trachytes from Serra Branca and Vulcão Central Unit; Fig. 6.16).

Accordingly, a second model (rare earth element (REE) model-2) with a mineral fractionating assemblage similar to the mineral modes of the most evolved alkaline xenoliths (3.5 % clinopyroxene, 45 % amphibole, 35 % plagioclase, 1.5 % apatite and 15 % ilmenite; Fig. 6.17) was carried out to derive the trachyte sample compositions. In this

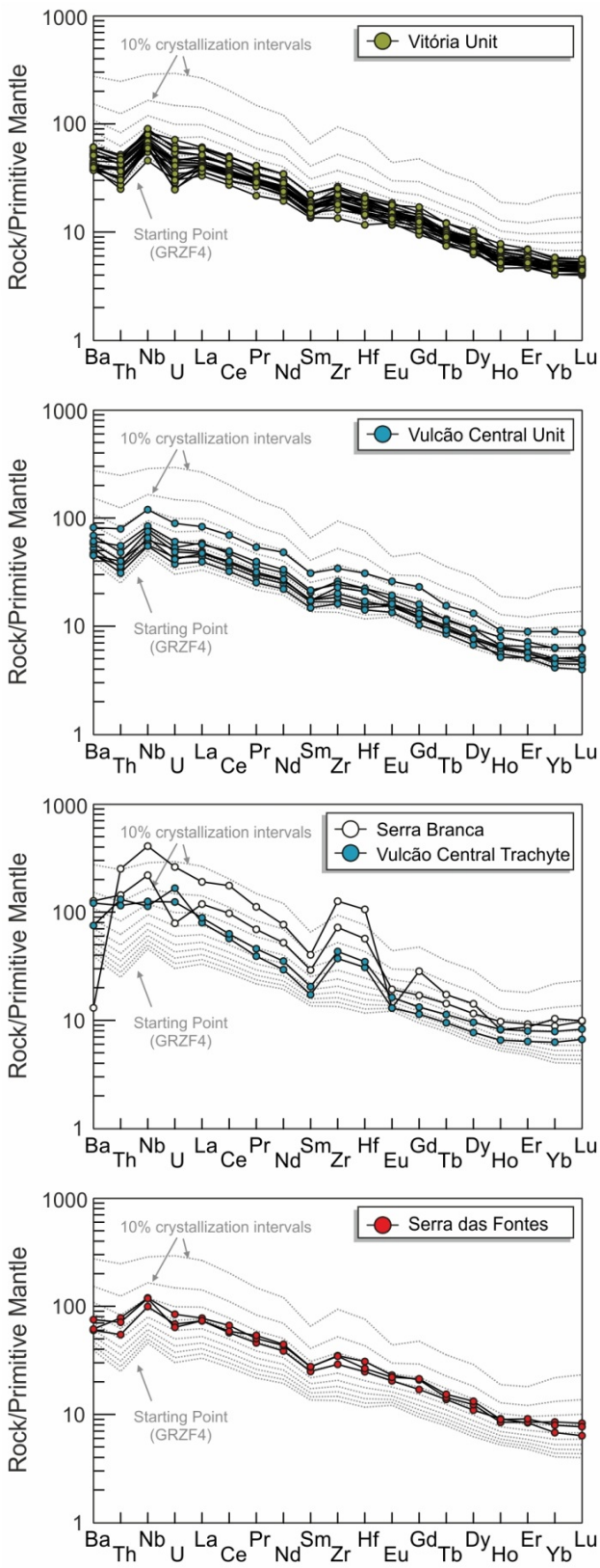

Fig. 6.16 - Primitive mantle (McDonough and Sun, 1995) normalized trace element patterns for the Rayleigh fractional crystallization model-1 starting from sample GRZF4 with 10 % crystallization steps (grey dashed lines, from 100 % melt to 10 % melt) compared to the lava samples from Graciosa Island. The fractionating assemblage is composed of 27 % olivine, 21 % clinopyroxene, 33 % amphibole, 12 % plagioclase and 7 % ilmenite. Partition coefficients used to calculate the model are listed in Table 6.8 of the electronic supplement.

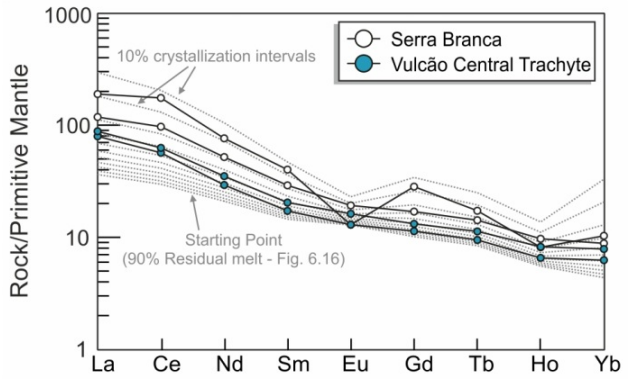

Fig. 6.17 - Primitive mantle (McDonough and Sun, 1995) normalized REE patterns for the fractional crystallization model-2 starting from the composition obtained for 90 % of residual melt in model-1. Serra Branca and Vulcão Central Unit trachytes are shown and compared to the 10 % crystallization intervals (grey dashed lines). For this model the fractionating mineral phases are 3.5 % clinopyroxene, 45 % amphibole, 35 % plagioclase, 1.5 % apatite and 15 % ilmenite. The REE-s included are those with available partition coefficients for all fractionated mineral phases (Table 6.8 of the electronic supplement).

case, the starting point was the residual melt resulting at 10 % of fractional crystallization of sample GRZF4 in the trace element model-1. Crystallization rates from 40 % to 80 % are needed to reproduce the composition of the trachytic samples.

As a conclusion, polybaric fractional crystallization is the dominant process controlling the differentiation of Graciosa magmas, producing lava flows that range from basalt to trachytes (syenites as frozen liquids), and magma chamber cumulates represented by alkaline gabbros. Primary magma compositions were likely very similar to samples GRZF12 and GRZF4.

Origin of the subalkaline xenoliths

The existence of subalkaline gabbros has been identified for the first time within the Azores archipelago. They are composed of olivine, clinopyroxene, plagioclase and scarce Cr-rich spinel. These mineral phases are characterized by much more primitive compositions than those of the alkaline gabbros (Fig. 6.7 and Fig. 6.9). However, the composition of the olivine (Fo_{84-74}) rules out their mantle origin (e.g., Stormer, 1973; Jurewicz and Watson, 1988). The bulk rock composition of the subalkaline group is more primitive in major elements and less enriched in all incompatible elements relative to the alkaline gabbros (Figs. 6.11 - 6.12). Furthermore, the bulk composition of the

subalkaline group clearly deviates from the composition of the lava flows (and alkaline xenoliths). Therefore, their genesis cannot be linked to the differentiation of primitive Graciosa magmas as described in section above. Nonetheless, their high MgO contents (up to 21.80 wt. %) and positive Eu/Eu* anomalies, which might reflect a net accumulation of plagioclase (see Appendix - Table II) likely indicate a cumulate origin for these gabbros.

In order to decipher the composition of the possible parental magma from which these subalkaline gabbros formed, equilibrium equations were applied (see section 6.6.1). These calculations indicate Mg# from 61 to 32 for the magmas in equilibrium with olivine (Mg#: 75 - 62) and clinopyroxene (Mg#: 85 - 70) in the subalkaline gabbros. In addition, the presence of extremely An-rich feldespars (An_{98-76}) places key constraints on the composition of the parental magma; several experimental studies have determined that such compositions are likely produced from refractory melts with CaO/Na_2O = 12 - 15, exceptionally high Al_2O_3 (~ 18 %), and Na_2O contents of ~ 1 % (Walter and Presnall, 1994; Panjasawatwong et al., 1995). Taking these results into account, along with the mean major element composition proposed for primitive Azores melts (e.g., Beier et al., 2008), the following composition has been estimated as a theoretical refractory parental melt: 45.5 wt. % SiO_2, 2 wt. % TiO_2, 15 wt. % Al_2O_3, 7 wt. % Fe_2O_3, 12.5 wt. % MgO, 13.5 wt. % CaO, 1.1 wt. % Na_2O, 1 wt. % K_2O and 0.5 wt. % P_2O_5. Several authors have proposed the existence of such refractory melts at shallow levels beneath ocean islands and mid-ocean ridges (Duncan and Green, 1980, 1987; Walter and Presnall, 1994; Panjasawatwong et al., 1995). They suggest that these refractory melts are rarely preserved, possibly due to effective mixing and homogenization with volumetrically dominant less refractory magmas, although they have been found as melt inclusions in phenocrysts and xenocrysts (e.g., Donaldson and Brown, 1977; Sobolev and Shimizu, 1993).

Several MELTS fractional crystallization model runs were carried out starting from this theoretical parental magma, to derive fractionated solids (cumulates) equivalent to the composition of the subalkaline gabbros. These MELTS runs were carried out both in polybaric and isobaric conditions, with cooling steps of 5 ºC and oxygen fugacity fixed

relative to the QFM buffer (see section above). Only the isobaric runs produced the fractionated phases observed in the subalkaline gabbros (olivine, clinopyroxene, plagioclase and Cr-rich spinel); moreover, the best results were obtained at 100 MPa (~ 3 km) in anhydrous conditions (MELTS-2; Table 6.2) and in a range of temperatures from ~ 1235 - 1120 ºC. In addition, in this MELTS-2 model the composition of the fractionated olivine, clinopyroxene and plagioclase are quite similar to the ones observed in the subalkaline xenoliths in the range of temperatures from 1215 ºC to 1135 ºC (MELTS-2; Table 6.2).

In conclusion, these xenoliths might be explained as cumulates resulting from isobaric fractional crystallization of a highly refractory melt at 100 MPa (~ 3 km depth) with a very restricted range of temperature and limited degree of fractionation.

Origin of the dunites

Two dunites were found within the Graciosa volcanic sequence; their mineral assemblage consists of approximately 90 % olivine, 5 % spinel and 5 % clinopyroxene. The olivine crystals have Fo contents from 92 to 90, CaO < 0.05 wt. % and 0.22 - 0.39 wt. % NiO. Moreover, spinel crystals have Cr# from 0.43 to 0.54 and TiO_2 contents (< 0.41 wt. %), in the range of those in abyssal peridotites (e.g., Dick and Bullen, 1984; Hekinian et al., 1993; Allan and Dick, 1996). These olivine and spinel compositions, and the HREE enrichment of the dunite (Fig. 6.12) suggest a restitic mantle origin.

The presence of olivine as the main mineral phase (~ 90 %) in these restites suggests that they were formed by a very high degree of partial melting. This however, seems unsuitable for the low degrees of mantle melting (< 5 %) producing alkaline magmas in the Azores (e.g., Beier et al., 2008, 2013). Therefore, these dunites may not be related to the Azorean alkaline melts, but rather might represent restites from the oceanic mantle lithosphere (depleted mantle) where higher degrees of partial melting are expected to produce MORB melts (e.g., Winter, 2010). On the other hand, the presence of clinopyroxene but lack of orthopyroxene indicates that the clinopyroxene likely has a metasomatic origin. The infiltration of Azorean alkaline melts into the overlying depleted

lithospheric mantle could result in the formation of metasomatic clinopyroxene by melt-mantle reaction (e.g., Pearson et al., 2003; Rehfeldt et al., 2008). The clinopyroxene is the most likely host of the LREE and other highly incompatible elements, causing the observed enrichment in these elements in the dunite (Fig. 6.12).

Together, the mineralogy, mineral chemistry, and whole rock chemistry of these dunites are consistent with an origin as olivine and spinel bearing lithospheric mantle restites that were subsequently metasomatized during melt-mantle reaction, producing clinopyroxene as a secondary mineral phase. However, the scarcity of dunites within the volcanic sequence and their small size complicate a more in-depth evaluation of their origin.

6.6.3 Mantle source

The Sr, Nd and Pb isotopic data for Graciosa magmas plot within the array common to most of the Azores archipelago (Fig. 6.13), with the exception of São Miguel Island which presents a distinct isotopic composition identified in previous studies (e.g., Widom et al., 1997; Beier et al., 2007; Elliott et al., 2007). These data are consistent with previously published data from the Terceira Rift, including Graciosa, Terceira and the western part of São Miguel Island, indicating a common magma source. The whole Graciosa dataset, including new data and those of the literature, form a linear trend in Sr-Pb, Nd-Pb and Pb-Pb diagrams (Fig. 6.13), which suggests the involvement of at least two mixing end-members including a depleted MORB and an enriched HIMU mantle component, in the genesis of Graciosa magmas. This source resembles the composition of the redefined FOZO mantle component, which is believed to be the most common mantle end-member found in ocean island basalts (Stracke et al., 2005; Beier et al., 2008).

The gabbroic xenoliths (both alkaline and subalkaline) display isotopic compositions in accord with the studied lavas, supporting a cogenetic origin. Moreover, one of the alkaline gabbros shows the most unradiogenic $^{206}Pb/^{204}Pb$ and $^{208}Pb/^{204}Pb$ isotope ratios obtained for Graciosa Island; its isotopic composition ($^{87}Sr/^{86}Sr \sim 0.7034$, $^{143}Nd/^{144}Nd \sim 0.5129$, $^{206}Pb/^{204}Pb \sim 18.7$, $^{207}Pb/^{204}Pb \sim 15.6$ and $^{208}Pb/^{204}Pb \sim 38.4$) appears to

represent the most depleted end-member composition (MORB) commonly found in the Azores. The isotopic composition of the dunite ($^{87}Sr/^{86}Sr$ = 0.7035, $^{143}Nd/^{144}Nd$ = 0.51294, $^{206}Pb/^{204}Pb$ = 19.70, $^{207}Pb/^{204}Pb$ = 15.59 and $^{208}Pb/^{204}Pb$ = 39.14; Fig. 6.13) is intermediate compared to the other analyzed samples (lavas and xenoliths), consistent with its proposed origin as a metasomatic reaction product between alkaline melts characteristic of Graciosa Island, and the underlying melt-depleted lithospheric mantle.

6.6.4 Evolution of magmatic processes in Graciosa Island

In terms of magmatic processes, lava flows and xenoliths of alkaline gabbro and syenite can be related by polybaric fractional crystallization (500 - 10 MPa). This fractional crystallization took place almost entirely at oceanic crustal depths from ~ 15 km to 1 km, in accordance with the crustal thickness calculated for the Azores plateau (12 - 14 km; Escartín et al., 2001; Luis and Neves, 2006; Matias et al., 2007). In order to reconstruct the sequence and temporal evolution of the magmatic events, the volcanostratigraphy and the $^{40}Ar/^{39}Ar$ ages have to be taken into account (Larrea et al., 2014; see chapters 4 and 5).

The shield stage in Graciosa Island started at least 1.05 Ma ago with the formation of the Serra das Fontes volcanic complex (Larrea et al., 2014; see chapter 5). It was initially a shield volcano mainly composed of basaltic to hawaiitic volcanic products. According to the presented fractional crystallization model, these products are the result of low fractionation rates of a primitive melt at ~ 10 - 15 km depth. At some point around 450 ka, the evolution of the Serra das Fontes magmatic plumbing system produced more evolved volcanic products (trachytes from Serra Branca volcanic complex) and hence a central composite volcano was formed in the central part of the current island. These trachytic products probably resulted from melt fractionation in a shallower magma chamber (~ 1 km; final stages of the polybaric fractional crystallization process; see section 6.6.2). This shield stage remained active for ca. 850 ky (Larrea et al., 2014; see chapter 5).

The erosive stage, originally described by Gaspar (1996) was characterized by volcanic inactivity and erosion of the former central composite volcano. This erosive stage lasted ca. 110 ky (Larrea et al., 2014; see chapter 5).

The rejuvenated stage generated two main volcanic units. At some point, the volcanism restarted on the NW of the island producing the Vitória Unit, covering most of the remaining volcanic units. For instance, the NE coast (nearby the *Quitadouro* volcano) was formed between 96.3 ± 32.3 ka and 45.7 ± 22.0 ka, and the most recent volcanic eruption within the unit took place at ~ 3.9 ka at *Pico Timão* (Larrea et al., 2014; see chapter 5). This unit is characterized by the presence of basaltic, low explosive volcanic episodes associated with the activity of monogenetic eruptive centers (Gaspar, 1996). The coalescence of these volcanic products produced the present NW platform. This younger volcanism, mafic in composition, indicates primitive magma recharge together with a small degree of fractionation in the plumbing system (~ 10 - 15 km).

Meanwhile, to the south of the oldest volcanic structures the formation of a new island started. The volcanism, associated with monogenetic cones of unknown age, was initially strombolian but minor surtseyan eruptions took place as well (Gaspar, 1996). Afterwards, the volcanism became associated with a main eruptive center. Successive lava flows and volcaniclastic eruptions (occasionally explosive) generated a stratovolcano (the Vulcão Central), followed by the formation of its caldera and a lava lake in a period of ~ 60 ky (Larrea et al., 2014; see chapter 5). The Vulcão Central Unit comprises the whole range of compositions from basaltic lava flows to trachytic domes and syenitic nodules (frozen trachytic melts). This implies high degrees of fractionation of primitive melts within the related magma plumbing system (~ 15 - 1 km).

The alkaline gabbros are magma chamber cumulates produced by fractional crystallization, likely at crustal depths (< 15 km). One gabbroic xenolith (GRZF1x1) hosted in a lower lava flow of the Vulcão Central volcanic sequence (GRZF1; VCU-d subunit) yielded a $^{40}Ar/^{39}Ar$ age of 865.6 ± 61.1 ka. This age is significantly older than that of the host lava (58.8 ± 19.2 ka) and suggests that the formation of the gabbro might be related to the Serra das Fontes - Serra Branca fractional crystallization process rather than to the

first volcanic stages of the Vulcão Central Unit. In addition, subalkaline gabbros, found for the first time in the Azores Islands occur within the Vitória Unit. Their origin appears to be related to fractionation of highly refractory melts at shallow depths (~ 3 km), although these melt compositions have not been identified within the Graciosa eruptive sequence.

6.7 Conclusions

In this work the magmatic evolution of Graciosa Island is investigated through a detailed study of the petrography, mineral chemistry, major and trace element geochemistry and Sr-Nd-Pb isotopic composition of the different magmatic products found in the island (lava flows and xenoliths). These data, together with the volcanostratigraphic sequence defined by Gaspar (1996) and the new $^{40}Ar/^{39}Ar$ ages in chapter 5, elucidate the processes of magmatic evolution through time beneath Graciosa.

Lava flows display porphyritic, microphorphytitic and trachytic textures based on the crystal size of their mineral assemblage. Mineral-melt equilibria show that most of them are phenocrysts in equilibrium with the host groundmass. Lava flows of the three volcanic complexes are related by polybaric fractional crystallization starting in a ~ 15 km deep magma chamber. Furthermore, the most evolved volcanic products (lavas and syenites) from Serra Branca and Vulcão Central units evolved by fractional crystallization in a shallower magma chamber (< 3 km). The alkaline xenoliths hosted in a Vulcão Central lava flow are magma chamber cumulates formed during fractional crystallization of basaltic magmas at crustal levels. Although subalkaline gabbros are also magma chamber cumulates, they appear to be related to the fractionation of a highly refractory melt that is not observed within the volcanic sequence of the island. The new Sr-Nd-Pb isotopic data resembles the compositions commonly found in the Azores and specifically, in the Terceira Rift. These isotopic compositions have been explained by source mixing between MORB and enriched HIMU mantle components, but they also resemble the composition of the redefined FOZO end-member component.

APPENDIX

Table I

Analytical procedures in the two different laboratories used for Graciosa Island whole rock analyses.

(1) IBERCRON laboratory, Universidad del País Vasco, Spain
(www.ikerkuntza.ehu.es)

http://tiny.cc/s8r05w

Samples were prepared by alkaline fusion with $LiBO_2$ in Pt-Au crucibles, followed by acid dissolution of the melt. The fusion process is as follows: 250 mg of sample and 500 mg of flux are put into the crucible with three to four drops of LiBr solution. The mixture is fused. The melted glass (in fact, dissolution of the mixture in the flux) is poured automatically onto a weighed polypropylene beaker containing 100 ml HNO_3 1N, with a few drops of HF to ensure stability of the HFSE. The acid solution is stirred ca. 10 min to ensure total dissolution. This primary solution is diluted gravimetrically to ca. 1:6500 in a mixture of HNO_3 0.32N and very diluted HF, and spiked with In (50 µg/m) and Bi (10 µg/m) standard solutions (see Mendinabeitia et al., 2008). The samples were run for major oxides and selected trace elements using a mass spectrometer with inductively-coupled plasma source (ICP-MS) X7 by Thermo Scientific updated to XSeries 2.

(2) LabGEOTOP laboratory, Institut de Ciències de la Terra Jaume Almera, Spain
(www.ija.csic.es)

http://tiny.cc/eds05w

Samples were prepared by acid digestion in closed environment; 100 mg of sample and 10 ml acid mixture of 5 ml of HF, 2.5 ml of HNO_3 and 2.5 ml of $HClO_4$ was added to a PFA EvapoCean® vessels. The vessels were then closed and heated at 135 ºC during 24 hours. After total dissolution of all samples, the vessels were cooled to room temperature. Each vessel was connected to a PFTE EvapoCean® elbow plus vessel and heated in the EvapoCean® heating block at 120 ºC overnight to evaporate and collect acids. The residue was dissolved in 1 ml of HNO_3 and brought to a final volume of 100 ml of MiliQ H_2O. Clear solutions were obtained in all cases. A procedural blank solution was also prepared. The samples were run for major oxides (excluding SiO_2 due to the digestion type) and selected trace elements using a high resolution mass spectrometer with inductively-coupled plasma source (HR-ICP-MS) Element XR byThermo Scientific.

Detection Limits of the analyzed elements:

Element	(1) IBERCRON	(2) LabGEOTOP
SiO_2	0.03 %	-
TiO_2	0.0003 %	0.001
Al_2O_3	0.083 %	0.006
$Fe_2O_3^T$	0.0033 %	0.006
MnO	0.0001 %	0.0001
MgO	0.0007 %	0.002
CaO	0.0107 %	0.004
Na_2O	0.0011 %	0.007
K_2O	0.0006 %	0.003
P_2O_5	0.0064 %	0.0003
Rb	0.716 ppm	0.444 ppm
Sr	0.088 ppm	1.282 ppm
Ba	0.08 ppm	7.634 ppm
Sc	0.243 ppm	0.04 ppm
V	1.072 ppm	0.412 ppm
Cr	20.052 ppm	0.321 ppm
Co	1.033 ppm	0.181 ppm
Ni	20.099 ppm	2.291 ppm
Cu	10.092 ppm	8.416 ppm
Zn	0.932 ppm	1.849 ppm
Y	0.04 ppm	0.061 ppm
Nb	1.056 ppm	0.089 ppm
Zr	1.084 ppm	0.246 ppm
Hf	0.103 ppm	0.005 ppm
Pb	-	0.683 ppm
U	0.006 ppm	0.012 ppm
Th	0.011 ppm	0.005 ppm
La	0.021 ppm	0.037 ppm
Ce	0.022 ppm	0.067 ppm
Pr	0.01 ppm	0.008 ppm
Nd	0.065 ppm	0.034 ppm
Sm	0.013 ppm	0.01 ppm
Eu	0.0001 ppm	0.007 ppm
Gd	0.012 ppm	0.013 ppm
Tb	0.0001 ppm	0.002 ppm
Dy	0.012 ppm	0.009 ppm
Ho	0.0001 ppm	0.002 ppm
Er	0.009 ppm	0.005 ppm
Tm	0.022 ppm	0.001 ppm
Yb	0.004 ppm	0.004 ppm
Lu	0.0001 ppm	0.002 ppm

Table II

Major (wt. %) and trace (ppm) element composition of the studied lavas and xenoliths from Graciosa Island.

Unit/Site	Serra das Fontes			Serra Branca		Vitória Unit		
Sample	GRZF8	GRZF28	GRZF29	GRZF13	GRZF20	GRZF2	GRZF3	GRZF4
	Lava	Lava	Lava	Lava	Lava	Lava	Lava	Lava
Texture	Microporph.	Microporph.	Microporph.	Trachytic	Trachytic	Microporph.	Microporph.	Porphyritic
Campaigne	1	2	2	2	2	1	1	1
wt. %								
SiO_2*	48.09	52.47*	50.84*	65.44	66.89*	48.80	48.84	47.28
TiO_2	3.99	3.78	3.58	0.47	0.57	2.58	2.61	2.42
Al_2O_3	15.57	14.54	15.61	16.57	15.19	16.05	15.81	15.32
$Fe_2O_3^T$	12.70	11.03	12.42	3.94	4.34	10.74	10.55	10.20
MnO	0.19	0.20	0.21	0.17	0.26	0.16	0.16	0.15
MgO	4.39	3.47	3.07	0.38	0.33	7.38	6.66	9.59
CaO	9.50	8.24	6.83	0.80	0.58	10.00	9.55	11.10
Na_2O	3.58	3.91	3.80	7.45	6.34	3.25	3.53	2.70
K_2O	1.44	1.41	1.30	4.56	4.93	1.21	1.33	0.83
P_2O_5	0.64	0.74	0.65	0.06	0.11	0.48	0.66	0.39
TOTAL	100.09	99.84	98.37	99.85	99.60	100.65	99.70	99.98
LOI	-0.28	0.16	1.62	0.28	0.40	-0.25	-0.55	-0.26
Mg#	27	25	21	9	7	43	41	51
(ppm)								
Rb	28	35	33	78	119	30	33	16
Sr	574	647	526	37	12	492	491	492
Ba	393	404	494	832	86	372	401	258
Sc	22	18	2	3	4	24	22	28
V	369	265	146	5	1	262	261	283
Cr	20	11	<DL	20	< DL	210	170	440
Co	30	28	18	1	< DL	33	31	39
Ni	20	< DL	< DL	20	0	80	60	140
Cu	40	39	34	10	< DL	30	30	40
Zn	110	102	187	110	127	80	90	70
Y	35.2	41.9	41.2	37.1	32.4	24.3	25.8	19.5
Nb	65	78	77	143	265	50	55	30
Zr	304	365	361	753	1315	212	236	141
Hf	7.0	8.7	7.5	16.0	29.8	4.8	5.4	3.3
Pb	-	2.4	2.9	8.0	6.4	-	-	-
U	1.38	1.70	1.29	1.59	5.26	1.13	1.26	0.61
Th	4.35	6.20	5.65	11.40	19.91	3.69	4.12	1.99
La	47.2	50.0	47.4	76.4	122.4	33.2	37.4	21.4
Ce	94.8	110.7	97.8	162.0	292.2	67.9	76.0	45.5
Pr	11.6	12.7	13.6	17.5	28.2	7.9	8.8	5.5
Nd	48.1	53.9	55.3	64.9	95.3	33.0	36.5	24.2
Sm	10.1	11.1	11.2	11.8	16.3	7.1	7.7	5.5
Eu	3.14	3.54	3.39	2.97	2.00	2.31	2.45	1.87
Gd	9.23	11.33	11.57	9.24	15.40	6.55	6.93	5.14
Tb	1.36	1.42	1.52	1.41	1.71	0.98	1.05	0.78
Dy	7.38	8.30	8.92	7.78	9.56	5.35	5.72	4.20
Ho	1.36	1.26	1.34	1.45	1.22	0.99	1.06	0.78
Er	3.67	3.72	3.99	4.04	3.79	2.65	2.83	2.10
Tm	0.49	0.61	0.61	0.58	0.67	0.36	0.39	0.29
Yb	3.00	3.76	3.51	3.91	4.56	2.23	2.40	1.79
Lu	0.43	0.56	0.52	0.66	0.67	0.34	0.36	0.27
Eu/Eu*	0.97	0.95	0.90	0.84	0.38	1.01	1.00	1.06
$^{87}Sr/^{86}Sr$	0.70358	-	-	-	0.70390	-	0.70336	-
$^{143}Nd/^{144}Nd$	0.512922	-	-	-	0.512883	-	0.512954	-
$^{206}Pb/^{204}Pb$	19.695	-	-	-	19.419	-	19.479	-
$^{207}Pb/^{204}Pb$	15.603	-	-	-	15.623	-	15.588	-
$^{208}Pb/^{204}Pb$	39.105	-	-	-	39.165	-	39.038	-

* Due to the analytical procedure of the samples analyzed in the LabGEOTOP laboratory (acid digestion; see Appendix - Table I), the SiO_2* content of these samples has been estimated as SiO_2 = 100 - Σ (total oxide content + LOI).
$Fe_2O_3^T$: total Fe expressed as Fe_2O_3; LOI: Loss On Ignition; < DL: below the detection limit.
Mg# = MgO/(FeO+MgO)·100 where FeO = 0.9·$Fe_2O_3^T$; Eu/Eu* = (Eu_N/((Eu_N+Gd_N)/2).
Microporph.: Microporphytitic; Orthocum.: Orthocumulate; Heteroadcum.: Heteroadcumulate; Equigran.: Equigranular; Inequigran.: Inequigranular; Alk. Gabbro: Alkaline gabbro; Subalk. Gabbro: Subalkaline gabbro.

Unit/Site	Vitória Unit							
Sample	GRZF9	GRZF10	GRZF11	GRZF12	GRZF17	GRZF21	GRZF22	GRZF23
	Lava	Lava	Lava	Lava	Lava	Lava	Lava	Lava
Texture	Microporph.	Microporph.	Microporph.	Porphyritic	Porphyritic	Microporph.	Porphyritic	Porphyritic
Campaigne	1	1	1	1	1	2	2	2
wt. %								
SiO_2*	47.50	47.25	48.16	47.81	46.92	48.98	50.12*	50.67*
TiO_2	2.97	2.94	3.06	2.45	2.55	2.84	2.81	2.92
Al_2O_3	15.48	15.29	15.62	14.04	15.19	15.80	14.39	14.31
$Fe_2O_3^T$	10.67	10.89	11.23	10.21	10.60	10.82	10.05	10.02
MnO	0.15	0.15	0.16	0.15	0.15	0.15	0.16	0.14
MgO	8.11	9.21	6.66	10.58	9.94	7.98	8.00	8.66
CaO	10.58	10.78	9.61	10.91	10.20	9.53	9.66	9.16
Na_2O	3.05	2.98	3.25	2.51	2.82	2.82	2.66	2.53
K_2O	0.97	0.89	1.16	1.00	0.95	0.81	0.89	0.68
P_2O_5	0.44	0.41	0.59	0.42	0.52	0.37	0.58	0.36
TOTAL	99.92	100.79	99.51	100.09	99.84	100.15	99.38	99.50
LOI	-0.01	-0.43	-0.07	-0.08	-0.06	-0.15	0.62	0.49
Mg#	45	48	39	53	51	45	46	48
(ppm)								
Rb	20	18	24	19	17	29	24	20
Sr	532	515	574	453	518	473	607	465
Ba	273	247	323	281	276	339	299	248
Sc	27	28	22	30	27	1	26	1
V	267	270	257	273	247	116	188	135
Cr	250	290	140	550	400	315	196	224
Co	38	41	35	42	42	27	43	30
Ni	100	130	60	200	140	139	126	161
Cu	40	40	30	60	30	40	46	43
Zn	80	80	110	80	70	118	80	128
Y	23.8	22.3	29.0	21.6	24.2	27.4	27.6	23.9
Nb	41	36	55	42	41	47	49	42
Zr	223	197	275	215	196	192	226	186
Hf	5.1	4.6	6.1	4.8	4.5	4.2	5.7	4.0
Pb	-	-	-	-	-	1.6	1.4	1.3
U	0.96	0.84	1.44	0.91	0.91	0.87	0.94	0.70
Th	2.96	2.56	3.82	2.92	3.13	3.38	3.52	2.57
La	29.1	26.2	39.2	27.6	27.9	27.9	31.2	23.3
Ce	62.5	57.1	83.6	59.2	59.6	58.7	70.5	50.3
Pr	7.6	7.0	10.1	7.1	7.2	7.4	8.6	6.7
Nd	33.0	30.3	42.9	30.3	30.9	29.8	37.0	27.1
Sm	7.2	6.8	9.0	6.4	6.9	6.7	7.8	5.7
Eu	2.35	2.20	2.85	2.06	2.22	2.04	2.66	1.79
Gd	6.50	6.21	8.30	5.79	6.83	6.84	7.74	5.69
Tb	0.96	0.92	1.20	0.86	1.03	0.90	0.97	0.79
Dy	5.19	4.91	6.39	4.64	5.47	5.39	5.62	4.62
Ho	0.94	0.89	1.16	0.84	0.98	0.82	0.83	0.69
Er	2.46	2.36	3.05	2.26	2.60	2.43	2.38	2.05
Tm	0.33	0.32	0.40	0.31	0.35	0.38	0.37	0.31
Yb	2.05	1.98	2.49	1.95	2.16	2.18	2.38	1.79
Lu	0.31	0.30	0.38	0.30	0.33	0.33	0.35	0.28
Eu/Eu*	1.03	1.01	0.99	1.01	0.97	0.91	1.03	0.95
$^{87}Sr/^{86}Sr$	-	-	-	-	-	-	0.70338	-
$^{143}Nd/^{144}Nd$	-	-	-	-	-	-	0.512945	-
$^{206}Pb/^{204}Pb$	-	-	-	-	-	-	19.633	-
$^{207}Pb/^{204}Pb$	-	-	-	-	-	-	15.592	-
$^{208}Pb/^{204}Pb$	-	-	-	-	-	-	39.131	-

Unit/Site	Vitória Unit							
Sample	GRZF24	GRZF25	GRZF26	GRZF27	GRZF30	GRZF31	GRZF32A	GRZF32B
	Lava	Lava	Lava	Lava	Lava	Lava	Lava	Lava
Texture	Porphyritic	Microporph.	Porphyritic	Porphyritic	Porphyritic	Microporph.	Porphyritic	Porphyritic
Campaigne	2	2	2	2	2	2	2	2
wt. %								
SiO_2*	47.54*	55.94*	50.09*	47.66*	48.81*	49.02*	46.18*	48.6*
TiO_2	2.60	2.44	2.76	2.97	3.04	3.10	3.28	3.22
Al_2O_3	16.13	13.31	15.52	14.42	13.59	14.17	14.56	13.55
$Fe_2O_3^T$	10.69	9.39	10.06	10.77	10.46	10.31	11.16	10.66
MnO	0.16	0.14	0.14	0.16	0.14	0.15	0.15	0.15
MgO	8.29	6.84	7.57	9.22	9.50	10.04	10.14	10.14
CaO	9.36	7.46	9.47	10.63	10.49	10.25	10.58	10.17
Na_2O	3.15	3.01	3.01	2.22	2.14	2.23	1.95	2.02
K_2O	0.87	0.93	0.80	0.53	0.70	0.58	0.43	0.51
P_2O_5	0.51	0.37	0.43	0.46	0.41	0.32	0.34	0.32
TOTAL	99.35	99.88	99.91	99.08	99.34	100.21	98.80	99.39
LOI	0.64	0.11	0.08	0.92	0.66	-0.21	1.19	0.60
Mg#	46	44	45	48	50	51	50	51
(ppm)								
Rb	25	32	22	8	16	12	7	12
Sr	565	492	558	616	629	470	514	497
Ba	349	399	284	270	252	245	270	258
Sc	2	1	1	31	31	1	1	1
V	120	174	201	317	402	142	117	160
Cr	258	275	245	322	166	375	366	471
Co	28	26	27	51	50	33	35	33
Ni	118	132	113	171	191	209	206	202
Cu	41	37	41	46	56	44	53	59
Zn	136	131	133	77	78	139	143	154
Y	29.5	27.8	26.5	25.2	24.8	23.6	26.4	25.7
Nb	46	52	45	44	44	39	41	42
Zr	232	261	200	209	220	169	198	188
Hf	4.9	5.3	4.3	5.5	5.6	4.1	4.3	4.2
Pb	1.9	2.1	0.9	1.2	1.5	1.3	1.2	1.8
U	0.92	1.09	0.83	0.64	0.78	0.51	0.50	1.63
Th	3.36	3.96	2.91	3.00	3.04	2.17	2.41	2.37
La	32.2	33.2	26.6	26.3	25.9	23.3	25.9	24.2
Ce	70.7	70.3	56.4	58.9	60.3	49.3	56.4	54.6
Pr	8.9	9.0	7.2	7.6	7.6	6.7	7.6	7.1
Nd	37.2	35.3	28.8	32.2	32.0	27.8	31.2	29.8
Sm	7.8	7.4	5.8	7.1	7.0	6.1	7.0	6.7
Eu	2.44	2.31	1.80	2.44	2.33	1.91	2.11	2.06
Gd	7.94	7.52	5.59	7.07	6.86	6.29	7.06	6.82
Tb	1.02	0.98	0.74	0.88	0.87	0.85	0.93	0.91
Dy	6.00	5.68	4.41	5.26	5.06	5.01	5.44	5.28
Ho	0.87	0.84	0.69	0.79	0.75	0.75	0.79	0.76
Er	2.57	2.54	2.06	2.20	2.16	2.19	2.37	2.28
Tm	0.39	0.38	0.32	0.35	0.35	0.33	0.35	0.33
Yb	2.28	2.25	1.98	2.17	2.15	1.93	2.04	2.00
Lu	0.34	0.35	0.31	0.31	0.32	0.29	0.30	0.29
Eu/Eu*	0.94	0.93	0.95	1.04	1.02	0.93	0.90	0.92
$^{87}Sr/^{86}Sr$	-	-	-	0.70340	-	-	-	-
$^{143}Nd/^{144}Nd$	-	-	-	0.512944	-	-	-	-
$^{206}Pb/^{204}Pb$	-	-	-	19.601	-	-	-	-
$^{207}Pb/^{204}Pb$	-	-	-	15.596	-	-	-	-
$^{208}Pb/^{204}Pb$	-	-	-	39.124	-	-	-	-

Unit/Site	Vitória Unit			Vulcão Central Unit				
Sample	GRZF33	GRZF34	GRZF35	GRZF1	GRZF5	GRZF6	GRZF7	GRZF14
	Lava	Lava	Lava	Lava	Lava	Lava	Lava	Lava
Texture	Porphyritic	Microporph.	Porphyritic	Porphyritic	Porphyritic	Microporph.	Porphyritic	Porphyritic
Campaigne	2	2	2	1	1	1	1	1
wt. %								
SiO_2*	47.76*	50.55*	49.25*	51.06	47.34	59.81	48.38	49.89
TiO_2	3.05	3.27	3.10	2.77	3.18	1.01	2.42	2.38
Al_2O_3	14.39	15.11	13.73	17.12	16.60	17.47	16.61	16.65
$Fe_2O_3^T$	10.95	11.35	10.32	10.61	10.33	6.08	9.72	9.96
MnO	0.16	0.16	0.15	0.17	0.14	0.15	0.14	0.16
MgO	9.69	6.56	9.22	4.17	7.01	1.15	6.87	6.08
CaO	10.70	9.16	10.45	8.14	10.70	3.22	10.45	9.06
Na_2O	2.19	2.94	2.15	4.22	3.03	6.22	3.18	3.64
K_2O	0.60	0.84	0.69	1.61	1.03	3.41	1.03	1.25
P_2O_5	0.34	0.48	0.41	0.55	0.46	0.31	0.40	0.56
TOTAL	99.86	100.48	99.52	100.42	99.83	98.84	99.21	99.63
LOI	0.13	-0.48	0.48	-0.06	0.77	0.42	-0.15	-0.27
Mg#	49	39	49	30	42	17	43	40
(ppm)								
Rb	14	26	14	31	19	81	19	27
Sr	520	577	568	542	600	307	527	547
Ba	259	336	271	452	297	794	310	380
Sc	1	2	33	19	24	5	24	20
V	161	139	250	253	287	30	265	230
Cr	334	130	370	< DL	160	< DL	190	120
Co	33	27	48	23	35	4	34	28
Ni	193	76	180	< DL	70	< DL	70	60
Cu	53	35	57	20	30	< DL	30	20
Zn	142	162	70	100	80	90	80	80
Y	26.7	32.0	25.9	28.9	22.9	31.9	20.6	24.8
Nb	39	59	45	52	43	82	36	41
Zr	189	265	220	272	210	452	169	194
Hf	4.1	5.8	5.7	6.3	4.8	9.8	4.0	4.5
Pb	1.5	1.9	1.4	-	-	-	-	-
U	0.61	1.19	0.58	1.08	0.84	2.50	0.76	1.04
Th	2.41	3.71	3.03	3.82	2.85	9.13	2.47	3.23
La	25.3	38.2	27.7	37.8	30.3	57.1	25.4	31.5
Ce	54.6	81.2	62.0	78.1	64.3	105.0	53.5	64.6
Pr	7.3	10.4	7.8	9.1	7.7	11.6	6.4	7.7
Nd	29.5	42.8	33.3	38.8	33.3	43.9	27.5	33.1
Sm	6.8	9.1	7.2	8.3	7.1	8.3	6.0	7.1
Eu	2.04	2.73	2.42	2.70	2.32	2.50	2.06	2.45
Gd	6.77	9.22	7.33	7.61	6.47	7.19	5.58	6.67
Tb	0.89	1.19	0.92	1.15	0.96	1.12	0.84	1.01
Dy	5.13	6.89	5.30	6.37	5.12	6.45	4.53	5.35
Ho	0.78	1.01	0.79	1.18	0.94	1.23	0.83	0.97
Er	2.28	3.02	2.26	3.14	2.49	3.49	2.22	2.58
Tm	0.34	0.45	0.35	0.43	0.33	0.51	0.30	0.35
Yb	1.99	2.57	2.16	2.76	2.00	3.48	1.83	2.22
Lu	0.30	0.38	0.32	0.43	0.30	0.56	0.27	0.35
Eu/Eu*	0.91	0.90	1.00	1.01	1.02	0.96	1.07	1.07
$^{87}Sr/^{86}Sr$	-	-	-	0.70343	-	-	-	0.70341
$^{143}Nd/^{144}Nd$	-	-	-	0.512926	-	-	-	0.512957
$^{206}Pb/^{204}Pb$	-	-	-	20.096	-	-	-	20.090
$^{207}Pb/^{204}Pb$	-	-	-	15.659	-	-	-	15.626
$^{208}Pb/^{204}Pb$	-	-	-	39.520	-	-	-	39.426

Unit / Site	Vulcão Central Unit					Baía da Folga		
Sample	GRZF15	GRZF16	GRZF18	GRZF19	GRZF36	GRZF 1x1	GRZF 1x2	GRZF 1x5
	Lava	Lava	Lava	Lava	Lava	Alk. gabbro	Alk. gabbro	Alk. gabbro
Texture	Porphyritic	Microporph.	Porphyritic	Porphyritic	Microporph.	Heteroadcum.	Heteroadcum.	Orthocum.
Campaigne	1	2	2	2	2	1	1	1
wt. %								
SiO_2*	48.93	57.12	49.68*	48.33*	55.74*	44.85	41.80	44.93
TiO_2	2.37	1.58	2.91	3.56	2.45	2.35	3.84	3.75
Al_2O_3	16.11	16.47	17.65	16.21	14.91	17.14	13.14	21.01
$Fe_2O_3^T$	10.31	6.96	10.05	10.12	9.35	9.73	14.54	9.32
MnO	0.16	0.14	0.16	0.15	0.19	0.19	0.29	0.08
MgO	6.97	2.97	3.89	7.04	2.81	7.25	10.48	3.38
CaO	9.43	5.36	9.15	10.46	6.60	10.83	10.82	13.29
Na_2O	3.45	4.59	3.88	2.98	4.78	3.55	2.51	2.96
K_2O	1.10	2.59	1.27	0.97	1.89	0.53	0.46	0.34
P_2O_5	0.52	0.37	0.74	0.47	1.05	0.58	0.56	0.62
TOTAL	99.36	98.15	99.43	100.34	99.82	97.04	98.47	99.71
LOI	-0.31	0.33	0.57	-0.34	0.18	0.14	0.31	0.01
Mg#	42	32	30	43	25	45	44	28
(ppm)								
Rb	24	74	31	26	49	12	10	12
Sr	527	348	653	627	598	670	488	833
Ba	342	493	400	296	536	358	281	186
Sc	22	10	19	26	15	18	15	15
V	241	119	144	239	112	200	246	304
Cr	140	50	17	147	< DL	125	140	< DL
Co	33	16	27	42	16	30	35	20
Ni	80	20	23	105	< DL	91	101	< DL
Cu	20	10	42	45	23	35	36	30
Zn	90	90	83	86	106	118	157	117
Y	23.9	26.8	32.7	25.5	44.7	40.4	44.2	15.4
Nb	37	74	55	49	78	48	51	15
Zr	176	390	256	239	357	112	122	71
Hf	4.2	8.7	6.3	5.9	8.7	3.3	3.6	1.8
Pb	-	6.0	2.2	1.4	2.7	-	-	-
U	0.87	3.35	1.22	0.98	1.80	0.26	0.20	0.29
Th	2.76	10.40	4.40	3.17	6.30	0.95	0.80	1.13
La	28.4	51.5	36.6	30.5	53.5	31.2	25.7	14.4
Ce	59.6	95.0	82.2	66.6	115.8	73.3	65.2	32.1
Pr	7.2	9.9	10.0	8.0	13.6	10.6	10.0	4.1
Nd	30.9	36.6	41.6	33.8	59.9	44.9	45.4	18.7
Sm	6.8	7.0	8.7	7.0	12.5	9.9	10.9	4.2
Eu	2.38	2.00	2.96	2.47	3.99	3.19	3.32	1.56
Gd	6.39	6.19	8.68	7.10	12.52	8.65	9.49	3.60
Tb	0.95	0.94	1.12	0.91	1.53	1.43	1.60	0.55
Dy	5.11	5.20	6.34	5.14	8.83	8.01	9.02	3.16
Ho	0.92	0.98	0.99	0.77	1.36	1.47	1.64	0.56
Er	2.48	2.80	2.84	2.24	3.90	3.83	4.23	1.37
Tm	0.34	0.40	0.46	0.37	0.64	0.52	0.55	0.18
Yb	2.11	2.77	2.80	2.24	3.93	3.04	3.25	1.04
Lu	0.32	0.45	0.42	0.33	0.59	0.42	0.45	0.14
Eu/Eu*	1.08	0.91	1.02	1.05	0.96	1.03	0.97	1.19
$^{87}Sr/^{86}Sr$	-	0.70337	-	0.70341	-	0.70340	-	-
$^{143}Nd/^{144}Nd$	-	0.512964	-	0.512937	-	0.512957	-	-
$^{206}Pb/^{204}Pb$	-	19.863	-	19.863	-	20.008	-	-
$^{207}Pb/^{204}Pb$	-	15.608	-	15.611	-	15.610	-	-
$^{208}Pb/^{204}Pb$	-	39.234	-	39.270	-	39.341	-	-

Unit / Site	Baía da Folga							Enxudreiro
Sample	GRZF 1x6	GRZF 1x8	GRZF 1x10	GRZF 1x13	GRZF1X19	GRZF1X22	GRZF1X24	GRENX-1
	Alk. gabbro	Alk. gabbro	Alk. gabbro	Alk. gabbro	Alk. gabbro	Alk. gabbro	Alk. gabbro	Syenite
Texture	Orthocum.	Orthocum.	Orthocum.	Orthocum.	Orthocum.	Orthocum.	Orthocum.	Inequigran.
Campaigne	1	1	1	1	2	2	2	2
wt. %								
SiO_2*	47.32	42.55	46.36	42.39	40.6*	37.15*	44.77*	69.63*
TiO_2	1.07	5.14	2.39	4.69	4.12	5.92	3.09	0.36
Al_2O_3	16.69	15.16	17.78	16.73	17.76	14.29	22.15	14.12
$Fe_2O_3^T$	9.43	12.59	9.66	13.33	19.04	17.18	9.98	2.82
MnO	0.11	0.17	0.12	0.13	0.15	0.16	0.09	0.10
MgO	6.74	6.64	3.87	7.70	5.22	11.70	4.35	0.31
CaO	15.00	10.97	13.05	9.36	10.11	10.71	12.24	1.55
Na_2O	2.15	2.69	3.23	2.93	2.69	2.40	2.86	6.68
K_2O	0.47	0.45	0.29	0.52	0.41	0.47	0.18	3.74
P_2O_5	0.03	4.57	1.97	0.27	0.12	0.10	0.08	0.09
TOTAL	99.03	100.95	98.73	98.08	100.26	100.14	99.84	99.47
LOI	0.37	1.39	0.36	0.54	-0.26	-0.14	0.15	0.53
Mg#	44	36	30	39	23	43	32	11
(ppm)								
Rb	9	12	14	11	8	5	1	85
Sr	762	704	894	611	615	475	912	184
Ba	152	282	249	239	178	229	129	651
Sc	16	17	17	17	< DL	< DL	< DL	< DL
V	321	355	239	390	487	430	186	3
Cr	66	< DL	< DL	< DL	< DL	< DL	72	< DL
Co	28	33	18	38	35	39	19	2
Ni	30	< DL	< DL	< DL	< DL	< DL	23	< DL
Cu	37	43	23	48	51	60	29	< DL
Zn	112	170	122	165	196	238	123	58
Y	16.1	51.2	32.1	27.4	17.4	34.8	8.5	18.0
Nb	9	48	27	33	19	29	11	100
Zr	51	135	106	105	76	90	37	36
Hf	1.6	3.6	2.6	2.9	2.0	2.7	1.0	1.0
Pb	-	-	-	-	0.8	1.2	< DL	3.7
U	0.11	0.48	0.58	0.33	0.20	0.13	0.09	3.27
Th	0.43	1.75	1.79	1.07	0.82	0.50	0.12	15.94
La	6.1	40.4	32.4	13.8	9.9	9.9	5.0	54.9
Ce	17.3	92.8	71.3	34.7	21.7	27.4	11.4	108.5
Pr	2.2	14.0	10.2	5.1	3.1	4.6	1.6	9.5
Nd	12.2	61.3	44.4	24.1	14.6	25.1	7.9	30.3
Sm	3.4	13.4	9.3	6.2	3.8	7.7	2.2	4.7
Eu	1.39	3.79	3.03	2.04	1.38	2.46	1.13	1.27
Gd	3.12	11.87	8.10	5.55	3.65	7.32	2.11	5.38
Tb	0.53	1.90	1.24	0.96	0.55	1.16	0.31	0.58
Dy	3.26	10.25	6.50	5.51	3.22	6.79	1.85	3.55
Ho	0.58	1.86	1.17	1.01	0.52	1.09	0.29	0.53
Er	1.42	4.68	2.87	2.55	1.43	2.86	0.80	1.70
Tm	0.19	0.60	0.35	0.34	0.22	0.43	0.12	0.31
Yb	1.13	3.46	2.09	2.00	1.24	2.26	0.65	1.96
Lu	0.15	0.47	0.29	0.28	0.18	0.33	0.09	0.27
Eu/Eu*	1.27	0.90	1.04	1.04	1.11	0.99	1.58	0.76
$^{87}Sr/^{86}Sr$	0.70338	-	-	-	-	-	-	-
$^{143}Nd/^{144}Nd$	0.512966	-	-	-	-	-	-	-
$^{206}Pb/^{204}Pb$	20.032	-	-	-	-	-	-	-
$^{207}Pb/^{204}Pb$	15.621	-	-	-	-	-	-	-
$^{208}Pb/^{204}Pb$	39.393	-	-	-	-	-	-	-

Unit/Site	Enxudreiro	Ponta Pesqueira					Quitadouro	
Sample	GRENX-2	GRZF17A	GRZF17B	GRZF17D	GRZF17C	GRZF17E	GRQUX1	GRQUX3
Texture	Syenite Inequigran.	Subalk. gabbro Inequigran.	Subalk. gabbro Inequigran.	Subalk. gabbro Inequigran.	Alk. gabbro Inequigran.	Alk. gabbro Orthocum.	Dunite Equigran.	Subalk. gabbro Inequigran.
Campaigne	2	1	2	2	2	2	2	2
wt. %								
SiO_2*	71.3*	49.1*	49.03*	50.61*	39.4*	45.3*	49.63*	45.01*
TiO_2	0.19	0.27	0.26	0.11	7.16	4.36	0.05	0.35
Al_2O_3	15.80	17.36	18.51	23.05	15.41	16.29	0.82	9.02
$Fe_2O_3^T$	2.44	4.17	4.07	1.83	15.89	11.08	9.35	8.12
MnO	0.06	0.07	0.07	0.04	0.16	0.12	0.14	0.13
MgO	0.15	12.52	8.67	5.68	6.90	6.87	39.31	21.80
CaO	0.86	14.80	17.36	15.67	13.13	13.07	0.81	15.03
Na_2O	5.63	0.98	1.45	1.60	1.53	1.90	0.03	0.48
K_2O	3.37	0.04	0.07	0.08	0.12	0.15	0.02	0.03
P_2O_5	0.04	‹LD	0.01	0.01	0.04	0.05	0.01	0.03
TOTAL	99.88	99.32	99.54	98.73	99.79	99.25	100.20	100.06
LOI	0.11	0.48	0.46	1.27	0.21	0.75	-0.20	-0.06
Mg#	6	76	70	77	32	40	82	74
(ppm)								
Rb	104	1	‹LD	‹LD	2	2	‹LD	‹LD
Sr	70	230	297	309	728	761	2	110
Ba	279	25	12	24	65	91	3	13
Sc	< DL	15	49	26	42	32	13	< DL
V	1	123	83	89	915	211	63	121
Cr	< DL	1029	227	170	< DL	327	4122	1048
Co	< DL	30	31	22	59	46	114	51
Ni	< DL	213	52	64	20	113	1524	347
Cu	‹LD	40	37	< DL	68	57	25	20
Zn	27	25	19	16	81	57	48	39
Y	28.1	6.4	4.8	2.2	13.1	11.5	0.6	5.4
Nb	136	< DL	2	1	18	18	< DL	1
Zr	24	19	8	8	86	77	3	14
Hf	0.8	0.6	0.3	0.2	2.8	2.4	< DL	0.4
Pb	2.7	-	0.7	0.7	0.8	‹LD	-	‹LD
U	3.90	0.05	0.15	0.15	0.15	0.13	-	0.02
Th	21.83	0.35	0.49	0.32	0.39	0.43	-	0.08
La	89.2	1.7	1.4	1.4	6.2	8.1	0.6	1.4
Ce	154.8	5.8	3.3	3.0	15.2	15.6	1.0	4.0
Pr	14.9	0.3	0.4	0.3	2.2	2.4	0.1	0.5
Nd	46.3	2.4	2.1	1.3	11.0	11.6	0.6	2.7
Sm	7.1	0.8	0.7	0.3	3.1	2.9	0.1	0.8
Eu	0.58	0.34	0.38	0.28	1.26	1.32	0.05	0.27
Gd	8.76	0.60	0.79	0.40	3.09	2.98	0.14	0.84
Tb	0.94	0.14	0.13	0.06	0.44	0.39	0.02	0.14
Dy	5.53	1.14	0.85	0.40	2.54	2.30	0.12	0.91
Ho	0.78	0.22	0.15	0.07	0.41	0.35	0.02	0.16
Er	2.52	0.49	0.42	0.19	1.08	0.97	0.07	0.46
Tm	0.40	0.08	0.07	0.03	0.17	0.15	0.02	0.07
Yb	2.39	0.51	0.45	0.21	1.05	0.94	0.11	0.44
Lu	0.34	0.07	0.06	0.03	0.15	0.14	0.02	0.07
Eu/Eu*	0.23	1.42	1.54	2.31	1.23	1.35	1.11	0.98
$^{87}Sr/^{86}Sr$	-	-	0.70356	-	0.70338	-	0.70351	-
$^{143}Nd/^{144}Nd$	-	-	0.513011	-	0.512947	-	0.512946	-
$^{206}Pb/^{204}Pb$	-	-	19.513	-	18.710	-	19.706	-
$^{207}Pb/^{204}Pb$	-	-	15.595	-	15.597	-	15.598	-
$^{208}Pb/^{204}Pb$	-	-	38.981	-	38.424	-	39.142	-

Unit / Site	Quitadouro		
Sample	GRQUX4 Subalk. gabbro	GRQUX5 Subalk. gabbro	GRQUX7 Subalk. gabbro
Texture	Inequigran.	Inequigran.	Inequigran.
Campaigne	2	2	2
wt. %			
SiO_2*	48.88*	49.3*	46.26*
TiO_2	0.14	0.28	0.25
Al_2O_3	13.07	22.47	16.21
$Fe_2O_3^T$	6.39	2.70	6.28
MnO	0.10	0.04	0.09
MgO	17.03	5.91	14.76
CaO	13.16	17.33	15.17
Na_2O	1.03	1.47	0.94
K_2O	0.07	0.04	0.05
P_2O_5	0.01	0.01	0.04
TOTAL	99.93	99.60	100.10
LOI	0.07	0.40	-0.10
Mg#	74	70	72
(ppm)			
Rb	1	‹LD	‹LD
Sr	148	342	183
Ba	23	21	13
Sc	32	33	< DL
V	66	49	63
Cr	953	325	1015
Co	64	19	33
Ni	320	77	225
Cu	35	16	17
Zn	39	19	34
Y	3.2	4.8	3.9
Nb	2	< DL	1
Zr	17	9	8
Hf	0.4	0.3	0.2
Pb	0.7	‹LD	‹LD
U	0.15	‹LD	0.02
Th	0.53	0.03	0.06
La	2.0	1.3	0.9
Ce	3.9	3.4	2.4
Pr	0.4	0.4	0.3
Nd	1.5	2.4	1.9
Sm	0.4	0.7	0.6
Eu	0.24	0.47	0.28
Gd	0.51	0.80	0.67
Tb	0.09	0.13	0.12
Dy	0.55	0.85	0.77
Ho	0.10	0.15	0.13
Er	0.29	0.40	0.39
Tm	0.05	0.07	0.06
Yb	0.32	0.43	0.36
Lu	0.05	0.06	0.05
Eu/Eu*	1.56	1.85	1.34
$^{87}Sr/^{86}Sr$	0.70378	-	-
$^{143}Nd/^{144}Nd$	0.512945	-	-
$^{206}Pb/^{204}Pb$	19.860	-	-
$^{207}Pb/^{204}Pb$	15.622	-	-
$^{208}Pb/^{204}Pb$	39.290	-	-

PART III: STUDY OF CORVO ISLAND

CHAPTER 7: CORVO ISLAND: A REVIEW

7.1 Geographic, geomorphologic and geotectonic setting

Corvo Island, in Portuguese the Island of the Crow, is the northernmost island of the Azores archipelago. It is located in the Atlantic Ocean between 39º 40' and 39º 44' N latitude and 31º 05' and 31º 08' W longitude. Together with the island of Flores, sited 17.9 km to the south, Corvo belongs to the Western Group of islands. These islands are situated on the American Plate, which is separated from the Eurasian and African plates by the Mid-Atlantic Ridge (Fig. 7.1).

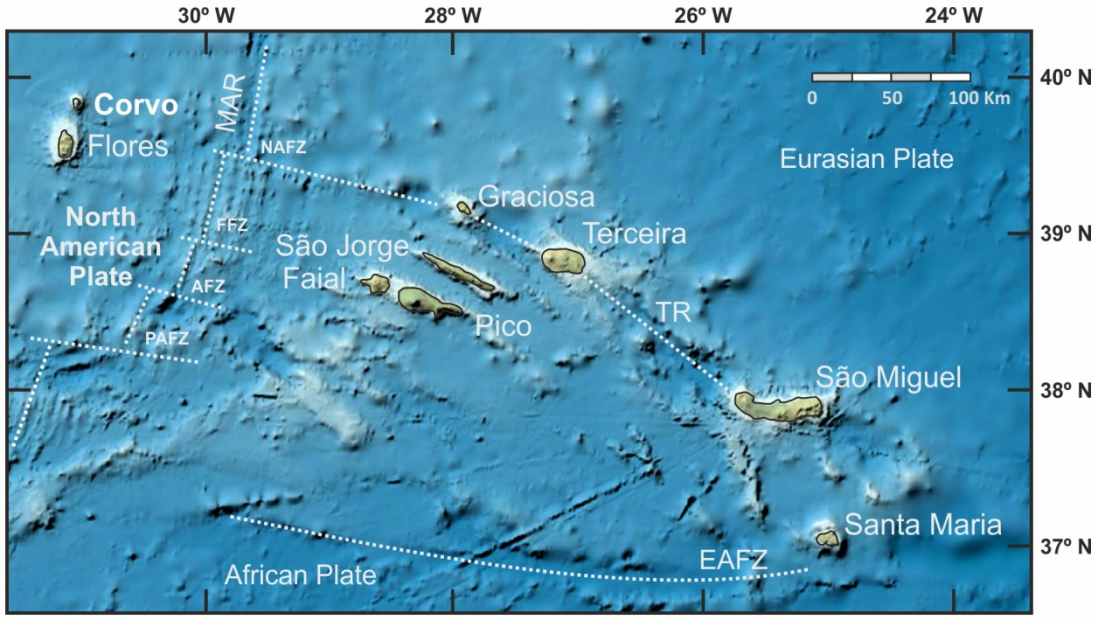

Fig. 7.1 - Location of Corvo Island within the Azores archipelago and general geotectonic setting of the studied area modified after the GEBCO world map 2013 (www.gebco.net). EAFZ: East Azores Fracture Zone; TR: Terceira Rift; MAR: Mid.Atlantic Ridge; NAFZ: North Azores Fracture Zone; FFZ: Faial Fracture Zone; AFZ: Açor Fracture Zone; PAFZ: Princess Alice Fracture Zone..

Corvo is the smallest island of the Azorean archipelago. It is up to 6 km long and 4 km wide, has an area of just 17.12 km² and approximately 425 inhabitants. The highest point of the island is located in the area known as *Estreitinho* at an altitude of 720 m (Forjaz et al., 2004).

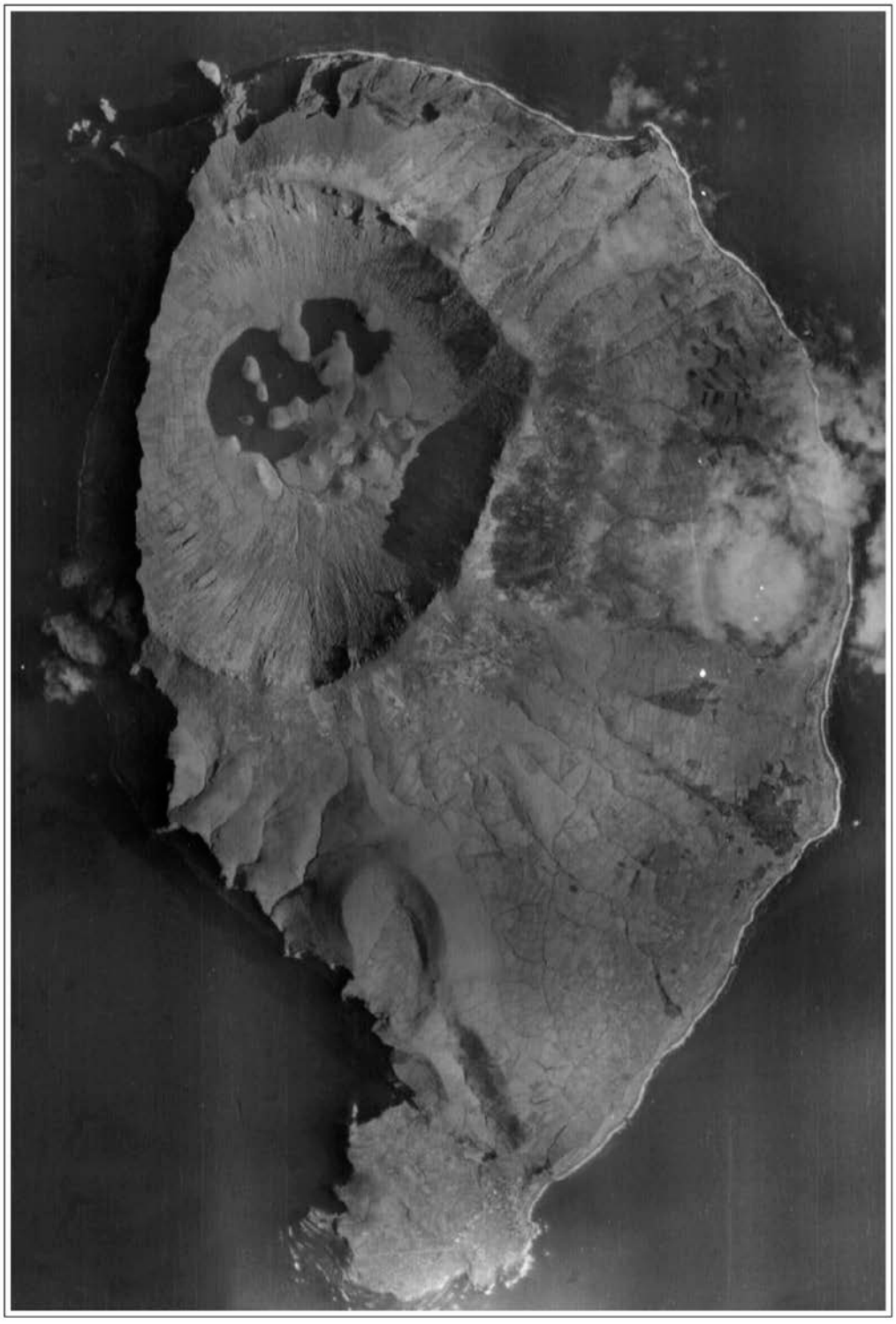

Fig. 7.2 - Aerial photo of Corvo Island by the US Air Force.

The island has an oval shape with a N-S elongated morphology (Fig. 7.2). The caldera centered on the north side of the island, locally known as *O Caldeirão* (Fig. 7.3), is the most prominent feature of Corvo landscape, comprising the 90 % of the island total surface area. This volcanic caldera has an elliptical shape, with a maximum diameter of 2.3 km and a depth of 300 m. Inside the caldera are several cinder and spatter cones (20 - 30 m in height) giving rise to small lakes, peat bogs and islets.

Fig. 7.3 - Corvo Island "*O Caldeirão*" showing the caldera arc, some dikes and the intracaldera cones, lakes, peat bogs and islets.

The island shows abrupt, high and steep cliffs (Fig. 7.4A-B), especially in the north, eastern and western coasts due to the strong wave erosion together with tectonic processes. These processes caused occasional landslides, which uncovered many basaltic dikes that cut the oldests volcanic units (Fig. 7.4A).

The southern part of the island is characterized by a flat platform, known as *fajã*, where the single town within the island is located (*Vila Nova do Corvo*; Fig. 7.4C). This *fajã* was formed by at least two lava flows from a secondary cone located on the caldera southern flank (França et al., 2002).

Volcanotectonic studies of Corvo (Dias, 2001) and Flores (Azevedo and Ferreira, 1999, 2006) Islands showed that the main structural direction (WNW-ESE) observed throughout the eastern islands of the Azores archipelago are not dominant in these western islands. Azevedo and Ferreira (2006) proposed that Flores and Corvo Islands are the emerged tops of a single larger edifice, built on a 10 Ma oceanic crust (Luis et al., 1994). Their N-S elongated shapes and their tectonic setting suggest an

Fig. 7.4 - Photographs of Corvo Island: (a) western coast, (b) eastern coast and (c) the *fajã* and *Vila Nova do Corvo* town.

evolution linked to the Mid-Atlantic Ridge (Azevedo and Ferreira, 1999, 2006; França et al., 2006*a*). Moreover, the westward displacement of Corvo from Flores at about 1 cm/year, together with the near-linear E-W northern and southern coastlines of Flores, reflect the structural control of the Mid-Atlantic Ridge and associated transform faults (Baptista et al., 1999).

7.2 History and previous studies

A non-official exploration during the period of the late 13th century mentioned obscure islands within the Atlantic Ocean. As a result of this first exploration, maps such as the *Genoves Atlas Medici* (1351) were published, and the first reference to an *Insula Corvi Marini* (island of the Marine Crow) in a seven island archipelago appeared. Later, on the *Atlas Catalán* of 1375 the Islands of Corvo and Flores were also named as the *Insula Corvi Marini*. The first sighting of Corvo Island by a Portuguese navigator (Diogo de Teive) might have occurred in 1452. Given its small size, this island was not occupied till the 16th century when a group of slaves from Cape Verde were sent to Corvo to farm the land and breed cattle. A permanent settlement was not possible until 1580, when some settlers from Flores increased the number of inhabitants.

The first geological work published on Corvo Island was the geological map (Zbyszewski et al., 1967) edited by the Portuguese Geological Survey. This map was the result of the first fieldwork campaign on the island led by Prof. Zbyszewski during the 60's, when five volcanic units were proposed for the evolution of the island.

At the beginning of the 21st century, earth scientists carried out a new field campaign on Corvo Island in order to publish the 1:10,000 geological map, together with a geomorphologic and neotectonic characterization of the island. These studies led to the establishment of a new volcanostratigraphical sequence (Dias, 2001; Azevedo et al., 2003). Concurrently, a Portuguese research team guided by Dr. Zilda França proposed a straightforward volcanostratigraphic succession based on the caldera-formation event (França et al., 2002), which in contrast to what was previously published (see section 7.3).

Scarce studies deal with the magmatic processes related to the evolution of Corvo Island. A few contributions focus on geochemical and isotopic data (França et al., 2003, 2006*a*) and anisotropy of magnetic susceptibility magma flow directions (AMS; Pueyo et al., 2006). In addition, there are some papers that focus on other Azorean Islands but compare the data with those from Corvo (White et al., 1976; White et al., 1979; Lemarchand, 1987; Beier et al., 2010). Recently, Genske (2012) studied the western Azores mantle source including Corvo and Flores Islands and using Sr-Nd-Pb-Hf-Os isotope systematic. These authors incorporated their new results within a broader assessment of the mantle source across the plateau. The present PhD Thesis represents the first in-depth investigation of magmatic processes based on petrology, mineralogy and major and trace element data (Larrea et al., 2012; chapter 8).

7.3 Volcanostratigraphy

The volcanostratigraphy of Corvo has been studied by previous authors (Dias, 2001; França et al., 2002; Azevedo et al., 2003). These authors proposed two different volcanostratigraphic successions based on different criteria. Dias (2001) and Azevedo et

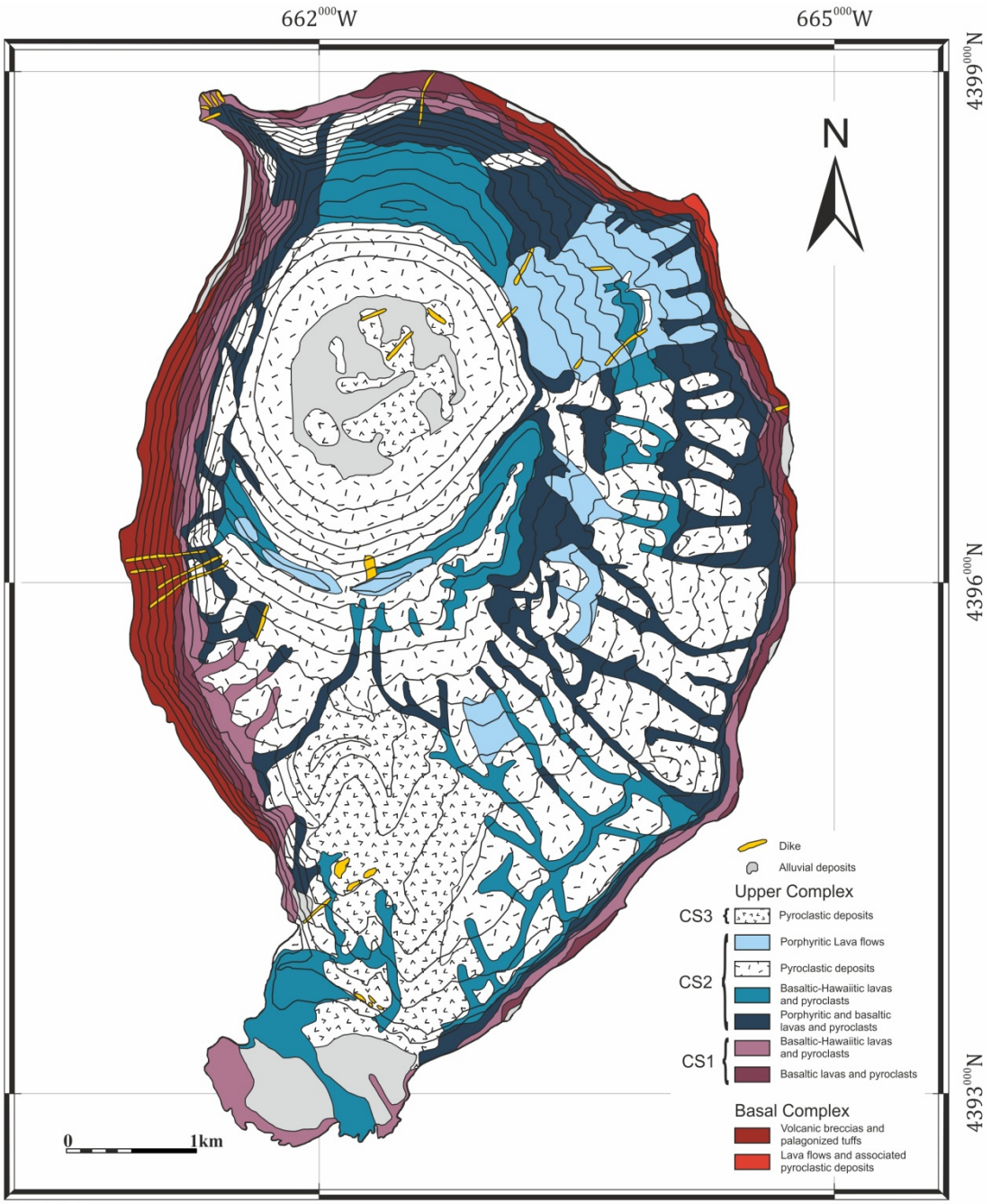

Fig. 7.5 - Geological map of Corvo Island modified from Dias (2001). Contour interval: 50 m.

al. (2003) followed the same criteria used for the establishment of the volcanostratigraphy of Flores island (e.g., Azevedo, 1998; Azevedo et al., 2006), which is mainly based on petrologic criteria. They recognized two main volcanic complexes on the island (Fig. 7.5): a) the Basal Complex (CB) associated to submarine volcanism and the formation of the proto-island, which comprises lava flows and associated pyroclasts, breccias and palagonized tuffs, and b) The Upper Complex (CS) formed by subaerial

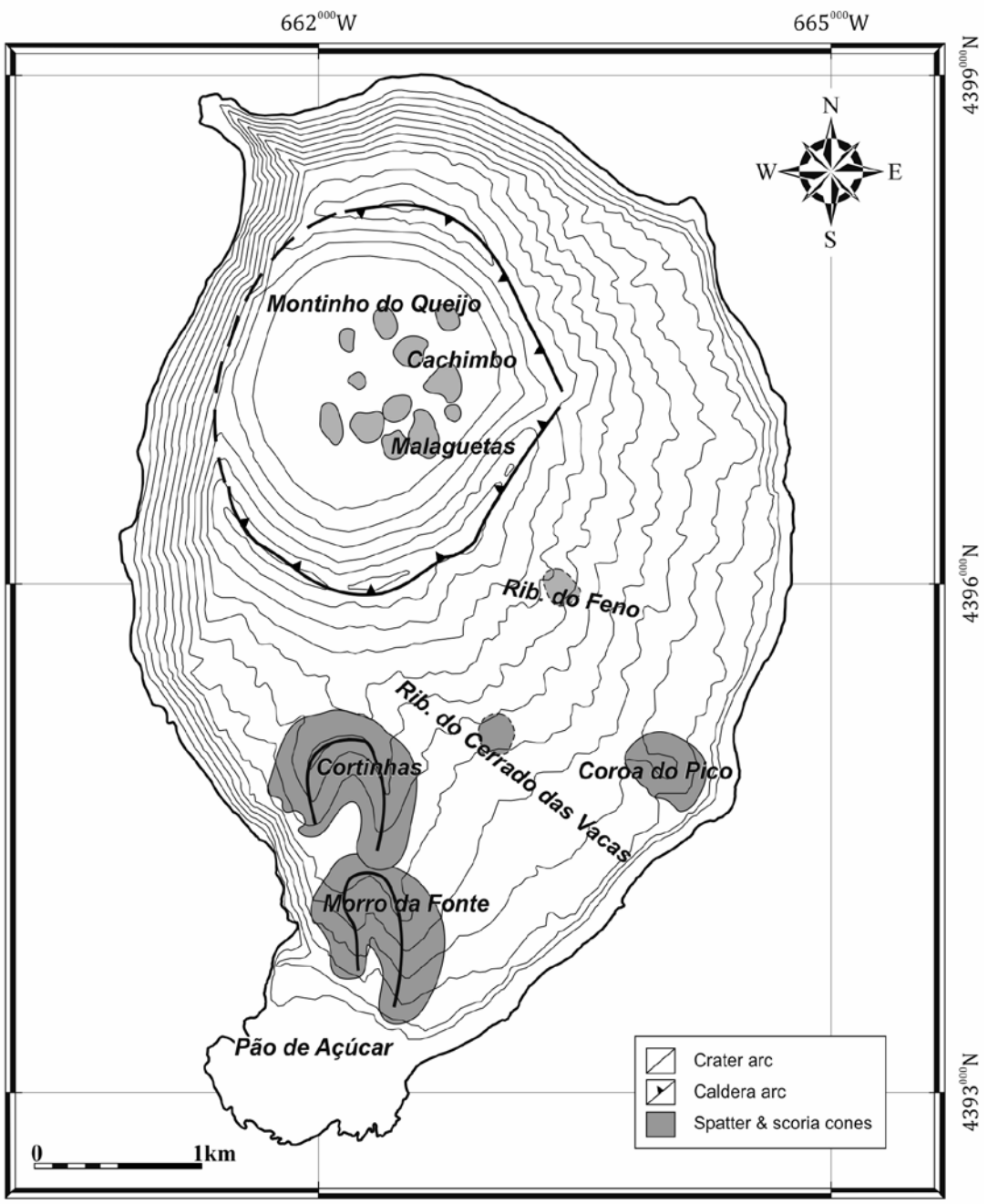

Fig. 7.6 - Morpho-volcanic scheme of Corvo Island modified from França et al. (2002). Contour interval: 50 m.

volcanism and divided into three volcanic units - lower (CS1), intermediate (CS2), and upper (CS3) units. The lower (CS1) and intermediate (CS2) units comprise basaltic and hawaiitic lava flows and associated pyroclasts, with major presence of pyroclasts in the CS2 unit. The upper unit (CS3) is entirely formed by pyroclastic deposits covering most of the total surface area of the island. Moreover, these authors dated three samples by K/Ar ages in order to obtain the ages of the different units. However, only two of the

samples yielded reliable age results according to field observations (Dias, 2001); 0.71 ± 0.49 Ma for the upper part of the CS1 unit and 0.43 ± 0.34 Ma for the lower part of the CS2 unit.

In contrast, França et al. (2002) proposed a straightforward volcanostratigraphic succession based on the caldera-formation event that includes three main units: (1) Pre-caldera, (2) Syn-caldera, and (3) Post-caldera units (Fig. 7.6).

The Pre-caldera unit (1) is formed by submarine volcanism (proto-island) (1a) followed by two subaerial phases divided into the Lower (1b) and Upper (1c) subunits. The submarine volcanism (1a) is represented by hydromagmatic deposits of submarine pyroclasts exposed in the SW and N cliffs. The Lower unit (1b) comprises a sequence of *pahoehoe* and *aa* lava flows that crop out mainly in the oriental cliff of the island; this sequence includes a primitive shield volcano, strombolian deposits, the upper lava flows (Fig 7.7) and the associated dikes. The Upper unit (1c) comprises secondary cones (*Coroa do Pico* and *Morro da Fonte*), buried cones (*Ribeira do Feno* and *Ribeira do Cerrado das Vacas*) and their related lava flows.

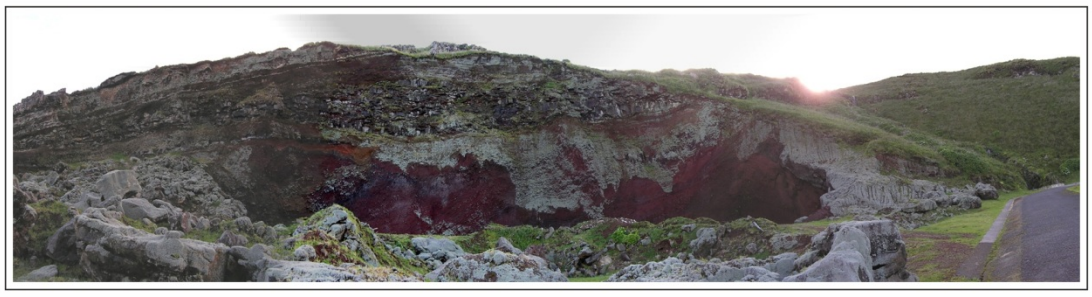

Fig. 7.7 - Pre-caldera Upper unit (1c): lava flows and associated pyroclastic deposits from Ribeira do Feno quarry.

The Syn-caldera unit (2) includes plinian to sub-plinian pumiceous deposits (Fig. 7.8), lahars, surges and other pyroclastic flows associated with the stratovolcano collapse and the caldera formation.

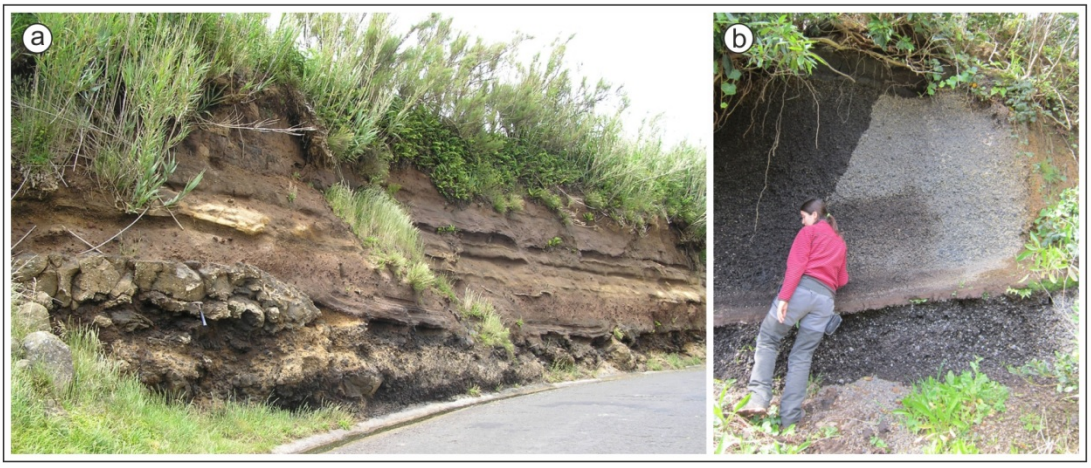

Fig. 7.8 - Syn-caldera unit (2): (a) Fine-grained pyroclastic deposits and (b) pumitic deposit associated to the stratovolcano collapse and the caldera formation event.

The Post-caldera unit (3) comprises the most recent lava flow (*Pão de Açúcar*; Fig. 7.9), the intracaldera pyroclastic and spatter cones (e.g., *Montinho do Queijo*, *Cachimbo* and *Malaguetas*) and the *Cortinhas* scoria cone and associated lava flows.

Fig. 7.9 - Pão de Açúcar: the most recent lava flow from the Post-caldera unit (3).

In Fig. 7.10 an attempt to compare both volcanostratigraphic successions is presented. The volcanostratigraphy by Dias (2001) is mainly based on the type of volcanic products and is closer to a lithostratigraphical characterization. In contrast, the volcanostratigraphy by França et al. (2002) is based on the volcanic events and their relative chronostratigraphy. Some minor similarities are found. Submarine volcanism on the island is indicated by both authors as the CB unit (Dias, 2001) and the Pre-caldera

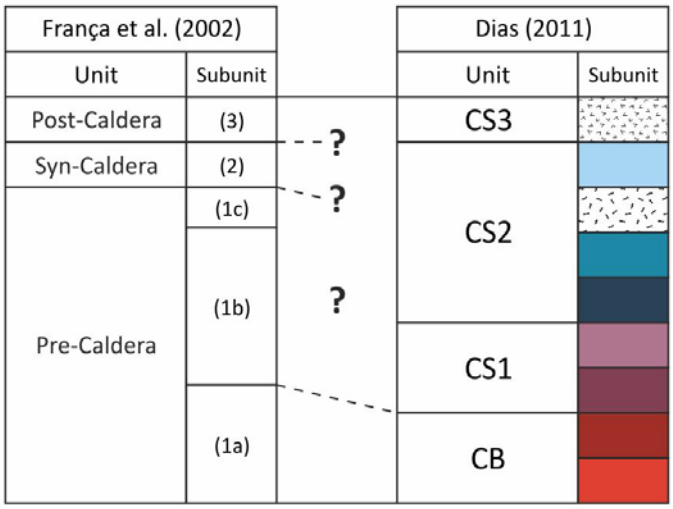

Fig. 7.10 - Comparison between the volcanostratigraphic succesions of Corvo by Dias (2001) and França et al. (2002). Unit abbreviations as explained in the text.

unit (1a) (França et al., 2002*)*. Moreover, pyroclastic, spatter and scoria cones are recognized in the CS3 unit by Dias (2001) and the Post-caldera unit (3) by França et al. (2002).

On the contrary, the (1b) and (1c) Pre-caldera units by França et al. (2002) are linked with difficulty to CS1 and CS2 units by Dias (2011). Additionally, the pumiceous deposits and pyroclastic flows associated to the caldera-forming event of the Syn-caldera (2) unit described by França et al. (2002) are omitted by Dias (2001). It is likely that these materials were not properly identified by Dias (2001) and wrongly included within the CS2 - pyroclastic subunit (Fig. 7.5 and Fig. 7.10).

As a consequence, the volcanostratigraphy proposed by Dias (2001) is not fully accepted by the scientific community, as it presents uncertainties and is not supported by the K/Ar ages obtained by himself. Consequently, the samples collected on Corvo Island (see chapter 8) are categorized according to the volcanostratigraphy proposed by França et al. (2002).

CHAPTER 8: MAGMATIC PROCESSES AND THE ROLE OF ANTECRYSTS IN THE GENESIS OF CORVO ISLAND LAVAS

8.1 Introduction

The aim of this study is to investigate the magmatic processes controlling the evolution of Corvo Island volcanism. Its small size and the existence of a single main eruptive center make it an ideal island for an in-depth study. This chapter presents detailed petrographic and geochemical data for representative samples of the complete volcanostratigraphic sequence (Pre-, Syn- and Post-caldera stages) including lava flows, dikes and cumulate gabbroic xenoliths hosted in a Pre-caldera lava flow. Based on the relative volcanostratigraphic positions of the studied samples, a comprehensive model that establishes a genetic link between the petrologically diverse materials is proposed.

8.2 Samples and analytical methods

All of the diverse igneous materials in Corvo (lava flows, dikes and xenoliths) were sampled for petrological and geochemical studies. Samples are categorized according to the volcanostratigraphy proposed by França et al. (2002) (see chapter 7). The three different units of the island were sampled in several locations (Fig. 8.1; UTM coordinates in chapter 3, Table 3.2). A total of 39 lava flow samples were collected, and are representative of the volcanic products of the whole island. Most samples were

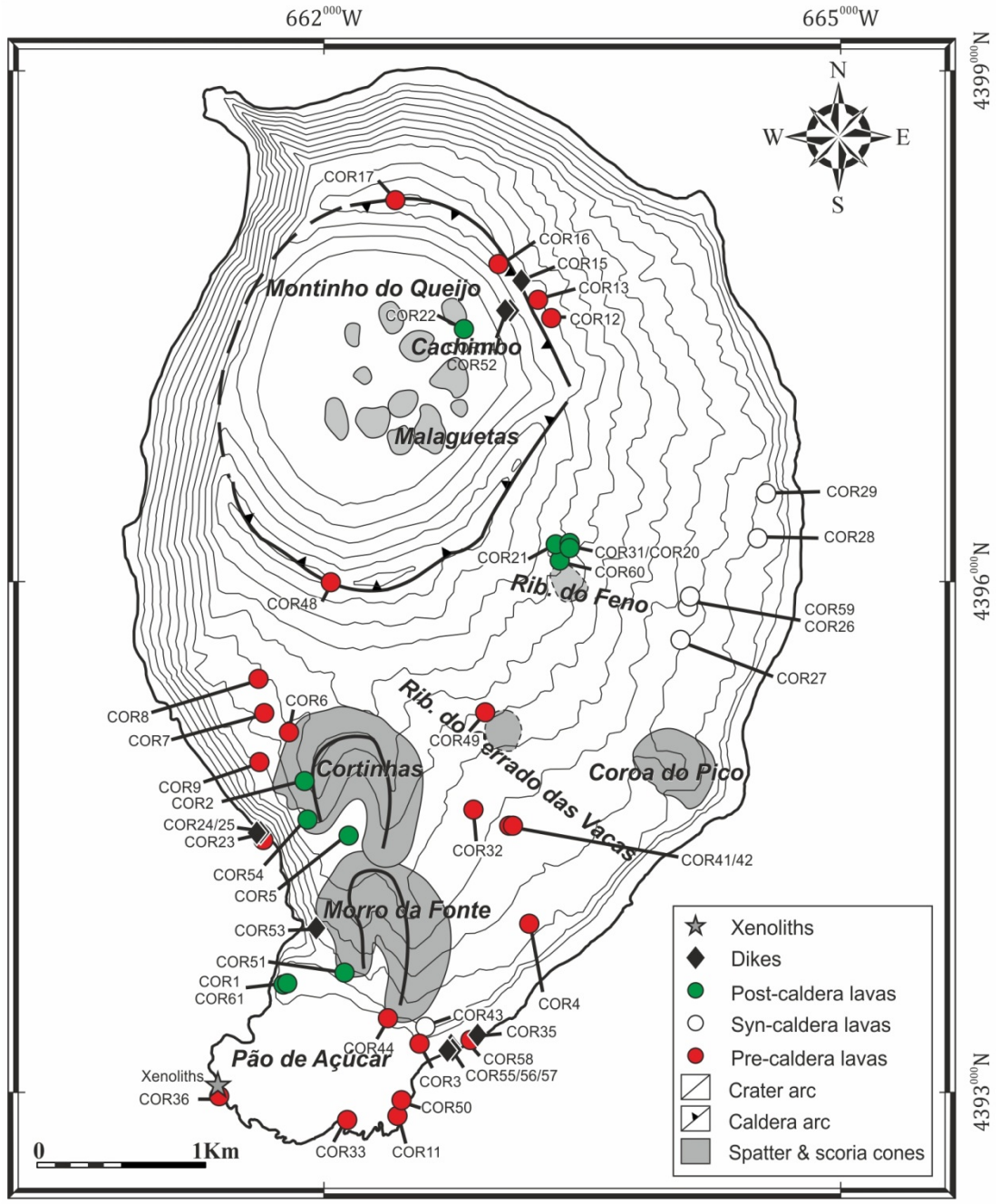

Fig. 8.1 - Morpho-volcanic scheme of Corvo Island and sampling sites (modified from França et al. (2006*a*)). Contour interval: 50 m.

collected from the Pre-caldera (22 samples) and Post-caldera (11 samples) stages owing to their relatively mafic compositions, which potentially preserve petrogenetic information regarding mantle source and melting processes. Most samples belong to the Pre-caldera stage because it accounts for ca. 90 % of the volcanic products of the island. Pumice and evolved lavas were sampled from the Syn-caldera stage (6 samples) in order to evaluate the complete evolutionary trend of the magmatic plumbing system.

Ten dikes, represented as N020E to N085E trending subvertical intrusions of 0.5 to 1.5 m thickness, were also sampled. These dikes were intruded into the Pre-caldera stage and are located in the southern area of the island and within the walls of the caldera (Fig. 8.2A-B). The xenoliths were found in a Pre-caldera lava flow in the southwest of the island (Fig. 8.2C-D); due to the small size of most xenoliths (< 5 cm), only 5 samples could be extracted for petrographic and/or geochemical analyses.

Several thin sections were studied from each sample. The petrographic study led to the selection of 13 representative thin sections for mineral analyses. These included 7 lava flows representative of the volcanostratigraphic sequence, 3 dikes and 3 xenoliths. Mineral compositions were determined on polished thin sections by electron microprobe (EMP). Lava flows were analyzed at the Centro Nacional de Microscopía Electrónica at the Universidad Complutense de Madrid (Spain), whereas dikes and xenoliths were analyzed at the Serveis Cientificotècnics of the Universidad de Barcelona. At the Universidad Complutense de Madrid, a JEOL JXA-8900 M electron microprobe equipped with five wavelength dispersive spectrometers was used; the beam diameter was 5 µm and elemental counting times were 10 s on the peak and 5 s on each of two background positions. At the Universidad de Barcelona, the selected samples were analyzed by a four-spectrometer CAMEBAX SX-50 electron microprobe; the beam diameter was 3 µm and the counting time was 20 s. In both cases, analyses were performed using an accelerating voltage of 15 kV and an electron beam current of 20 nA. Corrections for inter-elemental effects were made using a ZAF (atomic number (Z), absorption (A) and fluorescence (F)) procedure. Natural K- and Na-rich standards were previously analyzed by the electron probe in several experimental conditions to obtain maximum signal and minimum Na loss.

Samples for whole rock analysis, including 22 lava flows, 9 dikes and 3 xenoliths, were crushed in a manganese steel jaw-crusher and milled in an agate vibrating cup mill at the Servicios de Apoyo a la Investigación of the Universidad de Zaragoza (Spain). The major and trace element concentrations of lava flows, dikes and xenoliths were determined in three different laboratories according to the campaign in which they were collected

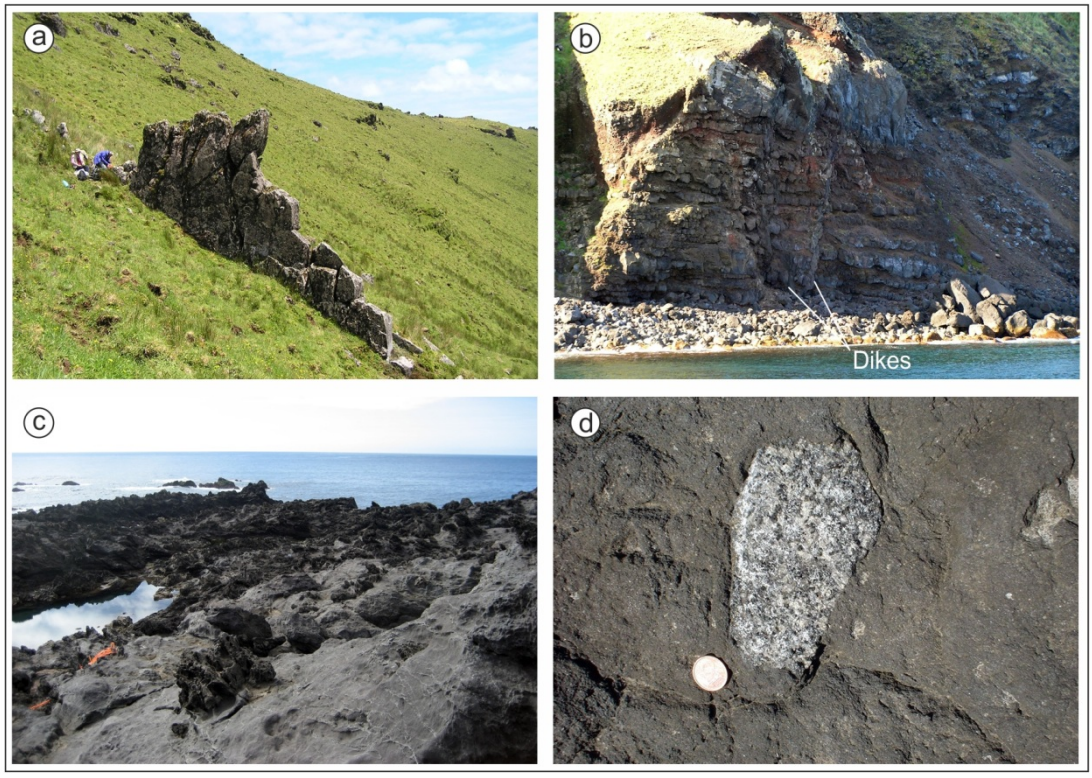

Fig. 8.2 - Photos of dike and xenolith sampling sites in Corvo Island. (a) Intracaldera dike (COR52); (b) dikes sampled in the eastern coast (COR56 and COR57); (c) Pre-caldera lava flow bearing the sampled xenoliths and (d) field appearance of a xenoliths from (c).

(Table 3.2). The major and trace element concentrations of lava flow samples (2001 fieldwork campaign) were determined the same year at the ACTLAB laboratory (Canada), using an ICP-OES Whole Rock Package and a trace element ICP-MS package. Whole rock analyses for dikes and xenoliths (2005 and 2001 fieldwork campaigns, respectively) were carried out in 2006. Major element contents were analyzed by X-Ray Fluorescence Spectrometry at the Servicio de Espectrometría y Difracción de rayos X of the Universidad de Oviedo. To determine concentrations of trace elements, these dike and xenolith samples were also analyzed at the Centro de Instrumentación Científica of the Universidad de Granada by ICP-MS. Details of the analytical procedures and detection limits are available in Appendix - Table I. In order to compare results from the different laboratories, the highest detection limits were considered for each element except Pb. Most Pb concentrations determined at the Centro de Instrumentación Científica in Granada are below the detection limit of the ACTLABS laboratory in Canada (5 ppm), whereas Pb abundances were resolveable by ICP-MS at Granada, with a detection limit of 0.001 - 0.01 ppm.

8.3 Petrology

Lava flows and dikes can be divided in two groups according to their texture: porphyritic rocks and microporphyritic rocks. The former group includes samples belonging to the Pre-caldera and Post-caldera units; the latter includes samples from all of the units (Pre-Syn- and Post-caldera).

The porphyritic rocks are holocrystalline and characterized by the presence of a variable proportion of large crystals (up to 15 mm in size) that are set in a fine-grained groundmass. According to their size, these large crystals are considered to be "macrocrysts" (2 - 10 mm) or "megacrysts" (> 10 mm). Due to the scarcity of megacrysts, large crystals will be referred to hereafter as macrocrysts. The macrocryst assemblage mainly comprises subhedral to anhedral olivine, clinopyroxene, and feldspars; some macrocrysts are corroded and present overgrowth rims. The groundmass is composed of feldspars, olivine, clinopyroxene and opaque minerals. The term "microcryst" is used for all groundmass crystals, which are smaller than 2 mm, and most of which are smaller than 0.5 mm. However, a larger and scarcer crystal population (0.5 - 2 mm) has been also recognized within the groundmass. The volume fraction of macrocrysts in these samples varies from 80 % to 8 % (Fig. 8.3A-B). Due to their large size, the proportion of macrocrysts varies even within different areas of the same sample; an estimate of the range of volume fractions of macrocrysts is presented in Appendix - Table II. In addition, a macrocryst aggregate composed of welded clinopyroxene and olivine was found in one of the studied samples.

The microporphyritic rocks include lava flows and dikes without macrocrysts (Fig. 8.3C-D). Those belonging to the Pre-caldera and Post-caldera units present a holocrystalline to hypocrystalline microporphyritic texture, sometimes indicating flow. The microporphyritic rocks resemble the groundmass of the porphyritic rocks. They are mainly composed of feldspars, minor olivine, clinopyroxene, opaque minerals, scarce amphibole and occasional glass. Most groundmass microcrysts are smaller than 0.5 mm, although scarce crystals of 0.5 - 2 mm are also recognized. The Syn-caldera samples are

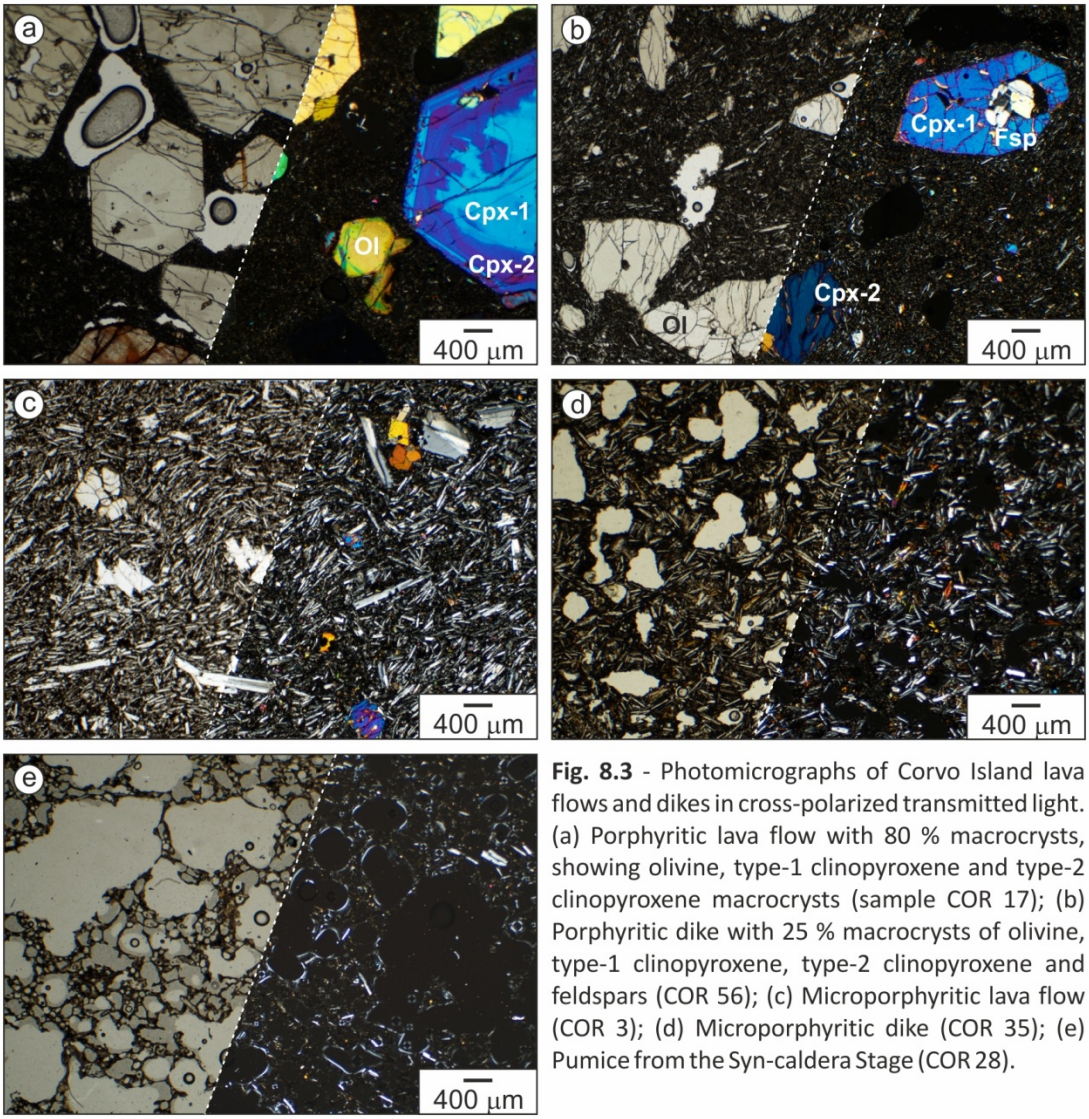

Fig. 8.3 - Photomicrographs of Corvo Island lava flows and dikes in cross-polarized transmitted light. (a) Porphyritic lava flow with 80 % macrocrysts, showing olivine, type-1 clinopyroxene and type-2 clinopyroxene macrocrysts (sample COR 17); (b) Porphyritic dike with 25 % macrocrysts of olivine, type-1 clinopyroxene, type-2 clinopyroxene and feldspars (COR 56); (c) Microporphyritic lava flow (COR 3); (d) Microporphyritic dike (COR 35); (e) Pumice from the Syn-caldera Stage (COR 28).

highly vesicular pumices mainly composed of glass with scarce microcrysts of feldspars, olivine, clinopyroxene and opaque minerals (Fig. 8.3E).

The xenoliths occur without any apparent preferred orientation in the field. They are 5 to 10 cm long and show subrounded shapes and sharp contacts with the host lava flow (Fig. 8.2D). They display a coarse-grained cumulate texture and are composed of variable proportions of olivine, clinopyroxene, feldspars, amphibole, opaque minerals and accessory apatite (Fig. 8.4). Clinopyroxene is present as 200 µm to 1cm subhedral-anhedral crystals, feldspar develops single or intergrown 200 µm to 9 mm subidiomorphic crystals and olivine, opaque minerals and apatite display 100 - 500 µm

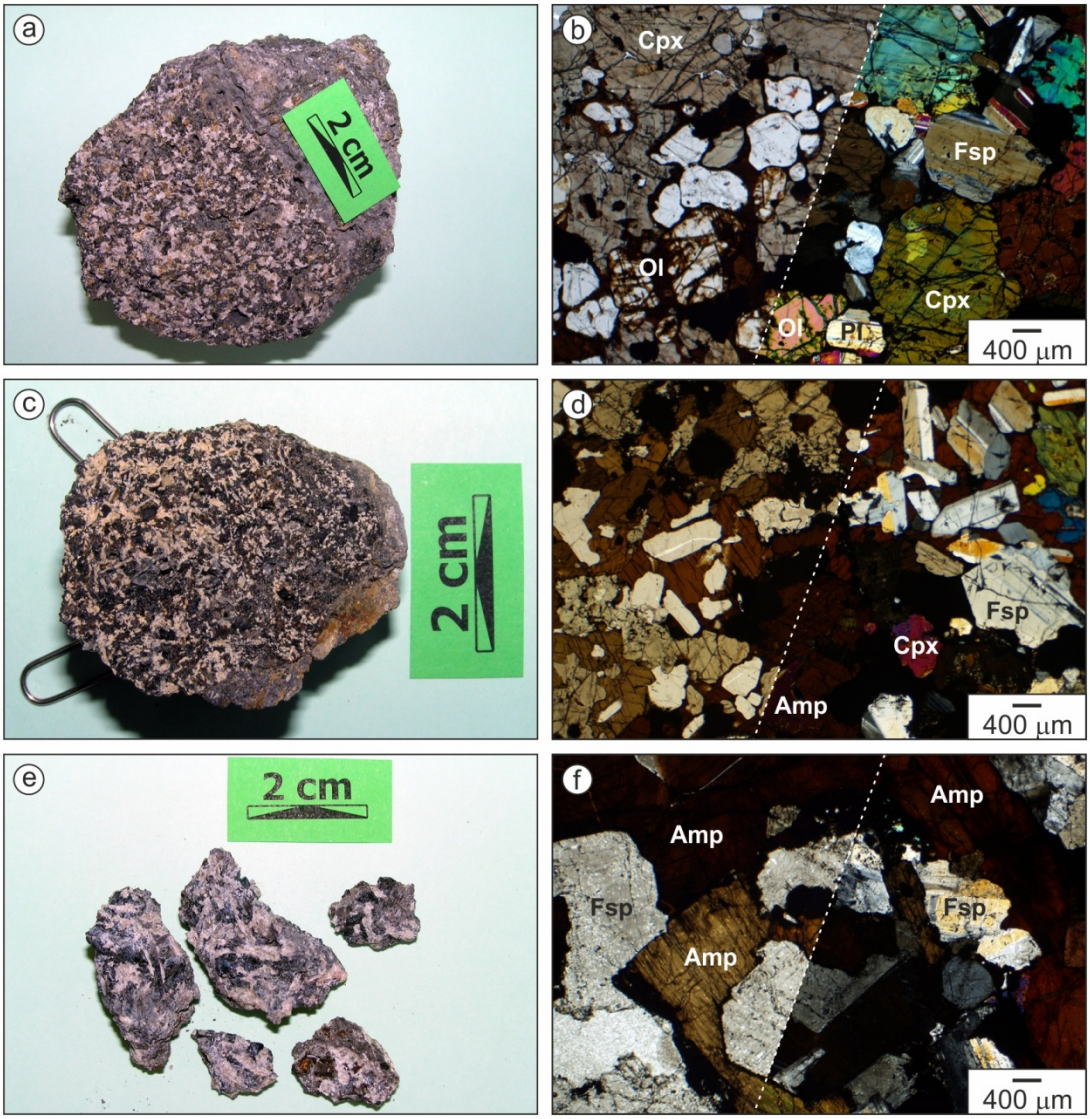

Fig. 8.4 - (a) Olivine-bearing gabbro (COR-ENC1) in hand specimen and (b) photomicrographs in plane- and cross-polarized transmitted light; (c) Pyroxene kaersutite gabbro (COR ENC-3) in hand specimen and (d) photomicrographs in plane- and cross-polarized transmitted light; (e) Kaersutite gabbro (COR-ENC4) in hand specimen and (f) photomicrographs in plane- and cross-polarized transmitted light.

subrounded crystals. Amphibole is present as poikilitic crystals up to 2 cm in size surrounding the aforementioned mineral phases. Therefore, the xenolith has a heteroadcumulate texture.

The xenoliths fall into three groups based on the classification of Le Maitre (2002): olivine-bearing gabbro (sample COR-ENC1; Fig. 8.4A-B), pyroxene kaersutite gabbro (samples COR-ENC2 and COR-ENC3; Fig. 8.4C-D) and kaersutite gabbro (samples COR-ENC4 and COR-ENC5; Fig. 8.4E-F). All of the xenoliths contain clinopyroxene, feldspars,

opaque minerals and kaersutite. In addition, the olivine-bearing gabbro contains olivine and the kaersutite gabbros contain apatite.

8.4 Mineral chemistry

Clinopyroxene, olivine, feldspars, amphibole, opaque minerals and apatite crystals were analyzed from lava flow, dike and xenolith samples. The different crystal types recognized in lava flow and dike samples (macrocrysts and microcrysts) and the crystals present in the different xenolith groups were analyzed. For a given mineral, the compositions of the different crystal types are compared to each other regardless of the rock type (porphyritic or microporphyritic) because the microporphyritic rocks are petrographically equivalent to the groundmass of the porphyric rocks.

8.4.1 Clinopyroxene

Macrocrysts and microcrysts of clinopyroxene from the lava flows and dikes as well as clinopyroxene crystals from the xenoliths are classified as augite and diopside (Morimoto et al., 1988; Fig. 8.5), and define an evolution trend from primitive compositions to more evolved ones (Fig. 8.6). Variations in per formula unit (p.f.u.) Ti, Cr, and Al contents and mg* (Mg/ ($Mg+Fe^{2+}+Fe^{3+}+Mn$) and Fe^{3+} contents calculated according to Droop (1987) most clearly differentiate macrocrysts and microcrysts of the lava flow and dike samples (Table 8.1 of the electronic supplement). The Ti vs. Al diagram (Fig. 8.6A) shows that clinopyroxene macrocryst compositions differ from clinopyroxene microcryst compositions. In the Cr vs. mg* diagram (Fig. 8.6B), where differences among the crystal types can be best distinguished, clinopyroxene macrocrysts can be divided into two types: type-1 macrocrysts (Wo_{47-46} En_{49-46} Fs_{4-8}) with 0.01 - 0.03 Ti, 0.10 - 0.18 Al and 0.03 - 0.01 Cr p.f.u., and type-2 macrocrysts (Wo_{49-48} En_{44-42} Fs_{7-10}) with higher Ti (0.03 - 0.06) and Al (0.18 - 0.32) and lower Cr (0.02 - 0.01) contents. Some type-1 macrocrysts have rims compositionally similar to the type-2 macrocrysts (Fig. 8.6A).

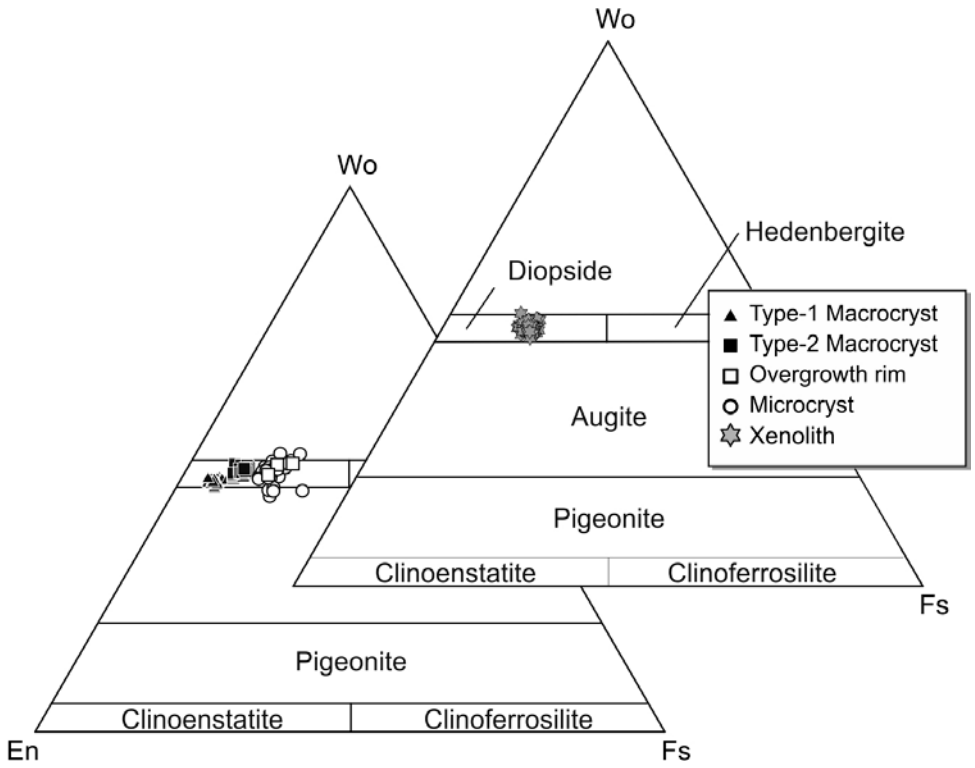

Fig. 8.5 - Clinopyroxene classification diagram wollastonite - enstatite - ferrosilite (Morimoto et al., 1988).

Both clinopyroxene macrocryst types occasionally develop overgrowths compositionally similar to the groundmass microcrysts. The microcrysts (Wo_{47-44} En_{41-35} Fs_{12-21}) contain the highest Ti (0.02 - 0.14) and Al (0.08 - 0.49) p.f.u. contents and less than 0.01 p.f.u. Cr. In the xenoliths, the Cr content is below 0.01 p.f.u. Ti and Al contents are always intermediate compared to those in clinopyroxene from lava flows and dikes (Fig. 8.6).

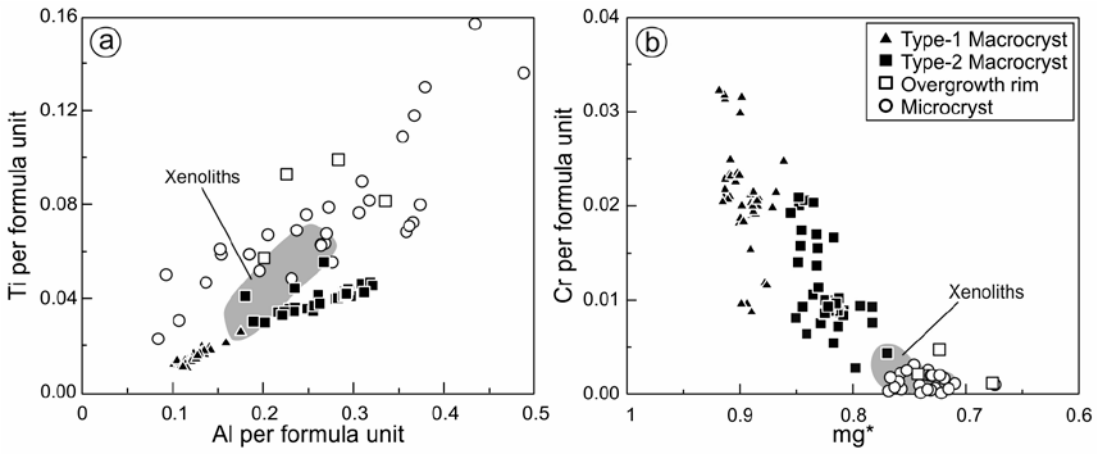

Fig. 8.6 - (a) Ti vs. Al and (b) Cr vs. mg* per formula unit diagrams of Corvo clinopyroxene compositions, analyzed by EMP.

8.4.2 Olivine

The microcrysts of lava flow and dike samples show normal zoning, with decreasing forsterite contents (Fo_{78-57}) and increasing MnO concentrations (0.33 - 1.01 wt. %) from core to rim (Table 8.2 of the electronic supplement). The macrocrysts are weakly zoned from core (Fo_{90}) to rim (Fo_{81}). They have the lowest MnO concentrations (0.07 - 0.36 wt. %), being more primitive in composition than the microcrysts. As observed for clinopyroxene macrocrysts, some olivine macrocrysts are characterized by an overgrowth rim similar in composition (Fo_{78-66} and 0.33 - 0.50 wt. % MnO) to the groundmass microcrysts. In the olivine-bearing gabbro, olivine crystals are characterized by a normal compositional zoning with Fo_{72-71} values and 0.38 - 0.53 wt. % MnO from core to rim.

8.4.3 Feldspars

Feldspar compositions are reported in Table 8.3 of the electronic supplement. The microcrysts in lava flow and dike samples range from labradorite to anorthoclase (An_{69-22} Ab_{30-70} Or_{1-8}). The macrocrysts have more primitive compositions that range from anorthite to bytownite (An_{88-70} Ab_{12-29} Or_{0-1}). Feldspar crystals within the xenoliths are classified as bytownite to andesine (An_{80-47} Ab_{20-51} Or_{0-2}). The ternary classification diagram Ab-An-Or for feldspars is shown in Fig. 8.7.

8.4.4 Amphibole

Amphibole crystals are very scarce in Corvo lava flows and dikes, occurring as microcrysts in two of the studied lava flows and one of the studied dikes. These microcrysts show quite varied compositions, classified as kaersutite, magnesiokatophorite and gedrite depending on their Ca, Na, Mg, Fe and Mn contents (Leake et al., 1997; Fig. 8.8). Amphibole macrocrysts are also uncommon; isolated macrocrysts have been found in the Syn-caldera evolved pumices and in the oldest lava

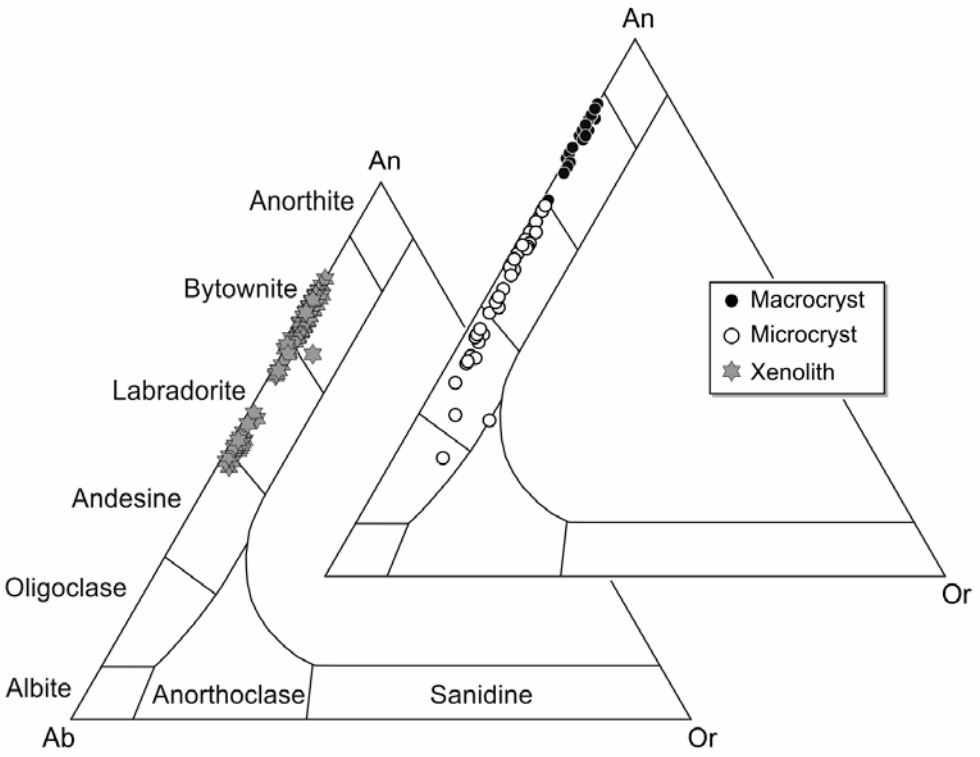

Fig. 8.7 - Ternary classification diagram Ab-An-Or for feldspars, showing the chemical variability of Graciosa lava and xenolith feldspars.

flow of the Pre-caldera unit. They are classified as kaersutite and hastingsite with 2.64 - 5.69 wt. % TiO_2 (Table 8.4 of the electronic supplement). In contrast, amphibole (kaersutite) is very common in the xenoliths (Fig.8.4).

8.4.5 Opaque minerals

Fe-Ti oxides occur mainly as microcrysts in lava flows and dikes. They are classified as ilmenite and Al-bearing titanomagnetite, and hematite-maghemite when they occur as weathering products (Table 8.5 of the electronic supplement). Ilmenite dominates in all the xenoliths, where hematite-maghemite weathering products are also present.

8.4.6 Apatite

Apatite is only present in kaersutite gabbros. It is classified as F-apatite and has variable contents of CaO (55.03 - 56.05 wt. %), P_2O_5 (41.32 - 42.02 wt. %), F (1.77 - 2.15 wt. %)

and Cl (0.9 - 1.41 wt. %) from core to rim of single crystals (Table 8.6 of the electronic supplement).

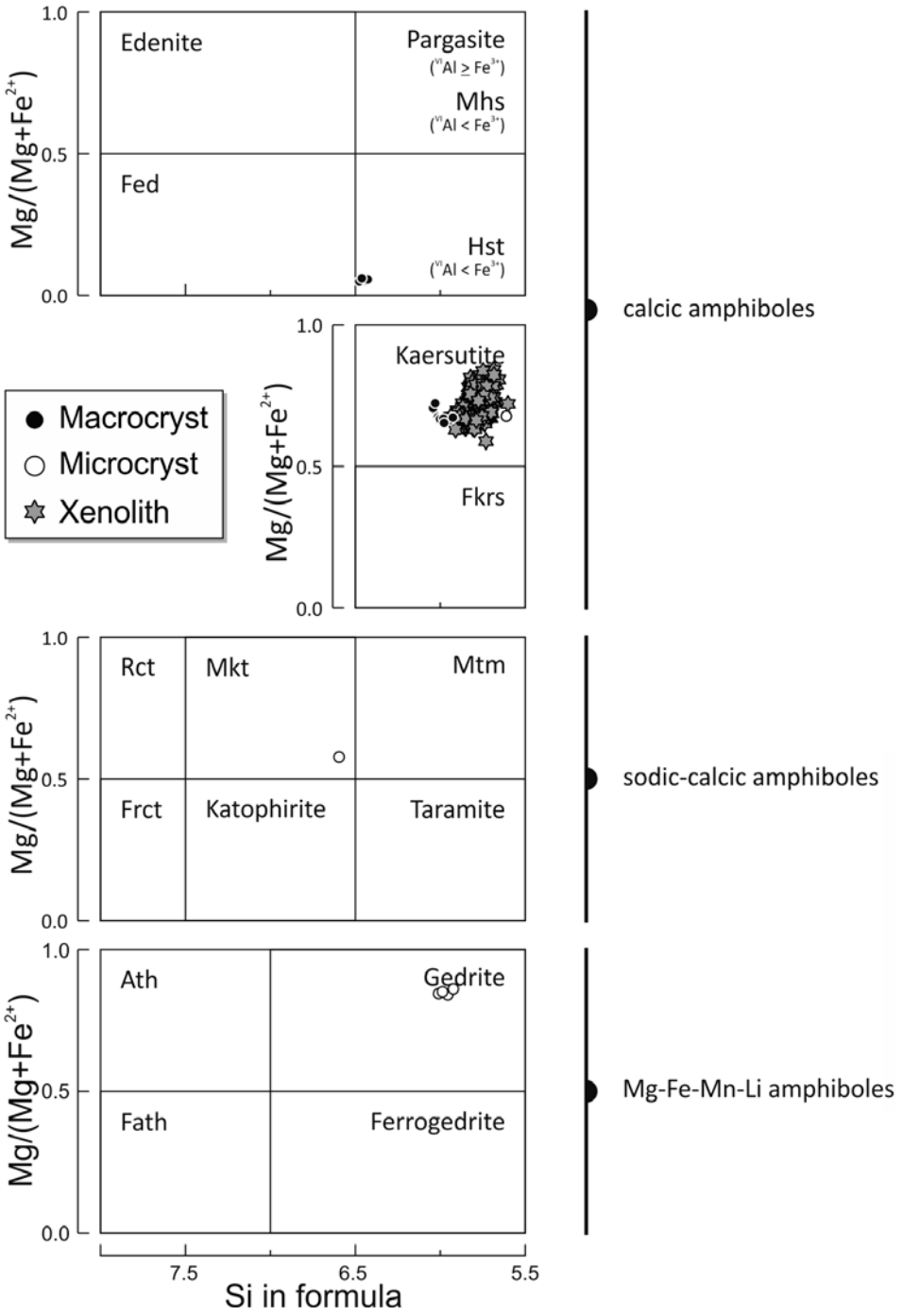

Fig. 8.8 - Amphibole classification diagrams (Leake et al., 1997). Mineral abbreviations are according to Whitney and Evans (2010).

8.5 Whole rock chemistry

8.5.1 Major and trace element compositions

Major and trace element concentrations of lava flow, dike and xenolith samples from the Pre-, Syn- and Post-caldera stages are given in Appendix - Table II. The lava flows and dikes from the three volcanostratigraphic units range in composition from picrobasalts to trachytes based on the Total Alkalis vs. Silica (TAS) diagram (Fig. 8.9; Le Bas et al., 1986). They appear to show a relatively well defined alkaline trend in the TAS diagram. However, in accordance with the petrographic observations, compositional differences are observed between the porphyritic and microporphyritic rocks. The porphyritic rocks range from alkaline picrobasalts to alkaline basalts, showing the most primitive compositions (15.41 - 4.93 wt. % MgO). The microporphyritic rocks range from hawaiites to trachytes with lower (5.55 - 0.11 wt. %) MgO contents. The analyzed samples have

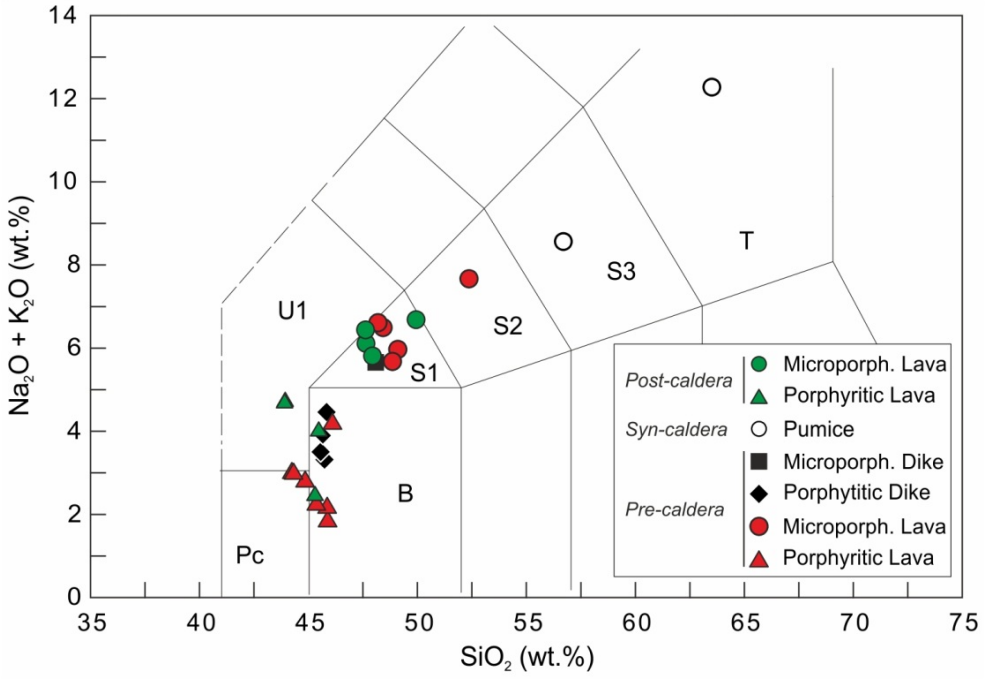

Fig. 8.9 - Total Alkalis vs. Silica (TAS) diagram for Corvo Island lava flows and dikes (after Le Bas et al. (1986)). Microporph.: microporphyritic; Pc: picrobasalt; U1: tephrite; B: basalt; S1: hawaiite, S2: mugearite; S3: benmoraite; T: trachyte.

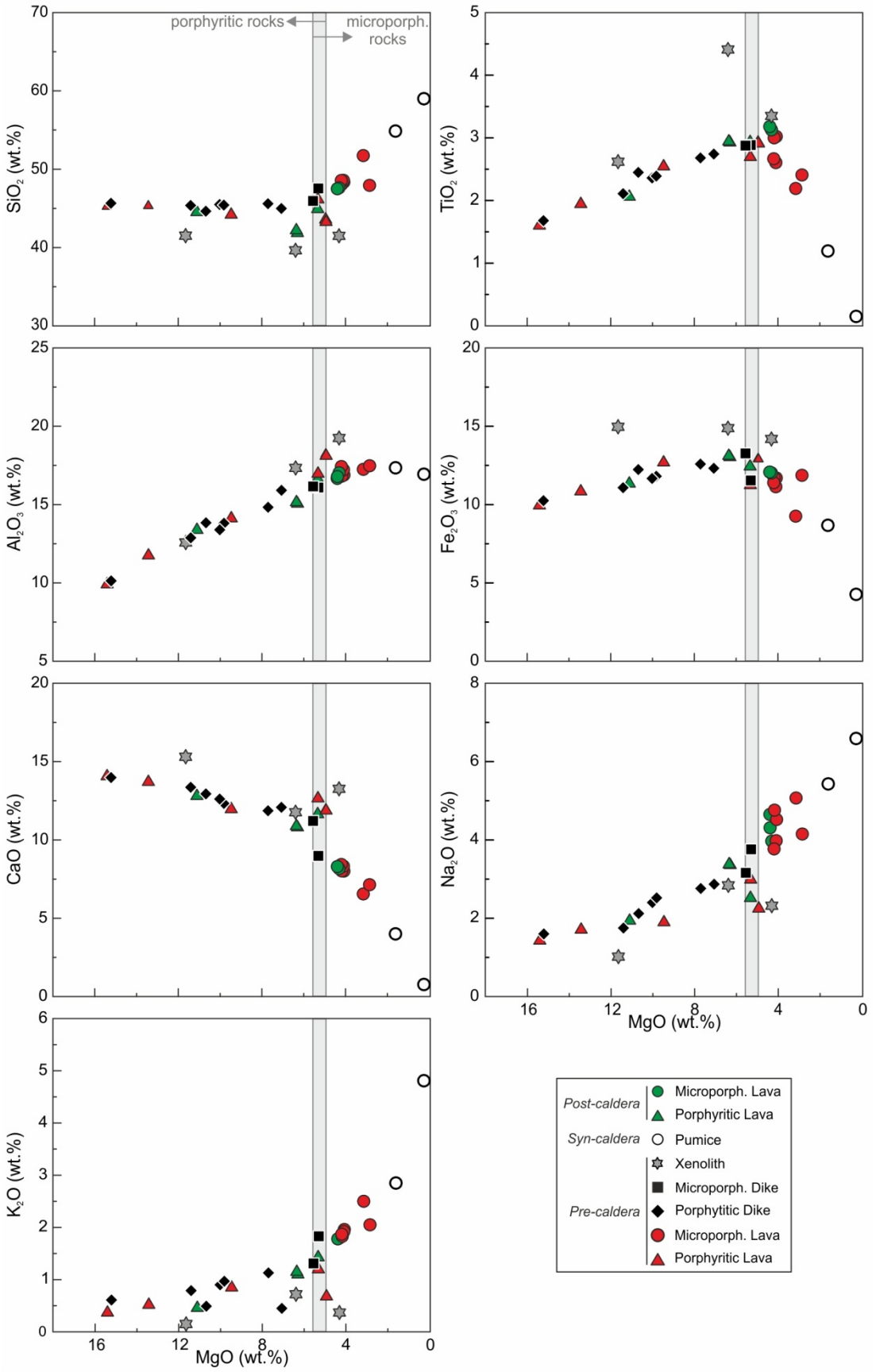

Fig. 8.10 - Major element contents plotted vs. MgO contents for lava flow, dike and xenolith samples from Corvo Island. Microporph.: Microporphyritic.

been plotted in Harker type diagrams vs. MgO. Porphyritic and microporphyritic rocks exhibit different slopes on these diagrams (Figs. 8.10 - 8.11).

The porphyritic rocks display a TiO_2, Al_2O_3, Fe_2O_3, Na_2O and K_2O increase and a CaO decrease with decreasing MgO, whereas in the microporphyritic rocks TiO_2, Al_2O_3, Fe_2O_3 and CaO decrease with decreasing MgO. The transition elements Cr, Ni, Cu, Sc and Co decrease with decreasing MgO, both for porphyritic and microporphyritic rocks. The behavior of V is different; it increases as MgO decreases in porphyritic rocks and decreases with decreasing MgO in microporphyritic rocks. Among the LILE, Ba and Rb define a single enrichment trend with decreasing MgO for both porphyritic and microporphyritic rocks, whereas Sr exhibits the same behavior as V. The HFSE Zr, Nb, Th, Hf, Ta, U, Pb and Y increase with decreasing MgO for both groups.

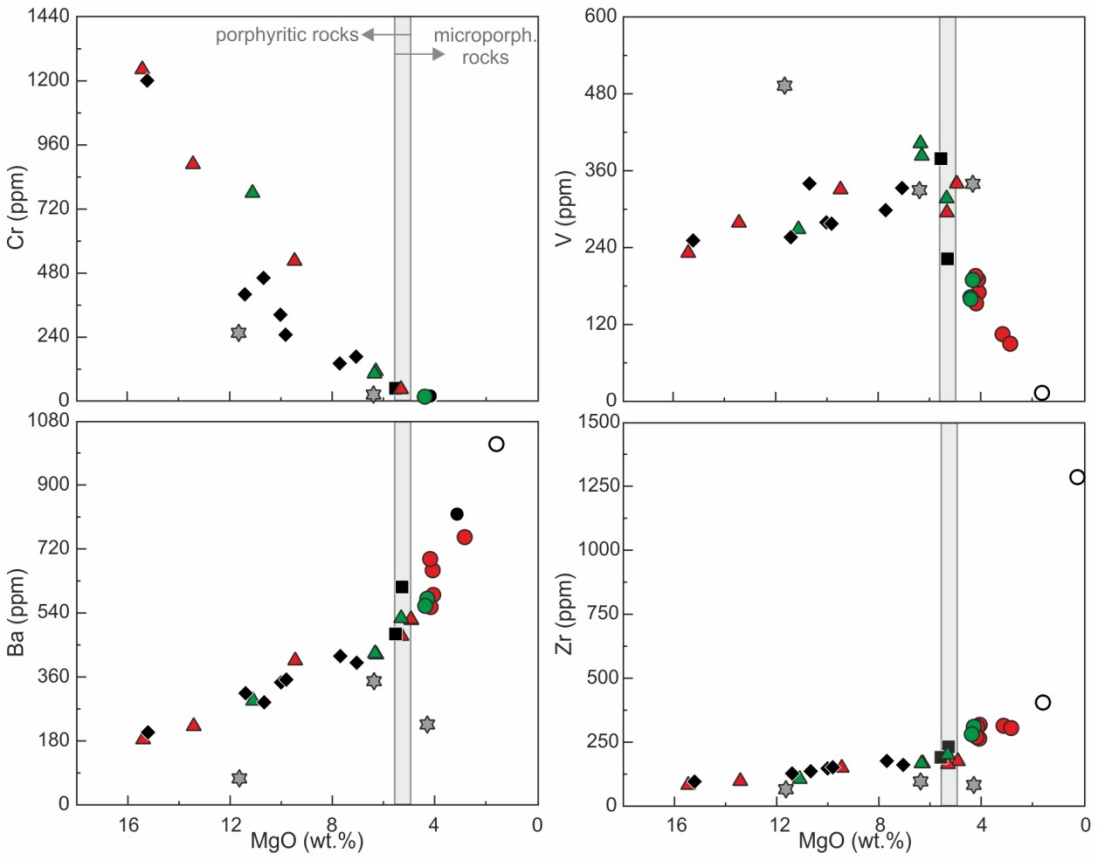

Fig. 8.11 - Selected trace element contents plotted vs. MgO contents for lava flow, dike and xenolith samples from Corvo Island. Symbols as in Fig. 8.10. Microporph.: Microporphyritic.

The xenoliths have similar trends to the porphyritic rocks for most major and trace elements. Their geochemical composition reflects the mineralogical and petrological observations, with the olivine-bearing gabbro having the highest MgO concentrations and the kaersutite gabbro the most evolved composition. Some elements (TiO_2, Fe_2O_3, Ni, V, Cu, Ba, Nb, Ta, Y) show different patterns, but clear variation trends cannot be defined owing to the scarcity of data.

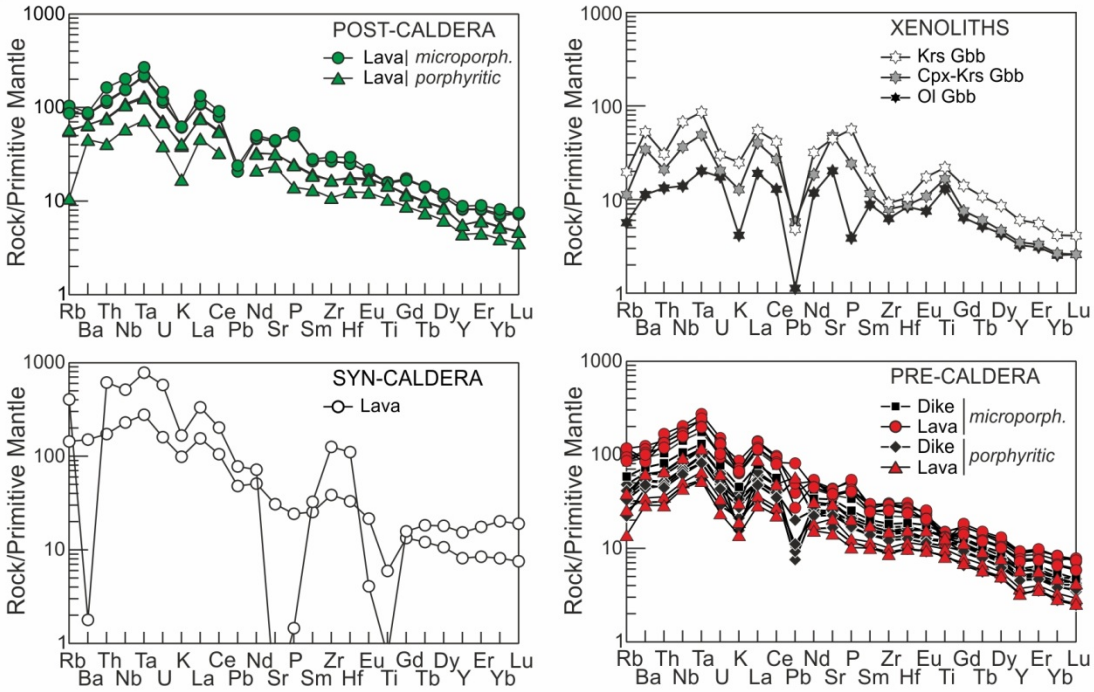

Fig. 8.12 - Primitive mantle-normalized (McDonough and Sun, 1995) multi-element diagrams for Corvo lava flows, dikes and xenoliths. Microporph.: Microporphyritic.

Primitive mantle-normalized multi-element patterns (Fig. 8.12) show similarities among the lava flows and dikes of Corvo Island, regardless of their volcanostratigraphic position and the presence or absence of macrocrysts; slight differences are marked by the pumices from the Syn-caldera unit and by the xenoliths. Although the normalized patterns of lava flow and dike samples are similar to each other, porphyritic samples are depleted in all incompatible elements compared to microporphyritic samples. Lava flows and dikes from the Pre-caldera stage and lava flows from the Post-caldera stage present negative K anomalies and Nb-Ta and La-Ce enrichments relative to primitive mantle. The Pb content is low in lava flows and dikes, being below the detection limit (20 ppm) in most of the samples; when measurable, it displays a negative anomaly except for two

lava flows (samples COR 4 and COR 7) and one dike (sample COR 15) from the Pre-caldera stage. Furthermore, Ti is slightly depleted and P shows a small positive anomaly in the microporphyritic samples compared to the porphyritic ones. The Syn-caldera pumices share the previous characteristics, but the most evolved sample (trachyte) is distinct with sharp depletions in Ba, Sr, P, Eu and Ti.

The multi-element patterns of the xenoliths are roughly parallel, sharing some features with lava flow and dike samples including the negative K and Pb anomalies and the Nb-Ta and La-Ce enrichments. The most pronounced differences are the positive Ti anomaly and the varied P contents with positive anomalies in the pyroxene kaersutite and kaersutite gabbros and a negative anomaly in the olivine-bearing gabbro.

8.6 Discussion

8.6.1 Origin of the macrocrysts

The macrocrysts are olivine, clinopyroxene (type- 1 and type-2) and plagioclase with more primitive compositions than the microcrysts (higher MgO contents in olivine and clinopyroxene and higher An values in plagioclase). However, the macrocrysts and microcrysts define a common evolution trend (e.g., Fig. 8.6 - 8.7), pointing to a comagmatic origin for these crystals. Accordingly, the macrocrysts cannot be xenocrysts foreign to the magmatic system. The Fo_{90-81} variations and CaO contents (0.25 - 0.42 wt. %) of the olivine macrocrysts indicate that they were not formed in the mantle (e.g., Stormer, 1973; Jurewicz and Watson, 1988), dismissing their origin as fragments of mantle xenoliths.

The macrocrysts could potentially be classified as phenocrysts cogenetic with the host groundmass. To test this hypothesis the Mg# (Mg# = MgO/(FeO+MgO)·100 and FeO = $0.9 \cdot Fe_2O_3^T$) of the liquids in equilibrium with olivine and clinopyroxene macrocrysts has been calculated. Iron-magnesium distribution coefficients of 0.30 ± 0.03 for olivine (Roeder and Emslie, 1970) and 0.26 ± 0.05 for clinopyroxene (Akinin et al., 2005) are

considered. Equilibrium diagrams (Fig. 8.13; Rhodes et al., 1979) are useful to illustrate these calculations. These results show that olivine macrocryst cores are in equilibrium with melts of Mg# 41 - 60 and clinopyroxene macrocryst cores with melts of Mg# 38 - 63. In contrast, olivine microcrysts are in equilibrium with melts of Mg# < 38 and clinopyroxene microcrysts with melts of Mg# < 35. According to these results, the macrocrysts crystallized from more primitive melts than the microcrysts. It is clear that macrocrysts that plot above the equilibrium curve in Fig. 8.13 are in disequilibrium with their host magma and therefore cannot be considered phenocrysts. Furthermore, some petrographic observations such as corroded cores and overgrowth rims (Fig. 8.3A), together with clear compositional differences between the macrocrysts and the groundmass microcrysts (e.g., Fig. 8.6-8.7), support disequilibrium between the macrocrysts and the host magma.

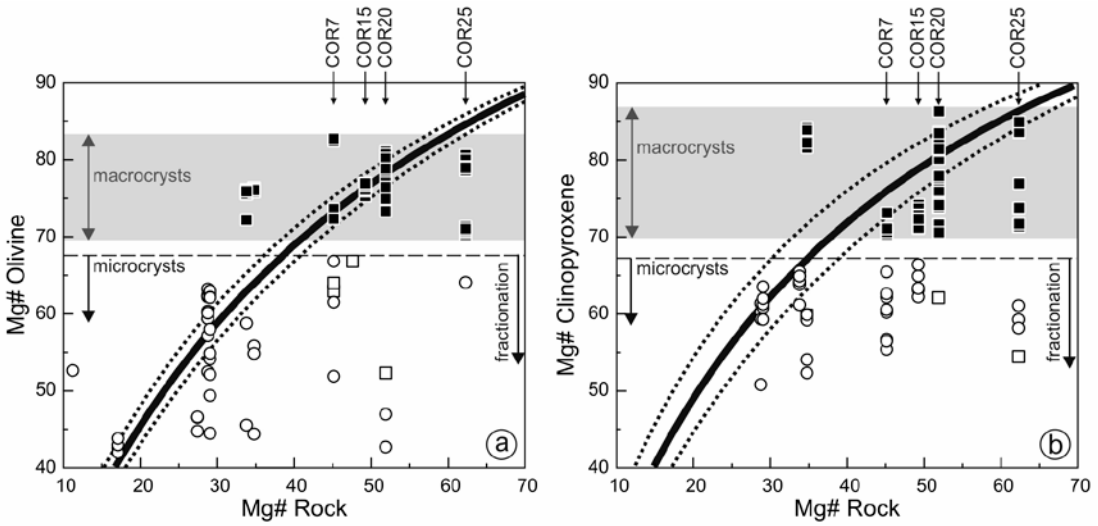

Fig. 8.13 - Mg# in mineral vs. Mg# in whole rock for olivine (a) and clinopyroxene (b). Black squares represent macrocryst cores, white squares represent macrocryst rims and white circles represent microcrysts. The bold continuous and the dotted curves (after Rhodes et al. (1979)) represent the range of equilibrium compositions between mineral and melt using an iron-magnesium distribution coefficient of 0.30 ± 0.03 for olivine (Roeder and Emsley, 1970) and 0.26 ± 0.05 for clinopyroxene (Akinin et al., 2005).

In conclusion, the macrocrysts are best described as “antecrysts”, i.e., large crystals that according to their chemical composition may not have shared common histories or crystallized from the magma in which they are now hosted, but rather may have grown within the same magmatic system but in a more primitive magma than that from which the microcrysts eventually grew (Charlier et al., 2005; Gill et al., 2006; Davidson et al.,

2007; Jerram and Martin, 2008). Antecrysts may have been previously observed in other Azorean Islands, although using different nomenclatures: xenocrysts in São Miguel (Beier et al., 2006), Pico (França et al., 2006*b*) and São Jorge Islands (Ribeiro, 2011) or phenocrysts with the highest Mg# in Terceira island (Madureira et al., 2011).

The analyzed olivine and clinopyroxene microcrysts belong to the groundmass of the porphyritic rocks and to the microporphyritic rocks. Given that they are compositionally equivalent, it is inferred that the microporphyritic rocks are equivalent to the groundmass of the porphyritic rocks. The analyzed microcrysts include the main, small microcryst population (< 0.5 mm) and also the scarcer and larger microcrysts (0.5 - 2 mm). All of the analyses show lower Mg# contents than the macrocrysts, and plot within or below the equilibrium curve in Fig. 8.13. The microcrysts are thus generally in equilibrium with the magma in which they are included, with some crystals falling below the equilibrium curve due to progressive fractionation of the magma.

8.6.2 The influence of the antecrysts on whole rock compositions

The porphyritic rocks from Corvo carry variable volume fractions of antecrysts, and have MgO contents > 4.93 wt. % (Mg# > 30). In contrast, the microporphyritic (antecryst-free) rocks have MgO contents < 5.55 wt. % (Mg# < 34). Strikingly, the MgO content of the porphyritic rocks increases monotonically with increasing proportions of mafic antecrysts in the rock (see top of Fig. 8.14); the highest MgO contents correlate with the highest proportions of mafic antecrysts in the rocks. This leads to the conclusion that the Mg-enrichment of the porphyritic rocks is controlled by the presence and proportion of mafic antecrysts (Vinet and Higgins, 2010; Ubide et al., 2012; Ubide, 2013). Furthermore, the petrographic and compositional results indicate that the groundmass of the porphyritic rocks is equivalent to the microporphyritic rocks. This indicates that the compositional differences between these rock-types cannot be explained by fractionation. Rather, the porphyritic rocks accumulated antecrysts, accounting for their primitive compositions. In consequence, the whole rock compositions of the magmas that accumulated a high fraction of antecrysts are much more primitive than they would be without the accumulation process, generating in some cases an apparent but false

"equilibrium" between the antecrysts and their host rock (see samples COR 15, COR 20 and COR 25 in Fig. 8.13A and samples COR 7, COR 15 and COR 25 in Fig. 8.13B), as also suggested for other settings (Sakyi et al., 2012; Ubide, 2013; Ubide et al., 2014).

The accumulation of antecrysts successfully explains the evolution trends of the porphyritic rocks in the Harker type diagrams (Figs. 8.10 - 8.11). The increase in most major element, LILE and HFSE abundances, and the decrease in CaO, Cr, Ni, Cu, Sc and Co with decreasing MgO, is related to the decreasing proportion of antecrysts. Contrary to other transition elements, V increases in rocks with lower proportions of antecrysts because V is almost exclusively incorporated in ilmenite and magnetite, but antecrysts of opaque minerals do not occur in the studied rocks. The composition of the rocks with lower percentages of antecrysts (e.g., 8 % of volume fraction) is more evolved and appears to be controlled by the composition of the groundmass. The accumulation of primitive antecrysts in porphyritic rocks can also explain their less enriched primitive mantle normalized multi-element patterns (Fig. 8.12), compared to microporphyritic samples.

To test the influence of the antecrysts on the whole rock compositions, the accumulation of each antecryst mineral phase has been modeled. Representative mineral compositions for antecrysts of olivine, clinopyroxene and plagioclase (Table 8.1) have been selected. The composition of the microporphyritic sample COR 35 (Appendix - Table II) is considered as a representative groundmass. The accumulation vectors for each mineral are represented in Fig. 8.14. Each vector represents the accumulation of up to 20 % of the respective antecryst mineral phase. The direction and length of

Table 8.1 - Selected analyses of antecrysts of olivine, clinopyroxene and plagioclase used for calculating the vector model (Fig. 8.14) and for the MINSQ model.

Mineral	Ol	Cpx	Pl
	Ax	Ax	Ax
SiO_2	39.0	49.6	46.4
TiO_2	0.0	1.1	0.0
Al_2O_3	0.0	4.7	33.5
Fe_2O_3	15.8	5.7	0.0
MnO	0.2	0.0	0.0
MgO	45.5	15.6	0.0
CaO	0.3	22.3	17.1
Na_2O	0.0	0.4	1.7
K_2O	0.0	0.0	0.1

Mineral abbreviations are according to Whitney and Evans (2010). Ax: Antecryst

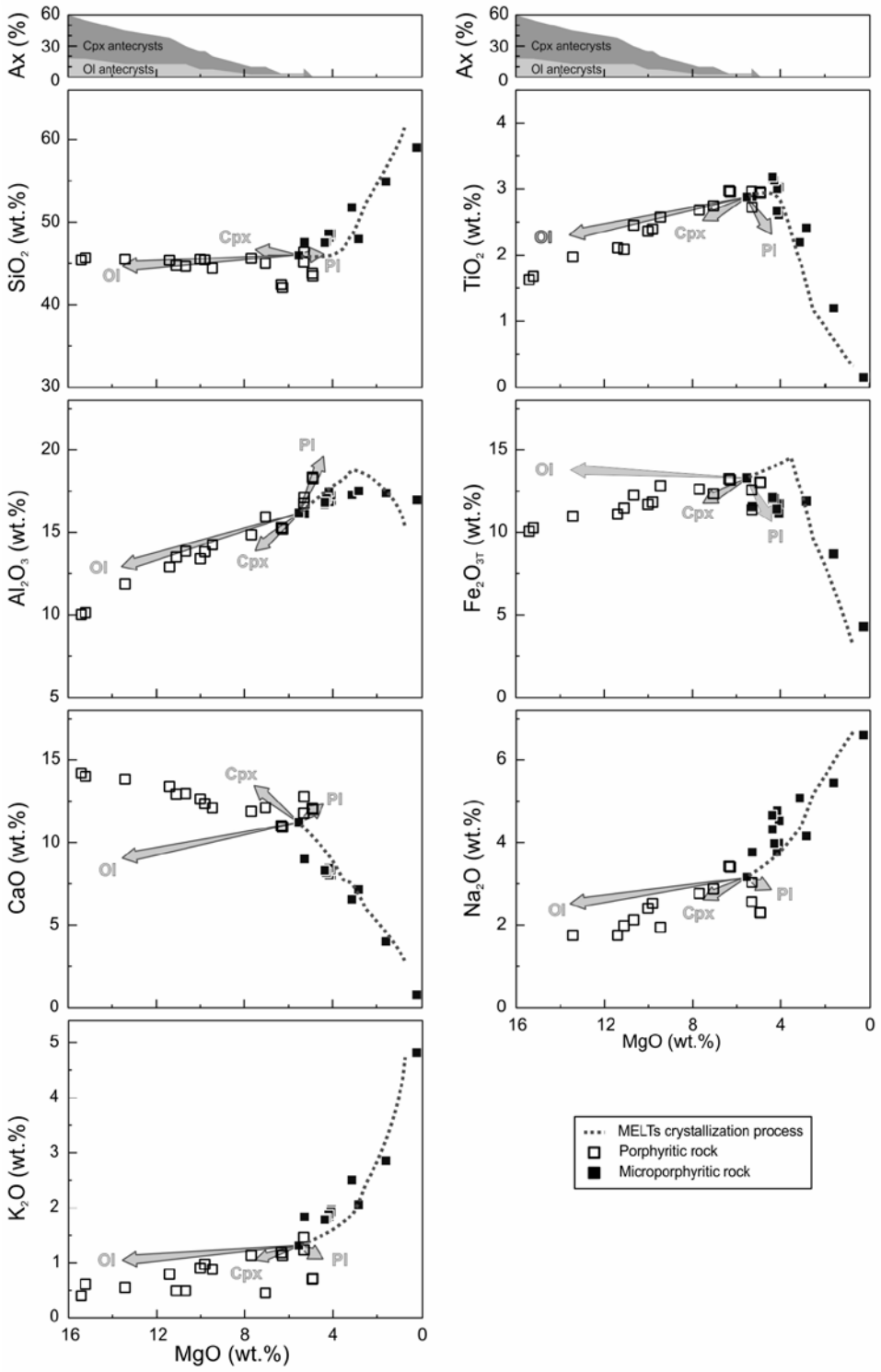

Fig. 8.14 - Major element contents plotted vs. MgO contents for porphyritic (white squares) and microporphyritic (black squares) lava flows and dikes (as in Fig. 8.10). Grey arrows represent accumulation trends of antecrysts from a microporphyritic sample (COR 35) towards 20 % of each antecryst phase. Dotted lines indicate the polybaric fractional crystallization trend modeled using the MELTS algorithm (Ghiorso and Sack, 1995; Asimow and Ghiorso, 1998) with a water content of 1 % and considering COR 35 sample as the initial composition. The best-fit MELTS model was obtained at an initial pressure of 500 MPa with decreasing steps of 7.5 MPa and cooling steps of 5 ºC. At the top of the figure the variation of the volume fraction of olivine and clinopyroxene antecrysts with MgO content has been represented. Note the direct relationship between the accumulation of mafic antecrysts in each rock and its MgO content. Mineral abbreviations - Whitney and Evans (2010).

the vectors allow evaluation of the influence of each antecryst phase on the whole rock compositions. Olivine antecrysts produce the greatest changes in all major element contents. The presence of olivine antecrysts increases the Fe_2O_3 content and decreases the SiO_2, TiO_2, Al_2O_3, CaO, Na_2O and K_2O concentrations in the rock. Clinopyroxene increases the SiO_2, CaO, Na_2O and K_2O concentrations and decreases the TiO_2, Al_2O_3 and Fe_2O_3 concentrations in the rock. The accumulation of plagioclase antecrysts produces the smallest effect for most major elements. This mineral decreases the TiO_2, Fe_2O_3, Na_2O and K_2O contents and increases the SiO_2, Al_2O_3 and CaO concentrations in the whole rocks.

The compositional trends defined by the porphyritic samples can be best reproduced by the accumulation of a combination of olivine and clinopyroxene antecrysts, consistent with the petrographic observations (see top of Fig. 8.14). The plagioclase vector does not match the whole rock compositional trends, indicating that the influence of plagioclase on whole rock compositions is minor. Accordingly, plagioclase antecrysts appear in low proportions in most samples (volume fraction < 5 %), except for samples COR 9, COR 9/R, COR 16 and COR 21 (6 - 4 wt. % MgO in Fig. 8.14) where the fraction of plagioclase antecrysts is higher (volume fraction up to 10 %) and accordingly the whole rock compositions follow the trends described by the plagioclase vector.

In order to quantify these observations, a least squares model has been developed using the MINSQ software (Herrmann and Berry, 2002). This method estimates the proportions of the constituent phases in a rock according to the composition of the phases and the whole rock. The considered constituents were the same as in the previous model: the compositions of olivine, clinopyroxene and plagioclase antecrysts from Table 8.1 and the whole rock composition of sample COR 35 (Appendix - Table II) as representative of the groundmass. The calculated proportions of each antecryst phase and the groundmass are summarized in Table 8.2. The results are consistent with the petrographic estimates (Appendix - Table II), further supporting the proposed influence of the accumulation of antecrysts on the whole rock compositions.

Table 8.2 - Proportions of antecryst and groundmass estimated by the MINSQ least square model.

Sample	Ol	Cpx	Pl	Groundmass	Residual SSQ*
COR 17	15.8	38.4	5.5	38.8	0.2
COR 12	12.9	29.2	5.9	51.4	0.7
COR 25	15.5	37.0	4.6	41.9	0.1
COR 9	0.0	0.0	9.7	87.3	4.8
COR 21	0.0	1.3	4.9	92.3	0.5
COR 16	0.0	6.6	10.4	83.2	0.3
COR 55	7.2	17.7	3.0	71.0	0.1
COR 57	7.4	14.9	3.7	73.0	0.1
COR 7	7.6	9.8	2.4	78.1	1.7
COR 14	3.1	5.8	5.6	84.1	0.9
COR 56	3.5	8.1	1.2	86.4	0.1
COR 15	9.2	15.8	4.8	68.8	2.2
COR 52	9.5	23.8	5.9	59.6	0.4
COR 20	10.1	18.8	6.8	62.4	0.9
COR 31	2.2	0.0	0.0	91.8	2.0

Residual SSQ* represents the sum of the differences between analysed and calculated weight percent
Mineral abbreviations are according to Whitney and Evans (2010).

8.6.3 Differentiation of Corvo Island magmas by fractional crystallization

Several studies have argued that primitive melts in Azores have MgO contents around 12 wt. % and Ni contents of 200 - 300 ppm (e.g., Beier et al., 2006; Beier et al., 2008; Madureira et al., 2011). Sample COR 20 has MgO and Ni contents close to these values (Appendix - Table II), but it is a porphyritic rock that carries a high proportion of antecrysts. As discussed above, the accumulation of antecrysts affects the composition of the rock and, therefore, the antecryst-bearing rocks should not be considered representative of primitive melt compositions to investigate magma differentiation. In contrast, the microporphyritic rocks from Corvo are only composed of microcrysts. The absence of inherited antecrysts in these rocks makes them suitable to identify primary magmatic processes affecting their evolution. They have MgO concentrations ranging from 5.55 to 0.1 % and their compositions lie within a single liquid trend of descent, pointing to a comagmatic origin. This idea is also suggested by the parallel normalized multi-elemental patterns (Fig. 8.12). Therefore, the mineralogy, texture and bulk-rock composition of the microporphyritic rocks from Corvo point to a common differentiation process. The presence of xenoliths with cumulate textures potentially indicates that

magmatic differentiation was controlled by fractional crystallization. This process has been tested both for major and trace elements.

MELTS modeling

The major element model has been carried out using the MELTS algorithm (Ghiorso and Sack, 1995; Asimow and Ghiorso, 1998), which is widely used for modeling magmatic processes (e.g., Kress and Ghiorso, 2004; Beier et al., 2006; Ustunisik and Kilinc, 2011). Sample COR 35 (Appendix - Table II), a microporphyritic dike from the Pre-caldera stage, is the least evolved of all the microporphyritic samples and, for this reason, it was chosen as the initial composition. The crystal fractionation model was tested in isobaric conditions at different pressures (10, 100, 300 and 500 MPa) and polybaric conditions (500 - 50 MPa, with dP/dT = 1.5) with cooling steps of 5 ºC, fixed fO_2 relative to the QFM buffer and different initial water contents (0.5, 1 and 2 % H_2O) consistent with the presence of amphibole (Eggler, 1972; Ustunisik and Kilinc, 2011); the parameters used in these MELTS runs are summarized in Table 8.3. The data are best modeled by polybaric fractionation starting at a pressure of 500 MPa (ca. 15 km depth) with a H_2O content of 1 %; the liquidus temperature for these conditions is 1202 ºC according to MELTS. The melt compositions obtained from the polybaric fractional crystallization model are compared to the compositions of Corvo lava flows and dikes in Fig. 8.14. The model compositions fit the increase of SiO_2, Na_2O, K_2O and Al_2O_3 and the decrease of TiO_2, Fe_2O_3 and CaO with increasing differentiation exhibited by the studied microporphyritic rocks.

This polybaric fractional crystallization model shows that the fractionated phases are olivine, plagioclase, clinopyroxene, opaque minerals, apatite and an additional ferromagnesian phase. The latter, with low Si and high Al and Ti contents, resembles the composition of kaersutite. The MELTS thermodynamic database does not include this Ti-rich amphibole (M.S. Ghiorso, pers. com.); therefore this ferromagnesian phase is interpreted as the amphibole (kaersutite) present in the studied xenoliths. Taking this

Table 8.3 - Parameters of the MELTS modeling runs (grey row indicates the best fit MELTS run).

Starting P (MPa)	% H_2O	dT (ºC)	dP (Mpa)	dP/dT	Buffer fO_2 QFM	Liquidus T (ºC)	Final P (MPa)	Final T (ºC)	Initial $logfO_2$	Final $logfO_2$
500	2	5	0	-	0	1177.15	500	910	-8.18	-11.9
500	1	5	0	-	0	1202.54	500	900	-7.9	-12.08
500	0.5	5	0	-	0	1217.58	500	905	-7.74	-11.99
300	2	5	0	-	0	1146.09	300	900	-8.7	-12.26
300	1	5	0	-	0	1170.31	300	900	-8.42	-12.26
300	0.5	5	0	-	0	1185.16	300	900	-8.24	-12.26
100	2	5	0	-	0	1114.45	100	990	-9.25	-10.97
100	1	5	0	-	0	1137.11	100	900	-8.96	-12.45
100	0.5	5	0	-	0	1157.03	100	900	-8.72	-12.45
10	2	5	0	-	0	ERROR	10	-	-	-
10	1	5	0	-	0	ERROR	10	-	-	-
10	0.5	5	0	-	0	1150.98	10	1095	-8.87	-9.57
500	2	5	7.5	1.5	0	1177.15	125	925	-8.27	-12
500	1	5	7.5	1.5	0	1202.54	50	900	-7.9	-12.5
500	0.5	5	7.5	1.5	0	1217.7	35	905	-7.74	-12.42

assumption into account, the obtained fractionated mineral assemblage and the composition of these minerals is broadly consistent with that of the xenoliths and groundmass microcrysts of the studied rocks (Table 8.4).

The studied xenoliths show cumulate textures, providing distinct petrographic evidence that they are magma chamber cumulates (e.g., Shamberger and Hammer, 2006). Furthermore, their bulk composition deviates from the composition of the lava flows and dikes, due to the accumulation of olivine, clinopyroxene, plagioclase, kaersutite, opaque minerals and apatite. For instance, their positive Ti anomaly can be related to kaersutite, Ti-rich clinopyroxene and opaque minerals, whereas the variable P contents can be related to the presence or absence of apatite (Fig. 8.12). All of these lines of evidence suggest that the xenoliths formed as cumulates by fractional crystallization.

Table 8.4 - Composition of the fractionated olivine, clinopyroxene and amphibole of the best-fit MELTS model and those of the studied xenoliths, lavas and dikes for comparison

Mineral Phases	MELTS	Xenoliths	Lavas and dikes Groundmass	Antecrysts
Olivine (Fo)	68 - 59	72 - 71	78 - 57	90 - 81
Clinopyroxene (Mg#)	64 - 51*	67 - 58	66 - 49	86 - 70
Kaersutite (Mg#)		57 - 44	51 - 49	-

* Mg# values for the ferromagnesian phases (including clinopyroxene and kaersutite) estimated by MELTS

Trace element modeling

The trace element modeling has been carried out by applying the fractional crystallization equation by Rayleigh (1896) to the concentrations of rare earth elements (REE) in the least evolved microporphyritic sample (COR 35). Crystallization steps of 10 %, from 100 % melt to 10 % melt, have been modeled. The percentages of each fractionated mineral phase have been established according to their average abundance in the most primitive xenoliths (olivine-bearing and pyroxene kaersutite gabbros; model-1 in Table 8.5), which agrees with the results of the major element (MELTS) model. The partition coefficients of these fractionated phases were taken from previous studies in alkali basalts with similar composition, and are listed in Table 8.7 of the electronic supplement.

Table 8.5 - Proportion of fractionating mineral phases used in the REE models of Fig. 8.15 - 8.16 and xenoliths modes for comparison

Mineral Phases	Model-1	Model-2	Olivine-bearing gabbro	Pyroxene-kaersutite gabbro	Kaersutite gabbro
Olivine	9	0	15	0	0
Clinopyroxene	31	3	50	16 - 21	3 - 4
Plagioclase	36	35	23	46 - 53	47 - 70
Kaersutite	17	45	5	21 - 30	15 - 40
Opaque	7	15	7	5 - 8	8 - 10
Apatite	0	2	0	0	1

The results of the REE model are compared to the composition of the microporphyritic rocks (Fig. 8.15). A good agreement is observed between the model and the microporphyritic lava flows and dikes from the Pre-caldera stage (30 - 50 % fractional crystallization) and Post-caldera stage (30 - 40 % fractional crystallization). However, no agreement was observed between the model and the Syn-caldera samples, which are MREE-depleted compared to the modeled compositions, especially for the trachyte sample. These differences could be explained by modal and partition coefficient changes during the fractional crystallization process (from 5.55 wt. % MgO to 0.1 wt. % MgO).

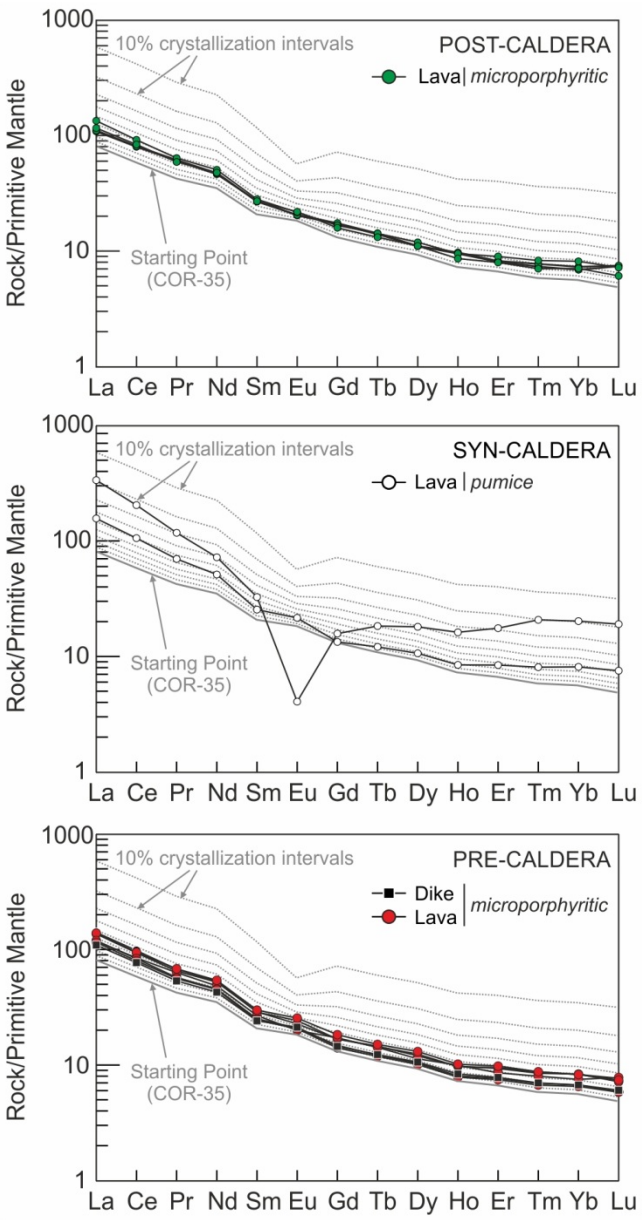

Fig. 8.15 - Primitive mantle (McDonough and Sun, 1995) normalized REE patterns for the fractional crystallization model-1 starting from sample COR 35 with 10 % crystallization intervals (grey dashed lines) compared to the microporphyritic lava flows and dikes of the Pre-caldera and Post-caldera stage and the Syn-caldera Pumices. Fractionating phases are listed in Table 8.5 (model-1).

Accordingly, the REE model was modified to incorporate fractionating phases equivalent to the most evolved xenolith (kaersutite gabbro; model-2 in Table 8.5) to derive compositions equivalent to those of the most evolved samples (1.61 - 0.11 wt. % MgO). The results are shown in Fig. 8.16A, where better agreement with the benmoreitic Syn-caldera sample is observed at ~ 50 % of the fractional crystallization. Partition coefficients used are listed in Table 8.7 of the electronic supplement.

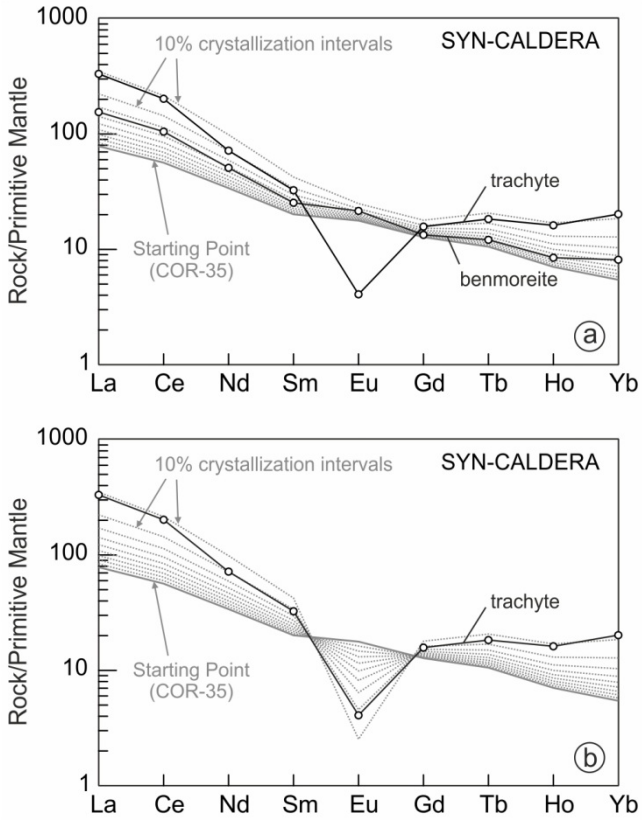

Fig. 8.16 - Primitive mantle (McDonough and Sun, 1995) normalized REE patterns for the fractional crystallization model-2 starting from sample COR 35 with 10 % crystallization intervals (grey dashed lines) compared to the Syn-caldera pumices. Fractionating phases are listed in Table 8.5 (model-2). The REE-s included are those for which partition coefficients are available for all the fractionated phases.

However, the negative Eu anomaly of the trachyte sample remains unexplained by this model. To explain such an anomaly, it is necessary to consider an increase in the Eu partition coefficients during fractional crystallization, as is common for feldspars and amphibole in evolved melts (e.g., Lemarchand et al., 1987). The model-2 has been repeated with higher partition coefficients for Eu in feldspars (D = 1.3) and amphibole (D = 2.7). The results at 90 % crystallization are very similar to the composition of the Syn-caldera trachyte sample (Fig. 8.16B). This agrees with the end of the MELTS fractional crystallization model, which corresponds to 10 % of melt remaining. Moreover, it is likely that partition coefficients of D > 1 for Sr, K and Ba in feldspars (e.g., Villemant, 1988), P in apatite and Ti in amphibole, would also explain the negative anomalies of the Syn-caldera trachyte sample (Fig. 8.12). Fractional crystallization is therefore the dominant process controlling variations in major and trace elements in Corvo microporphyritic samples, as demonstrated thermodynamically and numerically.

8.6.4 Magmatic evolution beneath Corvo Island

Given that the Pre- and Post-caldera lava flows and dikes are petrographically and compositionally equivalent, they are most likely related to the same magma chamber. According to the fractional crystallization model, this chamber was located at ~ 15 km depth. The xenoliths represent products of fractional crystallization of this magma chamber. Pre-caldera products were mainly erupted from the caldera vent, constructing ~ 90 % of the volume of the volcanic island. In contrast, most Post-caldera products were erupted from secondary cones in the caldera flanks.

The Syn-caldera stage is more evolved compositionally than the Pre- and Post-caldera stages. However, it can be related to the Pre-caldera microporphyritic compositions by fractional crystallization. The Syn-caldera stage is probably related to fractionation of the magma in a different, shallower magma chamber. The "*O Caldeirão*" provides evidence of the existence of a shallow magma chamber beneath the center of the volcano before the caldera collapse. Similar cases have been proposed for other Azorean Islands (the calderas of *Sete Cidades* and *Furnas* in São Miguel, and the *vulcão da Caldeira* in Faial; França et al., 2003). Residual evolved magmas of the Syn-caldera stage erupted within the caldera after its collapse, generating few, isolated intracaldera pyroclastic and spatter cones, which belong to the Post-caldera stage.

The Pre- and Post-caldera lava flows and dikes sometimes contain large antecrysts, which can reach more than 50 vol. % of the rock. These antecrysts show very homogeneous compositions and crystallized from more primitive magmas than those from which the groundmass of the rocks crystallized. They might be related to a different magma chamber, probably deeper than the one in which the Pre- and Post-caldera magmas fractionated, frequently replenished by primitive liquids and active during the entire evolution of the island.

In order for the antecrysts to be included in the ascending magmas, recharge from the antecryst forming chamber to the main fractionating chamber was necessary. Therefore, depending on the availability of antecrysts within the magmatic system, antecryst-

bearing or -free magmas erupted. Alternatively, given the high density and size of the antecrysts, they may not always have reached the surface. Both hypotheses agree with the occurrence of subvertical porphyritic and microporphyritic dikes which cross the volcanostratigraphical sequence, commonly interpreted as magma conduits (França et al., 2002, 2003). The scarcity of antecrysts with major resorption and recrystalization rims imply relatively short residence times within the host melts that carried them to the surface.

8.7 Conclusions

This chapter presents a detailed petrographic and geochemical study of the volcanic products of Corvo Island. These products are representative of the complete volcanostratigraphic sequence including lava flows, dikes and xenoliths. Two types of lava flows and dikes from the Pre-, Syn- and Post-caldera stages were distinguished based on their texture: porphyritic samples and microporphyritic samples; the former more Mg-rich.

Some melts accumulated variable proportions of olivine, clinopyroxene and plagioclase antecrysts (from 80 % to 8 % of the total volume fraction), generating porphyritic rocks. The antecrysts are large subhedral to anhedral crystals that did not crystallize from the magma represented by the groundmass where they are now hosted; instead, they crystallized in the same magmatic system from related but more primitive comagmatic magmas. The presence and composition of the antecrysts affects the whole rock compositions, which become more mafic with increasing proportions of antecrysts. This should be taken into account when using whole rock compositions to draw information on magmatic processes, where the most primitive compositions are commonly selected.

In consequence, microporphyritic rocks have been used to identify the magmatic processes involved in the generation of Corvo Island. These rocks are mainly composed of plagioclase, olivine, clinopyroxene and opaque microcrysts. The microporphyritic rocks of the three volcanic stages are related by polybaric fractional crystallization starting in an ~ 15 km deep magma chamber. The xenoliths included in these rocks are

cumulates related to this process. Syn-caldera melts evolved by fractional crystallization from Pre-caldera melts in a shallow magma chamber. Post-caldera melts derived from the same ~ 15 km deep magma chamber as Pre-caldera melts.

The antecrysts were formed in a deeper magma chamber that received continuous influxes of primitive magmas. Injection of these magmas into the fractionating chamber would provide antecrysts to ascending Pre- and Post-caldera melts.

APPENDIX

Table I

Analytical procedures in the three laboratories used for Corvo Island whole rock analyses.

(1) ACTLAB laboratory, Canada

(www.actlabs.com)

Major elements

http://tiny.cc/2wr05w

Trace elements

http://tiny.cc/i1r05w

Samples were prepared and analyzed in a batch system. Each batch contained a method reagent blank, certified reference material and 17 % replicates. Samples were mixed with a flux of lithium metaborate and lithium tetraborate and fused in an induction furnace. The molten melt was immediately poured into a solution of 5 % HNO_3 containing an internal standard, and mixed continuously until completely dissolved (~ 30 minutes). The samples were run for major oxides and selected trace elements (Code 4B) on a combination simultaneous/sequential Thermo Jarrell-Ash ENVIRO II ICP. The sample solution prepared under Code 4B was spiked with internal standards to cover the entire

mass range, was further diluted and was introduced into a Perkin Elmer SCIEX ELAN 9000 ICP-MS using a proprietary sample introduction methodology to analyze trace elements (code 4B2).

Calibration was performed using 7 prepared USGS and CANMET certified reference materials. One of the 7 standards was used during the analysis for every group of ten samples.

(2) Servicio de Espectrometría y DRX of the Universidad de Oviedo, Spain
(www.sct.uniovi.es)

http://tiny.cc/f4r05w

Major elements analyses were performed using glass beads of powdered rocks after fusion with lithium tetraborate.
Major elements were analyzed by X-Ray fluorescence (XRF) using WD-XRF PHILIPS PANALYTICAL 2404 spectrometer coupled with a Rh Tube. Precision of the XRF technique was better than ± 1 % relative.

(3) Centro de Instrumentación Científica Universidad de Granada, Spain
(cic.ugr.es)

http://tiny.cc/44r05w

Trace-element determinations were done by ICP-MS after HNO_3 + HF digestion of 0.100 g of sample powder in a Teflon-lined vessel at ~ 180 °C and ~ 200 p.s.i during 30 min, evaporation to dryness, and subsequent dissolution in 100 ml of 4 vol. % HNO_3. Instrument measurements were carried out in triplicate with a PE SCIEX ELAN-5000 spectrometer using Rh as internal standard. Precision was better than ± 2 % and ± 5 % relative for analyte concentrations of 50 and 5 ppm, respectively.

Detection Limits of the analyzed elements:

Element	(1) ACTLAB	(2) Servicio de Espectrometría y DRX	(3) Centro de Instrumentación Científica
Sample type	Lavas	Dikes and xenoliths	Dikes and xenoliths
SiO_2	0.01 %	0.01 %	-
TiO_2	0.00 %	0.00 %	-
Al_2O_3	0.01 %	0.01 %	-
$Fe_2O_3^T$	0.01 %	0.01 %	-
MnO	0.00 %	0.01 %	-
MgO	0.01 %	0.01 %	-
CaO	0.01 %	0.01 %	-
Na_2O	0.01 %	0.01 %	-
K_2O	0.01 %	0.01 %	-
P_2O_5	0.01 %	0.01 %	-
LOI	0.01 %	0.01 %	-
Rb	1 ppm	-	0.001 - 0.01 ppm
Cs	0.1 ppm	-	< 0.001 ppm
Sr	2 ppm	-	< 0.001 ppm
Ba	3 ppm	-	0.001 - 0.01 ppm
Sc	1 ppm	-	0.001 - 0.01 ppm
V	5 ppm	-	0.001 - 0.01 ppm
Cr	20 ppm	-	0.01-0.1 ppm
Co	1 ppm	-	< 0.001 ppm
Ni	20 ppm	-	0.001 - 0.01 ppm
Cu	10 ppm	-	0.001 - 0.01 ppm
Zn	30 ppm	-	0.001 - 0.01 ppm
Sn	1 ppm	-	0.001 - 0.01 ppm
Ga	1 ppm	-	< 0.001 ppm
Mo	2 ppm	-	0.001 - 0.01 ppm
Y	0.1 ppm	-	< 0.001 ppm
Nb	0.1 ppm	-	< 0.001 ppm
Ta	0.01 ppm	-	< 0.001 ppm
Zr	1 ppm	-	0.001 - 0.01 ppm
Hf	0.1 ppm	-	< 0.001 ppm
Pb	3 ppm*	-	0.001 - 0.01 ppm
U	0.01 ppm	-	< 0.001 ppm
Th	0.01 ppm	-	< 0.001 ppm
La	0.05 ppm	-	< 0.001 ppm
Ce	0.05 ppm	-	< 0.001 ppm
Pr	0.01 ppm	-	< 0.001 ppm
Nd	0.05 ppm	-	0.001 - 0.01 ppm
Sm	0.01 ppm	-	< 0.001 ppm
Eu	0.005 ppm	-	< 0.001 ppm
Gd	0.01 ppm	-	0.001 - 0.01 ppm
Tb	0.01 ppm	-	< 0.001 ppm
Dy	0.01 ppm	-	< 0.001 ppm
Ho	0.01 ppm	-	< 0.001 ppm
Er	0.01 ppm	-	< 0.001 ppm
Tm	0.005 ppm	-	< 0.001 ppm
Yb	0.01 ppm	-	< 0.001 ppm
Lu	0.002 ppm	-	< 0.001 ppm

Table II

Major (wt. %) and trace (ppm) element composition of the studied lavas, dikes and xenoliths from Corvo Island.

Unit	Pre-caldera Unit							
Sample	COR 23	COR 24	COR 25	COR 35	COR 11	COR 50	COR 55	COR 56
	Lava	Dike	Dike	Dike	Lava	Lava	Dike	Dike
Texture	Microporph.	Microporph.	Porphyritic	Microporph.	Microporph.	Microporph.	Porphyritic	Porphyritic
Vol. fraction of macrocrysts			15 - 20 % Ol 35 - 40 % Cpx < 5 % Pl				5 -10 % Ol 15 - 20 % Cpx < 5 % Pl	< 5 % Ol 5 - 10 % Cpx < 5 % Pl
wt %								
SiO_2	51.74	47.55	45.66	45.95	48.36	48.08	45.49	45.60
TiO_2	2.19	2.89	1.68	2.88	3.02	3.00	2.36	2.68
Al_2O_3	17.25	16.09	10.13	16.16	16.89	16.82	13.39	14.83
$Fe_2O_3^T$	9.26	11.54	10.25	13.27	11.70	11.70	11.67	12.59
MnO	0.22	0.21	0.15	0.20	0.23	0.23	0.18	0.20
MgO	3.15	5.30	15.22	5.55	4.08	4.18	10.02	7.71
CaO	6.55	8.98	13.98	11.21	8.01	8.02	12.61	11.86
Na_2O	5.07	3.76	1.60	3.16	4.52	4.76	2.40	2.76
K_2O	2.50	1.83	0.61	1.31	1.96	1.83	0.90	1.13
P_2O_5	0.84	0.70	0.24	0.52	1.06	1.11	0.40	0.46
LOI	1.22	1.08	0.83	-0.11	-0.07	0.10	0.10	0.10
TOTAL	98.77	98.85	99.52	100.21	99.83	99.73	99.42	99.82
Mg#	27.43	33.79	62.27	31.73	27.93	28.42	48.83	40.50
(ppm)								
Rb	70	49	19	35	70	63	21	28
Cs	0.5	0.3	0.2	0.3	0.9	0.2	0.1	0.1
Sr	718	738	330	663	864	848	483	568
Ba	817	613	204	481	590	556	344	418
Sc	8	15	43	22	10	9	33	28
V	104	222	251	378	170	153	279	298
Cr	< DL	47	1200	< DL	< DL	< DL	323	140
Co	12	27	56	45	23	18	44	41
Ni	< DL	53	324	54	31	< DL	140.95	82.00
Cu	< DL	60	181	68	15	17	89.22	92.68
Zn	121	106	67	109	128	106	76	82
Sn	4	1	< DL	6	3	2	< DL	1
Ga	23	21	12	22	22	21	17	19
Mo	3	3	< DL	2	2	3	2	2
Y	40.1	33.0	15.1	27.8	39.5	37.9	21.1	25.0
Nb	127.5	93.2	30.4	69.5	133.0	113.8	45.4	54.0
Ta	8.62	6.49	1.99	4.83	10.08	8.78	3.50	4.20
Zr	314	232	96	191	317	310	147	176
Hf	7.8	6.1	2.7	5.2	8.6	7.6	4.1	4.8
Pb	5	< DL	< DL	< DL	7	4	1.14	1.39
U	2.66	2.03	0.58	1.57	3.06	2.71	0.98	1.34
Th	11.30	8.30	2.52	6.48	13.33	10.70	4.02	4.87
La	90.2	70.3	21.5	50.8	87.7	75.6	33.2	39.9
Ce	162.9	128.1	41.9	94.5	155.5	140.7	64.1	78.5
Pr	17.06	13.52	4.75	10.42	16.45	15.93	7.76	9.36
Nd	65.9	53.2	20.2	42.4	64.8	60.1	30.3	37.2
Sm	11.60	9.78	4.14	8.18	11.67	10.84	6.16	7.41
Eu	3.73	3.27	1.42	2.73	3.48	3.06	1.92	2.34
Gd	9.11	7.89	3.58	6.94	9.12	9.33	5.67	6.64
Tb	1.43	1.22	0.55	1.05	1.44	1.41	0.84	1.00
Dy	8.37	7.14	3.25	6.08	8.11	7.63	4.74	5.59
Ho	1.45	1.25	0.58	1.05	1.45	1.48	0.89	1.05
Er	4.16	3.41	1.54	2.83	4.09	3.75	2.17	2.63
Tm	0.59	0.48	0.20	0.38	0.58	0.55	0.31	0.36
Yb	3.65	2.97	1.23	2.40	3.69	3.31	1.82	2.17
Lu	0.52	0.41	0.17	0.32	0.48	0.53	0.27	0.32
$(Tb/Yb)_N$	1.74	1.83	2.01	1.94	1.74	1.89	2.07	2.05

$Fe_2O_3^T$: total Fe expressed as Fe_2O_3; LOI: Loss On Ignition; < DL: below the detection limit.
Mg# = MgO/(FeO+MgO)·100 where FeO = 0.9·$Fe_2O_3^T$.
Mineral abbreviations are according to Whitney and Evans (2010); Microporph.: Microporphyritic

Unit	Pre-caldera Unit							
Sample	COR 57	COR 3	COR 4	COR 9	COR 9 /R	COR 7	COR 12	COR 13
	Dike	Lava	Lava	Lava	Lava	Lava	Lava	Lava
Texture	Porphyritic	Microporph.	Microporph.	Porphyritic	Porphyritic	Porphyritic	Porphyritic	Microporph.
Vol. fraction of macrocrysts	5 - 10 % Ol 15 - 20 % Cpx < 5 % Pl			< 2 % Ol 10 % Pl	< 2 % Ol 10 % Pl	5 - 10 % Ol 10 -15 % Cpx < 5 % Pl	10 - 15 % Ol 30 - 35 % Cpx < 5 % Pl	
wt %								
SiO_2	45.42	48.58	48.56	43.79	43.48	44.41	45.49	47.94
TiO_2	2.39	2.61	2.67	2.95	2.94	2.57	1.97	2.41
Al_2O_3	13.81	17.22	17.43	18.31	18.22	14.23	11.86	17.48
$Fe_2O_3^T$	11.81	11.14	11.40	13.01	12.99	12.80	10.95	11.87
MnO	0.18	0.21	0.21	0.19	0.19	0.19	0.17	0.23
MgO	9.82	4.10	4.20	4.95	4.93	9.47	13.43	2.85
CaO	12.33	8.32	8.43	12.04	11.98	12.07	13.81	7.14
Na_2O	2.52	3.98	3.77	2.30	2.29	1.94	1.75	4.15
K_2O	0.97	1.92	1.87	0.70	0.71	0.88	0.55	2.05
P_2O_5	0.40	0.83	0.82	0.51	0.51	0.42	0.26	0.87
LOI	0.15	0.26	0.40	1.34	1.34	1.26	-0.06	1.93
TOTAL	99.65	98.90	99.36	98.75	98.24	98.98	100.24	96.99
Mg#	48.03	29.03	29.05	29.72	29.66	45.12	57.68	21.06
(ppm)								
Rb	24	56	51	12	12	23	15	52
Cs	0.1	0.4	0.5	0.1	0.2	0.2	0.1	0.4
Sr	496	755	761	805	804	587	409	751
Ba	352	660	691	528	525	412	227	753
Sc	33	13	13	21	21	31	41	6
V	277	190	195	345	343	334	282	89
Cr	248	< DL	< DL	< DL	< DL	532	894	< DL
Co	44	26	27	44	44	55	61	22
Ni	132	37	37	74	72	173	266	29
Cu	85	32	31	97	103	98	110	13
Zn	77	115	120	96	112	99	61	127
Sn	< DL	2	2	2	2	3	1	2
Ga	17	23	22	23	23	19	14	25
Mo	2	2	< DL	< DL	< DL	< DL	< DL	2
Y	21.9	32.5	33.0	27.7	27.1	27.4	17.1	42.1
Nb	46.4	103.5	102.2	69.7	69.2	60.7	33.3	110.2
Ta	3.63	7.28	7.38	5.00	4.92	4.31	2.41	9.03
Zr	152	264	270	183	184	158	106	305
Hf	4.2	6.6	6.7	5.0	5.0	4.4	3.2	7.3
Pb	3.01	< DL	12	< DL	< DL	8	< DL	< DL
U	1.05	2.08	1.90	1.28	1.26	1.26	0.68	2.63
Th	4.11	9.50	9.46	6.16	6.16	5.30	2.84	10.65
La	34.2	74.0	76.9	51.3	51.1	56.9	23.5	89.0
Ce	66.3	132.9	138.6	92.5	91.8	80.9	46.0	157.2
Pr	8.05	14.17	14.49	10.23	10.07	9.82	5.31	17.19
Nd	32.2	56.0	56.5	41.1	40.4	39.1	22.7	67.3
Sm	6.42	9.91	10.18	7.84	7.77	7.06	4.75	12.09
Eu	1.97	3.17	3.20	2.65	2.62	2.38	1.66	3.92
Gd	5.97	7.64	8.05	6.52	6.52	6.15	4.30	9.95
Tb	0.88	1.18	1.21	1.00	0.98	0.91	0.67	1.49
Dy	4.96	6.81	7.00	5.71	5.68	5.23	3.76	8.82
Ho	0.92	1.17	1.20	1.01	0.99	0.91	0.65	1.52
Er	2.23	3.27	3.35	2.70	2.74	2.49	1.75	4.29
Tm	0.33	0.46	0.47	0.37	0.37	0.34	0.23	0.60
Yb	1.96	2.88	2.97	2.29	2.39	2.10	1.46	3.65
Lu	0.29	0.39	0.40	0.32	0.32	0.28	0.20	0.50
$(Tb/Yb)_N$	1.99	1.82	1.81	1.94	1.84	1.93	2.04	1.82

Unit	Pre-caldera Unit					Syn-caldera Unit	
Sample	COR 16	COR 17	COR 15	COR 14	COR 52	COR 28	COR 26
	Lava	Lava	Dike	Dike	Dike	Pumice	Pumice
Texture	Porphyritic	Porphyritic	Porphyritic	Porphyritic	Porphyritic	Glassy	Glassy
Vol. fraction	< 2 % Ol	15 - 20 % Ol	10 -15 % Ol	< 5 % Ol	10 - 15 % Ol		20 - 25 % Cpx
of macrocrysts	5 - 10 % Cpx	40 - 45 % Cpx	15 -20 % Cpx	5 - 10 % Cpx	25 - 30 % Cpx		
	10 % Pl	< 5 % Pl	< 5 % Pl	< 5 % Pl	< 5 % Pl		
wt %							
SiO_2	46.36	45.40	44.64	44.99	45.37	54.87	59.00
TiO_2	2.72	1.63	2.45	2.74	2.11	1.19	0.15
Al_2O_3	17.08	10.02	13.84	15.91	12.88	17.35	16.94
$Fe_2O_3^T$	11.35	10.05	12.24	12.32	11.08	8.68	4.27
MnO	0.18	0.15	0.17	0.19	0.18	0.27	0.22
MgO	5.32	15.41	10.68	7.07	11.41	1.61	0.11
CaO	12.76	14.17	12.94	12.08	13.36	4.00	0.77
Na_2O	3.03	1.47	2.12	2.87	1.75	5.43	6.59
K_2O	1.23	0.40	0.49	0.45	0.79	2.85	4.81
P_2O_5	0.49	0.21	0.34	0.43	0.35	0.50	0.03
LOI	-0.23	0.90	0.29	0.54	0.30	1.66	5.87
TOTAL	100.52	98.91	99.91	99.05	99.28	96.76	92.89
Mg#	34.25	63.02	49.23	38.94	53.37	17.09	2.78
(ppm)							
Rb	35	8	13	21	19	86	242
Cs	0.3	< DL	1.3	0.8	0.1	0.9	2.7
Sr	666	286	498	615	445	611	5
Ba	481	190	288	400	314	992	11
Sc	25	50	34	26	39	4	1
V	298	235	340	333	256	13	< DL
Cr	51	1250	460	166	399	< DL	< DL
Co	39	64	56	47	45	7	< DL
Ni	74	298	223	118	167	< DL	< DL
Cu	168	108	94	89	98	< DL	< DL
Zn	87	68	86	123	67	118	110
Sn	1	1	2	1	< DL	2	7
Ga	21	13	17	19	15	23	33
Mo	2	< DL	< DL	2	1	5	13
Y	26.1	15.8	20.2	23.5	19.5	35.5	69.7
Nb	62.6	28.4	43.2	58.9	40.6	150.7	338.1
Ta	4.53	1.94	3.03	4.20	3.02	10.25	28.88
Zr	172	91	136	161	127	405	1320
Hf	4.7	2.8	3.8	4.6	3.5	9.3	31.3
Pb	< DL	< DL	8.16	< DL	1.67	7	11
U	1.32	0.48	0.89	1.27	0.88	3.24	11.71
Th	5.42	2.30	3.75	5.19	3.55	13.77	48.95
La	43.4	18.5	30.7	42.4	30.6	100.4	215.4
Ce	83.0	37.5	58.3	79.0	58.4	175.8	338.7
Pr	9.11	4.42	6.59	8.62	7.03	17.62	29.65
Nd	37.3	19.2	27.8	35.3	27.7	63.7	89.7
Sm	7.43	4.09	5.60	6.92	5.65	10.29	13.21
Eu	2.53	1.45	1.95	2.39	1.76	3.32	0.63
Gd	6.25	3.79	4.86	5.79	5.06	7.26	8.57
Tb	0.98	0.58	0.76	0.89	0.77	1.20	1.81
Dy	5.55	3.37	4.38	5.16	4.17	7.17	12.15
Ho	0.95	0.58	0.75	0.88	0.80	1.26	2.41
Er	2.65	1.57	2.05	2.40	2.05	3.69	7.69
Tm	0.37	0.21	0.28	0.34	0.28	0.55	1.41
Yb	2.27	1.27	1.77	2.11	1.68	3.59	8.90
Lu	0.31	0.17	0.23	0.29	0.25	0.51	1.28
$(Tb/Yb)_N$	1.92	2.02	1.91	1.89	2.05	1.49	0.91

Unit	Post-caldera Unit							
Sample	COR 20	COR 21	COR 31	COR 31 /R	COR 22	COR 51	COR 5	COR 54
	Lava	Lava	Lava	Lava	Lava	Lava	Lava	Lava
Texture	Porphyritic	Porphyritic	Porphyritic	Porphyritic	Microporph.	Microporph.	Microporph.	Microporph.
Vol. fraction of macrocrysts	10 - 15 % Ol < 5 % Pl	< 2 % Ol <5 % Cpx 5 -10 % Pl	< 5 % Ol < 2 % Cpx < 2 % Pl	< 5 % Ol < 2 % Cpx < 2 % Pl				
wt %								
SiO_2	44.74	45.13	42.07	42.42	49.34	47.52	47.63	47.50
TiO_2	2.09	2.96	2.95	2.97	2.77	3.15	3.13	3.18
Al_2O_3	13.49	16.73	15.17	15.26	17.04	16.67	17.03	16.79
$Fe_2O_3^T$	11.45	12.54	13.14	13.22	10.79	11.99	12.02	12.08
MnO	0.17	0.19	0.19	0.19	0.21	0.22	0.22	0.23
MgO	11.11	5.33	6.30	6.35	3.90	4.40	4.31	4.39
CaO	12.91	11.75	10.91	10.99	7.27	8.30	8.17	8.30
Na_2O	1.98	2.56	3.40	3.42	4.17	4.65	3.97	4.31
K_2O	0.49	1.46	1.13	1.18	2.43	1.77	1.80	1.78
P_2O_5	0.29	0.55	0.51	0.50	0.85	1.08	1.03	1.10
LOI	1.22	0.75	-0.53	-0.53	1.39	0.10	0.95	0.30
TOTAL	98.72	99.20	95.77	96.50	98.76	99.75	99.31	99.66
Mg#	51.88	32.08	34.76	34.80	28.66	28.97	28.49	28.77
(ppm)								
Rb	6	37	34	33	57	53	62	51
Cs	0.8	0.3	0.3	0.3	0.4	0.2	0.3	0.1
Sr	464	681	633	635	726	867	888	862
Ba	299	531	429	432	571	557	580	559
Sc	35	24	23	22	12	11	11	11
V	272	319	386	406	153	162	189	159
Cr	786	< DL	119	110	< DL	< DL	< DL	< DL
Co	58	40	46	45	23	19	25	20
Ni	212	44	76	76	< DL	< DL	35	< DL
Cu	124	143	83	81	30	20	17	20
Zn	87	94	102	104	113	98	127	102
Sn	1	1	1	1	3	2	3	2
Ga	16	21	21	21	22	21	23	21
Mo	< DL	2	2	2	2	3	< DL	2
Y	19.8	28.4	26.8	25.7	33.6	36.6	39.5	36.5
Nb	38.5	73.1	71.9	69.5	107.1	101.0	132.7	102.5
Ta	2.69	5.14	4.84	4.66	7.38	7.88	9.94	8.16
Zr	114	209	175	175	278	278	310	281
Hf	3.5	5.4	5.0	4.8	7.1	7.0	8.3	7.1
Pb	< DL	< DL	< DL	< DL	< DL	3	< DL	3
U	0.79	1.59	1.46	1.42	2.26	2.30	2.97	2.43
Th	3.26	6.54	6.17	6.03	9.39	8.99	13.03	9.47
La	29.9	54.4	50.5	48.9	74.5	69.8	86.1	71.1
Ce	54.6	102.2	94.7	91.7	139.1	132.9	152.5	134.2
Pr	6.34	10.76	10.21	9.95	14.90	15.27	16.09	15.53
Nd	26.6	43.5	40.8	40.0	59.3	57.5	62.8	58.8
Sm	5.34	8.38	7.85	7.59	10.92	11.01	11.37	10.84
Eu	1.90	2.78	2.68	2.59	3.36	3.13	3.32	3.16
Gd	4.76	6.66	6.52	6.27	8.64	9.32	9.05	9.46
Tb	0.73	1.05	0.98	0.97	1.30	1.38	1.41	1.41
Dy	4.19	6.12	5.75	5.61	7.46	7.43	8.01	7.45
Ho	0.75	1.05	0.99	0.98	1.28	1.42	1.41	1.45
Er	1.97	2.84	2.70	2.66	3.49	3.54	3.93	3.60
Tm	0.27	0.41	0.37	0.36	0.48	0.50	0.56	0.53
Yb	1.73	2.49	2.35	2.30	3.13	3.04	3.59	3.22
Lu	0.24	0.34	0.32	0.32	0.41	0.50	0.49	0.51
$(Tb/Yb)_N$	1.89	1.88	1.86	1.87	1.86	2.02	1.74	1.95

Unit	Xenoliths		
Sample	COR-ENC1	COR-ENC3	COR-ENC4
	Gabbro	Gabbro	Gabbro
Texture	Heteroadcumulate	Heteroadcumulate	Heteroadcumulate
Vol. fraction of macrocrysts			
wt %			
SiO_2	41.52	41.50	39.65
TiO_2	2.62	3.35	4.41
Al_2O_3	12.58	19.25	17.34
$Fe_2O_3^T$	14.97	14.19	14.88
MnO	0.16	0.17	0.18
MgO	11.65	4.31	6.39
CaO	15.31	13.26	11.77
Na_2O	1.02	2.32	2.84
K_2O	0.12	0.37	0.72
P_2O_5	0.08	0.50	1.16
LOI	0.18	0.32	0.80
TOTAL	100.03	99.22	99.34
Mg#	46.38	25.24	32.31
(ppm)			
Rb	3	6	11
Cs	< DL	< DL	< DL
Sr	403	954	887
Ba	74	226	347
Sc	42	17	20
V	492	339	329
Cr	255	22	< DL
Co	47	24	26
Ni	72	< DL	< DL
Cu	22	27	27
Zn	61	77	98
Sn	< DL	< DL	< DL
Ga	17	21	20
Mo	6	15	8
Y	13.9	14.9	25.9
Nb	9.1	24.0	44.5
Ta	0.75	1.82	3.18
Zr	65	82	96
Hf	2.3	2.4	2.9
Pb	0.17	0.87	0.72
U	0.35	0.41	0.61
Th	1.06	1.68	2.46
La	12.3	26.1	35.3
Ce	21.5	44.7	69.3
Pr	3.27	5.67	9.30
Nd	14.6	23.1	39.8
Sm	3.60	4.70	8.40
Eu	1.16	1.66	2.68
Gd	3.49	4.11	7.67
Tb	0.52	0.60	1.07
Dy	2.90	3.14	5.79
Ho	0.56	0.59	1.05
Er	1.36	1.45	2.44
Tm	0.18	0.19	0.32
Yb	1.12	1.17	1.84
Lu	0.18	0.18	0.28
$(Tb/Yb)_N$	2.04	2.28	2.59

FINAL CONSIDERATIONS

FINAL CONSIDERATIONS

The present PhD Thesis is the first exhaustive study on the petrology, mineralogy and geochemistry of Graciosa and Corvo Islands. A detailed study of the mineral and whole rock compositions has allowed for the characterization of the different volcanological units and the investigation of the magmatic processes that control the evolution of the islands, enhancing the importance of antecryst accumulation in lava flows. Furthermore, Graciosa Island has been more extensively studied to make data comparable to the other two islands of the Terceira Rift. $^{40}Ar/^{39}Ar$ ages of the most remarkable volcanic events occurred during the growth of Graciosa Island provide a better understanding of its temporal evolution. Sr-Nd-Pb isotopic compositions have led to broader conclusions on the Azores mantle source.

Magmatic processes in Graciosa and Corvo Islands

A comprehensive investigation of the petrography of lavas and dikes from Graciosa and Corvo Islands has revealed the existence of two major rock-textures: porphyritic and microporphyritic. Moreover, trachytic and glassy textures are characteristic of the studied trachytes and pumices, respectively.

The main difference between the porphyritic and microporphyritic textures recognized in the studied samples is the presence of large crystals (macrocrysts). The porphyritic rocks show a variable proportion of these macrocrysts set in a fine-grained groundmass, whereas the microporphyritic rocks are macrocrysts-free and resemble the groundmass

of the porphyritic rocks. This study differentiated two crystal populations according to their size: macrocrysts (> 2 mm) and microcrysts (< 2 mm).

Further investigation of equilibrium conditions between these crystals and their host rocks has led to decipher their origin. Macrocrysts from Graciosa Island in equilibrium with the rock in which they are included are phenocrysts, whereas Graciosa and Corvo microcrysts and macrocryst rims are related to progressive fractionation of the magma. In contrast, most macrocrysts in Corvo rocks and isolated examples from Graciosa Island are in clear disequilibrium with their host magma, and are non-cogenetic antecrysts.

Additionally, the influence of these antecrysts on whole rock compositions has been shown, as rocks display more mafic compositions with increasing proportions of antecrysts. This is particularly important when using whole rock compositions to draw information on magmatic processes, where the most primitive compositions are commonly selected.

Consequently, only microporphyritic rocks have been used to identify the magmatic processes involved in the generation of Corvo Island, whereas both, porphyritic and microporphyritic rocks, have been considered for Graciosa Island studies. In both islands, fractional crystallization is the main magmatic process responsible for the formation of lava flows and alkaline gabbro xenoliths (also dikes in Corvo). These rocks can be related by a polybaric fractional crystallization starting in a ~ 15 km deep magma chamber, and the alkaline gabbros included in these rocks are magma chamber cumulates formed at crustal levels. The most evolved volcanic products (trachytic lavas, pumices and syenites) evolve by fractional crystallization in shallower magma chambers (< 3 km).

Subalkaline gabbros from Graciosa Island are also magma chamber cumulates, but related to fractionation of a highly refractory melt not observed within the volcanic sequence of any Azorean island to date.

Accordingly, in Graciosa Island the most primitive magmas start to fractionate at oceanic crustal depths of ~ 15 km and fractionation continues in polybaric conditions up to ~ 1 km depth. During the way up to the surface, phenocrysts grow in equilibrium with the host melts and microcryst grow almost entirely on surface conditions. Therefore, the existence of porphyritic or microporphyritic rocks depends exclusively on the initial composition of the melt and its fractionation rate, within the magma chamber and during ascent to surface prior to eruption.

In Corvo island, an accumulation process is required to explain the existence of porphyritic rocks. Primitive magmas in this island fractionated in a deeper magma chamber, in which the antecrysts crystallized. This chamber was frequently replenished by primitive liquids and was active during the entire evolution of the island. It provided antecrysts to the main fractionating chamber (located at ~ 15 km depth) where slightly more evolved melts fractionated giving rise to the crystallization of microcrysts in equilibrium with this melts. Therefore, depending on the availability of antecrysts within the magmatic system and the eruptive power of the magma, antecryst-bearing or antecryst-free magmas erupted and generated porphyritic or microporphyritic lava flows on surface, respectively.

Temporal evolution of Graciosa Island and future dating project

The most remarkable volcanic events taking place during the formation of Graciosa Island have been dated by $^{40}Ar/^{39}Ar$. These new ages together with previous K/Ar and ^{14}C geochronological data have been evaluated and considered to develop a new chronology for the evolution of Graciosa Island. New ages range from 1056 ± 28.0 ka to 3.9 ± 1.4 ka. The oldest age provides a new minimum age for the beginning of subaerial volcanism on the island.

The temporal stages commonly defined in oceanic islands (submarine, shield, erosional and rejuvenated) are developed much faster in Graciosa Island than in other islands from the Canary or Hawaii archipelagos. The shield stage remained active for ca. 850 ky, comprising the evolution of the primitive Serra das Fontes shield volcano to the evolved

Serra das Fontes - Serra Branca composite volcano. The erosive stage lasted ca. 110 ky and was characterized by volcanic inactivity and erosion of previous volcanic edifices. Strikingly, the rejuvenated stage has been extremely active (~ the last 100 ky) generating most of the current surface of the island, including the Vitória NW platform and Vulcão Central SE stratovolcano. Present-day activity is scarce on the island.

According to the new $^{40}Ar/^{39}Ar$ ages and previous dating experiments carried out in the Azores Islands, Graciosa Island is contemporaneous with São Jorge Island, and older than Pico, Faial and Terceira Islands from the Central Group. Overall, this Central Group is contemporaneous with the Western Group (Corvo and Flores Islands) but younger than the Eastern Group. The age of São Miguel remains unclear, while the easternmost island of Santa Maria is clearly the oldest. Therefore, this investigation contributes to the temporal evolution of the Azores archipelago, although it is necessary to obtain additional and improved age constraints on the different islands. For example, that study would include a dating project of the main volcanic events of Corvo Island; for these purpose, it is critical to first map the volcanic units as defined by França et al. (2002).

Mantle source

Sr-Nd-Pb isotope ratios obtained in Graciosa have been compared to previous isotopic data of the Azores archipelago, in order to characterize the mantle source of Graciosa Island magmas.

The isotopic dataset in Graciosa includes lavas and gabbroic xenoliths (both alkaline and subalkaline) and suggests the involvement of at least two mixing end-member mantle components in the genesis of Graciosa magmas: a depleted MORB and an enriched HIMU. In contrast, the isotopic composition of the studied dunite xenolith may not be related to the Azorean alkaline melts; its composition is consistent with an origin as an olivine- and spinel-bearing lithospheric mantle restite, subsequently metasomatized during alkaline melt-mantle reaction.

Overall, much work has focused on the nature of the source to the east of the MAR, trying to shed light on the geochemical heterogeneities found across the archipelago (e.g., São Miguel Island isotopic signature). For example, in recent times the average common isotopic composition of the Azores archipelago has been related to the composition of the redefined FOZO mantle component, which is believed to be the commonest mantle end-member found in ocean island basalts. However, the unusually enriched Pb isotope array found in certain lavas from São Miguel Island is explained by the presence of small-degree melts from recycled oceanic crust and this common FOZO-like enriched end-member.

In contrast, the nature of the mantle source forming the islands to the west of the MAR had been classically overlooked. However, a recent study of Sr-Nd-Pb-Hf-Os isotopes in Corvo and Flores Islands by Genske (2012) has found that these islands require a similar contribution from MORB and the enriched source present underneath the islands located to the east of the MAR. Therefore, this author offers a broader assessment of the mantle source across the plateau; nevertheless, more studies on the Azores mantle source are necessary to develop a model in agreement with all the available geophysical and geochemical (Sr, Nd, Pb, Hf, Os, He, Ne, B, O, Li isotope ratios) data.

CONSIDERACIONES FINALES

La presente Tesis Doctoral supone el primer estudio exhaustivo acerca de la petrología, la mineralogía y la geoquímica del vulcanismo de las Islas de Graciosa y Corvo, en el archipiélago de las Azores. El estudio detallado de la química mineral y de la geoquímica de roca total ha permitido caracterizar las diferentes unidades volcanoestratigráficas de cada isla, así como los procesos magmáticos que controlan su evolución magmática. También, ha sido puesto de manifiesto, el importante papel que juegan los procesos de acumulación de antecristales en la composición de las rocas que los albergan.

Con el objetivo de adecuar el conocimiento de la Isla de Graciosa con respecto a las demás islas que constituyen el Rift de Terceira (São Miguel y Terceira), se ha realizado un estudio geocronológico mediante el método $^{40}Ar/^{39}Ar$. De esta forma, la datación de los eventos volcánicos más importantes durante la formación de la isla ha permitido establecer su evolución temporal.

Además, el estudio de las relaciones isotópicas de Sr-Nd-Pb en las lavas y los xenolitos de la Isla de Graciosa, ha permitido ampliar la información sobre la fuente del manto que da lugar al magmatismo en la isla que, a su vez, aporta nueva información a la discusión general acerca de la fuente mantélica bajo el archipiélago de las Azores.

El estudio petrográfico de las coladas de lava y de los diques estudiados en las Islas de Graciosa y Corvo, ha permitido establecer dos tipos principales de texturas en estas rocas volcánicas: porfídicas y microporfídicas. No obstante, también han sido reconocidas texturas traquíticas en las muestras evolucionadas de Graciosa, así como texturas vítreas en las pumitas de Corvo.

La mayor diferencia existente entre las rocas porfídicas y las microporfídicas es la presencia o ausencia de grandes cristales (macrocristales). Las rocas porfídicas presentan una proporción variable de macrocristales incluidos en una matriz de grano fino (mesostasia); sin embargo, las rocas microporfídicas carecen de macrocristales y su aspecto es similar al de la mesostasia de las rocas porfídicas. De este modo, se han definido dos poblaciones cristalinas en base a su tamaño: macrocristales (> 2 mm) y microcristales (< 2 mm).

El estudio de las condiciones de equilibrio entre estas dos poblaciones de cristales y las rocas que las albergan, ha permitido establecer el origen de los mismos. Los macrocristales presentes en las muestras de Graciosa son en su mayoría fenocristales en equilibrio con la roca en la que se encuentran; además, los microcristales y los bordes de los macrocristales estudiados en ambas islas están relacionados con procesos de fraccionación magmática. Sin embargo, la mayor parte de los macrocristales estudiados en Corvo, y algún ejemplo aislado de la Isla de Graciosa, están claramente en desequilibrio con la roca en la que se encuentran, siendo por lo tanto, antecristales no cogenéticos con el resto de cristales estudiados.

Adicionalmente, se ha demostrado la influencia que ejercen estos macrocristales en la composición de la roca total, haciendo que una roca inicialmente pobre en MgO, aumente su contenido tanto en éste como en otros elementos, de manera directamente proporcional al contenido en antecristales acumulados en la roca. Esto, es especialmente relevante a la hora de escoger composiciones primitivas a partir de las cuales estudiar los procesos magmáticos que relacionan una suite de rocas, ya que rocas

que presentan un elevado contenido en MgO, pueden presentar acumulación de antecristales no cogenéticos y, por lo tanto, no pueden ser consideradas rocas primitivas de dicha suite.

Teniendo en cuenta lo anterior, sólo se han seleccionado rocas sin antecristales, para los modelos de los procesos magmáticos. Así, en la Isla de Corvo tan solo han sido utilizadas las rocas microporfídicas, mientras que para la Isla de Graciosa se han usado tanto las porfídicas como las microporfídicas. En ambas islas, la cristalización fraccionada en condiciones polibáricas ha resultado ser el principal proceso magmático que ha dado lugar a la formación de las coladas de lavas y de los xenolitos gabroicos de composición alcalina y, en el caso específico de la Isla de Corvo, a los diques estudiados. El proceso de cristalización fraccionada comenzó en una cámara magmática situada a unos 15 km de profundidad y los gabros alcalinos representan cumulados de cámara magmática formados en diferentes niveles corticales. Además, los productos volcánicos de composición más evolucionada (coladas de lava de naturaleza traquítica, pumitas y sienitas), se formaron en cámaras magmáticas más someras (< 3 km) como resultado de altas tasas de cristalización fraccionada. Igualmente, los gabros subalcalinos, descritos por primera vez en el archipiélago de las Azores, representan también cumulados de cámara magmática, pero en este caso relacionados con la fraccionación de fundidos altamente refractarios, no identificados hasta la fecha en las Islas Azores.

De acuerdo con el modelo de fraccionación polibárica establecido para la Isla de Graciosa, los fenocristales cristalizaron en equilibrio con los fundidos en los que se encontraban, mientras que los microcristales se formaron casi en condiciones superficiales. Por lo tanto, la existencia de rocas porfídicas o microporfídicas en Graciosa, depende exclusivamente de la composición inicial de los fundidos y de su tasa de fraccionación, tanto en la cámara magmática como durante su ascenso hasta el momento de la erupción.

Sin embargo, para explicar la formación de las rocas porfídicas presentes en la Isla de Corvo, es necesaria la existencia de un importante proceso de acumulación de antecristales. En este caso, los fundidos primitivos se fraccionaron en una cámara

magmática más profunda, dando lugar a la formación de antecristales; esta cámara tuvo que cumplir dos condiciones: (1) mantenerse activa a lo largo de todo el periodo de formación de la isla y (2) ser frecuentemente recargada por fundidos primitivos. De esta forma, los antecristales fueron incorporados en la cámara magmática principal (~ 15 km), donde fundidos ligeramente más evolucionados se fraccionaron, dando lugar a la formación de microcristales en equilibrio con esos fundidos. Por tanto, la presencia o ausencia de antecristales en las rocas de Corvo, está relacionada con la disponibilidad de los mismos en el sistema magmático, dando lugar así, a rocas porfídicas o microporfídicas en superficie.

Evolución temporal de la Isla de Graciosa y futuras dataciones

Se han datado mediante la técnica $^{40}Ar/^{39}Ar$ los eventos volcánicos más significativos que han tenido lugar a lo largo de la formación de la Isla de Graciosa. Las nuevas edades obtenidas, junto con la edades K/Ar y ^{14}C previas, han sido consideradas para establecer la evolución geocronológica de la isla. Se han obtenido 9 edades en coladas de lava y 1 edad en uno de los gabros alcalinos; estos resultados se distribuyen en un periodo comprendido entre 1056 (± 28,0) ka y 3,9 (± 1,4) ka, estableciendo, de este modo, una nueva edad mínima para el inicio del vulcanismo en la Isla de Graciosa.

Otra importante conclusión del estudio temporal de la Isla de Graciosa es que los estadios propios de evolución de una isla oceánica (etapa submarina, escudo, erosiva y de rejuvenecimiento), se han desarrollado mucho más rápido que en otras islas de los archipiélagos de Canarias o Hawai. En concreto, la etapa de escudo duró unos 850 ky, incluyendo la formación del volcán en escudo de Serra das Fontes y su evolución hacia un volcán de tipo compuesto (Serra das Fontes - Serra Branca). La etapa erosiva, caracterizada por la ausencia de volcanismo y una alta tasa de erosión de los edificios volcánicos anteriores, duró al menos 110 ky. Finalmente, la etapa de rejuvenecimiento ha sido extremadamente activa durante los últimos 100 ky, aunque la actividad actual es escasa. Durante este tiempo, se ha generado la mayor parte de la superficie actual de la isla, con la plataforma de Vitória al NO y el estratovolcán “Vulcão Central” al SE.

De acuerdo con las nuevas edades $^{40}Ar/^{39}Ar$, y con todas las edades previamente publicadas en las Islas Azores, la formación de la Isla de Graciosa es contemporánea a la formación de la Isla de São Jorge y más antigua que las Islas de Faial, Pico y Terceira pertenecientes al grupo central. A su vez, este grupo central es contemporáneo al grupo occidental (constituido por las Islas de Flores y Corvo). Con respecto a las islas del grupo oriental, Graciosa parece ser más reciente que las Islas de São Miguel (aunque su edad está en duda) y de Santa María, que es la isla más oriental y más antigua de todo el archipiélago de las Azores.

Cabe destacar que este trabajo de datación de la Isla de Graciosa contribuye al conocimiento general del archipiélago; sin embargo, serán necesarios nuevos estudios geocronológicos en algunas de estas islas para esclarecer la evolución temporal del archipiélago en su conjunto. Por ejemplo, estos estudios necesariamente deben incluir un proyecto de datación de la Isla de Corvo. No obstante, para poder alcanzar ese objetivo es necesario abordar la elaboración de una cartografía geológica con la distribución de las diferentes unidades volcánicas identificadas por França et al. (2002).

Fuente de manto

Nuevas determinaciones de las relaciones isotópicas de Sr-Nd-Pb en lavas y xenolitos de Graciosa han sido comparadas con datos isotópicos previos del archipiélago de las Azores, con el objetivo de caracterizar la fuente mantélica que ha dado lugar a la formación de los magmas en Graciosa.

El conjunto de datos isotópicos sugiere al menos dos componentes mantélicos en la génesis de los magmas de Graciosa: un componente empobrecido de tipo MORB y un componente enriquecido de tipo HIMU. Además, cabe resaltar que el estudio isotópico de una dunita muestreada en la isla, indica que su origen no está relacionado con los fundidos alcalinos de las Azores, sino que se trata de una restita compuesta exclusivamente por olivino y espinela, que posteriormente fue metasomatizada por estos fundidos alcalinos.

En general, la mayor parte de los estudios relacionados con la fuente mantélica de las Azores han sido desarrollados en las islas localizadas al este de la dorsal centro-atlántica, con el objetivo de investigar las heterogeneidades del manto encontradas a lo largo del archipiélago (e.g., la signatura isotópica de la Isla de São Miguel). En la actualidad, la comunidad científica empieza a relacionar la composición isotópica media de las Azores con la composición de manto recientemente redefinida como FOZO, la cual parece estar presente en la signatura isotópica de la mayor parte de islas oceánicas. Sin embargo, la inusual fuente enriquecida en Pb de alguna de las lavas de la Isla de São Miguel, requiere de la presencia de pequeñas proporciones de fundidos procedentes de corteza oceánica reciclada junto con esta fuente mantélica similar a FOZO.

Por el contrario, la fuente de manto del grupo occidental de islas (al oeste de la dorsal centro-atlántica) ha sido poco estudiada. Un estudio reciente de isótopos de Sr-Nd-Pb-Hf-Os en las Islas de Corvo y Flores, realizado por Genske (2012), ha demostrado que la composición isotópica en estas islas requiere la contribución de un componente empobrecido de tipo MORB, y de un componente enriquecido (como el localizado al este de la dorsal centro-atlántica).

Como consideración final, para obtener una visión más global de la composición del manto bajo las Azores, es necesario continuar estudiando la composición de las islas menos conocidas y tratar de poner en común todos los datos geofísicos y geoquímicos (isótopos de Sr, Nd, Pb, Hf, Os, He, Ne, B, O, Li).

REFERENCES

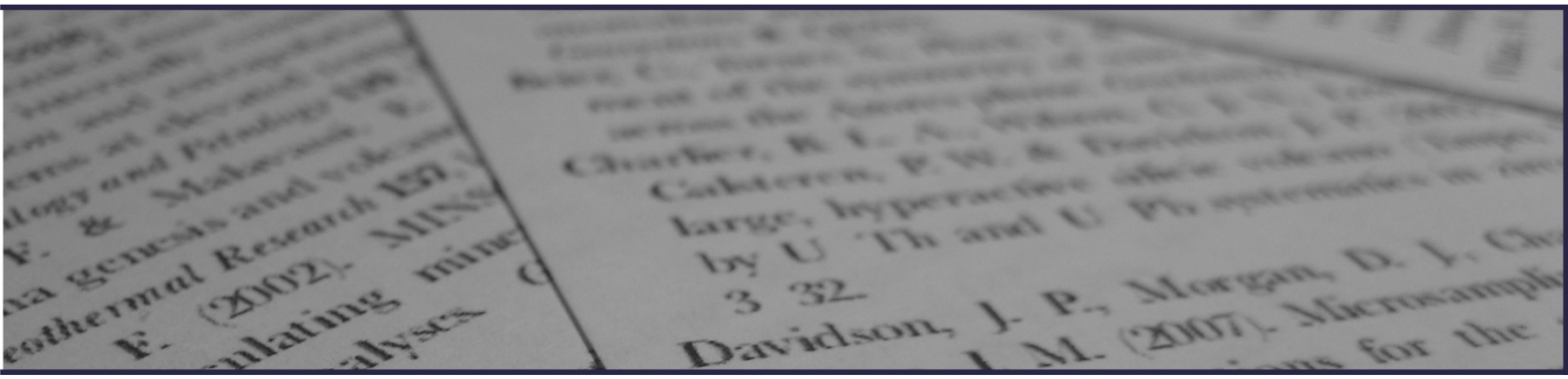

REFERENCES

Abdel-Monem, A.A., Fernandez, L.A. and Boone, G.M. (1975). K-Ar ages from the Eastern Azores group (Santa Maria, São Miguel and the Formigas Islands). *Lithos* **8**, 247-254.

Abdel-Monem, A.A., Watkins, N.O. and Gast, P.W. (1972). Potassium-argon ages, volcanic stratigraphy, and geomagnetic polarity history of the Canary Islands: Tenerife, La Palma and Hierro. *American Journal of Science* **272** (9), 805-825.

Adam, C., Madureira, P., Miranda, J.M., Lourenço, N., Yoshida, M. And Fitzenz, G. (2013). Mantle dynamics and characteristics of the Azores plateau. *Earth and Planetary Science Letters* **362**, 258-271.

Agostinho, J. (1937). Volcanic activity in the Azores, Report for 1933-1936. *Bulletin Volcanologique* **2** (11), 183-192.

Akinin, V.V., Sobolev, A.V., Ntaflos, T. and Richter, W. (2005). Clinopyroxene megacrysts from Enmelen melanephelinitic volcanoes (Chukchi Peninsula, Russia): application to composition and evolution of mantle melts. *Contributions to Mineralogy and Petrology* **150**, 85-101.

Allan, J.F. and Dick, H.J. (1996). *Cr-rich spinel as a tracer for melt migration and melt-wall rock interaction in the mantle: Hess Deep, leg 147*. In: Mevel, C., Gillis, K.M., Allan, J.F. and Meyer, P.S. (eds.) *Proceedings of the Ocean Drilling Program, Scientific Results, 147*. College Station,TX: Ocean Drilling Program, 157-172.

Almeida, M.H. (2001). *A fonte mantélica na região dos Açores: constrangimentos impostos pelas características geoquímicas de rochas vulcânicas e de xenolitos ultramáficos*. PhD Thesis, Dep. Geociências, Universidade dos Açores, São Miguel, Azores, Portugal.

Anderson, R.N., McKenzie, D. and Sclater, J.G. (1973) Gravity, bathymetry and convection in the Earth. *Earth and Planetary Science Letters* **18**, 391-407.

Asimow, P.D. and Ghiorso, M.S. (1998). Algorithmic Modifications Extending MELTS to Calculate Subsolidus Phase Relations. *American Mineralogist* **83**, 1127-1131.

Azevedo, J.M.M. (1998). *Geologia e Hidrogeologia da ilha das Flores (Açores - Portugal)*. PhD Thesis, Dep. Ciências da Terra, University of Coimbra, Coimbra, Portugal.

Azevedo, J.M.M., Alves, E.I. and Dias, J.L. (2003). Contributo para a interpretação vulcanostrutural da ilha do Corvo, Açores*. Ciências da Terra (UNL)* **5**, 2-3.

Azevedo, J.M.M. and Ferreira, M.R.P. (1999). Volcanic gaps and subaerial records of palaeo-sea-levels on Flores Island (Azores): tectonic and morphological implications. *Geodynamics* **28**, 117-129.

Azevedo, J.M.M. and Ferreira, M.R.P. (2006). The volcanotectonic evolution of Flores Islands, Azores (Portugal). *Journal of Volcanology and Geothermal Research* **156**, 90-102.

Baptista, P., Osório, J., Bastos, L., Fernandes, R. and Borges, F.S. (1999). Aplicação de técnicas geodésicas ao estudo do comportamento geodinâmico actual da Junção Tripla dos Açores. *GEOlogos* **5**, 1-12.

Baxter, P.J., Baubron, J.C. and Coutinho, R. (1999). Health hazards and disaster potential of ground gas emission at Furnas volcano, São Miguel, Azores. *Journal of Volcanology and Geothermal Research* **92** (1-2), 95-106.

Beier, C. (2006). *The magmatic evolution of Oceanic Plateaus: a case study from the Azores*. PhD Thesis, Faculty of Mathematics and Natural Sciences, University of Kiel, Germany.

Beier, C., Haase, K.M., Abouchami, W., Krienitz, M.S. and Hauff, F. (2008). Magma genesis by rifting of oceanic lithosphere above anomalous mantle: Terceira Rift, Azores. *Geochemistry, Geophysics, Geosystems* **9** (12), Q12013.

Beier, C., Haase, K.M. and Hansteen, T.H. (2006). Magma evolution of the Sete Cidades Volcano, São Miguel, Azores. *Journal of Petrology* **47**, 1375-1411.

Beier, C., Mata, J., Stöckhert, F., Mattielli, N., Brandl, P.A., Madureira, P., Genske, F.S., Martins, S., Madeira, J. and Haase, K.M. (2013). Geochemical evidence for melting of carbonated peridotite on Santa Maria Island, Azores. *Contributions to Mineralogy and Petrology* **165** (5), 823-841.

Beier, C., Stracke, A. and Haase, K.M. (2007). The peculiar geochemical signatures of São Miguel (Azores) lavas: Metasomatised or recycled mantle source? *Earth and Planetary Science Letters* **259**, 186-189.

Beier, C., Turner, S., Plank, T. and White, W. (2010). A preliminary assessment of the symmetry of source composition and melting dynamics across the Azores plume. *Geochemistry, Geophysics, Geosystems* **11** (2), Q02004.

Berthois, L. (1953). Contribuition à l'étude lithologique de l'archipel des Açores. *Comunicações dos Serviços Geológicos de Portugal* **34**, 96-116.

Botazzi, P., Tiepolo, M., Vannucci, R., Zanetti, A., Brumm, R., Foley, S.F. and Oberti, R. (1999). Distinct site preferences for heavy and light REE in amphibole and the prediction of Amph/LDREE. *Contributions to Mineralogy and Petrology* **137**, 36-45.

Bougault, H. and Treuil, M. (1980). Mid-Atlantic Ridge: Zero-age geochemical variations between Azores and 22N. *Nature* **286**, 209-212.

Bourdon, B., Langmuir, C.H. and Zindler, A. (1996). Ridge-hotspot interaction along the Mid-Atlantic ridge between 37º30' and 40º30 'N: the U-Th disequilibrium evidence. *Earth and Planetary Science Letters* **142**, 175-190.

Bourdon, B., Turner, S. and Ribe, N.M. (2005). Partial melting and upwelling rates beneath the Azores from U-series isotope perspective. *Earth and Planetary Science Letters* **239** (1-2), 42-56.

Bowin, C., Thompson, G. and Schilling, J.G. (1984). Residual geoid anomalies in Atlantic Ocean Basin: Relationship to mantle plumes. *Journal of Geophysical Research* **89**, 9905-9918.

Buforn, E., Udiás, A. and Colombás, M. (1988). Seismicity, source mechanisms and tectonics of the Azores-Gibraltar plate boundary. *Tectonophysics* **15**, 89-118.

Calvert, A.T., Moore, R.B., McGeehin, J.P. and Rodrigues da Silva, A.M. (2006). Volcanic history and $^{40}Ar/^{39A}r$ and ^{14}C geochronology of Terceira Island, Azores, Portugal. *Journal of Volcanology and Geothermal Research* **156**, 103-115.

Cannat, M., Briais, A., Deplus, C., Escartín, J., Georgen, J., Lin, J., Mercourier, S., Meyzen, C., Muller, M., Pouliquen, G., Rabain, A. and Da Silva, P. (1999). Mid-Atlantic Ridge - Azores hotspot interactions: along-axis migration of a hotspot-derived event of enhanced magmatism 10 to 4 Ma ago. *Earth and Planetary Science Letters* **173**, 257-269.

Carracedo, J.C. (2011). *Geología de Canarias I (Origen, evolución, edad y volcanismo)*. Editorial Rueda, Madrid.

Cazenave, A., Houry, S., Lago, B. and Dominh, K. (1992). Geosatderived geoid anomalies at medium wavelength. *Journal of Geophysical Research* **97**, 7081-7096.

Charlier, B.L.A., Wilson, C.J.N., Lowenstern, J.B., Blake, S., Van Calsteren, P.W. and Davidson, J.P. (2005). Magma generation at a large, hyperactive silicic volcano (Taupo, New Zealand) revealed by U-Th and U-Pb systematics in zircons. *Journal of Petrology* **46**, 3-32.

Cruz, J.V., Coutinho, R.M., Carvalho, M.R., Oskarsson, N. and Gislason, S.R. (1999). Chemistry of waters from Furnas volcano, São Miguel, Azores: fluxes of volcanic carbon dioxide and leached material. *Journal of Volcanology and Geothermal Research* **92**, 151-167.

Cruz, J.V. and França, Z. (2001). *Mineral and thermal waters in the Azores archipelago (Portugal): Geological setting and hydrogeochemical outline*. In: Seiler, K.P and Wohnlich, S. (eds.) *Proceedings of the XXXI IAH Congress - New Approaches to Characterising Groundwater Flow*. Munich, Balkema Publishers, 477-481.

Davidson, J.P., Morgan, D.J., Charlier, B.L.A., Harlou, R. and Hora, J.M. (2007). Microsampling and isotopic analysis of igneous rocks: implications for the study of magmatic systems. *Annual Review of Earth and Planetary Sciences* **35**, 273-311.

Davies, G.F. (1999). *Dynamic Earth: Plates Plumes and Mantle Convection*. Cambridge: University Press, Cambridge.

Davies, G.R., Norry, M.J., Gerlach, D.C. and Cliff, R.A. (1989). *A combined chemical and Pb-Sr-Nd isotope study of the Azores and Cap Verde hot-spots: the geodynamic implications*. In: Saunders, A.D and Norry, M.J. (eds.) *Magmatism in the Oceanic Basins.* Leicester: Geological Society Special Publications, 231-255.

Demand, J., Fabriol, R., Gerard, F., Lundt, F. and Chovelon, P. (1982). *Prospection géothermique, íles de Faial et de Pico (Açores)*. Rapport géologique, geochimique et gravimétrique. Technical report, BRGM 82 SGN 003 GTH.

DePaolo, D.J. and Manga, M. (2003). Deep Origin of Hotspots - the Mantle Plume Model. *Science* **300**, 920-921.

Dias, J.L.F. (2001). *Geologia e tectónica da Ilha do Corvo, contributos para o ordenamento do espaço físico*. PhD Thesis, University of Coimbra, Portugal.

Dick, H.J.B. and Bullen, T. (1984). Chromian spinel as a petrogenetic indicator in oceanic environments. *Contributions to Mineralogy and Petrology* **86**, 54-76.

Donaldson, C.H. and Brown, R.W. (1977). Refractory megacrysts and magnesium-rich melt inclusions within spinel in oceanic tholeiites: indicators of magma mixing and parental magma composition. *Earth and Planetary Science Letters* **37**, 81-89.

Dosso, L., Bougault, H., Langmuir, C., Bollinger, C., Bonnier, O. and Etoubleau, J. (1999). The age and distribution of mantle heterogeneity along the Mid-Atlantic Ridge (31 – 41 degrees N). *Earth and Planetary Science Letters* **170**, 269-286.

Droop, G.T.R. (1987). A general equation for estimating Fe^{3+} concentrations in ferromagnesian silicates and oxides from microprobe analyses, using stoichiometric criteria. *Mineralogical Magazine* **51**, 431-435.

Duncan, R.A. and Green, D.H. (1980). Role of multistage melting in the formation of oceanic crust. *Geology* **8**, 22-26.

Duncan, R.A. and Green, D.H. (1987). The genesis of refractory melts in the formation of oceanic crust. *Contributions to Mineralogy and Petrology* **96**, 326-342.

Eggler, D.H. (1972). Water-saturated and undersaturated melting relations in a Paricutin andesite and estimate of water content in natural magma. *Contributions to Mineralogy and Petrology* **34**, 261-271.

Elliott, T., Blichert-Toft, J., Heumann, A., Koetsier, G. and Forjaz, V.H. (2007). The origin of enriched mantle beneath São Miguel, Azores. *Geochimica et Cosmochimica Acta* **71** (1), 219-240.

Escartín, J., Cannat, M., Pouliquen, G. and Rabain, A. (2001). Crustal thickness of V-shaped ridges south of the Azores: Interaction of the Mid-Atlantic Ridge (36º-39º N) and the Azores hot spot. *Journal of Geophysical Research* **106** (10), 21719-21735.

Esenwein, P. (1930). Zur Petrografie der Azores. *Zeitschrift für Vulkanologie* **12** (3), 108-227.

Feraud, G., Kaneoka, J. and Allègre, C. (1980). K/Ar ages and stress pattern in the Azores: Geodynamic implications. *Earth and Planetary Science Letters* **46**, 275-286.

Feraud, G., Gastaud, J., Schmincke, H.U., Pritchard, G., Lietz, J. and Bleil, U. (1981). New K-Ar ages, chemical analyses and magnetic data of rocks from the islands of Santa Maria (Azores), Porto Santo and Madeira (Madeira Archipelago) and Gran Canaria (Canary Islands). *Bulletin Volcanologique* **44**, 359-375.

Ferreira, A. (1968). *Ilha Graciosa*. Livros Horizonte, Lisboa.

Ferreira, M.P. and Azevedo, J.M. (1995). *Evolução geológica do arquipélago dos Açores baseada na geocronologia*. Seminar Geologia Atlântica A.P.G. 9, Ponta Delgada (São Miguel, Açores).

Ferreira, T. and Oskarsson, N. (1999). Chemistry and isotopic composition of fumarole discharge of Furnas caldera. *Journal of Volcanology and Geothermal Research* **92**, 169-179.

Foulger, G.R. (2010). *Plates vs. Plumes: A geological controversy*. Wiley-Blackwell, Chichester, UK.

Forjaz, V.H. (1983). *Azores tectonic sketch*. Centro de Vulcanologia, Universidade dos Açores, São Miguel, Azores, Portugal. Unpublished Research Report.

Forjaz, V.H., França, Z. and Nunes, J.C. (2001). *Serretian: a new type of submarine eruptions*. In: Stewart, C. (ed.) *Cities on Volcanoes 2. Abstracts book*. Auckland, New Zealand.

Forjaz, V.H. and Pereira, V. (1976). *Carta Vulcanológica Preliminar da ilha Graciosa, scale 1:25.000*. São Miguel: Instituto de Geociências dos Açores, Portugal.

Forjaz, V.H., Tavares, J.M., Azevedo, E.M.V.B., Nunes, J.C., Santos, R.S., Barreiros, J.P., Gallagher, L., Barcelos, P.J.M., Silva, P.H., Cardigos, F., França, Z., Dentinho, T., Costa, M.P., Magalhães, L., Rodrigues, M.C., Gonçalves, J.P., Silva, V. and Serpa, V. (2004). *Atlas Básico dos Açores*. São Miguel: Observatótio Vulcanológico e Geotérmico dos Açores, Portugal.

França, Z. (1993). *Contribuição para o estudo dos xenólitos sieníticos do Arquipélago dos Açores*. M.S. Thesis, Geosciences Department, Universidade dos Açores, Ponta Delgada, São Miguel, Portugal.

França, Z. (2000). *Origem e evolução petrológica e geoquímica do vulcanismo da ilha do Pico*. PhD Thesis, Geosciences Department, Universidade dos Açores, Ponta Delgada, São Miguel, Portugal.

França, Z., Almeida, M.H. and Wallenstein, N. (1995). Ocurrência de xenólitos mantélicos numa lava da ilha do Pico. *Gaia* **11**, 47-52.

França, Z., Cruz, J.V., Nunes, J.C. and Forjaz, V.H. (2003). Geologia dos Açores: uma perspectiva actual. *Açoreana* **10** (1), 11-140.

França, Z., Lago, M., Nunes, J. C., Galé, C., Forjaz, V.H., Pueyo, Ó. and Arranz, E. (2006*a*). Geochemistry of alkaline basalts of Corvo Island (Azores, Portugal): preliminary data. *Geogaceta* **40**, 87-90.

França, Z., Nunes, J.C., Cruz, J.V., Duarte, H.F. and Forjaz, V.H. (2002). *Estudo preliminar do vulcanismo da Ilha do Corvo, Açores*. In: Garcia, F.G. and Valero, J.L. (eds.) *Procceedings da 3ª Assembleia Luso-Espanhola de Geodesia e Geofisica.* University Politécnica de Valencia, Valencia, Spain, Vol. 2., 727-730.

França, Z., Rodrigues, B. and Forjaz, V.H. (2010). *Retrospectiva petrogeoquímica dos Açores. Uma primeira aproximação*. In: Cotelo Neiva, J.M., Ribeiro, A., Victor, M., Noronha, F. and Ramalho, M. (eds.) *Geologia das Ilhas dos Arquipélagos dos Açores, Madeira e Geologia das* antigas Colónias, Publicação Comemorativa do "Ano Internacional do planeta Terra". Associação Portuguesa de Geólogos, Sociedade Geológica de Portugal, Vol. 3 (I), 3-16.

França, Z.T.M., Tassinari, C.C.G., Cruz, J.V., Aparicio, A.Y., Araña, V. and Rodrigues, B.N. (2006*b*). Petrology, geochemistry and Sr–Nd–Pb isotopes of the volcanic rocks from Pico Island, Azores (Portugal). *Journal of Volcanology and Geothermal Research* **156**, 71-89.

Gaspar, J.L. (1996*). Ilha Graciosa (Açores). História vulcanológica e avaliaçao do hazard*. PhD Thesis, Dep. Geociências, Universidade dos Açores, Portugal.

Gaspar, J.L. and Queiroz, G. (1995). *Carta vulcanológica das Açores, ilha Graciosa, sheet A and B, scale 1:10,000*. Graciosa: Azores University and Câmara Municipal de Santa Cruz da Graciosa, Portugal.

Gaspar, J.L., Queiroz, G., Pacheco, J.M., Ferreira, T. and Wallenstein, N. (2003). *Basaltic lava balloons produced during the 1998-2001 Serreta Submarine Ridge eruption (Azores)*. In: White, J., Clague, D. and Smellie, J. (eds.) *Subaqueous explosive volcanism. AGU Monograph*, Vol. 2, 205-212.

Genske, F.S., Turner, S.P., Beier, C. and Schaefer, B.F. (2012). The Petrology and Geochemistry of Lavas from the Western Azores Islands of Flores and Corvo. *Journal of Petrology* **53** (8), 1637-1671.

Gente, P. (1987). *Etude morphostructurale comparative de dorsales océaniques à taux d'expansion variés*. PhD Thesis, Univ. de Bretagne Occidentale, Brest, France.

Gente, P., Dyment, J., Maia, M. and Goslin, J. (2003). Interaction between the Mid-Atlantic Ridge and the Azores hot spot during the last 85 Myr: Emplacement and rifting of the hot spot-derived plateaus. *Geochemistry, Geophysics, Geosystems* **4** (10), 8514.

Georgen, J.E. and Sankar, R.D. (2010). Effects of ridge geometry on mantle dynamics in an oceanic triple junction region: Implications for the Azores Plateau. *Earth and Planetary Science Letters* **298**, 23-34.

Gertisser, R., Self, S., Gaspar, J.L., Kelley, S.P., Pimentel, A., Eikenberg, J., Barry, T.L., Pacheco, J.M., Queiroz, G. and Vespa, M. (2010). *Ignimbrite stratigraphy and chronology on Terceira Island, Azores*. In: Groppelli, G. and Viereck-Goette, L. (eds.) *Stratigraphy and Geology of Volcanic Areas*. Geological Society of America Special Paper, Vol. 464, 133-154.

Ghiorso, M.S. and Sack, R.O. (1995). Chemical Mass Transfer in Magmatic Processes. IV. A Revised and Internally Consistent Thermodynamic Model for the Interpolation and Extrapolation of Liquid-Solid Equilibria in Magmatic Systems at Elevated Temperatures and Pressures. *Contributions to Mineralogy and Petrology* **119**, 197-212.

Gill, J., Reagan, M., Tepley, F. and Malavassi, E. (2006). Arenal Volcano, Costa Rica. Magma Genesis and volcanological Processes. *Journal of Volcanology and Geothermal Research* **157**, 1-8.

Hartung, G. (1860). *Die Azoren in ihrer ausseren Erschreinung und nach ihrer geognostichen Natur*. Engelman Verlag, Leipzig.

Hauri, E.H., Wagner, T.P. and Grove, T.L. (1994). Experimental and natural partitioning of Th, U, Pb and other trace elements between garnet, clinopyroxene and basaltic melts. *Chemical Geology* **117**, 149-166.

Hawkesworth, C.J., Norry, M.J., Roddick, J.C. and Vollmer, R. (1979). $^{143}Nd/^{144}Nd$ and $^{87}Sr/^{86}Sr$ ratios from the Azores and their significance in LIL-element enriched mantle. *Nature* **280**, 28-31.

Hekinian, R., Bideau, D., Francheteau, J., Cheminee, J.L., Armijo, R., Lonsdale, P. and Blum, N. (1993). Petrology of the East Pacific Rise and upper mantle exposed in Hess Deep (Eastern equatorial Pacific). *Journal of Geophysical Research* **98**, 8069-8094.

Herrmann, W. and Berry, R.F. (2002). MINSQ - a least squares spreadsheet method for calculating mineral proportions from whole rock major element analyses. *Geochemistry: Exploration, Environment, Analysis* **2**, 361-368.

Hildenbrand, A., Madureira, P., Marques, F.O., Cruz, I., Henry, B. and Silva, P. (2008). Multi-stage evolution of a sub-aerial volcanic ridge over the last 1.3 Myr: S. Jorge Island, Azores Triple Junction. *Earth and Planetary Science Letters* **273**, 289-298.

Hildenbrand, A., Marques, F.O., Costa, A.C.G., Sibrant, A.L.R., Silva, P.F., Henry, B., Miranda, J.M. and Madureira, P. (2012). Reconstructing the architectural evolution of volcanic islands from combined K/Ar, morphologic, tectonic, and magnetic data: The Faial Island example (Azores). *Journal of Volcanology and Geothermal Research* **241-242**, 39-48.

Hipólito, A.R. (2009). *Geologia structural da ilha Graciosa: encuadramento no ámbito da junção tripla dos Açores*. M.S. Thesis, Dep. Geociências, Universidade dos Açores, São Miguel, Azores, Portugal.

Ijlst, L. (1973). Laboratory overflow-centrifuge for heavy liquid mineral separation. *American Mineralogist* **58**, 1088-1093.

Jerram, D.A. and Martin, V.M. (2008). *Understanding crystal populations and their significance through the magma plumbing system*. In: Annen, C. and Zellmer, G.F. (eds.) *Dynamics of crustal Magma Transfer, Storage and Differentiation*. London: Geological Society Special Publications, Vol. 304, 133-148.

Johnson, C.L., Wijbrans, J.R., Constable, C.G., Gee, J., Staudigel, H., Tauxe, L., Forjaz, V.H. and Salgueiro, M. (1998). $^{40}Ar/^{39}Ar$ ages and paleomagnetism of São Miguel lavas, Azores. *Earth and Planetary Science Letters* **160**, 637-649.

Jurewicz, A. and Watson, E.B. (1988). Cations in olivine, Part 1: Calcium partitioning and calcium-magnesium distribution between olivines and coexisting melts, with petrologic applications. *Contributions to Mineralogy and Petrology* **99**, 176-185.

Koppers, A.A.P. (2002). ArArCALC-software for $^{40}Ar/^{39}Ar$ age calculations. *Computer Geosciences* **28**, 605-619.

Krause, D.C. and Watkins, N.D. (1970). North Atlantic crustal genesis in the vicinity of the Azores. *Geophysical Journal of the Royal Astronomical Society* **19**, 261-283.

Krejci-Graf, V.K. (1961). Zur Geologie der Makaronesen. 8 - Die Caldeira von Graciosa, Azoren. *Zeitschrift der Deutschen Geologischen Gesellschaft* **113**, 85-95.

Kress, V.C. and Ghiorso, M.S. (2004). Thermodynamic modeling of post-entrapment crystallization in igneous phases. *Journal of Volcanology and Geothermal Research* **137**, 247-260.

Kuiper, K.F., Deino, A., Hilgen, F.J., Krijgsman, W., Renne, P.R. and Wijbrans, J.R. (2008). Synchronizing rock clocks of earth history. *Science* **320**, 500-504.

Larrea, P. (2010). *Petrología y geoquímica de los enclaves de la isla Graciosa Azores (Portugal)*. M.S. Thesis, Dep. of Earth Sci., University of Zaragoza, Zaragoza, Spain.

Larrea, P., Galé, C., Ubide, T., Widom, E., Lago, M. and França, Z. (under review). Magmatic evolution of Graciosa island (Azores, Portugal). *Journal of Petrology*.

Larrea, P., Galé, C., Ubide, T., Widom, E., Lago, M., França, Z. and Tierz, P. (2012). *Magmatic Evolution of the Western Azores Islands (Corvo and Flores)*. Abstract DI51A-2353 presented at 2012 Fall Meeting, AGU, San Francisco, California (USA).

Larrea, P., Lago, M., França, Z., Widom, E., Galé, C., Ubide, T. and Arranz, E. (2010). Enclaves in Graciosa Island (Açores, Portugal): preliminary data. *Geogaceta* **48**, 155-158.

Larrea, P., França, Z., Lago, M., Widom, E., Galé, C. and Ubide, T. (2013). Magmatic Processes and the Role of Antecrysts in the Genesis of Corvo Island (Azores Archipelago, Portugal). *Journal of Petrology* **54**, 769-793.

Larrea, P., Wijbrans, J.R., Galé, C., Ubide, T., Lago, M. , França, Z. and Widom, E. (2014). $^{40}Ar/^{39}Ar$ constraints on the temporal evolution of Graciosa Island, Azores (Portugal). *Bulletin of Volcanology*, doi: 10.1007/s00445-014-0796-8.

LaTourrette, T., Hervig, R. and Holloway, J. (1995). Trace element partitioning between amphibole, phlogopite, and basanite melt. *Earth and Planetary Science Letters* **135**, 13-30.

Laughton, A.S. and Whitmarsh, R.B. (1974). *The Azores-Gibraltar plate boundary*. In: Kristjansson, L. (ed.) *Geodynamics of Iceland and the North Atlantic area*. Dordrecht: D. Reidel, 62-81.

Laughton, A.S., Whitmarsh, R.B., Rusby, J.S.M., Somers, M.L., Revie, J., McCartney, B.S. and Nafe, J.E. (1972). A continuous East-west fault on the Azores-Gibraltar ridge. *Nature* **237**, 217-220.

Le Bas, M.J., Le Maitre, R.W., Strckeisen, A. and Zanettin, B. (1986). A chemical classification of volcanic rocks based on the total alkali–silica diagram. *Journal of Petrology* **27**, 745-750.

Le Douaran, S. and Francheteau, J. (1981). Axial depth anomalies from 10 to 50 north along the Mid-Atlantic Ridge: Correlation with other mantle properties. *Earth and Planetary Science Letters* **54**, 29-47.

Le Maitre, R.W. (2002). *Igneous rocks: a classification and glossary of terms*. Cambridge Univeristy Press, UK.

Leake, B.E., Wooley, A.R., Arps, C.E.S., Birch, W.D., Gilbert, M.C, Grice, J.D., Hawthorne, F.C., Kato, A., Kisch, H.J., Krivovichev, V.G., Linthout, K., Laird, J., Mandarino, J.A., Maresch W.V., Nickel, E.H., Rock, N.M.S., Schumacher, J.C., Smith, D.C., Stephenson, N.C.N., Ungaretti, L., Whittaker, E.J.W. and Youzhi, G. (1997). Nomenclature of Amphiboles: Report of the Subcommittee on Amphiboles of the International Mineralogical Association Commission on New Minerals and Mineral Names. *The Canadian Mineralogist* **35**, 219-246.

Lemarchand, F. (1987). Les series volcaniques de Fayal (Acores): Étude petrologique et geochimique. *Canadian Journal of Earth Sciences* **24**, 334-353.

Lemarchand, F., Benoit, V. and Calais, G. (1987). Trace element distribution coefficients in alkaline series. *Geochimica et Cosmochimica Acta* **51**(5), 1071-1081.

Leterrier, J., Maury, R.C., Thonon, P., Girard, D. and Marchal, M. (1982). Clinopyroxene composition as a method of identification of the magmatic affinities of paleo-volcanic series. *Earth and Planetary Science Letters* **59** (1), 139-154.

Lourenço, N. (2007). *Tectono-magmatic processes at the Azores triple junction*. PhD thesis, Faculty of Marine Sciences and Environmen, Algarve Univ., Portugal.

Lourenço, N., Miranda, J.M., Luis, J.F., Ribeiro, A., Mendes-Victor, L., Madeira, J. and Needham, H. (1998). Morpho-tectonic analysis of the Azores Volcanic Plateau from a new bathymetric compilation of the area. *Marine Geophysical Research* **20**, 141-156.

Luis, J.F. and Miranda, J.M. (2008). Reevaluation of magnetic chrons in the North Atlantic between 35 N and 47 N: Implications for the formation of the Azores Triple Junction and associated plateau. *Journal of Geophysical Research: Solid Earth* **113**, B10105.

Luis, J.F., Miranda, J.M., Galdeano, A. and Patriat, P. (1998). Constraints on the Structure of the Azores Spreading Center from Gravity Data. *Marine Geophysical Research* **20**, 157-170.

Luis, J.F., Miranda, J.M., Galdeano, A., Patriat, P., Rossignol, J.C. and Mendes-Victor, L.A. (1994). The Azores triple junction evolution since 10 Ma from aeromagnetic survey of the Mid-Atlantic Ridge. *Earth and Planetary Science Letters* **125**, 439-459.

Macdonald, G.A., Abbott, A.T. and Peterson, F.L. (1983). *Volcanoes in the Sea, The Geology of Hawaii*. University of Hawaii Press, Honolulu.

Machado, F. (1959). Submarine pits of the Azores plateau. *Bulletin of Volcanology* **21**, 109-116.

Madeira, J. and Ribeiro, A. (1990). Geodynamic models for the Azores triple junction: a contribution from tectonics. *Tectonophysics* **184** (3-4), 405-415.

Madureira, P. (2006). *Geoquímica elementar e isotópica (He e Ne) das lava máficas da ilha Terceira: evidencias para uma origen profunda da pluma dos Açores*. PhD Thesis, Evora University, Portugal.

Madureira, P., Moreira, M., Mata, J. and Allègre, C.J. (2005). Primitive helium and neon isotopes in Terceira island (Azores archipelago). *Earth and Planetary Science Letters* **233**, 429-440.

Madureira, P., Mata, J., Mattielli, N., Queiroz, G. and Silva, P. (2011). Mantle source heterogeneity, magma generation and magmatic evolution at Terceira Island (Azores archipelago): constraints from elemental and isotopic (Sr, Nd, Hf, Pb) data. *Lithos* **126**, 402-418.

Mallmann, G. and O'Neill, H. (2009). The Crystal/Melt Partitioning of V during mantle Melting as a Function of Oxygen Fugacity Compared with some other Elements (Al, P, Ca, Sc, Ti, Cr, Fe, Ga, Y, Zr and Nb). *Journal of Petrology* **50** (9), 1765-1794.

Marques, F.O., Catalão, J.C., DeMets, C., Costa, A.C.G. and Hildenbrand, A. (2013). GPS and tectonic evidence for a diffuse plate boundary at the Azores Triple Junction. *Earth and Planetary Science Letters* **381**, 177-187.

Matias, L., Dias, N.A., Morais, I., Vales, D., Carrilho, F., Madeira, J., Gaspar, J.L., Senos, L. and Silveira, A.B. (2007). The 9th of July 1998 Faial Island (Azores, North Atlantic) seismic sequence. *Journal of Seismology* **11** (3), 275-298.

Maund, J.G. (1985). *The volcanic geology, petrology and geochemistry of Caldeira volcano, Graciosa, Azores and its bearing on contemporaneous felsic-mafic oceanic island volcanism*. PhD Thesis, University of Reading, United Kingdom.

McDonough, W.F. and Sun, C.C. (1995). Composition of the Earth. *Chemical Geology* **120**, 223-253.

McDougall, I. and Harrison, T.M. (1999). *Geochronology and Thermochronology by the $^{40}Ar/^{39}Ar$ Method*. Oxford University Press, New York.

McKenzie, D. (1972). Active tectonics of the Mediterranean region. *Geophysical Journal of the Royal Astronomical Society* **30**, 109-185.

McKenzie, D. and O'Nions, R.K. (1991). Partial melt distributions from inversion of rare Earth element concentrations. *Journal of Petrology* **32**, 1021-1091.

Meireles, R.P., Farandaf, C., Gliozzi, E., Pimentel, A., Zanon, V. and Ávila, S.P. (2012). Late Miocene marine ostracods from Santa Maria island, Azores (NE Atlantic): Systematics, palaeoecology and palaeobiogeography. *Revue de Micropaléontologie* **55** (4) 133-148.

Mendinabeitia, S.G., Sánchez-Lorda, M.E. and Gil-Ibarguchi, J.I. (2008). Simultaneous determination of major to ultratrace elements in geological samples by fusion-dissolution and inductively coupled plasma mass spectrometry techniques. *Analytica Chimica Acta* **625** (2), 117-130.

Millet, M.A., Doucelancea, R., Bakerb, J.A. and Schianoa, P. (2009). Reconsidering the origins of isotopic variations in Ocean Island Basalts: Insights from fine-scale study of São Jorge Island, Azores archipelago. *Chemical Geology* **265** (3-4), 289-302.

Moniz, A. (1884). *Ilha Graciosa (Açores) - Descripção Historica e Topographica*. Angra do Heroísmo, Terceira.

Morais, J. (1953). Furnas dos Açores. *Memórias e notícias* **35**, 48-75.

Morgan, W.J. (1972). Deep mantle convection plumes and plate motions. *Bulletin - American Association of Petroleum Geologists* **56**, 203-213.

Morimoto, N., Fabries, J., Ferguson, A.K., Ginzburg, I.V., Ross, M., Seifert, F.A., Zussman, J., Aoki, K. and Gottardi, G. (1988). Nomenclature of pyroxenes. *Bulletin de Minéralogie* **111**, 535-550.

Needham, H.D. and Francheteau, J. (1974). Some characteristics of the rift valley in the atlantic ocean near 36°48' north. *Earth and Planetary Science Letters* **22**, 29-43.

Neves, M.C., Miranda, J.M. and Luis, J.F. (2013). The role of lithospheric processes on the development of linear volcanic ridges inthe Azores. *Tectonophysics* **608**, 376-388.

O'Connor, J.M., Stoffers, P., Wijbrans, J.R. and Worthington, T.J. (2007). Migration of widespread long-lived volcanism across the Galápagos Volcanic Province: Evidence for a broad hotspot melting anomaly? *Earth and Planetary Science Letters* **263**, 339-354.

Panjasawatwong, Y., Danyushevsky, L.V. Crawford, A.J. and Harris, K.L. (1995). An experimental study of the effects of melt composition on plagioclase – melt equilibria at 5 and 10 Kbar: implications for the origin of magmatic high-An plagioclase. *Contributions to Mineralogy and Petrology* **118**, 420-432.

Paster, T.P., Schauwecker, D.S. and Haskin, L.A. (1974). The behavior of some trace elements during solidification of the Skaergaard layered series. *Geochimica et Cosmochimica Acta* **38** (10), 1549-1577.

Pearson, D.G., Canil, D. and Shirey, S.B. (2003). *Mantle sample included in volcanic rocks: xenoliths and diamonds*. In: Carlson, R.W. (ed.) *Treatise on geochemistry: the mantle and core*. Amsterdam: Elsevier, 171–276.

Pueyo, Ó., Gil, A., Lago, M., França, Z. and Galé, C. (2006). Magma flow directions in Azores basaltic dykes from AMS data: preliminary results from Corvo island. G*eogaceta* **40**, 83-86.

Rayleigh, J.W.S. (1896). Theoretical considerations respecting the separation of gases by diffusion and similar processes. *Philosophical Magazine* **42**, 77-107.

Rehfeldt, T., Foley, S.F., Jacob, D.E., Carlson, R.W. and Lowry, D. (2008). Contrasting types of metasomatism in dunite, wehrlite and websterite xenoliths from Kimberley, South Africa. *Geochimica et Cosmochimica Acta* **72** (23), 5722–5756.

Rhodes, J.M., Dungan, M.A., Blanchard, D.P. and Long, P.E. (1979). Magma mixing at mid-ocean ridges: Evidence from basalts drilled near 22ºN on the Mid-Atlantic Ridge. *Tectonophysics* **55**, 35-61.

Ribeiro, A. (1982). Tectónica de placas: aplicação à sismotectónica e à evolução da fronteira de placas Açores-Gibraltar. *Geonovas* **1**, 87-96.

Ribeiro, L. (2011). *Petrologic and Geochemical Characterization of São Jorge Island Volcanism, Azores*. PhD Thesis, Dep. Geociências, University of Aveiro, Portugal.

Rodrigues, B., Alves, C.M.A., Serralheiro, A., Forjaz, V.H. (1995). Nota prévia sobre a petrología e geoquímica da ilha de Santa Maria, açores. *Memórias da Academia das Ciências* **46**, 71-91.

Roeder, P.L. and Emslie, R.F. (1970). Olivine-liquid equilibrium. *Contributions to Mineralogy and Petrology* **29**, 275-289.

Sakyi, P.A., Tanaka, R., Kobayashi, K. and Nakamura, E. (2012). Inherited Pb isotopic records in olivine antecryst-hosted melt inclusions from Hawaiian lavas. *Geochimica et Cosmochimica Acta* **95**, 169-195.

Salgueiro, M.A.O. (1991). Estudo paleomagnético e cronología estratigráfica de formações vulcânicas da Ilha de Santa Maria, Açores. *Archipélago* **9**, 83-99.

Saucier, H. (1965). A propos du probleme des calderas. Observations dans l'ile Graciosa, (Acores). *Comunicações dos Serviços Geológicos de Portugal* **48**, 213-246.

Schilling, J.G. (1975). Azores mantle blob: Rare-Earth evidence. *Earth and Planetary Science Letters* **25**, 103-115.

Schminke, H.U. (2004). *Volcanism*. Springer-Verlag Berlin Heidelberg, New York.

Schneider, B., Kuiper, K., Postma, O. and Wijbrans, J. (2009). $^{40}Ar/^{39}Ar$ geochronology using a quadrupole mass spectrometer. *Quaternary Geochronology* **4**, 508-516.

Searle, R. (1980). Tectonic pattern of the Azores spreading center and triple junction. *Earth and Planetary Science Letters* **51**, 415-434.

Serralheiro, A. and Madeira, J. (1993). Stratigraphy and geochronology of Santa Maria Island (Azores). *Açoreana* **7** (4), 575-592.

Shamberger, P.J. and Hammer, J.E. (2006). Leucocractic and Gabbroic Xenoliths from Hualalai Volcano, Hawai'i. *Journal of Petrology* **47**, 1785-1808.

Skulski, T., Minarik, W. and Watson, E.B. (1994). High-Pressure experimental trace-element partitioning between clinopyroxene and basaltic melts. *Chemical Geology* **117**, 127-147.

Sleep, N.H. (1990). Hotspots and mantle plumes: some phenomenology. *Journal of Geophysical Research* **95**, 6715-6736.

Sobolev, A.V. and Shimizu, N. (1993). Ultra-depleted primary melt included in an olivine from the Mid-Atlantic Ridge. *Nature* **363**, 151-154.

Steiger, R.H. and Jäger, E. (1977). Subcommission on geochronology - convention on use of decay constants in geochronology and cosmochronology. *Earth and Planetary Science Letters* **36**, 359-362.

Stormer, J. (1973). Calcium zoning in olivine and its relationship to silica activity and pressure. *Geochimica et Cosmochimica Acta* **27**, 1815-1821.

Stracke, A., Hofmann, A.F. and Hart, S.R. (2005). FOZO, HIMU, and the rest of the mantle zoo. *Geochemistry, Geophysics, Geosystems* **6** (5), Q05007.

Thibaud, R., Gente, P. and Maia, M. (1998). A systematic analysis of the Mid-Atlantic Ridge morphology and gravity between 15N and 40N: Constraints of the thermal structure. *Journal of Geophysical Research* **103**, 223-243.

Todt, W., Cliff, R., Hanser, A. and Hofmann, A. (1996). *Evaluation of a $^{202}Pb/^{205}Pb$ double spike for high - precision lead isotope analysis*. In: Basu, A. and Hart, S. (eds.) *Earth Processes: Reading the Isotopic Code*. Washington: Geophysical Monograph Series, 429-437.

Turner, S., Hawkesworth, C., Rogers, N. and King, P. (1997). U-Th isotope disequilibria and ocean island basalt generation in the Azores. *Chemical Geology* **139** (1-4), 145-164.

Ubide, T. (2013). *The Cretaceous Alkaline Magmatism in Northeast Iberia. Igneous Processes and Geodynamic Implications*. PhD Thesis, Dep. de Ciencias de la Tierra, Universidad de Zaragoza, Zaragoza, Spain.

Ubide, T., Arranz, E., Lago, M., Galé, C. and Larrea, P. (2012). The influence of crystal settling on the compositional zoning of a thin lamprophyre sill: a multimethod approach. *Lithos* **132-133**, 37-49.

Ubide, T., Galé, C., Arranz, E., Lago, M. and Larrea, P. (2014). Clinopyroxene and amphibole crystal populations in a lamprophyre sill from the Catalonian Coastal Ranges (NE Spain): A record of magma history and a window to mineral-melt partitioning. *Lithos* **184-187**, 225-242.

Ubide, T., Wijbrans, J.R., Galé, C., Arranz, E., Lago, M. and Larrea, P. (under review). Age of the Cretaceous alkaline magmatism in northeast Iberia: implications for the Alpine cycle in the Pyrenees. *Tectonics*.

Udías, A. and Arroyo, A. (1972). Plate tectonics and the Azores-Gibraltar region. *Nature Physical Science* **237**, 565-571.

Ustunisik, G. and Kilinc, A. (2011). The role of fractional crystallization, magma recharge, and magma mixing in the differentiation of the Small Hasandag volcano, Central Anatolia, Turkey. *Lithos* **125**, 984-993.

Villemant, B. (1988). Trace-element evolution in the Phlegrean fields (Central Italy): fractional crystallization and selective enrichment. *Contributions to Mineralogy and Petrology* **98**, 169-183.

Villemant, B., Jaffrezic, H., Joron, J.L. and Treuil, M. (1981). Distribution Coefficients of Major and Trace-Elements - Fractional Crystallization in the Alkali Basalt Series of Chaine-Des-Puys (Massif Central, France). *Geochimica et Cosmochimica Acta* **45** (11), 1997-2016.

Vinet, N. and Higgins, M.D. (2010). Magma Solidification Processes beneath Kilauea Volcano, Hawaii: a Quantitative Textural and Geochemical Study of the 1969-1974 Mauna Ulu Lavas. *Journal of Petrology* **51** (6), 1297-1332.

Viveiros, F., Ferreira, T., Silva, C., and Gaspar, J.L. (2009). Meteorological factors controlling soil gases and indoor CO_2 concentration: A permanent risk in degassing areas. *Science of The Total Environment* **407** (4), 1362-1372.

Vogt, P.R. (1976). Plumes, subaxial pipe flow and topography along the mid-oceanic ridge. *Earth and Planetary Science Letters* **29**, 309-325.

Vogt, P.R. and Jung, W.Y. (2004). The Terceira Rift as hyper-slow hotspot-dominated oblique spreading axis: A comparison with other slow-spreading plate boundaries. *Earth and Planetary Science Letters* **218**, 77-90.

Walker, G.P.L. (1990). Geology and volcanology of the Hawaiian Islands. *Pacific Science* **44** (4), 315-347.

Walter, M.J. and Presnall, D.C. (1994). Melting behavior of simplified lherzolite in the system CaO-MgO-Al_2O_3-SiO_2-Na_2O from 7 to 35 Kbar. *Journal of Petrology* **35**, 329-359.

Weinstein, Y., Weinberger, R. and Calvert, A. (2013). High-resolution $^{40}Ar/^{39}Ar$ study of Mount Avital, northern Golan: reconstructing the interaction between volcanism and a drainage system and their impact on eruptive styles. *Bulletin of Volcanology* **75**, 712.

White W.D. and McKenzie, D. (1989). Magmatism at rift zones: the generation of volcanic continental margins and flood basalts. *Journal of Geophysical Research* **94**, 7685-7730.

White, W.M. and Schilling, J.G. (1978). The nature and origin of geochemical variation in the Mid-Atlantic Ridge basalts from the central North Atlantic. *Geochimica et Cosmochimica Acta* **42**, 1501-1516.

White, W.M., Schilling, J.G. and Hart, S.R. (1976). Evidence for the Azores mantle plume from strontium isotope geochemistry of the Central North Atlantic. *Nature* **263**, 659-663.

White, W.M., Tapia. M.D.M. and Schilling, J.G. (1979). The petrology and geochemistry of the Azores Islands. *Contributions to Mineralogy and Petrology* **69**, 201-213.

Whitney, D.L. and Evans, B.W. (2010). Abbreviations for names of rock-forming minerals. *American Mineralogist* **95**, 185-187.

Widom, E. and Shirey, S.B. (1996). Os isotope systematics in the Azores: implications for mantle plume sources. *Earth and Planetary Science Letters* **142** (3-4), 451-465.

Widom, E., Gill, J.B. and Schmincke, H.U. (1993). Syenite Nodules as a Long-Term Record of Magmatic Activity in Agua de Pao Volcano, Sao Miguel, Azores. *Journal of Petrology* **34** (5), 929-953.

Widom, E., Carlson, R.W., Gill, J.B. and Schmincke, H.U. (1997). Th-Sr-Nd-Pb isotope and trace element evidence for the origin of the Sao Miguel, Azores, enriched mantle source. *Chemical Geology* **140**, 49-68.

Wijbrans, J., Németh, K., Martin, U. and Balogh, K. (2007). $^{40}Ar/^{39}Ar$ geochronology of Neogene phreatomagmatic volcanism in the western Pannonian Basin, Hungary. *Journal of Volcanology and Geothernmal Research* **164**, 193-204.

Wijbrans, J., Schneider, B., Kuiper, K., Calvari, S., Branca, S., De Beni, E., Norini, G., Corsaro, R.A. and Miraglia, L. (2011). $^{40}Ar/^{39}Ar$ geochronology of Holocene basalts; examples from Stromboli, Italy. *Quaternary Geochronology* **6**, 223-232.

Wilson, J.T. (1963). A possible origin of the Hawaiian Islands. *Canadian Journal of Physics* **41**, 863-870.

Winter, J.D. (2010). *Principles of igneous and metamorphic petrology*. Pearson Prentice Hall, Upper Saddle River, USA.

Witt-Eickschen, G. and Harte, B. (1994). Distribution of trace elements between amphibole and clinopyroxene from mantle peridotites of the Eifel (western Germany); an ion-microprobe study. *Chemical Geology* **117** (1-4), 235-250.

Yang, T., Shen, Y., Van der Lee, S., Solomon, S.C. and Hung, S.H. (2006).Uppermantle structure beneath the Azores hot spot from finite-frequency seismic tomography. *Earth and Planetary Science Letters* **250**, 11-26.

Yu, D., Fontignie, D. and Schilling, J.G. (1997). Mantle plume-ridge interactions in the central North Atlantic: A Nd isotope study of Mid-Atlantic Ridge basalts from 30N to 50N. *Earth and Planetary Science Letters* **146**, 259-272.

Zack, T. and Brumm, R. (1998). *Ilmenite/liquid partition coefficients of 26 trace elements determined through ilmenite/clinopyroxene partitioning in garnet pyroxene*. In: Gurney, J.J., Gurney, J.L., Pascoe, M.D. and Richardson, S.H. (eds.) *7th International Kimberlite Conference*. Cape Town, South Africa: Red Roof Design, 986-988.

Zbyszewski, G. (1970). Levantamentos geológicos da ilha Graciosa (Açores), Memórias Academia Ciências Lisboa. *Ciências* **14**, 163-171.

Zbyszewski, G., Medeiros, A., Ferreira, V.O. and Assunçao, C.T. (1967). *Carta Geológica de Portugal na escala 1:25.000, notícia explicative da folha da ilha do Corvo (Açores)*. Lisboa: Serv. Geol. Portugal.

Zbyszewski, G., Medeiros, A., Ferreira, V.O. and Assunção, C.T. (1972). *Carta Geológica de Portugal na escala 1:25.000, notícia explicative da folha da ilha da Graciosa (Açores)*. Lisboa: Serv. Geol. Portugal.

ELECTRONIC SUPPLEMENT

Supplementary files for this PhD Thesis can be obtained on request to the author (plarreamarquez@gmail.com) and include the following auxiliary material:

- Chapter 5: full $^{40}Ar/^{39}Ar$ data results reported as given by the ArArCALC2.5 software.

- Chapter 6: electron microprobe results and structural formulae for olivine (Table 6.1), clinopyroxene (Table 6.2), feldspars (Table 6.3), amphibole (Table 6.4), opaque minerals (Table 6.5), apatite (Table 6.6), zircon, biotite, sphene and quarz (Table 6.7) analyzed from Graciosa lavas and xenoliths. Partition Coefficients used for the Rayleigh fractional crystallization models (Table 6.8).

- Chapter 8: electron microprobe results and structural formulae for clinopyroxene (Table 8.1), olivine (Table 8.2), plagioclase (Table 8.3), amphibole (Table 8.4), Fe-Ti oxides (Table 8.5) and Apatite (Table 8.6) analyzed from Corvo lavas, dikes and xenoliths. Partition Coefficients used for the Rayleigh fractional crystallization models (Table 8.7).